



**HAL**  
open science

# Non-Linear Dynamics in Semiconductor Nano-Structures for Signal Processing

Grégory Moille

► **To cite this version:**

Grégory Moille. Non-Linear Dynamics in Semiconductor Nano-Structures for Signal Processing. Optics [physics.optics]. Université Paris Saclay (COmUE), 2016. English. NNT : 2016SACLS174 . tel-01399135

**HAL Id: tel-01399135**

**<https://theses.hal.science/tel-01399135>**

Submitted on 18 Nov 2016

**HAL** is a multi-disciplinary open access archive for the deposit and dissemination of scientific research documents, whether they are published or not. The documents may come from teaching and research institutions in France or abroad, or from public or private research centers.

L'archive ouverte pluridisciplinaire **HAL**, est destinée au dépôt et à la diffusion de documents scientifiques de niveau recherche, publiés ou non, émanant des établissements d'enseignement et de recherche français ou étrangers, des laboratoires publics ou privés.

NNT: 2016SACLS174

**THALES**

**université**  
PARIS-SACLAY

THÈSE DE DOCTORAT  
DE  
L'UNIVERSITÉ PARIS-SACLAY  
PRÉPARÉE À  
L'UNIVERSITÉ PARIS-SUD

ÉCOLE DOCTORAL N°572  
Ondes et Matière  
Specialité de Doctorat: Optique & Photonique

Par

**Grégory Moille**

**Non-Linear Dynamics in Semiconductor  
Nano-Structures for Signal Processing**

Thèse présentée et soutenue à Palaiseau, le 4 Juillet 2016

**Composition du Jury**

Prof. Xavier Checoury (IEF, Université Paris Sud, France) ..... Président du Jury  
Prof. Dr. Allard P. Mosk (Utrecht University, Netherlands) ..... Rapporteur  
Prof. Christophe Peucheret (Foton - CNRS UMR, France) ..... Rapporteur  
Dr. Emilien Peytavit (IEMN, France) ..... Examineur  
Dr. Alfredo De Rossi (Thales Research & Technology, France) ..... Directeur de Thèse  
Dr. Sylvain Combrié (Thales Research & Technology, France) ..... Membre Invité

© Gregory Moille, 2016

All rights reserved

*All the pieces matter*

---

DET. LESTER FREAMON



# Remerciements

---

---

Tout d'abord, je tiens à remercier mon directeur de thèse, **Alfredo de Rossi**, qui a su m'apporter toute son aide et son expérience afin de mener ce projet à bien. Grâce à lui, j'ai appris ce que la recherche scientifique est, et ce que la science a à nous apporter.

Bien entendu, toutes ces vérités ci-dessus énoncées ne seraient vraies que si je prends aussi en compte la participation, et non des moindres, de mon encadrant **Sylvain Combrié**. Celui-ci fut autant indispensable, et sa contribution aussi importante que celle de mon directeur de thèse.

Ils ont su me guider de la meilleure des façons durant ces années. Je tiens aussi à leur présenter toute ma gratitude sur les enseignements et les discussions fertiles autour d'autres sujets que la science, et qui à mon goût, m'ont au moins tout autant apportées que leurs enseignements scientifiques.

Au terme de cette thèse, je pense, non seulement avoir rencontré deux collaborateurs pour des projets futurs, mais aussi deux scientifiques de très grande qualité ainsi que deux personnes possédant des qualités humaines remarquables.

Je tiens à remercier **Xavier Checoury** d'avoir accepté d'être le président du jury de cette thèse. Je remercie aussi **Christophe Peucheret** et **Allard P. Mosk** d'avoir accepté d'être rapporteurs, et leurs remarques pertinentes qu'ils ont su apporter à ce manuscrit. Enfin, je remercie **Emilien Peytavit** d'avoir accepté de faire parti de ce jury de thèse.

Je remercie **Gaëlle Lehoucq**, **Stephane Xavier** pour leurs soutiens et leur aide dans les étapes de fabrication des échantillons qui ont rendu cette thèse possible.

Aussi, je tiens à remercier les différents collaborateurs du groupe. Tout d'abord **Laurence Morgenroth** et **François Neuilly** qui ont rendu possible la fabrication d'une étape clé dans la réussite de cette thèse; l'ALD. Je remercie **Charlotte Tripon-Canselliet** pour les designs RF du projet. Aussi,

je tiens à remercier **Marie-Rose Sauvage** et **Guy Jestin** de la DGA qui ont suivi de très près le projet AUCTOPUSS. Je remercie les collaborateurs de l'IEF et LPN. Je tiens aussi à remercier **Chad Husko** qui, surtout en fin de thèse et dans la préparation de mon futur scientifique, peut être considéré comme le troisième encadrant.

Je remercie **Arnud Brignon** et **Daniel Dolfi** pour leurs dans les projets liés à cette thèse. Je remercie aussi toutes les personnes du laboratoire, qui ont contribué de prêt ou de loin a ce manuscrit: **Jérôme Bourderionnet**, **Aude Martin**, **Gilles Feugnet**, **Ludovic Mayer**, **Thierry Debuisschert** et **Matthieu Dupont-Nivet**.

Je remercie **David Shafer**, qui a pris le temps d'améliorer mon anglais et m'a grandement aidé dans les différents documents dans la langue de Shakespeare. Je le remercie aussi pour toutes les choses que j'ai pu apprendre à ses côtés, de l'histoire de Paris à la vie d'Antonin Artaud pour ne citer que cela.

Je remercie mes parents **Odette** et **Yves** qui m'ont toujours soutenu et encouragé quelques soient mes choix et, qui durant cette thèse ont toujours su répondre présent.

Je tiens aussi à remercier en particulier **Alison Shafer**. Elle a su m'aider et me soutenir durant ces années. Du mieux qu'elle a pu, elle a su apporter une parole à la fois bienveillante et réconfortante, remettant parfois, et pour le mieux, en perspective les affres d'une thèse. Ce manuscrit n'aurait pas été possible sans son aide. Pour ceci, elle aura pour toujours ma plus grande gratitude.

Enfin, **Gaïa** (mon chat), qui quoi qu'il arrive, reste fidèle à elle même.

# Contents

---

---

<b>Introduction</b>	<b>1</b>
<b>1 State of the Art</b>	<b>5</b>
1.1 Background and Concepts . . . . .	7
1.1.1 Sampling Vs Under-Sampling . . . . .	8
1.1.2 Optical Clocks . . . . .	10
1.1.3 Optically Assisted Sampling . . . . .	11
1.2 Photo-Conductive Switches . . . . .	12
1.2.1 Pioneer Work on Photoconductive Switches . . . . .	12
1.2.2 Use of Low-Temperature Grown GaAs . . . . .	13
1.2.3 Toward 1.5 $\mu\text{m}$ Photoconductive Switches on GaAs . . . . .	15
1.3 All-Optical Switches . . . . .	16
1.3.1 What is the All-Optical Switching? . . . . .	17
1.3.2 Physical Concept of All-Optical Switching Using Plasma Effect . . . . .	19
1.3.3 Technology Comparison . . . . .	20
References for Chapter 1 . . . . .	23
<b>2 Photonic Crystal Fabrication</b>	<b>31</b>
2.1 Self-Suspended Membrane . . . . .	33
2.1.1 Process for All-Optical Switches . . . . .	33
2.1.2 Toward Photoconductive Switch Fabrication — Metal Issues . . . . .	35
2.2 Polymer Adhesive Bonding for Photoconductive Switches . . . . .	40
2.2.1 Contact and Crystallization of Polymer . . . . .	41
2.2.2 Substrate Thinning . . . . .	43
2.3 Conclusion . . . . .	46
References for Chapter 2 . . . . .	47
<b>3 Theory and Modeling</b>	<b>49</b>
3.1 Carrier Transport in Patterned Semiconductor Structures . . . . .	51
3.1.1 Carrier Dynamics in Semiconductor and Approximations . . . . .	51
3.1.2 Drift-Diffusion Model . . . . .	53
3.1.3 Ambipolar Approximation . . . . .	56
3.1.4 Implementation with Finite Element Method . . . . .	57
3.2 Coupled Mode Theory . . . . .	61
3.2.1 Formalism . . . . .	62
3.2.2 Device Design and Experimental Benchmark . . . . .	64

3.2.3	Non-Linear Dynamics . . . . .	65
3.2.4	Free Carriers Dynamics . . . . .	67
3.2.5	Green's Function Formalism . . . . .	69
3.2.6	Impact of the Geometry on the Dynamics . . . . .	72
3.2.7	Linear Absorption . . . . .	75
3.2.8	Summary of the Green's Formulation Carrier Dynamics in CMT . . . . .	77
3.3	Conclusion . . . . .	77
	References for Chapter 3 . . . . .	79

## **4 All-Optical Signal Processing 83**

4.1	All-Optical Gate Made in InP . . . . .	85
4.1.1	Sample and Design . . . . .	85
4.1.2	Pump-Probe Measurement and Carrier Dynamics . . . . .	85
4.1.3	Homodyne Pump-Probe Measurement . . . . .	90
4.2	All-Optical Operation Using InP Photonic Crystal . . . . .	92
4.2.1	Wavelength Conversion At 10GHz . . . . .	92
4.2.2	All-Optical Frequency Down Conversion of Microwave Signal At 10GHz . . . . .	94
4.3	Gallium Arsenide Surface Mitigation Using Atomic Layer Deposition . . . . .	97
4.3.1	New Design and Waveguide Positions . . . . .	99
4.3.2	ALD Passivation . . . . .	101
4.3.3	Dynamics of the Free Carriers . . . . .	103
4.3.4	Passivation Effects . . . . .	106
4.3.5	Other Material . . . . .	107
4.4	All-Optical Operation Using GaAs Photonic Crystal . . . . .	109
4.4.1	Operation At GHz Rates . . . . .	109
4.4.2	Ultra-Fast Gating . . . . .	111
4.5	Towards Faster InP Photonic Crystal All-Optical-Gates . . . . .	114
4.5.1	Sample Description . . . . .	114
4.5.2	Time-Resolved Spectral Analysis . . . . .	116
4.5.3	Results and Discussion . . . . .	117
4.5.4	Modeling of P-Doped All-Optical Gates . . . . .	119
4.6	Conclusion . . . . .	120
	References for Chapter 4 . . . . .	122

## **5 Photo-conductives Switches at Telecom Wavelength 127**

5.1	Sample Design . . . . .	129
5.1.1	Optical Design . . . . .	130
5.1.2	Microwave Design . . . . .	138
5.1.3	Integration of Microwave Lines with Optical Resonator . . . . .	139
5.2	Results and Discussions . . . . .	141
5.2.1	Sample Basic Characterizations . . . . .	141
5.2.2	Microwave Characterization . . . . .	142
5.2.3	Signal Processing Operations . . . . .	149
5.3	Perspectives . . . . .	151
5.4	Conclusion . . . . .	153
	References for Chapter 5 . . . . .	155

<b>Conclusion and Perspectives</b>	<b>157</b>
<b>A Modeling</b>	<b>161</b>
A.1 Analytic Formulation for PN Junction . . . . .	161
A.1.1 PN Junction . . . . .	161
A.1.2 Carrier Density . . . . .	162
A.1.3 Band Diagram . . . . .	163
A.1.4 Current . . . . .	163
A.2 Coupled Mode Theory -- Supplementaries . . . . .	163
A.2.1 Approximations in the CMT . . . . .	163
A.2.2 Calculation of the Kerr and TPA Nonlinear Terms . . . . .	164
A.2.3 Approximations in Modeling the Carriers . . . . .	165
<b>B All-Optical Signal Processing</b>	<b>167</b>
B.1 Parameters Used for Modelling Pump-Probe Experiment . . . . .	167
<b>Acronyms</b>	<b>171</b>
<b>List of Symbols</b>	<b>173</b>
<b>Chemical Elements</b>	<b>175</b>
<b>List of Figures</b>	<b>180</b>
<b>List of Tables</b>	<b>181</b>



# Introduction

---

Digital signals are ubiquitous as also witnessed by our experience in every day life. The resulting ever increasing demand in bandwidth for communication and processing is producing a paradigm change in information technologies. In this picture, high-performance Analogical to Digital Converter (ADC) play a crucial role. On the one hand electric signals generated by sensors, imaging systems, radar, ... are analog, and on the the other hand data communications are nowadays based on complex modulation formats, ultimately resulting in analog signals. Therefore, high performance ADCs are therefore the interface between communication or sensing and computing; thus, their performance has a dramatic impact on the whole system.

The performance of ADCs has increased dramatically in terms of accuracy, thus the number of bits used are representing the analog value. However, their of bandwidth and speed performance did not follow the same trend. More precisely, accuracy, hence Effective Number Of Bits (ENOB) turns out to decrease very fast as the sampling rate increases above a few GHz. Timing jitter in the opening of the sampling gate has been identified as the dominant issue preventing accurate sampling at high speed. This has prompted radically new approaches involving the use of Mode-Locked Laser (MLL), because it has been shown that they are able to generate extremely regular trains of pulses with timing jitter orders of magnitude better than any electronic counterpart.

A variety of different architectures of photonic ADCs based on MLLs have been proposed and are currently actively investigated. This PhD thesis focuses on the optically assisted electronic sampling, where the the optical clock is used to control the opening of an electronic switch, and therefore bring a high accuracy operation. This minimizes the changes to existing electronic sampling systems and is promised to a relatively fast deployment. This approach was explored as early

as in the 70's, based on a photoconductive switch architecture. The system entails a coplanar line with a discontinuity on a semiconductor substrate. A laser pulse generates free carriers which close the switch and allow a sample of the electric signal to pass. The proof of concept was thus established long ago, however, critical issues such as speed and amplitude of the response have motivated the development of more suitable materials.

This PhD project has developed in the context of the research on high-performance photonic-assisted sampling at Thales and brings a major innovation, namely nanoscale patterning of the photoconductive switch. This allows the use of highly optimized and available fiber model-locked lasers as optical clocks. The underlying physics is enhanced nonlinear absorption owing to strong optical confinement into diffraction limited dielectric resonators. Thus, carrier can be generated efficiently in Gallium Arsenide, which is the preferred material for photoconductive switches. This conciliates the conflicting goals: keeping dark current low, which requires a large electronic band gap, such as in GaAs, and resorting to more affordable laser sources, operating in the Telecom spectral band, thus limiting the electronic band gap.

The foundations of this work have been established with recent research on nonlinear dynamics in GaAs Photonic Crystal (PhC) resonators at TRT. That provided knowledge on the design, fabrication and the physics, however the integration within a microwave coplanar line set a number of challenges and technical issues which were to be solved. First of all, a new design was required such that the quality factor of the PhC resonator is not spoiled by absorption in the nearby conductor. Second, the transport of photo-carriers due to the electric field was still poorly understood, as in such nano-patterned structures the role of geometry through strong surface effects requires an adequate modeling. On top of that, the fabrication of electrodes adds a number of supplementary fabrication steps which turned out to adversely affect the fabrication of high-quality PhCs resonators. Finally, surface recombination had to be mitigated in order to allow the population of photo-carriers to reach a large enough density.

This PhD project has reached the main objective, since the concept of a GaAs photoconductive switch based on a photonic crystal resonator has been demonstrated. Microwave signals up to 20 GHz have been successfully frequency down-converted to the first Nyquist band. The direction

---

towards optimized devices based on this design is now established. An important aspect of this approach is the energy efficiency, namely the relatively limited power budget. This is apparently at odds with the nonlinear nature of the operating principle, and, more importantly, brings an additional benefit in the context of the "green photonics" agenda.

Besides, the technology of nonlinear photonic crystals has been pushed forwards in many respects. First, surface passivation of complex geometries, such as PhCs, has been validated using Atomic Layer Deposition. This has enabled the demonstration of all-optical gates with 10 ps response. A new model for all-optical switches, accounting for the carrier diffusion rigorously, has been developed. The role of carrier transport in nano-patterned photoconductive switches has been understood and lays the foundations for the future development of optimized devices. Finally, all-optical sampling has been investigated as an alternative route for high-performance analog to digital conversion, for more long-term applications.

This manuscript is structured as follows. Chapter 1 describes the technological context of photonic assisted analog to digital conversion and low-jitter pulsed laser sources. The concepts of photo-conductive and all-optical sampling are also introduced. Finally, a state of the art of all-optical switches is summarized. Chapter 2 is devoted to the fabrication technology of the PhC photoconductive switch. I discuss here the several hurdles which have been overcome in the course of this project. Chapter 3 covers the theory and the modeling. This covers the solution of the drift-diffusion equations in complex geometries, and the discussion of surface effects and the implementation of a suitable model coupling carrier dynamics with the optical field in the cavity. Chapter 4 is about the experimental characterization of nonlinear PhC resonators and their use in the context of all-optical signal processing. An important aspect here is the demonstration of improved performances owing to the mitigation of the surface recombination. Also, GaAs is compared with other materials, specifically InP. Chapter 5 is devoted to the demonstration of a photoconductive PhC switch. Details covering the modeling are given in the appendix.



# Chapter 1

## State of the Art

---

---

In this chapter, a state of the art of the signal processing domain is discussed, especially with a focus on the limitation introduced by using electronic clock. In the perspective of larger bandwidth, lower clock jitter, and lower power consumption, it is introduced the benefit of using optical clock, either by performing electro-optic signal processing through photoconductive switch or by all-optical signal processing. It is also discussed why, with the target of using Telecom input sources as the clock, the use of the photonic crystal platform is highly suited for the optical signal processing.

### Contents

---

1.1	Background and Concepts . . . . .	7
1.1.1	Sampling Vs Under-Sampling . . . . .	8
1.1.2	Optical Clocks . . . . .	10
1.1.3	Optically Assisted Sampling . . . . .	11
1.2	Photo-Conductive Switches . . . . .	12
1.2.1	Pioneer Work on Photoconductive Switches . . . . .	12
1.2.2	Use of Low-Temperature Grown GaAs . . . . .	13
1.2.3	Toward 1.5 $\mu\text{m}$ Photoconductive Switches on GaAs . . . . .	15
1.3	All-Optical Switches . . . . .	16
1.3.1	What is the All-Optical Switching? . . . . .	17
1.3.2	Physical Concept of All-Optical Switching Using Plasma Effect . . . . .	19
1.3.3	Technology Comparison . . . . .	20
	References for Chapter 1 . . . . .	23

---



## 1.1 | Background and Concepts

With the development of communications, digital signals take a preponderant place in our everyday life, leading analog to digital conversion being a crucial point in electronic devices. Even if bandwidth and resolution are always tending to increase, the development of electronic converters from the state of the art is still highly challenging to follow this demanding trend. Numerical data systems such as high-performance computers, servers, high-speed network, radars, instrumentations, or even 3D imaging systems need ultra-broadband analog/digital conversion with Giga-samples per second (Gsamp/s) sampling rate for a resolution of at least 10 bits.

In the same way, microprocessors domain for Digital Signal Processing (DSP), on which lies a large range of applications, evolves tremendously fast, pushed by the development of high-performance numerical calculation, leading to a faster sampling system. However, the development of ADC, even if they are the key interface between digital and analog world, is still not fast enough to match applications.

Since 1999, no spectacular breakthrough happened in the electronics ADC domain, where improvements were only progressive, accordingly to Walden analysis [1]. Signal to noise ratio of electronics sampling systems is reaching the static and dynamics limitations. Indeed, as shown in Fig. 1-1, thermal noise appears as the major noise mechanism for high resolution and low bandwidth coders, where temporal aperture jitter and ambiguity (*i.e.* metastability of the ADC at high sampling speed) are the main factor limiting high speed converter [2]. The temporal aperture jitter corresponds to the deviation from true periodicity of a presumed periodic signal, in other words, the noise induced by the fact that the clock repetition rate is not ideal.

It is linked to the fact that thermal noise power increased proportionally with the coder bandwidth, whereas time jitter noise has a quadratic dependence on frequency. Thus, over a certain input frequency, time jitter limits the sampler resolution. Recently, a RMS jitter of 100 fs has been demonstrated with electronics ADC [3], nevertheless an Effective Number Of Bits (ENOB) of 8 has never been demonstrated over 5 GHz [4].

Several approaches have been studied further to improve the high-speed coder performances such as interlacing, over-sampling, *etc* .... It is worth to point out that some of those coder architectures mixes several techniques such as over-sampling and interlacing.

Another limiting element for high-speed ADCs is their power consumption. Thus, high-speed

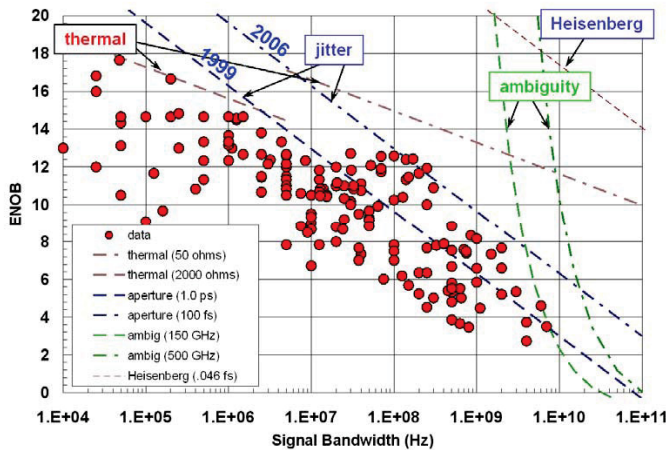


**Fig. 1-1** | Effective number of bits versus input frequency (from Walden *et al.* [1]). Physical limitation of the Effective Number of Bits (ENOB) are plotted in dashed lines

ADCs from refs. [5, 6] both reach bandwidth over 20 Gsamp/s, but with the cost of a power consumption of 1.2 W for 6 bits resolution and 10 W for 8 bits. Portable application of such modules is hardly conceivable, where the battery providing the energy would run out of charge too quickly. Also, such power consumption would lead to a large thermal dissipation, another drawback for portable application where efficient, thus large, heat-sinks cannot be implemented

### 1.1.1 | Sampling Vs Under-Sampling

Precisions are brought here on how to process analog signal by sampling. Sampling consists in the digitalization of an analog signal by extracting the values of the signal samples according to a fixed frequency (*i.e.* the clock frequency  $f_1$ ). This series of time samples is then converted into a digital value according to a binary coding. The gate, however, has an opening time ( $\tau_{gate}$ ), which determines the maximum frequency of the signal which could be processed.

Indeed, following the Shannon criterion [7], a signal at the frequency  $f_0$  must be sampled at a frequency greater than twice the signal frequency ( $f_1 > 2 \times f_0$ ) to avoid any information losses. However, when the sampling frequency is below twice the signal frequency ( $f_1 < 2 \times f_0$ ), and the  $n^{\text{th}}$  frequency component of the clock still follows the Shannon criterion in the instantaneous band, aliasing occurs. This regime is called undersampling. This can be useful, for instance, for the frequency down-conversion of high-frequency signals.

To understand the implications of aliasing in both the time and frequency domain, let us first consider three different cases for the sampling of a sine input signal. First, when  $f_1 = 4f_0$  (Fig. 1-2(a)) it is clear that an adequate number of samples have been taken to preserve the information

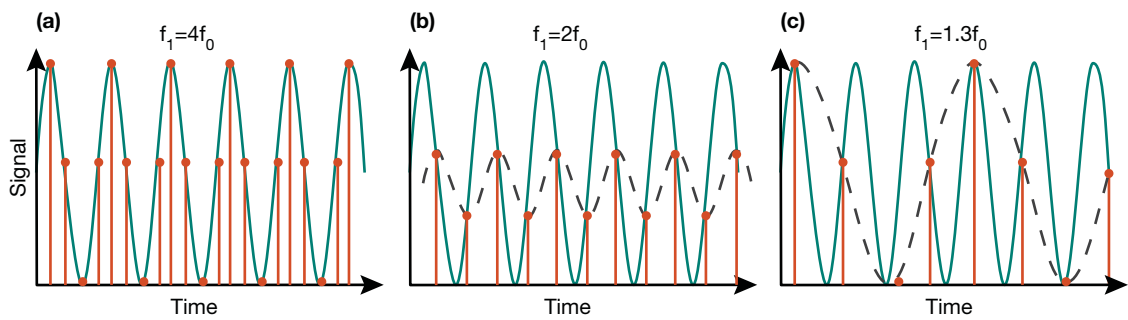


**Fig. 1-2** | Schematic of sampling for (a) the case of sampling when the clock is at a frequency  $f_1 = 4f_0$  – (b) clock at the Shannon criterion – (c) Case of undersampling when aliasing is appearing

about the sinewave. For the second case, the limit of the Shannon criterion is reached, and the ambiguous limiting condition of  $f_1 = 2f_0$  (Fig. 1-2(b)) where the input signal information are lost unless the sampling points are taken at the peaks of the sine function, which is highly unlikely. However, in the case of clock frequency below the Shannon criterion (Fig. 1-2(c)), the information obtained from the samples gives a sine function with the same amplitude than the input signal but with a frequency lower than  $f_1/2$ , thus the out-of-band signal is aliased into the Nyquist bandwidth between the DC frequency and  $f_1/2$ . As the sampling rate is decreased, and the analog input frequency  $f_0$  approaches the sampling frequency  $f_1$ , the aliased signal approaches the continuous signal (DC) in the frequency spectrum. This is the case of undersampling

Classical sampling over the Shannon criterion (when  $f_1 > 2f_0$ ) or undersampling ( $f_1 > f_0$ ) both have advantages and drawbacks. The main advantage of sampling is the processing gain as the number of samples taken is relatively high. The processing gain (*i.e.* the SNR of the processed signal) follows the trend :  $G_{proc} = 10 \log \left( \frac{f_1/2}{BW} \right)$ , where  $BW$  is the bandwidth of the signal. Therefore, increasing the sampling rate increases the processing gain.

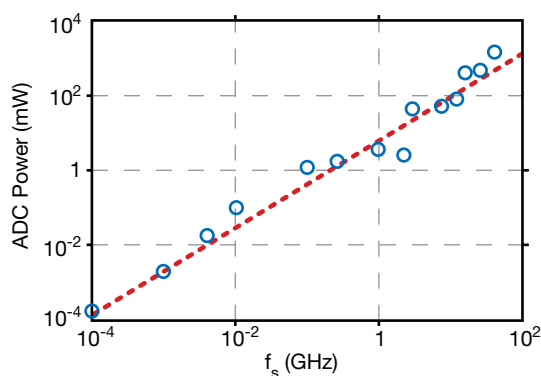


**Fig. 1-3** | Power consumption of the Analog to Digital Converter regarding the input signal frequency (image taken from [8]).

However, sampling at a high amount of samples by second leads to major drawbacks such as high power consumption (Fig. 1-3). Therefore, in the classical sampling processing chain, another block for frequency-down convert the sampled signal is introduced using a mixer. Thus, the output signal is brought to the frequency baseband using an Intermediate Frequency (IF) (Fig. 1-4(a)). The applications designer selects this IF. However, in the aim of simplifying the processing chain, thus reducing power consumption, using under-sampling already bring the sampled signal between the DC and  $f_1/2$ , thus in the first Nyquist band. No further stage of down-frequency conversion is needed (Fig. 1-4(b)) as this operation is inherently done during the undersampling process. Therefore, the signal under-sampled can directly be sent to a *hold* system in the processing chain.

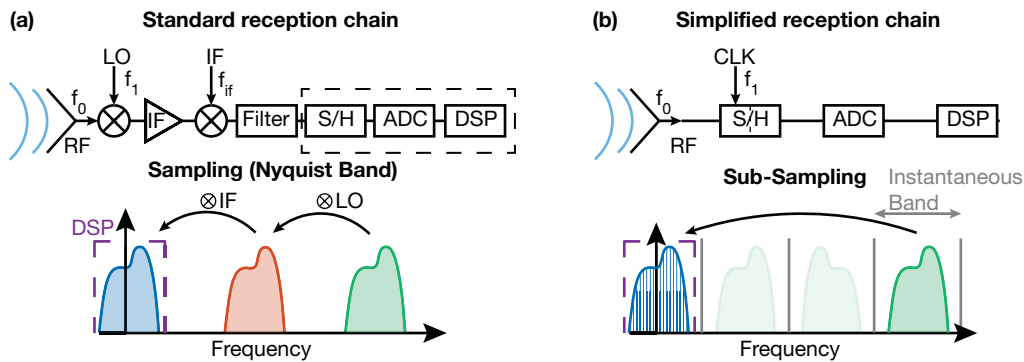


**Fig. 1-4** | (a) Signal processing chain used in the sampling case, where a first frequency translation is made through a Local Oscillator (LO), and then brought in the band with an other mixer with the Intermediate Frequency (IF) – (b) Sampling and frequency down-conversion case, where the clock is an impulsional equispaced train. The frequency down conversion is automatically done by having  $f_1 < 2f_0$

### 1.1.2 | Optical Clocks

To overcome the limitations of electronics and its limited temporal aperture jitter, in particular for high-speed applications such as very high-speed communication or electronic warfare, a new family of samplers had been proposed mixing optics and electronic quantifications. This approach lies on the unique characteristics brought by the optical domain. The potential of optics to improve the sampling bandwidth became obvious since the pioneer works initiated by Auston [9], Taylor [10], Tsunoda and Goodman [11] at the end of the 70s. A huge number of architectures based on those photonics approaches have been since proposed.

The main advantages of these optically assisted samplers are the fact that, on the one hand, the sampling mechanism taking place could be made highly linear while presenting a good isolation between the optic pulses and the signal to be sampled, and on the other hand, MLLs could be used

to generate very low temporal aperture jitter clock. Indeed, MLLs are pulsed optical sources where the repetition rate, which can be higher than 10 GHz, is extremely stable. The stability is such that the frequency comb in the spectral domain could be used to perform frequency metrology. It has been demonstrated that the time uncertainty between to pulses could drop as low as  $10^{-15}$  [12]. In 2012, Professor Kärtner's group from MIT has measured the phase noise (Fig. 1-5(a)) of a solid state MLL (Fig. 1-5(b)) at  $-203$  dBc/Hz at high frequency<sup>1</sup> and a temporal jitter of only 13 attoseconds<sup>2</sup> [13]. Highly more compact and cost-effective as solid state lasers, fiber MLLs also allow to reach remarkable precision, where the temporal aperture jitter is easily under 1 fs [14]

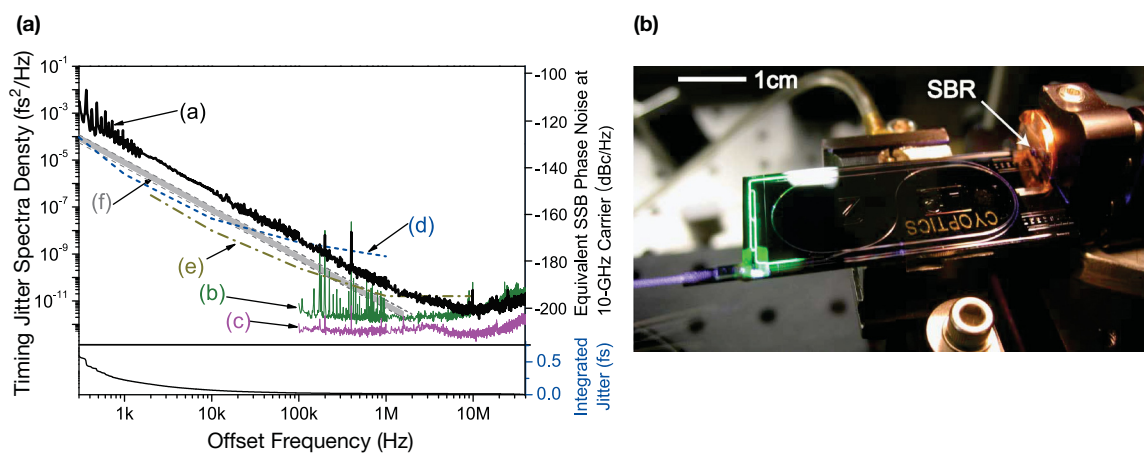


**Fig. 1-5** | (a) Jitter aperture regarding frequency, with below, the integrated jitter (image from [14]) – (b) Integrated mode-locked laser (image from [15])

### 1.1.3 | Optically Assisted Sampling

The use of optics, aside from bringing a lower aperture jitter, enables to carry the signal with low losses and multiplex broadband Radio Frequency (RF) signals thanks to optical fibers. Moreover, optical fibers are lighter, more robust and immune against electromagnetic perturbations when compared to standard radio-frequency cables. The ability to do so without degrading the opto-electronic link performance has long been unattainable. Recent advances in photonic systems (modulators, lasers, detectors) show that it is now possible to transport analog broadband signals over long distances with negligible degradations [16, 17], opening up many potential applications.

The accuracy of the clock is even more crucial that the center frequency of the sampled signal

<sup>1</sup>Where the radio-frequency carrier is considered at 10 GHz

<sup>2</sup>Measured by integrating the continuum noise until the Nyquist frequency of the pulse train, therefore 41 MHz.

( $f_{in}$ ) is high, because any temporal aperture jitter  $T_j$  translates into a noise according to the formula  $SNR = 20 \log \left( \frac{1}{\sqrt{2\pi} f_{in} T_j} \right)$  [18], where  $SNR$  is the signal over noise ratio. For example, if  $f_{in} = 10$  GHz and  $T_j = 10$  fs, then the signal to noise ratio associated with the window opening error is  $SNR = 67$  dB. This results in an upper limit to the number of effective bit  $ENOB = \frac{SNR - 1.76}{6.02}$

Comparing ADC technologies with these two criteria is shown in Fig. 1-5. It appears clearly that the opening jitter of the *gate* of the sampler is the limiting factor for a high signal to noise ratio. This is directly related to the clock properties which control the gate. Currently, the temporal aperture jitter in the electronic ADCs is around 100 fs.

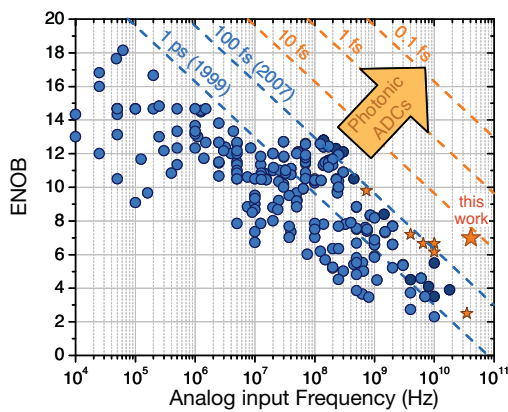


**Fig. 1-6** | Effective number of bits versus input frequency (from Khilo *et al.* [19]). The further improvement brought by the optical domain are highlighted through the dashed lines

Due to their very low intrinsic jitter, MLLs are used as a clock for the control of ADC. We call this mode *sampling assisted photonics*. The first *photonics* sampling systems are at the level of the best *traditional* ADC (Fig. 1-6). Recently, a consortium led by MIT (Prof. E. Ippen) demonstrated a photonic ADC limited by a jitter of about 15 fs, which is an order of magnitude better than traditional ADC [19].

This justifies a keen interest in the photonics ADC approach and motivates the study proposed here.

## 1.2 | Photo-Conductive Switches

### 1.2.1 | Pioneer Work on Photoconductive Switches

The first and a maybe more intuitive way to process RF signal with an optical clock is to use a photoconductive switch system. The principle of a photoconductive switch was first introduced in pioneer work of Auston in the mid-70s [9], where the RF electric signal is carried through a microstrip line where a discontinuity (*i.e.* a gap) is introduced. A high resistivity semiconductor is

placed in this discontinuity (in the case of Auston, Silicon with a resistivity of  $10^4 \Omega \cdot \text{cm}$ ), making the transmitted signal through the gap weak. This discontinuity is lightened from the top by the optical clock. Carriers are photogenerated in the RF discontinuity, reducing the resistivity of the gap. Therefore, the RF signal can cross the discontinuity when carriers are present in the semiconductor (ON state). When carriers are fully recombined, the resistivity of the material returns to its high initial state value (OFF state). Thus, the full dynamics of the gate is determined by the carrier lifetime of the material.

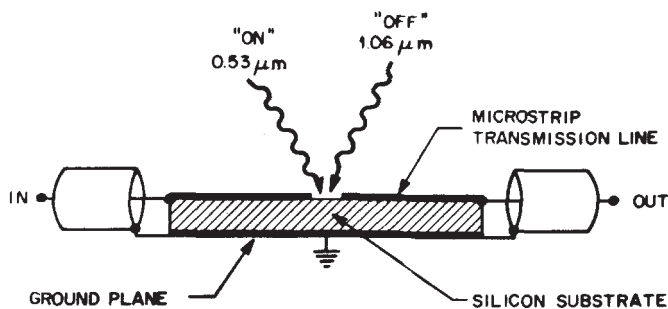


Fig. 1-7 | Auston's schematic of a photoconductive switch made in Si based on a push-pull approach, leading to tenth of picosecond resolution (image taken from [9]).

Because of long carrier lifetime on Si, Auston developed a *push-pull* approach to fastening the electrical response of the photoconductive switch. First, an optical pulse at 530 nm generates carriers at the top of the Si bulk, providing the ON state. Then, a delayed pulse at  $1.06 \mu\text{m}$  wavelength lightens the MicroWave (MW) gap, generating carriers in the whole Si bulk. Thus, a short circuit is made between the transmission line and the ground: an OFF state is reached. This technique allows to sample signal with a time resolution of about 30 ps. However, the main drawbacks of this technique are the use of two delayed pulses, and the fact that even with a fast recovery, the sampling frequency rate of the ON state is still driven by the recovery of the carrier lifetime, as the carriers enabling the short-circuit need to have recombined before another optical clock pulses generate another ON state.

### 1.2.2 | Use of Low-Temperature Grown GaAs

Since this pioneering work, many improvements were made to provide good photoconductive switches with only one pulse for the optical clock.

To provide good temporal resolution, reducing the carrier lifetime has been thoroughly investigated. The most direct way of reducing carrier lifetime is to introduce trap defects. Usually, ion-implantation is the preferred solution to reduce carrier lifetime in Silicon [20] or III-V ma-

terial [21]. Non-radiative recombination through traps are described by the Shockley-Reed-Hall model such that:

$$R = \frac{NP - n_i^2}{P + N + 2n_i \cos\left(\frac{E_i - E_t}{k_B T}\right)} N_t v_{th} \sigma \quad (1.1)$$

where,  $N, P$  are the electron and hole concentrations respectively,  $n_i$  is the intrinsic carrier concentration,  $E_t$  is the energy level position of the traps,  $E_i$  the intrinsic energy,  $\sigma$  the cross-section of the trap,  $v_{th}$  the thermal velocity and  $N_t$  the density of traps. Thus, increasing the trap density will increase the recombination rate accordingly, leading to a shorter carrier lifetime defined as

$$\tau = \frac{1}{N_t v_{th} \sigma}.$$

However, increasing the trap density leads to higher dark current, thus lower OFF resistance. This is problematic as the better the ON/OFF resistance ratio is, the better the signal to noise ratio will be. The dark current in the case of undoped photoconductive switches with a high density of traps follows two different physical mechanisms [22]: generation-recombination current without illumination and trap-assisted tunneling current. The first one tends to create carriers thermally at the energy trap leading to a further recombination, thus to a current. The second one corresponds to the leap of generated carriers from one trap state at a given position in space to the other one further away. These two dark currents are both proportional to the density of traps [22–24], therefore reducing the OFF resistance.

Focusing on III-V material, especially GaAs, was on great interest as the intrinsic carrier mobility is larger than in Silicon, therefore, leading to a better conductivity under illumination as  $G \propto (N\mu_n + P\mu_p)$ , where  $\mu_{n,p}$  is the mobility for the electrons and holes respectively.

However, the same issue of long carrier lifetime in bulk GaAs happens, reducing the bandwidth of photoconductive switches made of this material without using the *push-pull* trick. To further decrease the carrier lifetime to a few picoseconds, the density of defects needs to be extremely high, which is hard to achieve with ion-beam implantation without further degradation of the crystalline properties of the material. However, since the work of Smith *et al* showing that GaAs grown with Molecular Beam Epitaxy (MBE) at low temperature (LTG) enables a carrier lifetime of 1.6 ps [25]. Further investigations led by Gupta *et al.* demonstrated that carrier lifetime could be reduced below the picosecond using this material [26]. All these studies made the low-temperature technique the premium choice to grow fast carrier lifetime materials. Since then, LTG-GaAs is the material of choice for photoconductive switches. Besides, it was shown that introducing many

defects to deteriorate the carrier lifetime through a low-temperature process does not degrade the OFF resistance [27]. One explanation for this still high OFF resistance is the fact that low temperature growing process creates defect clusters (through As clusters), instead of uniformly distributed ones [28]. Therefore, the process of trap-assisted tunneling is significantly reduced as the defects are spatially well separated from each other.

This material has been thoroughly investigated for GHz [29–31] and THz applications [32–36]. Last, and not least, it also had been proven to be CMOS compatible [37].

All those approaches, for THz or GHz applications, use direct absorption of light to photo-generate carriers. Therefore, the input light needs to have an energy higher than the GaAs band gap ( $E_g=1.424$  eV) which corresponds to a wavelength below 870 nm. Using such wavelength does not benefit from the different improvements made by telecom wavelength range light sources. It is true that efficient 800 nm fiber MLLs exist and are commercialized, however, for industrial application, compact and low-cost 1.5  $\mu\text{m}$  MLLs (either made of fiber or semiconductors) are common and are the easiest wavelength range for further integration.

### 1.2.3 | Toward 1.5 $\mu\text{m}$ Photoconductive Switches on GaAs

In order to use 1.5  $\mu\text{m}$  input wavelength to photo-generate carriers in regular GaAs, non-linear interactions must happen, *i.e.* Two Photon Absorption (TPA). In this process, two photons with an energy lower than the semiconductor band gap are simultaneously absorbed, thus adding their energy which is higher than the band-gap energy, to create an electron-hole pair. The generation rate corresponding to this phenomenon is:

$$G(\mathbf{r}, t) = \frac{K_{TPA}}{\hbar\omega V_{TPA}} |\mathbf{E}(\mathbf{r}, t)|^4 \quad (1.2)$$

with  $\omega$  the pulsation of the input light,  $V_{TPA}$  the generation volume through the TPA process (see section 3.2 for further details),  $\mathbf{E}(\mathbf{r}, t)$  the electric field vector in the structure,  $K_{TPA} = \beta_{TPA} c_0^2 / 2$ , where  $\beta_{TPA}$  is the TPA coefficient.

Using cavities to enhance the optical electric field, the two-photon absorption process can become energetically efficient enough. Moreover, reducing the carrier generation volume  $V_{TPA}$  can significantly improve this process.

PhCs, which are a periodic modulation of the optical index of a material by creating holes in it [38], can provide high  $Q$ -factor cavities. Cavities  $Q$ -factor over a million are now commonly

modeled and fabricated using different design [39–43], resulting in a photon lifetime in the cavity in the range of the nanosecond.

Also, PhC cavities have been proven to be the smallest modal volume in the range of dielectric cavities designs available at the time this thesis was written [44], with a routinely achieved volume of  $2(\lambda/2n)^3$ , which is twice the diffraction limit.

Combining strong confinement with a long cavity lifetime results into a dramatic enhancement of light-matter interaction, and of nonlinear effects in particular. This is crucial, as the change in refractive index induced by an optical field is intrinsically weak so that a large optical irradiance (of the  $\text{GW}\cdot\text{cm}^2$  in semiconductors and much more in silica glass [45]) is typically required to achieve a noticeable effect. Therefore, using PhC cavity leads to an efficient TPA process and high generated carrier concentration (in the order of  $10^{17} \text{ cm}^{-3}$ ).

In PhC technology, classically grown (in contrast with the LTG-GaAs) GaAs or InP are used, therefore no intentional traps defects are created. However, the volume over surface ratio is in the order of 100 nm, lower than the carrier diffusion (see section 3.1). Thus, the surface states play a crucial role in the carrier dynamics.

Surfaces being a break of the symmetry in the crystalline structure of the III-V material, defects are naturally created tending to recombine carriers. Thanks to this property, the average carrier lifetime in PhC structure are is the order of 100 ps for InP and the picoseconds range for GaAs normally grown. Even if LTG-GaAs still provide a high OFF resistance, using a classical GaAs is still better, due to the lower concentration of defect.

In conclusion, PhC cavities enable the two-photon absorption process to efficiently photo-generate carriers at  $1.5 \mu\text{m}$  incident optical wavelength, while the carrier lifetime is still suitable for GHz switching operation without the use of deteriorated material.

### 1.3 | All-Optical Switches

Using an optical clock to lower the clock jitter and thus, reducing error in the signal processing with the under-sampling scheme can be done in an optoelectric way where only the clock is in the optical domain while the signal remains in the electric one. However, these operations could be done entirely in the optical domain. The main advantages brought by doing it this way is the very low transmission losses through long distance using fiber optics. Also, this enables to put

aside the antenna from the signal processing chain (*i.e.* radio on fiber), import point for radar antennas. Therefore, instead of using an electric RF signal which needs to be converted priorly to be processed, doing the operation optically avoids unnecessary conversion thus could be more power efficient. Another crucial point for an onboard system is the dissipated heat. Using electrical sampling devices, high-frequency generation operations results in a significant thermal dissipation. Using all-optical signal processing, this heat does not occur. Finally, optical non-linear effect such that Kerr effect, four-wave mixing or even carrier dispersion through inter-subband transition could process the signal at a really high frequency up to the THz [46, 47]. However, in this thesis, we will focus on the photogenerated carrier dispersion effect changing the optical index locally. This effect is lower than the ones cited above but has been proven to be highly efficient with a single switch operation at 1 fJ[48].

### 1.3.1 | What is the All-Optical Switching?

All-optical switching refers to a nonlinear process whereby a physical system changes its state in response to an optical excitation, such that optical response to any other simultaneous or following optical excitation is modified. As an example, an optical resonator filled with a material with an index of refraction dependent on the intensity of the optical field is bistable. Gibbs [49] demonstrated optical bistability where a cell containing sodium vapor was inserted in a Fabry-Pérot optical cavity. Na vapors, when excited near to its optical transition, respond by modifying the effective refractive index and, as a result, the resonance of the cavity becomes power-dependent (Fig. 1-8a). When the cavity is excited, its resonance will change, which will reduce the initial detuning. As a consequence, more optical energy will be stored in the cavity. This triggers a positive feedback, eventually resulting in a steep increase of the stored energy as the excitation overcomes a threshold  $P_2$ . Similarly, a sharp transition occurs when the power is reduced below a level of  $P_1 < P_2$ . When the input power level is set between  $P_1$  and  $P_2$ , the cavity can either be in a state of large or small stored energy, only depending on the *history* (Fig. 1-8b). The system investigated by Gibbs represented the first implementation of an optical memory based on the nonlinear index change.

An optical memory and, more generally, all-optical switching devices are unique as they enable the processing of optically encoded signals without conversion in the electrical domain. This could greatly simplify the architecture of optical routers, and thereby enhance their potential for

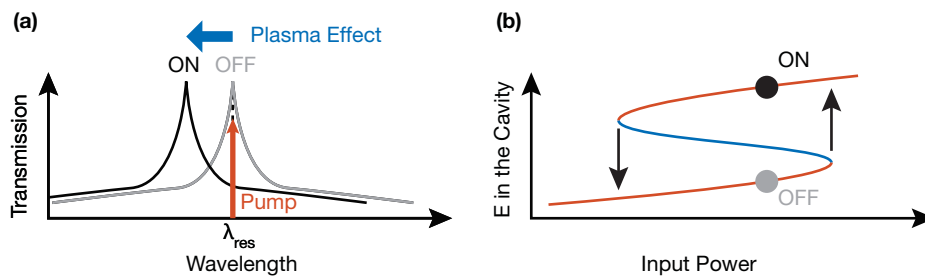


**Fig. 1-8** | Switching based on a resonant cavity. a) The optical excitation induces a nonlinear shift of the transmission spectra. This corresponds to a positive feedback leading to a bistable response revealed in the plot on the right (b). The two stable branches (on and off states) are represented in red.

miniaturization. More generally, an optical switching device would complement existing optical technologies, where they could be used for signal pre-processing.

On a more fundamental standpoint, nonlinear optical cavities offer a rich phenomenology: a Hopf bifurcation is associated with the transition from bistability to self-pulsing [50], a regime where the level of the energy inside the cavity spontaneously undergoes a periodic oscillation, although the input is constant. Interestingly, the frequency of the oscillation can be controlled. Recently, within a collaboration between the group of Prof. Trillo and TRT, this phenomenon was predicted in PhC cavities owing to carrier-induced nonlinear index change [51] and later on demonstrated experimentally by others [52]. A related optical phenomenon also demonstrated in nonlinear PhC cavities is the excitability [53, 54]. A radically different effect is obtained if the nonlinear response is faster than the cavity photon lifetime. In this case, the *color* of the photons stored in the cavity can be changed adiabatically [55], a process reminiscent of acoustic frequency chirp induced in string musical instruments as the strain is increased suddenly. Similarly, a fast change of the cavity Q-factor could be used to trap energy into it for an arbitrarily long lapse of time [56].

The practical interest in all-optical switching and the perspective to implement these original concepts into an entirely new class of devices depends strongly on the availability of a photonic technology ensuring integration, a fast response, and manufacturability. In this perspective, semiconductor integrated photonic circuits appear as a suitable candidate, as semiconductors have two advantages, compared to other optical materials: first, processing technologies are extremely advanced. This is true for silicon, hence the recent emphasis on Silicon Photonics, but also for III-V materials, such as InP and related alloys. Complex optical structures with sub-wavelength patterning are feasible. Combined with their large refractive index, this enables an extremely tight optical

confinement. Remarkably, a single-mode optical cavity confining the energy within a volume of about  $2(\lambda/2n)^3$ , that is twice the diffraction limit, is routinely achieved using two-dimensional photonic crystals. Secondly, the non-linearity of semiconductor is high enough to provide power efficient non-linear operations.

### 1.3.2 | Physical Concept of All-Optical Switching Using Plasma Effect

Switching and optical bistability were demonstrated in PhC cavities based on Silicon [57]. The switching results from two-photon absorption exciting plasma of free carriers. These photo-generated carriers result in the modification of the absorption coefficient, thus the optical index  $n$  by a value  $\delta n$ . Three different mechanism appears in the index change [58]: band-gap shrinkage, band-gap filling (Burstein-Moss effect) and free-carrier dispersion. In the case of the use of InP or GaAs photonic crystal cavities using TPA at  $1.5 \mu\text{m}$ , the band-gap shrinkage contribution is highly negligible [58–60]. At this wavelength, the major contribution remains the free-carrier dispersion, which modifies the reactive index and tends to blue shift the resonance of the cavity (Fig. 1-8a), and leads to a bistability (Fig. 1-8b).

The whole recovery dynamics of the system, for relatively short photon lifetimes (of the order of the picoseconds), is entirely dependent of the carrier lifetime. As previously mentioned, PhCs enable a fast carrier recombination owing to the surface over volume ratio. However, in the case of electro-optics systems, as the active material was placed between two electrodes, the whole carrier concentration in between of these contacts was playing a role in the resistance modification of the RF gap, even if they are diffusing away from their generation area. Thus, the dynamics of such system is mostly driven by the carrier lifetime. Here, only the carrier concentration profile overlapping with the optical mode have an effect on the refractive index modification of the resonance, leading to the definition of an effective carrier concentration  $N_{eff}(t) = \frac{1}{2} \int_V N(\mathbf{r}, t) \mathbf{U}(\mathbf{r}) dV$ , where  $\mathbf{U}(\mathbf{r})$ , is the electrical spatial mode of the cavity. Therefore, the dynamics of the all-optical switch is determined by the carrier lifetime but also the carrier propensity to diffuse away from the generation area, *i.e.* the optical mode. As the generation volume in PhC cavity is very small, carrier diffusion happens to be faster than carrier recombination in most of the III-V material or Si [61]. Therefore, the trend of the effective carrier concentration follows, in the first approximation, a double exponential decay with a fast time constant corresponding to the fast diffusion and a slower one depending on the carrier recombination at the surface (Fig. 1-9)

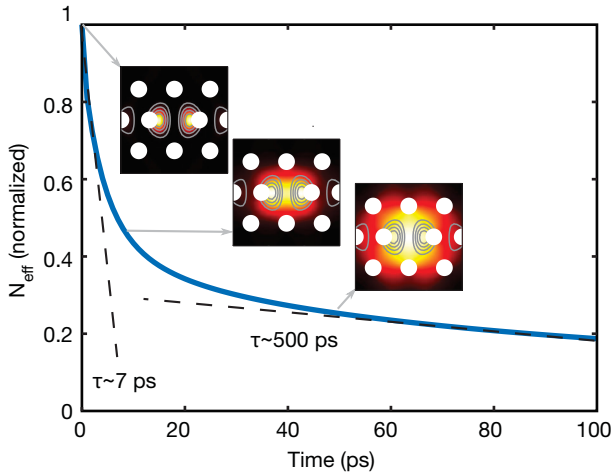


**Fig. 1-9** | Normalized effective concentration in time, modeled with FEM tool. The two exponential decays are represented through their characteristic time with dashed lines. The insets correspond to the normalized concentration profile  $N_{eff}$  (red mapping) at the corresponding time. The concentration profile at  $t = 0$  is represented with gray level lines.

Using free-carrier dispersion based all-optical switch has been proven to be still fast enough to efficiently make a switch operation in the order of the tenth of picoseconds, using Si [57, 62], InP [59, 63, 64] and encouraging results using GaAs [65]. However, this last material presents a carrier lifetime so short that carrier concentration does not build up enough to provide an efficient refractive index change. In this thesis, a focus was done on this material and an efficient improvement by conforming coating was observed, leading to the enhancement of the carrier lifetime allowing all-optical processing using GaAs for the first time (*c.f* section 4.3).

The next step to move from a signal switch to an efficient signal processing system was already shown in 2013 using InP here in Thales, allowing wavelength conversion up to 10 GHz frequency repetition [66], and all-optical signal processing though under-sampling at 12 GHz [67]. However, using InP, this frequency rate is the above limit, and other techniques need to be used to go faster, such as ion-implantation [62] or quantum-well-based PhC InP slab to even reduce further carrier lifetime [68]

### 1.3.3 | Technology Comparison

A variety of chip-scale all-optical switches has been implemented on different materials and geometries. A tentative comparison is attempted here by considering two criteria: the energy required for switching ( $E_{sw}$ ) and the recovery time ( $\tau_r$ ) characterizing the response. In the specific case of nonlinear resonators (quality factor  $Q$  and mode volume  $V$ ) and in the continuous wave limit, it is shown that the minimum power for observing bistable switching is  $P_{min} \propto n_2 V Q^{-2}$  [83], assuming instantaneous (e.g. Kerr) index change  $\Delta n = n_2 I$ . This suggests a connection between

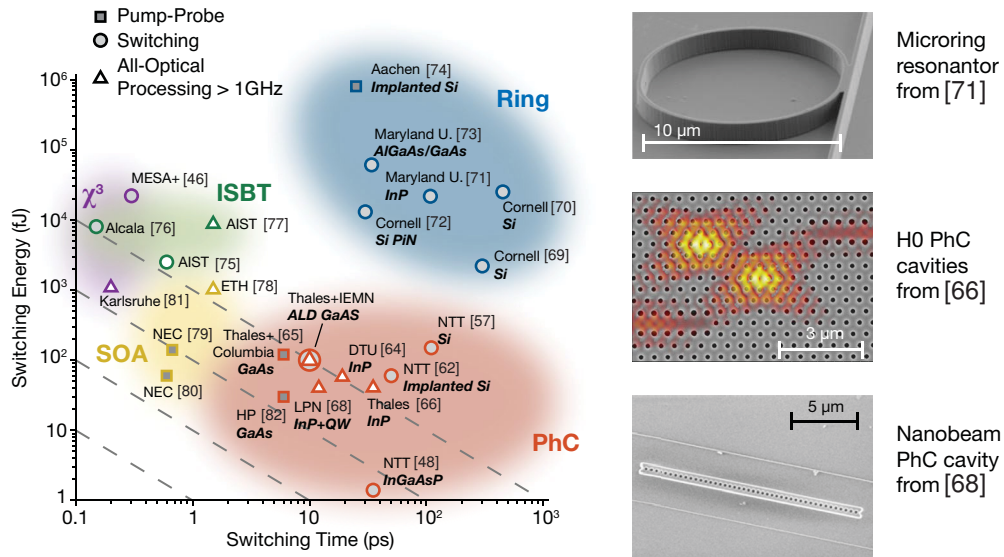


**Fig. 1-10** | Comparison of switching devices as a function of the recovery time  $\tau_r$  and switching energy  $E_{sw}$ . Marks relates to the degree of maturity of the devices. Squares: dynamics only, filled circles: switching with contrast  $> 3$  dB, filled triangles: switching with control pulse repetition rate  $> 1$  GHz. On the right, SEM images of the different cavity types for all-optical switching.

the device bandwidth, namely the recovery time,  $\Delta\omega = 1/\tau_r \propto Q^{-1}$ , and the operating power  $P_{min} \approx E_{sw}/\tau_r$ , i.e.:

$$E_{sw}\tau_r = const \times n_2V \quad (1.3)$$

Thus, keeping the same technology (hence the nonlinear response of the material  $n_2$ ) and geometry ( $V$ ) still leaves the possibility of optimizing either for speed or energy. Although nonlinearity cannot always be considered to be instantaneous, and might entail a more involved dependence on the optical field, the above equation still provides guidance for comparing results represented in Fig. 1-10.

Additional symbols (triangles for all-optical switching at a clock repetition rate over 1 GHz, circle for switching under this repetition rate and squares for only pump-probe measurement) have been added to underline the maturity of the switch for practical operation. The First is the measurement of the device dynamics, e.g. how fast it recovers and how much energy it needs, using pump-probe techniques (squares in Fig. 1-10). The second level (circles) implies effective switching action, whereas the optical control and the signal are distinguishable and true gating operation can be demonstrated (increase of the transmission with  $> 3$  dB contrast). The upper level relates to handling a repetition rate for switching (hence the pump pulse rate) which is

meaningful for applications; here we set the threshold at  $f_{rep} > 1$  GHz (triangles).

The general conclusion is that, indeed, faster devices tend to require more energy. It is also apparent that devices with smaller mode volume (e.g. photonic crystal vs. ring cavities) or larger nonlinear response (e.g. quaternary InGaAsP alloy vs. GaAs) will consume less energy. Plasmonic cavities volume can be much smaller, potentially allowing for a substantial enhancement of the optical field; however, this comes at the expense of a strong interaction with the electron plasma and, as a consequence, the photon lifetime tends to approach the electron-electron scattering time, which is about 10 fs in ordinary metals. This explains why plasmonic resonances are very broad [84]. Thus, the relevant figure of merit in switching, which weights the index change with absorption, is spoiled by the very large attenuation of the optical field in plasmonic resonators. If efficiency is a goal, then losses is a concern.

More advanced materials, exploiting, for instance, enabling inter-subband transitions, have demonstrated very fast all-optical switching (e.g. optical demultiplexing from 160 Gb/s to 40 Gb/s) [77]. Active devices (SOA) have been widely used and enabled the demonstration of fast gating, however, they need electric bias to ensure gain, and thus leads to a higher power consumption (not reported in Fig. 1-10). Furthermore, they are arranged in the so-called *push-pull* configuration, where the slow time constant is canceled out, but still prevents use with fast repetition rates. What is specific to our device is that it is qualified for all-optical signal processing (rep. rate  $> 1$  GHz) and provides a relatively short gating window (10 ps).

## References for Chapter 1 – State of the Art

- [1] R. H. Walden. *Analog-to-digital converter survey and analysis*. IEEE J. Select. Areas Commun. **17** (1999). – pp. 7–8.
- [2] P. W. Juodawlkis, J. C. Twichell, G. E. Betts, J. J. Hargreaves, R. D. Younger, J. L. Wasserman, F. J. O'Donnell, K. G. Ray, and R. C. Williamson. *Optically sampled analog-to-digital converters*. IEEE Transactions on Microwave Theory and Techniques **49** (2001). – p. 7.
- [3] B. Murmann. *A/D converter trends: Power dissipation, scaling and digitally assisted architectures*. 2008 IEEE Custom Integrated Circuits Conference. (2008). – p. 7.
- [4] T. D. Gathman and J. F. Buckwalter. *An 8-bit Integrate-and-Sample Receiver for Rate-Scalable Photonic Analog-to-Digital Conversion*. IEEE Trans. Microwave Theory Techn. **60** (2012). – p. 7.
- [5] P. Schvan, J. Bach, C. Falt, P. Flemke, R. Gibbins, Y. Greshishchev, N. Ben-Hamida, D. Pollex, J. Sitch, S.-C. Wang, and J. Wolczanski. *A 24GS/s 6b ADC in 90nm CMOS*. 2008 IEEE International Solid-State Circuits Conference - Digest of Technical Papers. (2008). – p. 8.
- [6] K. Poulton, R. Neff, B. Setterberg, and B. Wuppermann. *A 20-GSample/s 8b ADC with a 1-MByte Memory in 0.18-um CMOS*. (2003). – p. 8.
- [7] R. J. Marks. *Introduction to Shannon sampling and interpolation theory*. Springer-Verlag New York, Inc., 1991. – p. 8.
- [8] M. Elbadry and R. Harjani. *Quadrature Frequency Generation for Wideband Wireless Applications*. Springer, 2015. – p. 9.
- [9] D. H. Auston. *Picosecond optoelectronic switching and gating in silicon*. Appl. Phys. Lett. **26** (1975). – pp. 10, 12–13, 131.
- [10] H. Taylor. *An optical analog-to-digital converter - Design and analysis*. IEEE J. Quantum Electron. **15** (1979). – pp. 10, 94.
- [11] Y. Tsunoda and J. W. Goodman. *Combined optical AD conversion and page composition for holographic memory applications*. Appl. Opt. **16** (1977). – pp. 10, 94.
- [12] R. Holzwarth, M. Zimmermann, T. Udem, and T. W. Hansch. *Optical clockworks and the measurement of laser frequencies with a mode-locked frequency comb*. IEEE J. Quantum Electron. **37** (2001). – p. 11.
- [13] A. J. Benedick, J. G. Fujimoto, and F. X. Kärtner. *Optical flywheels with attosecond jitter*. Nature Photon. **6** (2012). – p. 11.
- [14] T. K. Kim, Y. Song, K. Jung, C. Kim, H. Kim, C. H. Nam, and J. Kim. *Sub-100-as timing jitter optical pulse trains from mode-locked Er-fiber lasers*. Opt. Lett. **36** (2011). – p. 11.

- [15] H. Byun, A. Hanjani, D. Pudo, J. Shmulovich, E. P. Ippen, and F. X. Kärtner. *Integrated Low-Jitter 400-MHz Femtosecond Waveguide Laser*. IEEE Photon. Technol. Lett. **21** (2009). – p. 11.
- [16] T. R. Clark, M. Currie, and P. J. Matthews. *Digitally linearized wide-band photonic link*. J. Lightwave Technol. **19** (2001). – p. 11.
- [17] J. D. McKinney and K. J. Williams. *Sampled Analog Optical Links*. IEEE Transactions on Microwave Theory and Techniques **57** (2009). – p. 11.
- [18] G. C. Valley. *Photonic analog-to-digital converters*. Opt. Exp. **15** (2007). – p. 12.
- [19] A. Khilo, S. J. Spector, M. E. Grein, A. H. Nejadmalayeri, C. W. Holzwarth, M. Y. Sander, M. S. Dahlem, M. Y. Peng, M. W. Geis, N. A. DiLello, J. U. Yoon, A. Motamedi, J. S. Orcutt, J. P. Wang, C. M. Sorace-Agaskar, M. A. Popović, J. Sun, G.-R. Zhou, H. Byun, J. Chen, J. L. Hoyt, H. I. Smith, R. J. Ram, M. Perrott, T. M. Lyszczarz, E. P. Ippen, and F. X. Kärtner. *Photonic ADC: overcoming the bottleneck of electronic jitter*. Opt. Exp. **20** (2012). – p. 12.
- [20] P. J. Simpson, M. Vos, I. V. Mitchell, C. Wu, and P. J. Schultz. *Ion-beam-induced damage in silicon studied using variable-energy positrons, Rutherford backscattering, and infrared absorption*. Phys. Rev. B **44** (1991). – p. 13.
- [21] M. B. Johnson, T. C. McGill, and N. G. Paulter. *Carrier lifetimes in ion-damaged GaAs*. Appl. Phys. Lett. **54** (1989). – p. 14.
- [22] V. Gopal, S. K. Singh, and R. M. Mehra. *Analysis of dark current contributions in mercury cadmium telluride junction diodes*. Infrared Phys. Technol. **43** (2002). – p. 14.
- [23] S. Velicu, R. Ashokan, and S. Sivananthan. *A model for dark current and multiplication in HgCdTe avalanche photodiodes*. J. Electron. Mater. **29** (2000). – p. 14.
- [24] J. Y. Wong. *Effect of trap tunneling on the performance of long-wavelength  $Hg_{1-x}Cd_xTe$  photodiodes*. IEEE Trans. Electron Devices **27** (1980). – p. 14.
- [25] F. W. Smith, H. Q. Le, V. Diadiuk, M. A. Hollis, A. R. Calawa, S. Gupta, M. Frankel, D. R. Dykaar, G. A. Mourou, and T. Y. Hsiang. *Picosecond GaAs-based photoconductive optoelectronic detectors*. Appl. Phys. Lett. **54** (1989). – p. 14.
- [26] S. Gupta, M. Y. Frankel, J. A. Valdmanis, J. F. Whitaker, G. A. Mourou, F. W. Smith, and A. R. Calawa. *Subpicosecond carrier lifetime in GaAs grown by molecular beam epitaxy at low temperatures*. Appl. Phys. Lett. **59** (1991). – p. 14.
- [27] I. S. Gregory, C. Baker, W. R. Tribe, M. J. Evans, H. E. Beere, E. H. Linfield, A. G. Davies, and M. Missous. *High resistivity annealed low-temperature GaAs with 100 fs lifetimes*. Appl. Phys. Lett. **83** (2003). – p. 15.
- [28] A. C. Warren, J. M. Woodall, J. L. Freeouf, D. Grischkowsky, D. T. McInturff, M. R. Melloch, and N. Otsuka. *Arsenic precipitates and the semi-insulating properties of GaAs buffer layers grown by low-temperature molecular beam epitaxy*. Appl. Phys. Lett. **57** (1990). – p. 15.

- [29] C. Tripon-Canseliet, M. Zegaoui, G. Jestin, C. Coinon, P. Berger, G. Baili, A. Descamps-Mandine, I. Maksimovic, D. Decoster, J. M. Hodé, D. Dolfi, and J. Chazelas. *High dynamic range single channel sampling of wideband RF signals using ultra-fast nanoscale photoconductive switching*. *Electron. Lett.* **52** (2016). – p. 15.
- [30] C. Tripon-Canseliet, S. Faci, D. Decoster, A. Pagies, S. F. Yoon, K. L. Pey, and J. Chazelas. *Nano photoconductive switches for microwave applications*. *SPIE OPTO.* (2013). – p. 15.
- [31] S. El Amari, A. De Angelis, D. Arnaud-Cormos, V. Couderc, and P. Leveque. *Characterization of a Linear Photoconductive Switch Used in Nanosecond Pulsed Electric Field Generator*. *IEEE Photon. Technol. Lett.* **23** (2011). – pp. 15, 131.
- [32] E. R. Brown, K. A. McIntosh, K. B. Nichols, and C. L. Dennis. *Photomixing up to 3.8 THz in low-temperature-grown GaAs*. *Appl. Phys. Lett.* **66** (1995). – p. 15.
- [33] K. A. McIntosh, E. R. Brown, K. B. Nichols, O. B. McMahon, W. F. DiNatale, and T. M. Lyszczarz. *Terahertz photomixing with diode lasers in low-temperature-grown GaAs*. *Appl. Phys. Lett.* **67** (1995). – p. 15.
- [34] E. R. Brown, F. W. Smith, and K. A. McIntosh. *Coherent millimeter-wave generation by heterodyne conversion in low-temperature-grown GaAs photoconductors*. *J. Appl. Phys.* **73** (1993). – p. 15.
- [35] S. Kono, M. Tani, P. Gu, and K. Sakai. *Detection of up to 20 THz with a low-temperature-grown GaAs photoconductive antenna gated with 15 fs light pulses*. *Appl. Phys. Lett.* **77** (2000). – p. 15.
- [36] Y. C. Shen, P. C. Upadhyaya, E. H. Linfield, H. E. Beere, and A. G. Davies. *Ultrabroadband terahertz radiation from low-temperature-grown GaAs photoconductive emitters*. *Appl. Phys. Lett.* **83** (2003). – p. 15.
- [37] C. Kadow, S. B. Fleischer, J. P. Ibbetson, J. E. Bowers, and A. C. Gossard. *Subpicosecond carrier dynamics in low-temperature grown GaAs on Si substrates*. *Appl. Phys. Lett.* **75** (1999). – p. 15.
- [38] J. D. Joannopoulos and S. G. Johnson. *Photonic Crystals*. Springer Science & Business Media, 2001. – pp. 15, 130, 164.
- [39] F. Alpeggiani, L. C. Andreani, and D. Gerace. *Effective bichromatic potential for ultra-high Q-factor photonic crystal slab cavities*. *Appl. Phys. Lett.* **107** (2015). – p. 16.
- [40] E. Kuramochi, E. Grossman, K. Nozaki, K. Takeda, A. Shinya, H. Taniyama, and M. Notomi. *Systematic hole-shifting of L-type nanocavity with an ultrahigh Q factor*. *Opt. Lett.* **39** (2014). – p. 16.
- [41] E. Kuramochi, M. Notomi, S. Mitsugi, A. Shinya, T. Tanabe, and T. Watanabe. *Ultrahigh-Q photonic crystal nanocavities realized by the local width modulation of a line defect*. *Appl. Phys. Lett.* **88** (2006). – pp. 16, 134–135.

- [42] Y. Lai, S. Pirotta, G. Urbinati, D. Gerace, M. Minkov, V. Savona, A. Badolato, and M. Galli. *Genetically designed L3 photonic crystal nanocavities with measured quality factor exceeding one million*. *Appl. Phys. Lett.* **104** (2014). – p. 16.
- [43] Z. Han, X. Checoury, L.-D. Haret, and P. Boucaud. *High quality factor in a two-dimensional photonic crystal cavity on silicon-on-insulator*. *Opt. Lett.* **36** (2011). – pp. 16, 134.
- [44] Z. Zhang and M. Qiu. *Small-volume waveguide-section high Q microcavities in 2D photonic crystal slabs*. *Opt. Exp.* **12** (2004). – pp. 16, 65, 72, 85, 115.
- [45] R. W. Boyd. *Nonlinear Optics*. Academic Press, 2013. – pp. 16, 66, 76, 164.
- [46] E. Yüce, G. Ctistis, J. Claudon, E. Dupuy, R. D. Buijs, B. de Ronde, A. P. Mosk, J.-M. Gérard, and W. L. Vos. *All-optical switching of a microcavity repeated at terahertz rates*. *Opt. Lett.* **38** (2013). – pp. 17, 21, 112.
- [47] N. Iizuka, K. Kaneko, and N. Suzuki. *Sub-picosecond all-optical gate utilizing aN intersub-band transition*. *Opt. Exp.* **13** (2005). – p. 17.
- [48] K. Nozaki, T. Tanabe, A. Shinya, S. Matsuo, T. Sato, H. Taniyama, and M. Notomi. *Sub-femtojoule all-optical switching using a photonic-crystal nanocavity*. *Nature Photon.* **4** (2010). – pp. 17, 21, 68, 75–76.
- [49] H. M. Gibbs, S. L. McCall, and T. N. C. Venkatesan. *Differential Gain and Bistability Using a Sodium-Filled Fabry-Perot Interferometer*. *Phys. Rev. Lett.* **36** (1976). – p. 17.
- [50] K. Ikeda and O. Akimoto. *Instability Leading to Periodic and Chaotic Self-Pulsations in a Bistable Optical Cavity*. *Phys. Rev. Lett.* **48** (1982). – p. 18.
- [51] S. Malaguti, G. Bellanca, A. de Rossi, S. Combrié, and S. Trillo. *Self-pulsing driven by two-photon absorption in semiconductor nanocavities*. *Phys. Rev. A* **83** (2011). – p. 18.
- [52] N. Cazier, X. Checoury, L.-D. Haret, and P. Boucaud. *High-frequency self-induced oscillations in a silicon nanocavity*. *Opt. Exp.* **21** (2013). – p. 18.
- [53] A. M. Yacomotti, F. Raineri, C. Cojocaru, P. Monnier, J. A. Levenson, and R. Raj. *Nonadiabatic Dynamics of the Electromagnetic Field and Charge Carriers in High-Q Photonic Crystal Resonators*. *Phys. Rev. Lett.* **96** (2006). – p. 18.
- [54] M. Brunstein, A. M. Yacomotti, I. Sagnes, F. Raineri, L. Bigot, and A. Levenson. *Excitability and self-pulsing in a photonic crystal nanocavity*. *Phys. Rev. A* **85** (2012). – p. 18.
- [55] M. Notomi and S. Mitsugi. *Wavelength conversion via dynamic refractive index tuning of a cavity*. *Phys. Rev. A* **73** (2006). – p. 18.
- [56] M. F. Yanik, S. Fan, and M. Soljačić. *High-contrast all-optical bistable switching in photonic crystal microcavities*. *Appl. Phys. Lett.* **83** (2003). – p. 18.
- [57] T. Tanabe, M. Notomi, S. Mitsugi, A. Shinya, and E. Kuramochi. *All-optical switches on a silicon chip realized using photonic crystal nanocavities*. *Appl. Phys. Lett.* **87** (2005). – pp. 19–21, 68, 86.

- [58] B. R. Bennett, R. A. Soref, and J. A. Del Alamo. *Carrier-induced change in refractive index of InP, GaAs and InGaAsP*. IEEE J. Quantum Electron. **26** (1990). – pp. 19, 67, 75–76, 117.
- [59] M. Heuck, S. Combrié, G. Lehoucq, S. Malaguti, G. Bellanca, S. Trillo, P. T. Kristensen, J. Mørk, J. P. Reithmaier, and A. de Rossi. *Heterodyne pump probe measurements of nonlinear dynamics in an indium phosphide photonic crystal cavity*. Appl. Phys. Lett. **103** (2013). – pp. 19–20, 68–69, 86, 117.
- [60] A. de Rossi, M. Lauritano, S. Combrié, Q. V. Tran, and C. Husko. *Interplay of plasma-induced and fast thermal nonlinearities in a GaAs-based photonic crystal nanocavity*. Phys. Rev. A **79** (2009). – pp. 19, 66.
- [61] T. Tanabe, H. Taniyama, and M. Notomi. *Carrier Diffusion and Recombination in Photonic Crystal Nanocavity Optical Switches*. J. Lightwave Technol. **26** (2008). – pp. 19, 72, 74, 117.
- [62] T. Tanabe, K. Nishiguchi, A. Shinya, E. Kuramochi, H. Inokawa, M. Notomi, K. Yamada, T. Tsuchizawa, T. Watanabe, H. Fukuda, H. Shinojima, and S. Itabashi. *Fast all-optical switching using ion-implanted silicon photonic crystal nanocavities*. Appl. Phys. Lett. **90** (2007). – pp. 20–21, 68, 97.
- [63] Y. Yu, E. Palushani, M. Heuck, N. Kuznetsova, P. T. Kristensen, S. Ek, D. Vukovic, C. Peucheret, L. K. Oxenløwe, S. Combrié, A. de Rossi, K. Yvind, and J. Mørk. *Switching characteristics of an InP photonic crystal nanocavity: Experiment and theory*. Opt. Exp. **21** (2013). – pp. 20, 69.
- [64] Y. Yu, H. Hu, L. K. Oxenløwe, K. Yvind, and J. Mørk. *Ultrafast all-optical modulation using a photonic-crystal Fano structure with broken symmetry*. **40** (2015). – pp. 20–21.
- [65] C. Husko, A. de Rossi, S. Combrié, Q. V. Tran, F. Raineri, and C. W. Wong. *Ultrafast all-optical modulation in GaAs photonic crystal cavities*. Appl. Phys. Lett. **94** (2009). – pp. 20–21, 68, 72, 98, 107.
- [66] S. Combrié, G. Lehoucq, A. Junay, S. Malaguti, G. Bellanca, S. Trillo, L. Ménager, J. P. Reithmaier, and A. de Rossi. *All-optical signal processing at 10 GHz using a photonic crystal molecule*. Appl. Phys. Lett. **103** (2013). – pp. 20–21, 65, 85–86, 106, 110, 117, 158.
- [67] G. Moille, A. de Rossi, G. Lehoucq, A. Martin, L. Bramerie, M. Gay, and S. Combrié. *A Highly Linear All Optical Gate Based on Coupled Photonic Crystal Cavities*. Nonlinear Photonics. (2014). – pp. 20, 158.
- [68] A. Bazin, K. Lenglé, M. Gay, P. Monnier, L. Bramerie, R. Braive, G. Beaudoin, I. Sagnes, and F. Raineri. *Ultrafast all-optical switching and error-free 10 Gbit/s wavelength conversion in hybrid InP-silicon on insulator nanocavities using surface quantum wells*. Appl. Phys. Lett. **104** (2014). – pp. 20–21, 86, 114.

- [69] Y. H. Wen, O. Kuzucu, T. Hou, M. Lipson, and A. L. Gaeta. *All-optical switching of a single resonance in silicon ring resonators*. *Opt. Lett.* **36** (2011). – p. 21.
- [70] V. R. Almeida, C. A. Barrios, R. R. Panepucci, and M. Lipson. *All-optical control of light on a silicon chip*. *Nature* **431** (2004). – p. 21.
- [71] T. A. Ibrahim, R. Grover, L. C. Kuo, S. Kanakaraju, L. C. Calhoun, and P. T. Ho. *All-optical AND/NAND logic gates using semiconductor microresonators*. *IEEE Photon. Technol. Lett.* **15** (2003). – p. 21.
- [72] Q. Xu and M. Lipson. *All-optical logic based on silicon micro-ring resonators*. *Opt. Exp.* **15** (2007). – p. 21.
- [73] T. A. Ibrahim, V. Van, and P. T. Ho. *All-optical time-division demultiplexing and spatial pulse routing with a GaAs/AlGaAs microring resonator*. *Opt. Lett.* **27** (2002). – p. 21.
- [74] M. Waldow, T. Plötzing, M. Gottheil, M. Först, J. Bolten, T. Wahlbrink, and H. Kurz. *25ps all-optical switching in oxygen implanted silicon-on-insulator microring resonator*. *Opt. Exp.* **16** (2008). – pp. 21, 97.
- [75] G. W. Cong, R. Akimoto, K. Akita, T. Hasama, and H. Ishikawa. *Low-saturation-energy-driven ultrafast all-optical switching operation in (CdS/ZnSe)/BeTe intersubband transition*. *Opt. Exp.* **15** (2007). – pp. 21, 86.
- [76] L. Monteagudo-Lerma, S. Valdueza-Felip, F. B. Naranjo, P. Corredera, L. Rapenne, E. Sariannidou, G. Strasser, E. Monroy, and M. González-Herráez. *Waveguide saturable absorbers at 1.55  $\mu\text{m}$  based on intraband transitions in GaN/AlN QDs*. *Opt. Exp.* **21** (2013). – p. 21.
- [77] R. Akimoto, S. Gozu, T. Mozume, and H. Ishikawa. *Monolithically integrated all-optical gate switch using intersubband transition in InGaAs/AlAsSb coupled double quantum wells*. *Opt. Exp.* **19** (2011). – pp. 21–22, 86.
- [78] R. P. Schrieck, M. H. Kwakernaak, H. Jackel, and H. Melchior. *All-optical switching at multi-100-Gb/s data rates with Mach-Zehnder interferometer switches*. *IEEE J. Quantum Electron.* **38** (2002). – p. 21.
- [79] S. Nakamura, Y. Ueno, and K. Tajima. *Femtosecond switching with semiconductor-optical-amplifier-based Symmetric Mach–Zehnder-type all-optical switch*. *Appl. Phys. Lett.* **78** (2001). – pp. 21, 86.
- [80] H. Ju, S. Zhang, D. Lenstra, H. de Waardt, E. Tangdionga, G. D. Khoe, and H. J. S. Dorren. *SOA-based all-optical switch with subpicosecond full recovery*. *Opt. Exp.* **13** (2005). – p. 21.
- [81] C. Koos, P. Vorreau, T. Vallaitis, P. Dumon, W. Bogaerts, R. Baets, B. Esembeson, I. Biaggio, T. Michinobu, F. Diederich, W. Freude, and J. Leuthold. *All-optical high-speed signal processing with silicon–organic hybrid slot waveguides*. *Nature Photon.* **3** (2009). – p. 21.

- 
- [82] R. Bose, J. S. Pelc, S. Vo, C. M. Santori, and R. G. Beausoleil. *Carrier dynamics in GaAs photonic crystal cavities near the material band edge*. *Opt. Exp.* **23** (2015). – pp. 21, 72, 105.
- [83] M. Soljačić, M. Ibanescu, S. G. Johnson, Y. Fink, and J. D. Joannopoulos. *Optimal bistable switching in nonlinear photonic crystals*. *Phys. Rev. E* **66** (2002). – p. 20.
- [84] J. B. Khurgin and G. Sun. *Scaling of losses with size and wavelength in nanoplasmonics and metamaterials*. *Appl. Phys. Lett.* **99** (2011). – p. 22.



# Chapter 2

## Photonic Crystal Fabrication

---

---

In this chapter, the fabrication of photonic crystals is discussed. First, the self-suspended membrane process flow is described, corresponding to the classic all-optical application structures made here, in Thales. For photoconductive switch applications, further process steps consisting of metal depositions are necessary. However, this leads to unexpected issues: self-suspended membranes are not freed by the under-etching solution when metal is present on top of the III-V material. Several attempts consisting of modifying the chemistry of the etching process have been made, nonetheless unsuccessful. These issues led to consider another process flow, consisting of replacing air as a cladding material with silica, using adhesive bonding of III-V on silicon. In the second part of this chapter, the bonding process is discussed and the whole process of the photoconductive switch detailed.

### Contents

---

2.1	Self-Suspended Membrane . . . . .	33
2.1.1	Process for All-Optical Switches . . . . .	33
2.1.2	Toward Photoconductive Switch Fabrication — Metal Issues . . . . .	35
2.2	Polymer Adhesive Bonding for Photoconductive Switches . . . . .	40
2.2.1	Contact and Crystallization of Polymer . . . . .	41
2.2.2	Substrate Thinning . . . . .	43
2.3	Conclusion . . . . .	46
	References for Chapter 2 . . . . .	47

---



## 2.1 | Self-Suspended Membrane

Bragg reflections provide in-plane light confinement in PhC, while total internal reflection enables vertical light confinement. Therefore, optical index of the cladding materials (*i.e.* above and below the PhC) needs to be lower than the III-V slab one. Air is certainly the first medium to come in mind speaking of a low optical index. Using air implies the PhC to be suspended, thus have material below the PhC removed. Therefore, a sacrificial layer is added in the epitaxial stack, between the substrate and the targeted III-V slab, with the only role to be removed. This type of structure has been the fabrication choice here in Thales for all-optical applications, and the process flow is now mature. However, for electro-optic systems, metal deposition steps are necessary, which implied to change the process-flow accordingly. The process-flow previously developed for self-suspended membranes is discussed, and the attempts to deposit metal layers on top of this membrane are developed, along with the self-suspended membrane under-etching issue when metallic pads are present.

### 2.1.1 | Process for All-Optical Switches

The material is a crucial point in the fabrication of self-suspended membrane. The carriers are generated through a TPA process only in the cavity, letting the waveguide transparent at the working wavelength of  $\lambda = 1500$  nm. Thus, the energy bandgap of the semiconductors needs to be higher than  $E_g = \frac{hc}{\lambda} = 0.83$  eV, and ideally close to the energy of the two absorbed photons (*i.e.*  $E = 1.65$  eV), to avoid thermal relaxation. If only III-V alloys are considered, the material suiting our applications are represented in the green panel of Fig. 2-1. Mainly, GaAs and InP are used for III-V PhC where TPA is desired.

Once the material, either GaAs or InP, is chosen, the sacrificial layer needs to be picked carefully. Two primary considerations have to be studied: the material needs to be as much as possible lattice matched with the target PhC slab material to avoid constraints, defects or even cracks during the growth; the sacrificial material needs to be etched by a chemical solution highly selective with the membrane material. Figure 2-1 provides a diagram of III-V alloys regarding their band-gap and their lattice constant. Following the vertical dotted lines plotted from GaAs or InP will provide lattice matched materials. Usually, the sacrificial layer is chosen when the lattice matched alloy has a concentration of indium or arsenic sufficient enough for respectively GaAs and InP targeted

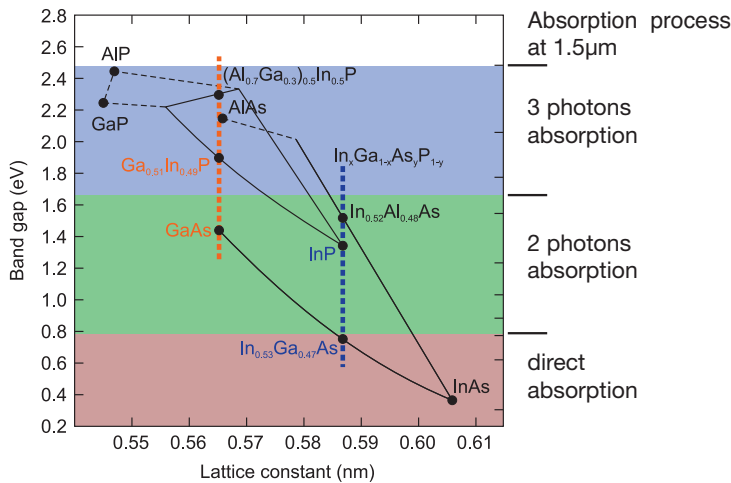


**Fig. 2-1** | III-V alloyed lattice matched diagram (data taken from [85]). In red dotted line, the lattice matched material for GaAs, in blue for InP. The color parts of the diagram correspond to the absorption regime for an input light at 1550nm, relative to the alloy band-gap.

membrane material, as the etching selectivity is high [86].

Once the materials have been carefully chosen, the epitaxial sample is made by Metalorganic Chemical Vapor Deposition (MOCVD). In this thesis, when GaAs is chosen as the targeted PhC material, the sacrificial layer is GaInP, whereas InGaAs acts as the sacrificial layer for InP PhC. In this following section, only the description of GaAs based PhC fabrication will be discussed.

The process flow used in this thesis can be divided into four main parts: electron-beam lithography (ebeam) lithography, hard mask etching, III-V dry etching and chemical under-etching to free the membrane.

In Thales, PhC are made using ebeam lithography, where, as its name stands, an electron beam is used to write the desired pattern, *i.e.* a mask, on an electron-sensitive resist. This technique allows a high resolution, necessary for PhCs fabrication. Nonetheless, other lithography techniques exist and have been proved to be efficient for fabricating PhC. Those include deep-ultraviolet (deep-UV) lithography [87], where fabrication of high quality factor PhC has been recently demonstrated [88, 89]. In Thales, ebeam was chosen because of its high flexibility. Indeed the mask can be easily changed by just modifying a file, thus reducing cost compared to optical lithography where quartz masks need to be bought for each new layout.

The first e-beam lithography layer consist of metallic marks (10 nm Ti and 80 nm Pt) following a specific pattern (Fig. 2-2). Then, for the second and further lithography layers, the ebeam machine aligns and focuses the beam on those marks, making the alignment more precise. In the masks used, 10 alignments marks are patterned, enabling ten successive lithography steps. Indeed, one mark is used for each layer processed.

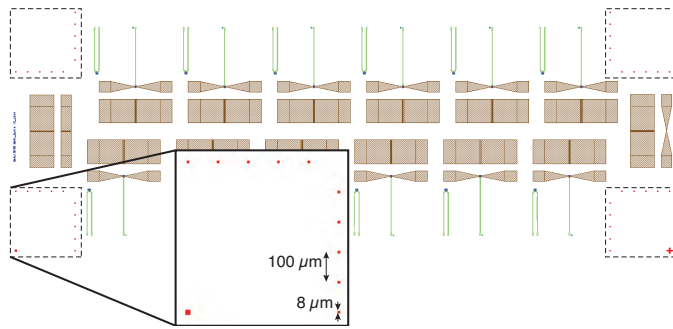


**Fig. 2-2** | Layout example. In dotted black frame, the mark emplacement. The inset represents a zoom of the bottom left hand mark set.

To write the desired pattern design, *i.e.* the mask, a sensitive resist (PMMA) is used, and deposited on top of the sample by spin-coating. To transfer the mask to the III-V, an Inductively Coupled Plasma (ICP) process is performed. However, in our process-flow, the  $\text{SiCl}_4$  process is done at the temperature of  $165^\circ\text{C}$ ., which is too hot for the resist. Thus, the resist will burn, leading to an unsuccessful transfer process.

Therefore, prior to the ebeam lithography, a hard mask of  $\text{SiO}_2$  is deposited by Plasma-Enhanced Chemical Vapor Deposition (PECVD) at  $340^\circ\text{C}$ . The mask patterned on the resist is then transferred to the  $\text{SiO}_2$  using a ICP machine (Oxford) in Reactive-Ion Etching (RIE) mode, with  $\text{CHF}_3$  and  $\text{O}_2$  (ration 25/1) to ensure a low roughness. After removing the resist, it is safe to transfer the patterned mask from the hard  $\text{SiO}_2$  mask to the GaAs.

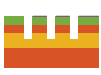
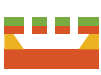
The last step for the PhC fabrication consists of freeing the membrane by removing the sacrificial GaInP layer. The sample is immersed in a chemical solution of HCl (50%) and  $\text{H}_3\text{PO}_4$  (50%) which provides a selective etching between GaInP and GaAs [90]. This step lasts about 20 min to ensure the complete etching of the sacrificial material.

A summary of the process flow for the PhC based on GaAs is reported on table 2.1 below:

### 2.1.2 | Toward Photoconductive Switch Fabrication — Metal Issues

The principle of photoconductive switches consists in reducing the resistance of the semiconductor placed in the Micro-Wave (MW) gap made in PhC, according to the repetition rate of the clock laser. Given this, the generated carriers in the PhC cavities have to be collected by the metallic pads for current circulation. Carriers exhibit a short diffusion length in PhC, therefore, the closer the metal is from the cavity, the better it is. Given this, the metallization is performed on top of the self-suspended membrane, where the mechanical strains of the structure are weak. Performing the metal deposition between step 3 and 4 (*c.f.* table 2.1) allows the stack structure to be mechanically

**Table 2.1** | Self-suspended photonic crystal membrane fabrication summary (case of GaAs).

Step	Remarks	Schematic Structure
1. Resist patterning	e-beam lithography	
2. Hard mask transfer	ICP CHF <sub>3</sub> -O <sub>2</sub>	
3. III-V etching	ICP SiCl <sub>4</sub>	
4. Under-etching GaInP	HCl-H <sub>3</sub> PO <sub>4</sub>	

■ GaAs      ■ GaInP      ■ Resist      ■ SiO<sub>2</sub>

strength enough for handling the rest of the process-flow as the sacrificial layer is still present. However, the under-etching step is done while metal is on top of the membrane.

Two steps of metal deposition are performed to fabricate the microwave lines: a small area providing ohmic contact close to the PhC and, above it, the MW line. The ohmic contact is made by alternating the deposition of Au/Ge, Ni and Au layers to a total height of 100 nm. The sample after undergoes a flash annealing at 380°C (30 sec, 2 min time raise) to transform the different metal layers into an alloy of GaAs-Ga/Au-Ni/As/Ge-Au/Ga-NiGaGe-AuGa -Ni [91]. In this situation, Germanium is considered to dope the GaAs, providing a transition region between the semi-conductor and the metal for better ohmic contacts [92].

The microwave pads are made by the deposition of 200 nm gold on top of the ohmic contact.

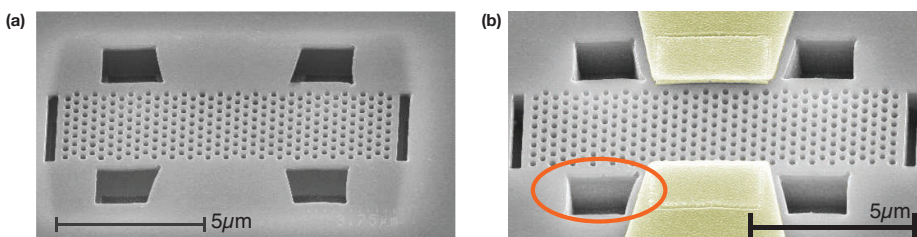


**Fig. 2-3** | SEM image of two structures from the same sample. (a) without any metal – (b) with ohmic contact and microwave pads. The circle point out the fact that in (a) the under-etch was efficient, not in (b).

Depositing metal at the step previously mentioned leads to a crippling issue. Indeed, it was observed that the chemical sacrificial layer removal is prevented by the metallic pads. This problem was reproduced with several samples (Fig. 2-3(b)), even though self-suspended membranes are freed on the same sample where no metal is present close to the PhC (Fig. 2-3(a)). It is clear from

the halo around the structure without metal that under-etching was well performed, whereas walls, made of GaInP, in the opening are still present in the structure with metallic pads. No sacrificial layer removal is highly problematic as no vertical confinement is provided.

On the samples made for testing the under-etching process, two designs have been implemented. The first one is the PhCs for the photoconductive switch application. The second consists of several beams patterned in the membrane material between the two electrodes. This structure makes it easier to observe with Scanning Electron Microscopy (SEM) if the GaInP was effectively or not removed under GaAs.

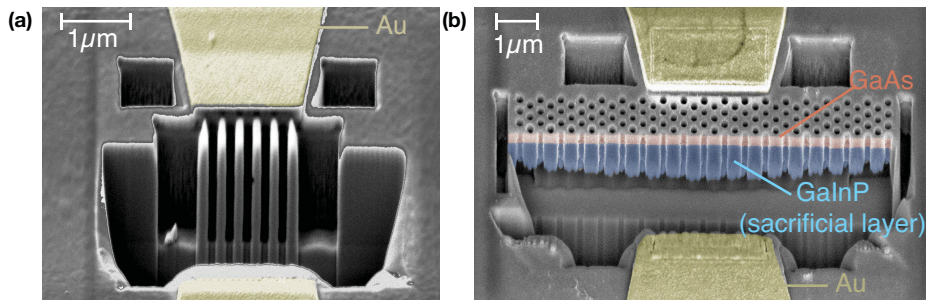


**Fig. 2-4** | SEM image of FIB cut of the sample after under etching trying a) for a beam nanopatterning b) photonic crystal nanopatterning.

To further investigate the behavior of the under-etching process, a Focused Ion Beam (FIB) cut was performed to reveal the III-V stack on structure with metallic pads. As seen in Fig. 2-4, the layer of GaInP was partially removed from the bottom. However, the etching depends on the distance between the pads, as far away from them, the etching seems to have been more efficient.

Several hypotheses could explain such chemical etching behavior. 1) First, the metal could change the solution wettability and/or the solution tends to form bubble over the PhC because of the metal. Therefore, HCl might not go through the holes and etch the GaInP layer. 2) Secondly, the metal would modify the electrochemical potential of either the mixture and/or the material, changing the reaction behavior and preventing the etching GaInP. 3) Finally, HCl and/or  $\text{H}_3\text{PO}_4$  could react with the metal. Reactors are then used and wasted with the metal reaction, decreasing the effective concentration of the etching solution for the sacrificial layer removal, thus limiting its removal.

To verify each hypothesis, several chemical etchings were performed under different conditions.

1. To answer the first assumption,  $\text{MaO}_2$  has been added to the solution. Mainly, this would raise the wettability of the solution (Fig. 2-5(a)). Unfortunately, no improvement has been noticed using this technique. The metal does not impact the ability of the solution to go

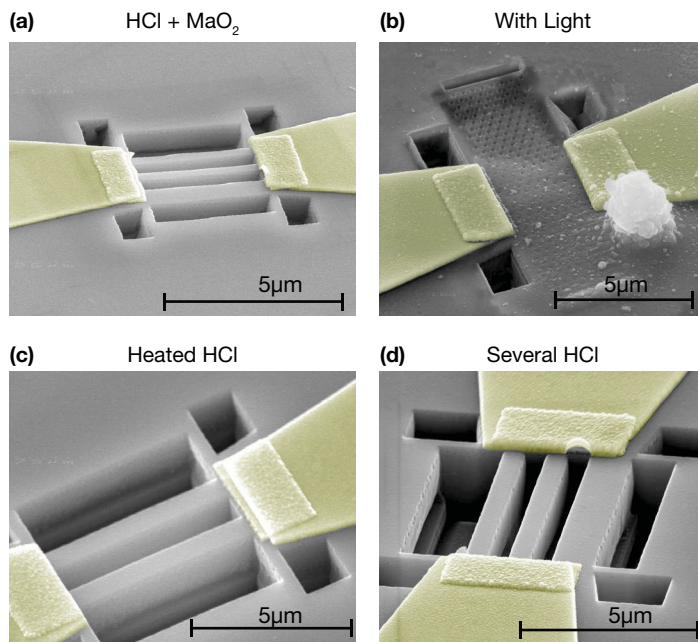


**Fig. 2-5** | Several different attempts to under etch the GaInP sacrificial layer.

through the PhC holes.

2. About the chemical potential change induced by the metal, two experiments have been tried. The first one consists of chemically etching the GaInP layer under illumination using a white light source. It has been proven that lightening during chemical etching can change the material selectivity of the solution [93]. This first attempt (Fig. 2-5(b)) did not etch the GaInP but instead provided a chemically deposited material on top of the PhC. The second attempt consisted of heating the solution, as this reaction between HCl and GaInP is highly dependent on the temperature [94]. Therefore, following the Arrhenius law, this would change the activation energy of the chemical reaction and could etch more effectively the sacrificial layer. It is clear that heating the solution does not provide an efficient under-etching (Fig. 2-5(c)).
3. Finally, if the reaction is limited by other reactions between HCl and metal, immersing the sample in several newly mixed HCl–H<sub>3</sub>PO<sub>4</sub> solution would lead to an improvement in the sacrificial layer removal. In Fig. 2-5(d), 5 solutions of HCl solution have been used, each of them freshly mixed before the etching attempt. The try corresponds to a total immersing time of 100 min. The SEM image reveals that this process could have led to an improvement, removing more material on the bottom of the GaInP layer. However, as seen in Fig. 2-4, no etching is performed close to the GaAs. Even if the chemical reaction is limited by non-desired

one between HCl and the metals, multiplying the etching attempt does not free efficiently the GaAs slab.

Currently, the metal used for both metal deposition is gold (an alloy of gold for the ohmic contact, gold only for the microwave pad). As the under-etching issue is due to the presence of such metal near the PhC, by changing it, the electrochemical potential of the contact changes, then the etching behavior can be altered.

The ohmic contact has been changed to an alloy of titanium and platinum, and the microwave pads by platinum only. Under-etching was processed as usual using HCl – H<sub>3</sub>PO<sub>4</sub> for 20 min, which removed the GaInP sacrificial layer. A FIB cut was performed to obtain a closer look at the self-suspended membrane (Fig. 2-6). The membrane is obviously well released. However, another issue appeared: the GaAs is etched around the ohmic contact. This is a crucial drawback because, even with a self-suspended membrane providing light confinement vertically, and therefore enabling carrier generation in the cavity, those carriers cannot be collected as the contact is separated from the structure.

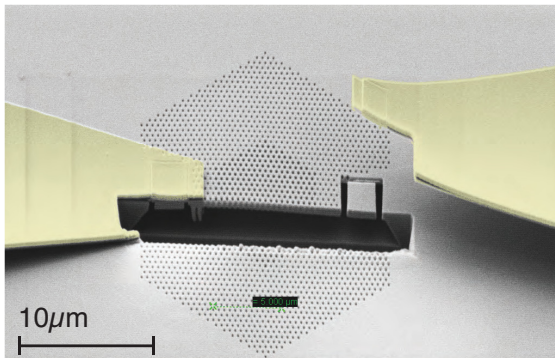


**Fig. 2-6** | SEM image of FIB cut of the sample after under etching for a Ti/Pt contact.

Finally, depositing metal between the steps 3 and 4 of the original self-suspended process flow (*c.f.* table 2.1) could be avoided. Ohmic contact and microwave pad can be deposited after under-etching over the already freed self-suspended membrane. Unfortunately, the mechanical strength of the PhC slab is too weak for further process steps, especially resist deposition. It is evident in Fig. 2-7 that after only one spin-coating, the PhC membrane are already cracked (mostly all structures of the sample were broken). Even if during this step, enough structures would have been rescued, it means that all of these nonbroken structures still have to go through metal deposition, metal lift-off, and the second step of metal layer. The position in the process flow for the metal layer does not provide a reliable enough method for fabricating photoconductive switch.

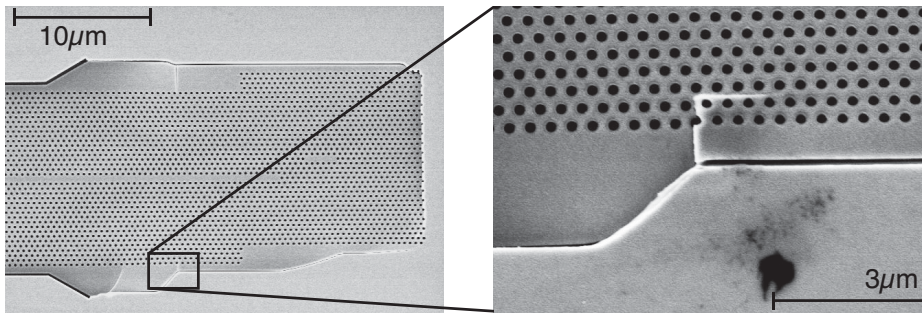


Fig. 2-7 | Cracked membrane after resist deposition prior to metal deposition.

## 2.2 | Polymer Adhesive Bonding for Photoconductive Switches

Carrier generation is obtained by TPA in photonic crystal cavities, with the in-plane and out-plane confinement. The out-plane confinement of light is achieved if the optical index of the PhC slab is higher than the one of the outside material. However, even if air has the smallest refractive index, other material can provide lower refractive index than III-V alloys. Using dielectric material such as  $\text{SiO}_2$  (optical index  $n = 1.46$ ) is sufficient to confine vertically the light. Moreover, this gives the mechanical strength to deposit metal on top of GaAs as we are not in the presence of a self-suspended membrane anymore. This type of structure with  $\text{SiO}_2$  below the GaAs slab can be obtained by bonding a wafer of GaAs on top of a silicon one.

Bonding III-V material of silicon is of great interest to integrate III-V active materials on top of low cost and low loss circuitry provided by the silicon photonics platform [95]. Several techniques for bonding these materials exist [96] such as atomic forces bonding [97] or adhesive bonding using a polymer to glue two wafers together [98]. In this thesis, we will focus only on the adhesive bonding as it is less compelling and match our expectation for integrated optics application.

Adhesive bonding was extensively used for laser integration made in III-V material, such as InP on silicon [99]. The principle of adhesive bonding is based on using a polymer contacting a silicon wafer and the III-V epitaxy. After annealing, the glue crystallizes and bonds together the two wafers. A substrate removal process is then needed to reveal the desired III-V layer. In this section, bonding GaAs on silicon will be discussed. The process described in this thesis is based on the one developed in-house by C. Wilhelm [100] on other materials than the one used here, and further for bonding with GaAs.

### 2.2.1 | Contact and Crystallization of Polymer

The polymer used for the adhesive bonding of the III-V material on silicon is, in this case, the Cycloten 3022-46 commercialized by DOW Chemicals, and is part of the family called BCB. To present the product in a liquid form, solvents are added to the solution. For this type of BCB, mesitylene is used (chemical formulation:  $C_9H_{12}$ ). The bonding process is described in Fig. 2-8 and can be summarized in 3 main steps: 1) polymer deposition 2) contacting wafers 3) annealing under press.

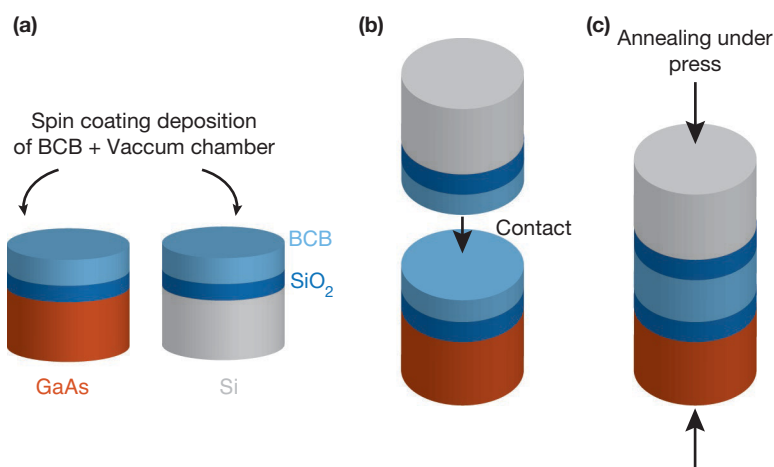


**Fig. 2-8** | Major steps of III-V on silicon bonding using polymer adhesive: (a) deposition and vacuum chamber to avoid bubbles, (b) contact, (c) annealing under pressure.

The first step is the polymer deposition on both the GaAs epitaxy and on silicon substrate (Fig. 2-8(a)). To effectively achieve it, an intense cleaning of both wafers is first done using an ultrasonic cleaning with acetone, then rinsing with isopropanol. This step is necessary to avoid any specks of dust that would be stuck under the BCB, which would further lead to cracks on the target bonded III-V material. Then, a promoter is needed to improve BCB adhesion on the wafers. The manufacturer describes that the promoter used (AP3000, sold by DOW Chemical too) is more efficient deposited on top of dielectric [101]. Therefore, before all those steps, a 250 nm thick layer of  $SiO_2$  is deposited using PECVD (340°C deposition temperature). The promoter is deposited using two steps of spin-coating: a slow one at 27 rotations per minutes (rpm) during 15 seconds with the lid open to obtain a homogeneous deposition; then with the lid closed during 30 seconds, a fast rotation at 4000 rpm. Finally, the same protocol than for the promoter is used to spin-coat the BCB on top of both the III-V and the silicon wafers.

To avoid bubbles in the polymer, that could have been created during the deposition process, the two samples are placed in a vacuum chamber at a pressure of about 1 mBar during 5 min.

The second main step consists of contacting the silicon and the GaAs wafer (Fig. 2-8(b)), which is performed manually by aligning one side of the silicon wafer with one of the flipped GaAs. Then, by gently letting the III-V go down on the silicon, the contact is made. An additional pressure directed outwards the samples is applied manually after contacting to avoid any bubbles due to the contacting.

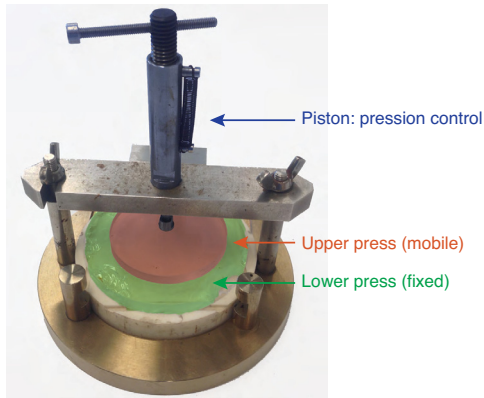


**Fig. 2-9** | Photography of the press used to bond the III-V on silicon for this thesis.

Finally, the last step is the annealing of the bonded sample to crystallize the BCB, performed under pressure (Fig. 2-8(c)). The press used is represented in Fig. 2-9, consisting of a fixed and a mobile plates which are perfectly plane to distribute the pressure uniformly through the sample. The pressure, controlled with a screw linked to a spring, is estimated to be roughly 30 kg by wafer.

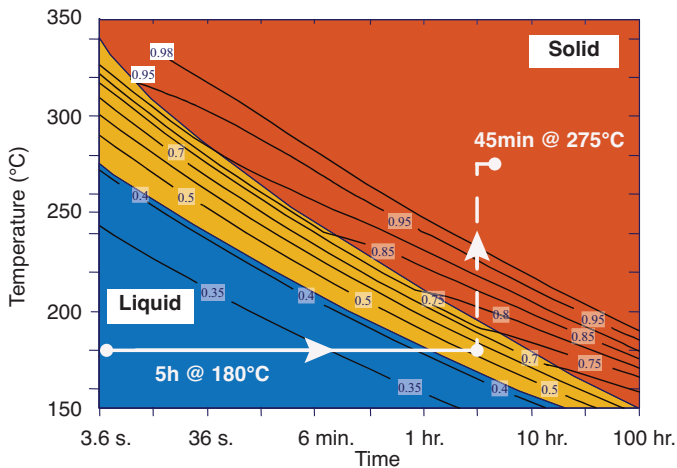


**Fig. 2-10** | Phase of BCB as a function of time and temperature from ref. [101]. In blue the liquid phase and in red the solid phase. The different black lines represent the corresponding ratio of solid/liquid phase. In white, the path followed to anneal and crystallized the BCB.

The annealing process is composed of two stages. The first one consists of a low-temperature one to evaporate the solvent while keeping the BCB in a liquid form. Thus, solvent gas can still flow out from the polymer without creating any bubbles. As the mesitylene, solvent used to dilute the BCB, has an ebullition point of 164.7°C, the first annealing is done at 180°C during 5 hours, where

the BCB remains liquid (Fig. 2-10). The second annealing consists in a fast high temperature baking at 275°C for 45 min to crystallize completely the BCB, as BCB is 99% solid at this temperature (Fig. 2-10).

### 2.2.2 | Substrate Thinning

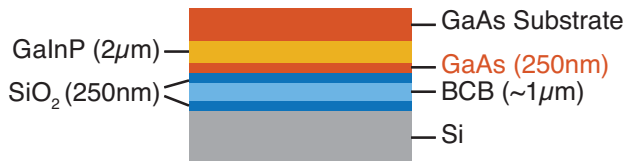


**Fig. 2-11** | Structure of the bonded sample prior to etching. The GaInP layer acts as an etch-stop layer, while the GaAs layer in red is the targeted layer.

When the GaAs stack is bonded to the silicon wafer, it is necessary to remove the III-V substrate to reveal the targeted material, which is in our case a 250 nm thick layer of GaAs. In our case, the substrate being the same material as the targeted slab one, an etch stop layer is necessary between these two. Here, GaInP is used thanks to its high etching selectivity with the considered etching solution. The description of the different layers before chemical thinning is described in figure 2-11.

Prior to thinning the substrate, proper removal of the undesired leaked BCB on top of the III-V substrate is mandatory. Such crystallized polymer would block the etching process (Fig. 2-12) and thus make the sample unusable for further process. BCB cleaning is performed using a RIE plasma composed of O<sub>2</sub> (50 sccm) and CHF<sub>3</sub> (20 sccm) at a pressure of 100mT and a RF power of 50W. This process etches the BCB at a speed of 220 nm/min. Then, to be certain to remove all undesired polymer, the sample is processed using this recipe during 10 min.

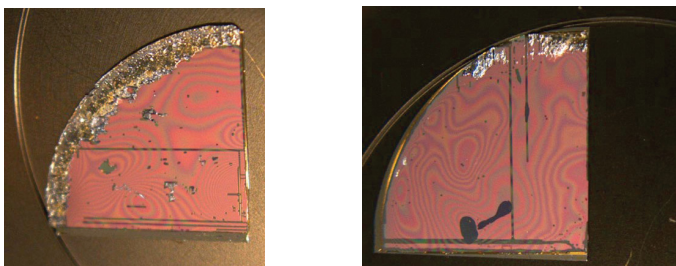
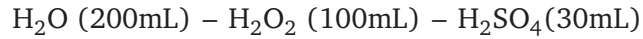


**Fig. 2-12** | Examples of samples where the BCB was not cleaned enough before substrate chemical thinning. The silver parts are the substrate still present on the thinned sample.

Substrate thinning could be achieved by several methods, mainly chemical, mechanical or a combination of both of these. In this case, the removal of the 200µm GaAs substrate is done chemically. Different solutions being selective with GaInP are reported in the literature provid-

ing good results [102], such as ammoniac ( $\text{NH}_4\text{OH}$  [103, 104]), citric acid ( $\text{C}_6\text{H}_8\text{O}_7$  [105]), orthophosphoric acid ( $\text{H}_3\text{PO}_4$  [106]) or sulfuric acid ( $\text{H}_2\text{SO}_4$  [107]). All those recipes are based on oxido-reduction reactions, thus hydrogen peroxide ( $\text{H}_2\text{O}_2$ ) is added to each of those solutions.

For this process, sulfuric acid is used and the solution recipe, commonly called *Caro's etch*, consists of:



This process provides an etching rate of roughly  $5\mu\text{m}/\text{min}$  [86] and is still highly selective with the GaInP layer (150:1 [108]).

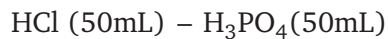
To improve and fasten the chemical etching of the GaAs substrate, the sample is placed in a rotatory holder. To avoid etching inhomogeneity, the holder changes his rotatory direction every 20 min. The process for a substrate of  $200\mu\text{m}$  lasts about 1 hour and 30 minutes.



**Fig. 2-13** | (a) Bonded sample prior to substrate removal – (b) Sample after GaAs substrate removal – (c) Bonded sample at the end of process after etch stop layer removal.

The substrate removal step can be visually determined as finished when the revealed surface corresponds to a mirror (Fig. 2-13(b)). In this case, we know that we reached an epitaxial layer, thus the etching-stop layer of GaInP.

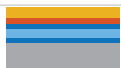
The solution to remove the etch-stop has to be selective with the GaAs, the targeted layer. A commonly used mixture is based on chloride acid diluted into orthophosphoric acid and/or water [109, 110], providing a good selectivity with GaAs [90]. In this case, mix between chloride acid and orthophosphoric acid is used:



This solution provides an etch rate of about  $0.6\mu\text{m}/\text{min}$  [94]. The sample is immersed in it for about 5 min. Again, the end of the process can be determined visually, because of the good selectivity between GaInP and GaAs, when several fringes are revealed due to the thinness of the GaAs layer and the non-uniformity of the BCB(Fig. 2-13(c)).

A summary of the bonding and substrate thinning process for GaAs sample is reported below (table 2.2):

**Table 2.2** | Adhesive bonding process summary (case of GaAs).

Step	Duration	Remarks	Schematic Structure
1. Spin coating AP300	15s	27rpm	
	30s	4000rpm	
2. Spin coating BCB	15s	27rpm	
	30s	4000rpm	
3. Vacuum Chamber	5min		
4. Contact and press	–	≈ 10kg	
5. Annealing 1	5h	180°C	
6. Annealing 2	45min	275°C	
7. BCB Cleaning	10min	O <sub>2</sub> – CHF <sub>3</sub> RIE plasma	
8. Substrate removal	≈ 1h30min	H <sub>2</sub> SO <sub>4</sub> – H <sub>2</sub> O <sub>2</sub> – H <sub>2</sub> O	
9. Etch-stop layer removal	≈ 5min	HCl – H <sub>3</sub> PO <sub>4</sub>	

GaAs

GaInP

BCB

SiO<sub>2</sub>

Si

Using this bonded GaAs on silicon as a started wafer, the process-flow for fabricating PhC remains the same than in the previous section 2.1. As no removal of the sacrificial layer step is needed here, the metal can be deposited in the same way than in section 2.1.2. Light confinement is enabled by optical index difference between SiO<sub>2</sub> and GaAs while the metal is on the top of GaAs for collecting the photo-generated carriers (Fig. 2-14).

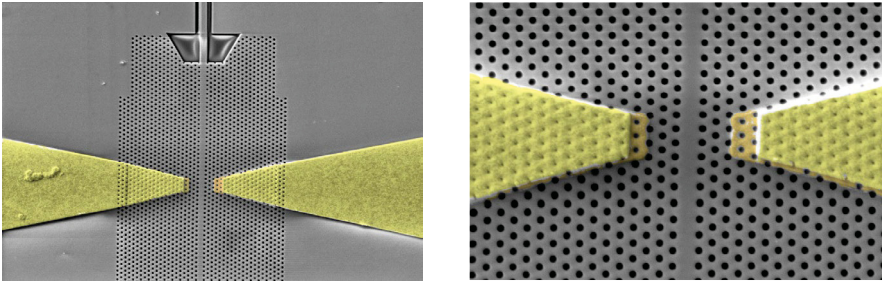


**Fig. 2-14** | Photoconductive switch sample made in GaAs bonded on silicon. The metal is represented in yellow color. The microwave pad are shifted from the ohmic contact for better alignment precision.

## 2.3 | Conclusion

In this chapter, PhC fabrication has been discussed and different process flows have been pointed out for fabricating such structure. Self-suspended membranes provide the best vertical confinement as the index contrast is the highest accessible. However, for photoconductive switch applications, needing metallic contacts, this process flow is not suitable. Instead, it is wiser to consider III-V on silicon adhesive bonding. It provides both mechanical strength for metal deposition and absence of under-etching process. It has been developed in this Ph.D. and demonstrated here that quarter of 2-inch wafer could be successfully and reproductively bonded on top of a silicon wafer, where the full sample is after usable for further processing. The full process-flow for photoconductive switch fabrication using as a start wafer the bonded sampled has been successfully achieved.

In chapter 4 where all-optical signal processing is discussed, all the structures will be self-suspended membranes. However, in chapter 5, metal MW lines are used, thus, only bonded structures are used.

## References for Chapter 2 – Photonic Crystal Fabrication

- [85] M. Grundmann. *The Physics of Semiconductors*. "Band Structure", pp. 139–181. Springer Science & Business Media, 2010. – p. 34.
- [86] S. J. Pearton. *Handbook of Compound Semiconductors*. "Wet and Dry Etching of Compound Semiconductors", pp. 370–441. Elsevier, 1996. – pp. 34, 44.
- [87] W. Bogaerts, V. Wiaux, D. Taillaert, S. Beckx, B. Luyssaert, P. Bienstman, and R. Baets. *Fabrication of photonic crystals in silicon-on-insulator using 248-nm deep UV lithography*. *IEEE J. Sel. Topics Quantum Electron.* **8** (2002). – p. 34.
- [88] M. Settle, M. Salib, A. Michaeli, and T. F. Krauss. *Low loss silicon on insulator photonic crystal waveguides made by 193nm optical lithography*. *Opt. Exp.* **14** (2006). – p. 34.
- [89] Y. Ooka, T. Tetsumoto, A. Fushimi, W. Yoshiki, and T. Tanabe. *CMOS compatible high-Q photonic crystal nanocavity fabricated with photolithography on silicon photonic platform*. *Sci. Rep.* **5** (2015). – p. 34.
- [90] S. B. Phatak and G. Kelner. *Material-Selective Chemical Etching in the System InGaAsP/InP*. *J. Electrochem. Soc.* **126** (1979). – pp. 35, 44.
- [91] M. Ogawa. *Alloying behavior of Ni/Au-Ge films on GaAs*. *J. Appl. Phys* **51** (1980). – p. 36.
- [92] S. M. Sze and K. K. Ng. *Physics of Semiconductor Devices*. John Wiley & Sons, Inc., 2006. – pp. 36, 67, 118–119.
- [93] J. B. Williamson. *Dopant-Type Selective Electroless Photoetching of Zn-Diffused InP and InGaAs/InP Heterostructures*. *J. Electrochem. Soc.* **140** (1993). – p. 38.
- [94] F. Ren, C. R. Abernathy, S. J. Pearton, L. W. Yang, and S. T. Fu. *Novel fabrication of self-aligned and microwave power heterojunction bipolar transistors*. *Solid-State Electron.* **38** (1995). – pp. 38, 44.
- [95] M. J. R. Heck, J. F. Bauters, M. L. Davenport, D. T. Spencer, and J. E. Bowers. *Ultra-low loss waveguide platform and its integration with silicon photonics*. *Laser Photon. Rev* **8** (2014). – p. 40.
- [96] G. Roelkens, L. Liu, D. Liang, R. Jones, A. Fang, B. Koch, and J. Bowers. *III-V/silicon photonics for on-chip and intra-chip optical interconnects*. *Laser Photon. Rev* **4** (2010). – p. 40.
- [97] M. M. R. Howlader, M. J. Deen, and T. Suga. *Nanobonding: A key technology for emerging applications in health and environmental sciences*. *Jpn. J. Appl. Phys.* **54** (2015). – p. 40.
- [98] F. Niklaus, G. Stemme, and J. Q. Lu. *Adhesive wafer bonding*. *J. Appl. Phys* **99** (2006). – p. 40.
- [99] A. W. Fang, H. Park, O. Cohen, R. Jones, M. J. Paniccia, and J. E. Bowers. *Electrically pumped hybrid AlGaInAs-silicon evanescent laser*. *Opt. Exp.* **14** (2006). – p. 40.

- [100] C. Wilhelm. “Controlling semiconductor nanowire light emission by a photonic crystal cavity - towards integrated nanolasers ” PhD Thesis. 2015. – p. 40.
- [101] *CYCLOTENE 3000 Series Advanced Electronic Resins*. DOW Chemicals. – pp. 41–42.
- [102] A. R. Clawson. *Guide to references on III–V semiconductor chemical etching*. Materials Science and Engineering: R: Reports **31** (2001). – p. 44.
- [103] L. Desplanque. “Caractérisation électro-optique de composants térahertz par échantillonnage Franz-Keldysh subpicoseconde” PhD Thesis. 2003. – p. 44.
- [104] F. Ding, L. Wang, S. Kiravittaya, E. Müller, A. Rastelli, and O. G. Schmidt. *Unveiling the morphology of buried In(Ga)As nanostructures by selective wet chemical etching: From quantum dots to quantum rings*. Appl. Phys. Lett. **90** (2007). – p. 44.
- [105] M. Tong, K. Nummila, A. Ketterson, I. Adesida, C. Caneau, and R. Bhat. *InAlAs/InGaAs/InP MODFET’s with uniform threshold voltage obtained by selective wet gate recess*. IEEE Electron Device Lett. **13** (1995). – p. 44.
- [106] S. Combrié. “Etude et réalisation de structures en cristaux photoniques pour les applications de traitement du signal optique” PhD Thesis. 2006. – p. 44.
- [107] W. T. Tsang and S. Wang. *Profile and groove-depth control in GaAs diffraction gratings fabricated by preferential chemical etching in  $H_2SO_4$ - $H_2O_2$ - $H_2O$  system*. Appl. Phys. Lett. **28** (1976). – p. 44.
- [108] D. Danzilio and A. Hanson.  *$In_{0.5}Ga_{0.5}P$  Etch-Stop Process for PHEMT Manufacturing* Tech. Report. 1999. – p. 44.
- [109] J. R. Lothian, J. M. Kuo, F. Ren, and S. J. Pearton. *Plasma and wet chemical etching of  $In_{0.5}Ga_{0.5}P$* . J. Electron. Mater. **21** (1992). – p. 44.
- [110] H. Dämbkes, U. König, and B. Schwaderer. *InGaAs/InP heterobipolar transistors for integration on semi-insulating InP substrates*. Electron. Lett. (1984). – p. 44.

# Chapter 3

## Theory and Modeling

---

---

In this chapter, the different tools used to model the optical and electrical properties of the PhC resonators are discussed. Given the complex nanoscale geometry, and therefore the preponderant role of the surface, the carrier dynamics is highly complex and require modeling tools. Besides modifying the resistance of the material, carriers change the refractive index of the PhC cavity, thus shifting the resonance frequency. The modeling tools required to simulate both physical aspects has been developed during this thesis.

First, carrier dynamics in such nano-structured is addressed and a modeling tool based on the Finite Element Method (FEM), best suited method for such complex geometry, is described. The implemented model is discussed with complete verification by confronting the results to the analytical resolutions. The next section describes the modeling of all-optical switching dynamics using time domain the Coupled Modes Theory (CMT), and the new formalism developed during this Ph.D. A detailed explanation for the free-carrier plasma effect switching computation will be provided, using the result of the FEM calculation through an impulse response formalism.

### Contents

---

3.1	Carrier Transport in Patterned Semiconductor Structures . . . . .	51
3.1.1	Carrier Dynamics in Semiconductor and Approximations . . . . .	51
3.1.2	Drift-Diffusion Model . . . . .	53
3.1.3	Ambipolar Approximation . . . . .	56
3.1.4	Implementation with Finite Element Method . . . . .	57
3.2	Coupled Mode Theory . . . . .	61
3.2.1	Formalism . . . . .	62
3.2.2	Device Design and Experimental Benchmark . . . . .	64
3.2.3	Non-Linear Dynamics . . . . .	65
3.2.4	Free Carriers Dynamics . . . . .	67
3.2.5	Green's Function Formalism . . . . .	69

---

3.2.6	Impact of the Geometry on the Dynamics . . . . .	72
3.2.7	Linear Absorption . . . . .	75
3.2.8	Summary of the Green's Formulation Carrier Dynamics in CMT . . . . .	77
3.3	Conclusion . . . . .	77
	References for Chapter 3 . . . . .	79

---

### 3.1 | Carrier Transport in Patterned Semiconductor Structures

The physics behind the devices investigated here relates to the dynamics of optically excited free carriers. This is a well-known topic since the 60's. The dynamical response in active devices has been deeply investigated in the 90's. The focus was on sub-picosecond phenomena, where an accurate description of sub-picosecond time-scale was required [111–117]. A naive picture is the excitation of carriers and their diffusion-recombination under a distribution gradient, with or without external electric fields. Indeed, we show that this description is correct within the timescale of interest to us, namely longer than 1ps as the excitation pulse is of the order of a few picoseconds. Therefore, the model is given by the well-known drift-diffusion equation.

On the other hand, the difficulty and the originality pointed in this thesis lies in the complex geometry of the device, where the typical distance to the interface is comparable or smaller than the diffusion length. It means that the geometry through the carrier surface recombination rules the dynamics.

#### 3.1.1 | Carrier Dynamics in Semiconductor and Approximations

Carrier dynamics in semiconductor are fully described in the semi-classical model following the Maxwell-Boltzmann equation:

$$\frac{\partial f}{\partial t} + \mathbf{v} \cdot \nabla_{\mathbf{r}} f + \frac{q\mathbf{E}}{\hbar} \cdot \nabla_{\mathbf{k}} f = \sum_{\mathbf{k}'} [S(\mathbf{k}', \mathbf{k}) f(\mathbf{r}, \mathbf{k}', t) (1 - f(\mathbf{r}, \mathbf{k}, t))] - [S(\mathbf{k}, \mathbf{k}') f(\mathbf{r}, \mathbf{k}, t) (1 - f(\mathbf{r}, \mathbf{k}', t))] \quad (3.1)$$

Where  $f$  is a distribution function in space, momentum and time,  $\mathbf{r}$  is the position,  $\mathbf{k}$  the momentum,  $\mathbf{v}$  the group velocity and  $\mathbf{E}$  the electric field. The right hand side of the equation corresponds to the collision term. However, solving this equation in three dimensions, with a time dependency, resulting in six independent variables: three equations for space, and three for momentum. Even if numerical methods have greatly improved during the past few years thanks to the improvement of computation power, and therefore leading to accurate solution of the above equation using Monte-Carlo algorithm (*i.e.* computational algorithm based on random sampling to obtain the result of an equation), this is still very challenging. Thus, to obtain a simpler model, further approximation will be made to obtain the carrier distribution in space and time.

The most common approximation in the semiconductors transport study is to define a distribution function, which follows a Fermi-Dirac distribution  $f(E) = \frac{1}{1+\exp((E-E_f)/k_B T)}$ , where  $E_f$  is the Fermi level and corresponds to the energy where the distribution function is  $\frac{1}{2}$ . Here, we do not attempt to model the momentum space as we are only interested in the carrier spatial distribution. Therefore, it is possible to define a population distribution at equilibrium for both electrons and holes in the semiconductor related to  $E_f$ , the valence band energy  $E_v$  and the conduction band energy  $E_c$ , under the approximation where the difference between each energy level is greater than  $4k_B T$ :

$$N_0 = N_c \exp\left(\frac{E_f - E_c}{k_B T}\right) \quad (3.2a)$$

$$P_0 = N_v \exp\left(\frac{E_v - E_f}{k_B T}\right) \quad (3.2b)$$

Where  $N_c$  and  $N_v$  are the effective state densities for the conduction and the valence band respectively and defined as  $N_c = 2 \left(\frac{2\pi m_N^* k_B T}{h^2}\right)^{3/2}$  and  $N_v = 2 \left(\frac{2\pi m_P^* k_B T}{h^2}\right)^{3/2}$ , with  $m_{N,P}^*$  being the effective mass of electron or holes.

To describe the flow of current, quasi-Fermi level for both electrons and holes,  $F_n$  and  $F_p$  respectively, are introduced such that:

$$N = N_c \exp\left(\frac{F_n - E_c}{k_B T}\right) \quad (3.3a)$$

$$P = N_v \exp\left(\frac{E_v - F_p}{k_B T}\right) \quad (3.3b)$$

Another approximation made here is that the carrier temperature  $T$  is the same as the lattice temperature, which means that during this thesis, phenomena such as carrier heating or spectral hole burning will not be taken into account. It is coherent with the time-scale of the phenomena of interest which is of the order of the picoseconds, while carrier heating is ten times faster [118].

Moreover, ballistic regime is completely neglected here. This is consistent with the mean free path  $L_D$  of the carrier in GaAs ( $\max(L_D) = \frac{v_{sat}\mu_n m_N^*}{q} = 30$  nm) which is much smaller than the average distance before carriers reach a surface, thus recombine (about 100 nm); and coherent with the dielectric relaxation time  $\tau_{rlx}$  ( $\max(\tau_{rlx}) = \frac{\epsilon_0 \epsilon_r}{q \mu_n N_{inj}} \simeq 10$  fs) order of magnitude smaller than the time-scale for our corresponding applications.

These approximations being made, the carrier dynamics in the PhC can be modeled with the drift-diffusion equations, which are coupled electrostatically with the Poisson equation.

### 3.1.2 | Drift-Diffusion Model

#### 3.1.2.1 | Drift Diffusion Formulation

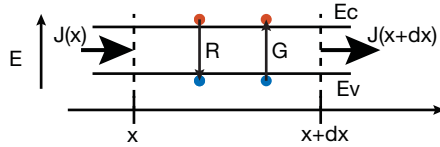


**Fig. 3-1** | Schematic of the continuity assumption between  $x$  and  $x + dx$  with ingoing and outgoing currents and with generation (G) and recombination (R).

The Drift-Diffusion equations describe the motion of carriers enforcing the conservation of the particles, *i.e.* the continuity condition. Let us consider a 1D semiconductor between the coordinate  $x$  and  $x + dx$  (Fig. 3-1). The variation of the carrier concentration in time between  $x$  and  $x + dx$  is the difference between the incoming and outgoing flux, *i.e.* current, plus the possible carrier generation/recombination mechanisms:

$$\frac{\partial N(x, t)}{\partial t} dx = \frac{1}{q} (\mathbf{J}_n(x) - \mathbf{J}_n(x + dx)) + GR(x, t) dx \quad (3.4a)$$

$$\frac{\partial P(x, t)}{\partial t} dx = \frac{1}{q} (\mathbf{J}_p(x) - \mathbf{J}_p(x + dx)) + GR(x, t) dx \quad (3.4b)$$

Where  $N, P$  are the carrier density for the electrons and holes respectively,  $G(x, t) + R(x, t)$  the generation and recombination term (which will be further defined in sections 3.1.2.2, 3.1.2.3 and 3.2) and  $q$  the module of the electron charge. The equations in 3D space are:

$$\frac{\partial N(x, t)}{\partial t} = \frac{1}{q} \nabla \cdot \mathbf{J}_n(x, t) + G(x, t) + R(x, t) \quad (3.5a)$$

$$\frac{\partial P(x, t)}{\partial t} = \frac{1}{q} \nabla \cdot \mathbf{J}_p(x, t) + G(x, t) + R(x, t) \quad (3.5b)$$

In a semiconductor, two contributions exist for the current density, namely the diffusion and the drift current. First, the diffusion is described by Fick's law [119, 120]:

$$\mathbf{J}_n^{diff} = qD_n(\nabla \cdot N) \quad (3.6a)$$

$$\mathbf{J}_p^{diff} = -qD_p(\nabla \cdot P) \quad (3.6b)$$

Where  $D_{n,p}$  is the diffusion coefficient for electrons and holes respectively which is linked to the carrier mobility though the Einstein relationship [121]  $D_{n,p} = \frac{\mu_{n,p} k_B T}{q}$

Secondly, carriers in a semiconductor, when subjected to an electric field, accelerate leading to

a drift velocity depending on the electric field and of the charge of the particle for its orientation. At low electric field, this velocity becomes linear with the electric field,  $\mathbf{v}_{n,p} = \pm\mu_{n,p}\mathbf{E}$ , . It creates a current, described by the local Ohm law [122]:

$$\mathbf{J}_{n,p}^{drift} = (N, P)\mathbf{v} \quad (3.7)$$

However, the quasi-Fermi levels are linked to the carrier concentrations. Thus, current contribution can be rewritten accordingly to these quasi-Fermi energy levels. Indeed, after some algebra and reinjecting eq. (3.3) in eq. (3.6) and eq. (3.7), gives the simple expression for the total current  $\mathbf{J}_{n,p} = \mathbf{J}_{n,p}^{drift} + \mathbf{J}_{n,p}^{diff}$ :

$$\mathbf{J}_n = -\frac{\mu_n}{q}N\nabla F_n \quad (3.8a)$$

$$\mathbf{J}_p = \frac{\mu_p}{q}P\nabla F_p \quad (3.8b)$$

It is thus straightforward that when quasi-Fermi level are constant in space, no current occurs.

Finally, using eq. (3.8) in eq. (3.5) and linking the holes and electrons by the Poisson equation, we can define the Drift-Diffusion equations system:

$$\frac{\partial N(x, t)}{\partial t} + \frac{\mu_n}{q}N\nabla F_n = G(x, t) + R(x, t) \quad (3.9a)$$

$$\frac{\partial P(x, t)}{\partial t} - \frac{\mu_p}{q}P\nabla F_p = G(x, t) + R(x, t) \quad (3.9b)$$

$$-\varepsilon_0\varepsilon_r\nabla^2\phi = q(P - N + N_d - N_a) \quad (3.9c)$$

Where  $\phi(x, t)$  is the potential in the structure, taking into account both external and internal electric field,  $N_a$  and  $N_d$  are the acceptor and donor dopant concentrations respectively.

This formulation is used for the further numerical calculation of the carrier diffusion in the PhC.

### 3.1.2.2 | Carrier Recombination

Several carrier recombination mechanisms occur in a semiconductor. First, band-to-band recombination (Fig. 3-2(a)) which occurs when the electron or holes move from the conduction and valence band respectively to an empty state in the other band, resulting in a radiative recombination in direct bandgap material like GaAs. The recombination rate of such process,  $R_{rad}$  is:

$$R_{rad} = \frac{NP - n_i^2}{\tau_{rad}} \quad (3.10)$$

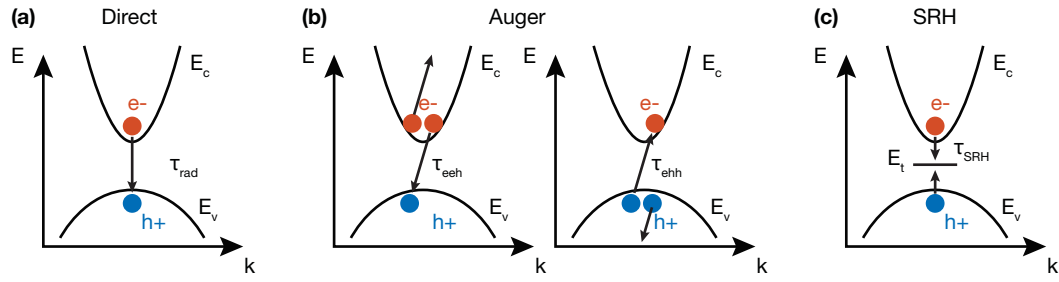


**Fig. 3-2** | Main recombination processes occurring in semiconductors: (a) band to band recombinations – (b) Auger recombinations – (c) Trap assisted recombinations.

Where  $n_i$  is the intrinsic carrier density (usually close to  $10^{10}$  to  $10^{12}$   $\text{cm}^{-3}$  in common semiconductors).

The second one, Auger recombination (Fig. 3-2(b)), is a three body interaction which becomes large at large injected level. It follows almost the same process than the band-to-band recombination whereas the carrier has an excess energy, compared to the band edge of the conduction and valence for electron and holes respectively, which is given to a third party particle. For instance, an electron recombines with a hole, giving part of its energy to another electron which is excited and further relaxes to the edge of the band, emitting a phonon (Fig. 3-2(b)).

$$R_{Aug} = N \frac{NP - n_i^2}{\tau_{ehh}} + P \frac{NP - n_i^2}{\tau_{eeh}} \quad (3.11)$$

Finally, the trap-assisted recombinations, also called Shockley-Read-Hall (SRH) recombinations (Fig. 3-2(c)), where the electrons or holes move from their respective band to a trap state in the band-gap of the semiconductor at an energy  $E_t$ :

$$R_{SRH} = \frac{1}{\tau_{SRH}} \frac{NP - n_i^2}{N + P + 2 \cosh(E_t/k_B T)} \quad (3.12)$$

Those processes are characterized by their lifetimes  $\tau$ . Under a photo-excitation generating a carrier concentration of  $N = P = 1 \times 10^{17}$   $\text{cm}^{-3}$ , the respective lifetimes are  $\tau_{Aug} = 100$   $\mu\text{s}$  [123–126],  $\tau_{rad} \simeq 100$  ns [123, 124, 127] and  $\tau_{SRH} \simeq 1$  ns [124]. As the smallest carrier lifetime process dominates the global carrier recombination dynamics (*i.e.*  $\tau_{tot}^{-1} = \sum \tau^{-1}$ ) it is obvious that SRH recombination is the dominating process in GaAs and thus, only this one will be considered in the following thesis for bulk recombination.

### 3.1.2.3 | Surface Recombinations

In PhCs, the large surface over volume ratio leads to a preponderant role of the surface carrier dynamics. Surfaces naturally result in carrier recombination. Indeed, surfaces are a periodicity break of the crystal, therefore, create defects in the semiconductor band-gap. Given this, the most suitable model to reproduce this process is the SRH one. However, this last model takes into account volume concentrations and not surface ones. The Stevenson-Keys model [128], which is derivated from the SRH leads the same formalism but instead of providing a carrier lifetime to estimate the recombination rate, it is changed to a recombination velocity  $v_{rec}$  such that:

$$R_{SK} = v_{rec} \frac{N_s P_s - (n_{i_s})^2}{(N_s + P_s + 2 \cosh(E_s/k_B T))} \quad (3.13)$$

Where the subscript  $s$  stands for the carrier surface density, and  $E_s$  the trap position at surface. This last one is highly dependent on the material and surface treatments.

Using the Shockley formula to link the surface recombination with the carrier lifetime [129]:

$$\tau_{tot}^{-1} = \tau_{bulk}^{-1} + L^{-1} v_{rec} \quad (3.14)$$

Where  $\tau_{bulk}$  is the total carrier lifetime in the bulk semiconductor (see section 3.1.2.2),  $L$  is the average length carriers have to travel before reaching a surface,  $v_{rec}$  is the surface recombination velocity and  $\tau_{tot}$  is the carrier lifetime taking into account both bulk and surface contributions. Knowing that PhC average travel length for carrier is about 100 nm (considering carriers generated in the center of the membrane which consists of 200 nm height) and using carrier recombination velocity given in the literature ( $10^5 \text{ cm.s}^{-1}$  for GaAs [130]), this gives a total carrier lifetime of about 1 ps. Therefore, by comparing bulk lifetime (*i.e.*  $\tau_{tot} \simeq 1 \text{ ns}$ ) with the one from surface recombination, it is evident that the latter plays a crucial role in the geometry considered here.

### 3.1.3 | Ambipolar Approximation

An important case of carrier dynamics is the local absorption of photons creating electron-hole pairs (Fig. 3-3(a)). Therefore, at the initial time of the generation,  $N = P$  everywhere as the generation for both holes and electrons is the same. A diffusion process occurs, wherein III-V materials, the electrons diffuse faster than the holes (Fig. 3-3(b)). However, in the case of a coulombian interaction between holes and electrons stronger than an external electric field or

chemical potential gradient, the internal electric field created by the difference of charge of the particles tends to stick both carrier types together. Then, it leads to  $N = P$  everywhere at any time. In this case, the Poisson equation is satisfied as the electric potential at every point is null (Fig. 3-3(c)).

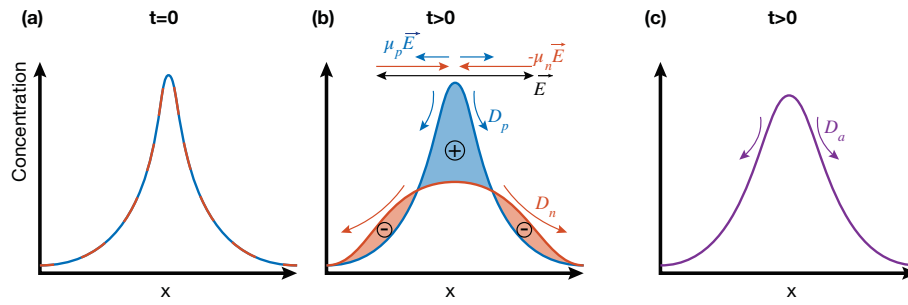


**Fig. 3-3** | (a) Initial state where the concentration of electron and holes are equal  $N = P$  – (b) after some time, the diffusion process occurs for both carriers relatively to their diffusion constant. An electric field  $E$  is created from the charge difference leading to a coulombian force – (c) the ambipolar approximation where it is consider  $N = P$  and the carrier diffuse with the ambipolar diffusion coefficient.

Therefore, the electrons and holes can be considered as a single entity without charge, leading to no current, with a diffusion constant  $D_a = \frac{D_n\mu_p + D_p\mu_n}{\mu_n + \mu_p}$ . The equations eq. (3.9) can be simplified to:

$$\frac{\partial N}{\partial t} + \nabla \cdot (-D_a \nabla \cdot N) = GR \quad (3.15)$$

### 3.1.4 | Implementation with Finite Element Method

To model the carrier dynamics in PhC, a Finite Time Difference Domain (FDTD) method could be implemented to compute the resolution of those coupled equations. However, the mesh would be extremely fine due to the geometry and the need to reproduce PhC holes and surfaces accurately. In opposition, the FEM provides a way to solve the equations with an adaptive mesh, which can reproduce the complex PhC geometry in the best way. However, this method is somewhat complex, using discretization of the expression, further projected on the so-called basis functions. Therefore, such implementation from scratch is highly challenging. This is why a commercial software (COMSOL [131]) has been used to benefit effectively from the power of the FEM computation for the drift-diffusion equations.

### 3.1.4.1 | Implementations of the Drift-Diffusion Formalism in COMSOL

The proprietary platform COMSOL for solving Partial Differential Equations (PDE) provides a general differential equation (called *coefficient form PDE*) of the form:

$$e_a \frac{\partial^2 \mathbf{U}}{\partial t^2} + d_a \frac{\partial \mathbf{U}}{\partial t} + \nabla \cdot (-\mathbf{c} \nabla \cdot \mathbf{U} - \boldsymbol{\alpha} \cdot \mathbf{U} + \boldsymbol{\gamma}) + \boldsymbol{\beta} \nabla \cdot \mathbf{U} + \mathbf{a} \mathbf{U} = \mathbf{f} \quad (3.16)$$

Where  $\mathbf{U}$  could be a vector, therefore, all coefficients are either square matrix or vectors accordingly to the equation above. This is really useful as it allows the user to fully link coupled equations such as in the drift-diffusion model, by defining  $\mathbf{U} = (N \ P \ V)^\top$ . Therefore, the implementation of eq. (3.9) leads to the coefficient definitions:

$$e_a = 0 \quad d_a = \begin{pmatrix} 1 & 0 & 0 \\ 0 & 1 & 0 \\ 0 & 0 & 0 \end{pmatrix} \quad \mathbf{c} = \begin{pmatrix} 0 & 0 & 0 \\ 0 & 0 & 0 \\ 0 & 0 & \varepsilon_0 \varepsilon_r \end{pmatrix} \quad \boldsymbol{\alpha} = \begin{pmatrix} -\frac{\mu_n}{q} \nabla \cdot \mathbf{F}_n & 0 & 0 \\ 0 & \frac{\mu_p}{q} \nabla \cdot \mathbf{F}_p & 0 \\ 0 & 0 & 0 \end{pmatrix}$$

$$\boldsymbol{\gamma} = 0 \quad \mathbf{a} = \begin{pmatrix} 0 & 0 & 0 \\ 0 & 0 & 0 \\ q & -q & 0 \end{pmatrix} \quad \mathbf{f} = \begin{pmatrix} GR \\ GR \\ 0 \end{pmatrix}$$

This method of implementation has two main advantages. The first one is to strongly coupled inside the COMSOL core the drift-diffusion and the Poisson equations. Thus the equations are solved consistently. Secondly, this lets us control each element of the equations and thus to tailor these equations in with our needs (things impossible with a proprietary module, where everything is pre-compiled).

The boundary conditions using the *coefficient form PDE* are either Dirichlet, forcing each component of  $\mathbf{U}$  at a specified value, or generalized Neumann. This last one is used to represent the

surface recombination, and is implemented such that:

$$\mathbf{n} \cdot (-c\nabla \cdot \mathbf{U} - \alpha \cdot \mathbf{U} + \gamma) = \mathbf{g} - \mathbf{q} \cdot \mathbf{U} \quad (3.17a)$$

$$\mathbf{g} = \begin{pmatrix} \frac{n_i^2}{S(N+P+2 \cosh(E_s/k_B T))} & 0 & 0 \\ 0 & \frac{n_i^2}{S(N+P+2 \cosh(E_s/k_B T))} & 0 \\ 0 & 0 & 0 \end{pmatrix} \quad (3.17b)$$

$$\mathbf{q} = \begin{pmatrix} \frac{P}{S(N+P+2 \cosh(E_s/k_B T))} & 0 & 0 \\ 0 & \frac{N}{S(N+P+2 \cosh(E_s/k_B T))} & 0 \\ 0 & 0 & 0 \end{pmatrix} \quad (3.17c)$$

### 3.1.4.2 | Model Verifications

To verify the accuracy of our drift-diffusion solver, some cases for which analytic formulation can be written are considered. First, an abrupt PN junction is computed, which can only be calculated in the full drift-diffusion formalism as the ambipolar approximation does not stand. The different formulas for calculating the carrier concentrations, the band diagram and the current for different applied bias are summarized in appendix A.1. This structure was computed with a doping for both  $P$  and  $N$  of  $N_a = N_d = 1 \times 10^{22} \text{ m}^{-3}$ , and the results are shown in Fig. 3-4

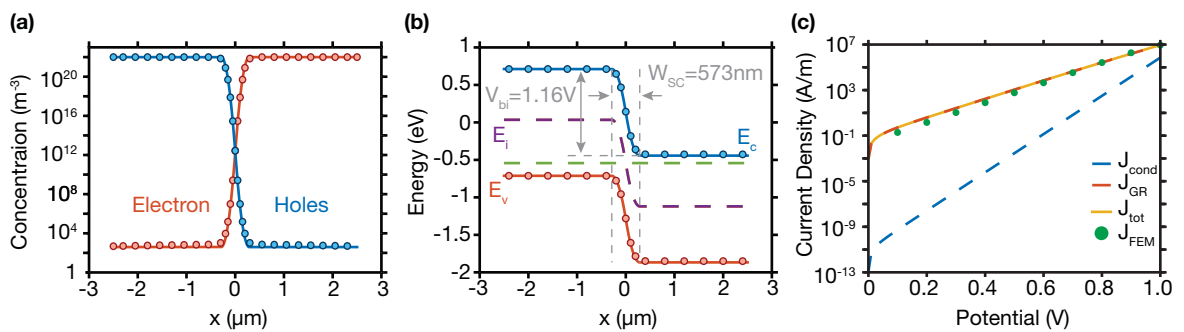


**Fig. 3-4** | (a) Carrier concentration for an abrupt PN junction with a donor and acceptor concentration of  $N_a = N_d = 10^{22} \text{ m}^{-3}$ . The solid lines are the analytic results, while the circles are the FEM ones – (b) Band Diagram of the PN junction. – (c) Current Density versus applied voltage.

Calculations were performed in a 3D system, to insure that our model could compute 3D PhC structure. However, to compare with the analytic solution, which can be obtained from 1-dimension

system, a cylinder with small radius compared to its length is considered. The generation and the doping profile are uniform in the radial direction to emulate a 1D-like structure. Figure 3-4a and b are considered in the case of no applied external voltage, and represent the steady state given by the FEM modeling (circles). Those results match the analytic theory (solid lines). Figure 3-4c is the current circulating through the structure when an external bias is applied from the side of the N-doped (while the P-doped sided is maintained at  $\phi = 0$ ). Here too, the computation converges to the analytic formulation.

However, the above verification only stands for the steady state, while we are interested in computing the carrier dynamical response in PhCs. The case which has an easy analytical formula is the diffusion of Gaussian concentration in time, where no generations neither recombinations occur, without external electric field applied and in the absence of doping (*i.e.* the steady state of such system correspond to a carrier concentration equal to the intrinsic one). Thus, the ambipolar approximation stands, solving this equation for initial condition corresponding to a Gaussian gives the concentration profile in time:

$$\partial_t \hat{n}(k, t) = D_a k^2 \hat{n}(k, t) \quad (3.18)$$

$$\Rightarrow n(x, t) = \frac{1}{\sqrt{4\pi D_a t}} \exp\left(-\frac{x^2}{4D_a t}\right) \quad (3.19)$$

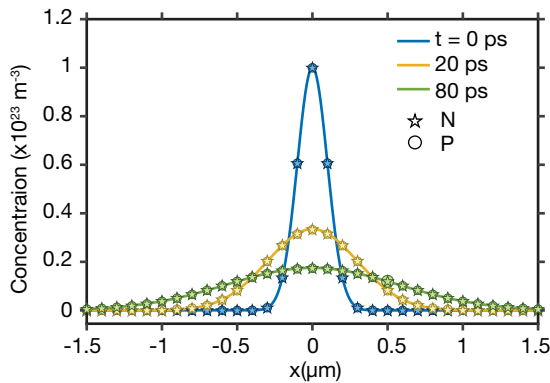


**Fig. 3-5** | Concentration of the electrons and holes for the times  $t = 0, 20$  and  $80$ ps. The circles correspond to the holes, the stars the electron, while the solid line is the analytic ambipolar results

The simulation was performed in COMSOL using the drift-diffusion coupled equation (eq. (3.9)). The first important thing to notice is the fact that ambipolar approximation stands here. Therefore, both electrons and holes must follow the same concentration profile for each time. The results shown in Fig. 3-5 exhibit a good agreement with the ambipolar approximation between holes and electron, as their concentration profiles correspond. Also, the analytical formulation matches the

computation, this verifies that electrons and holes diffuse in our solver with the ambipolar diffusion coefficient  $D_a$ .

The third test case performed here is to ensure that current conservation is ensured in the structure. To do so, a bias is applied from one side of the same structure considered in the second test verification. The initial condition for carriers are considered to be  $N = P = n_i$ , and a generation term corresponding to the same space profile than the initial condition of Fig. 3-5, multiplied by a temporal Gaussian of parameter  $\sigma = 5 \times 10^{-12}$  ps centered at 20 ps. The total current consists of the drift diffusion as mentioned above, and also the displacement current  $\mathbf{J}_{disp} = \epsilon_0 \epsilon_r \frac{\partial \mathbf{E}}{\partial t}$ .

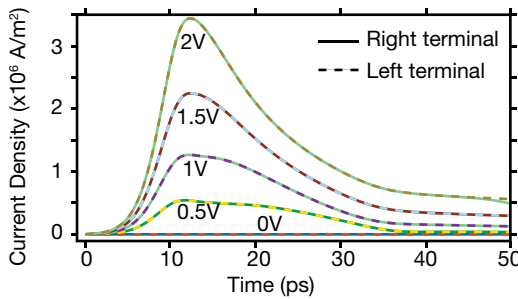


**Fig. 3-6** | Current for different applied voltage calculated at the right terminal (solid lines) and at the left one (dashed lines)

The current was calculated at the two boundaries of the structure (*i.e.* right and left terminal) for different applied bias. We note that the total current remains the same at both terminals for each applied bias (Fig. 3-6), therefore, the current is conserved in the whole structure.

Thanks to all these verifications, we can assume that the drift-diffusion model implemented with FEM in COMSOL is accurate enough.

### 3.2 | Coupled Mode Theory

To adequately model the dynamics of the photonics crystal cavity in time, carrier dynamics which described the current and the optical change modification of the structure though plasma effect, need to be linked with the optical excitation. The straightforward implementation would be to introduce the drift-diffusion equations in the optical computation using FDTD. However, as it was previously mentioned, FDTD is not the most suited way to model carrier dynamics in PhC. Moreover, the characteristic time step of the optical simulation is of the order of  $\frac{\lambda}{20c} < 0.1$  fs where, for the carrier, it is about under the picosecond.

Since, the optical confinement of the optical mode is entirely determined by the PhC geometry, the carrier effect can still be considered as a perturbation. Therefore, an ensemble of optical resonators coupled to waveguides is conveniently described by the Coupled Mode Theory in the time domain [132]. The underlying assumption is that the optical field can be described in terms of normal modes in the waveguides and in the cavities. This approximation is correct as long as cavity modes are well confined, i.e. leakage can be treated as a small perturbation. While a more general case is conveniently treated using *quasi normal modes* [133, 134], here the optical leakage is dominated by coupling into the cavity modes and the loaded Q factor is well above  $10^3$ . In single-mode cavities such as  $H_0$  can be shown that the energy density is about Q times stronger than in the waveguide (see discussion appendix) and, therefore, the approximation is good enough.

### 3.2.1 | Formalism

For the sake of simplicity, we shall consider the case of a single resonator (Fig. 3-7) coupled to two waveguides, serving as an input (port a) and an output (port b), with strengths  $\gamma_a = |\kappa_a|^2$  and  $\gamma_b = |\kappa_b|^2$  respectively.

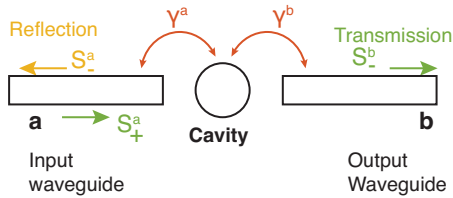


**Fig. 3-7** | Schematic once cavity coupled to an input (port a), and an output waveguide (port b).

The complex envelopes of the incoming “+” and outgoing “-” waveguide modes are represented as vectors  $\mathbf{S}_{in} = (S_{+,a}, S_{+,b})^\top$  and  $\mathbf{S}_{out} = (S_{-,a}, S_{-,b})^\top$  with subscript letters denoting the ports. The normal modes of the waveguides are normalized such that  $|\mathbf{S}_{in}|^2 = P_{in}$  and  $|\mathbf{S}_{out}|^2 = P_{out}$  representing the input and output powers (Fig. 3-7). The electric field in the cavity  $\mathbf{E}(\mathbf{r}, t) = A(t)\mathbf{U}(\mathbf{r})$  is factorized into the complex envelope  $A(t)$  and the normal mode  $\mathbf{U}(\mathbf{r})$ , which is normalized with the condition:

$$\frac{1}{2} \int \varepsilon_0 \varepsilon_r |\mathbf{U}(\mathbf{r})|^2 d\mathbf{r} = 1 \quad (3.20)$$

which defines the mode volume  $V_{mod}^{-1} = \frac{\varepsilon_0 \varepsilon_r}{2} \max(|\mathbf{U}|^2)$ . Consequently, the energy in the cavity is  $W_{cav}(t) = |A(t)|^2$ .

The motion equations [132] for the envelopes  $A$ , input  $S_{in}$  and outputs  $S_{out}$  are rewritten in the matrix formalism:

$$\partial_t A = M A - \mathbf{R} S_{in} \quad (3.21a)$$

$$S_{out} = \mathbf{Q} A + \mathbf{P} S_{in} \quad (3.21b)$$

with  $\mathbf{R}$ ,  $\mathbf{Q}$  and  $\mathbf{P}$ :

$$\mathbf{R} = \begin{pmatrix} \kappa^a & \kappa^b \end{pmatrix} \quad (3.22a)$$

$$\mathbf{Q} = \begin{pmatrix} \kappa^a & \kappa^b \end{pmatrix}^\top \quad (3.22b)$$

$$\mathbf{P} = \begin{pmatrix} 1 & 0 \\ 0 & 1 \end{pmatrix} \quad (3.22c)$$

In the linear limit,  $M = -i\omega_0 - (\Gamma_0 + \gamma_a + \gamma_b)/2$ , with  $\omega_0/(2\pi)$  the frequency of the normal mode and  $\Gamma_0$  the internal losses of the resonator. With little loss of generality, we consider hereafter the situation where excitation is applied to port  $a$ , and therefore  $S_{+,b} = 0$ .

This formalism can be generalized to handle an arbitrary number of cavities and waveguides. A crucial assumption is that the resonators are weakly coupled together, such that super-modes are conveniently described in the tight-binding approximation. Recently it has been shown that in some case, *e.g.* chain of PhC cavities, some corrections are needed [135], which can be integrated in our model.

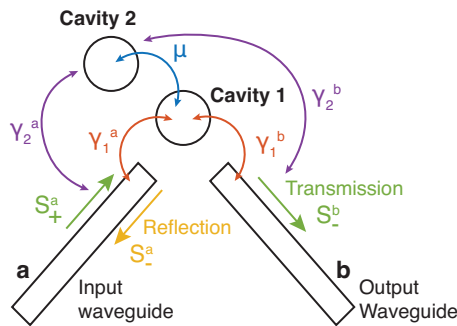


**Fig. 3-8** | Two coupled cavities and access waveguides and related parameters in the CMT model.

An interesting case entails two resonators with two waveguides (Fig. 3-8). Then:

$$\partial_t \mathbf{A} = \partial_t (A_1 \ A_2)^\top = \mathbf{M} \mathbf{A} - \mathbf{R} S_{in} \quad (3.23)$$

Subscripts in  $A_k$  relates to the two cavities and  $\mathbf{M} = M_{kl}$  is a  $2 \times 2$  matrix:

$$M_{kl} = i\omega_{k,0} - \frac{1}{2} \left( \Gamma_{0,k} + |\kappa_{k,a}|^2 + |\kappa_{k,b}|^2 \right) \delta_{kl} \quad (3.24a)$$

$$M_{kl} = \left( i\mu - \kappa_{1,a}\overline{\kappa_{2,a}}e^{-i\beta_{12}} - \kappa_{1,b}\overline{\kappa_{2,b}}/2 \right) (1 - \delta_{kl}) \quad (3.24b)$$

$\Gamma_{0,k}$  is the photon decay rate, due to internal losses,  $\mu$  the cavity mutual coupling,  $\gamma_{k,(a,b)}$  the cavity to waveguide coupling, the overline denotes complex conjugation and  $\delta_{kl}$  the Kronecker delta coefficient.  $\mathbf{Q}$ ,  $\mathbf{R}$  and  $\mathbf{P}$  have the form:

$$\mathbf{R} = \begin{pmatrix} \kappa_{1,a} & \kappa_{1,b} \\ \kappa_{2,a}e^{-i\beta_{12}} & \kappa_{2,b}e^{-i\beta_{12}} \end{pmatrix} \quad (3.25a)$$

$$\mathbf{Q} = \begin{pmatrix} \kappa_1^a & \kappa_2^a e^{-i\beta_{12}} \\ \kappa_1^b & \kappa_2^b e^{-i\beta_{12}} \end{pmatrix} \quad (3.25b)$$

$$\mathbf{P} = \begin{pmatrix} 1 & 0 \\ 0 & 1 \end{pmatrix} \quad (3.25c)$$

The generalization to an arbitrary number of coupled cavities and input/output ports is straightforward and  $\mathbf{R}$ ,  $\mathbf{P}$  and  $\mathbf{Q}$  are determined based on the energy conservation [132].

### 3.2.2 | Device Design and Experimental Benchmark

As an example, Fig. 3-9 represents the transmission spectra of PhC devices entailing waveguides and two coupled cavities from three different materials: InP, GaAs, and ALD-coated GaAs. The differences in the line-shapes are due to slightly different designs, as schematically represented in Fig. 3-8. The CMT reproduces the experimental transmission well with the fitted parameters listed in table 3.1. We point out that Fabry-Pérot modulation and other fast modulation of the spectra are absent here, owing to a design minimizing the length of the waveguides (and so coherent scattering) and the use of adiabatic tapers to avoid reflection at their terminations.

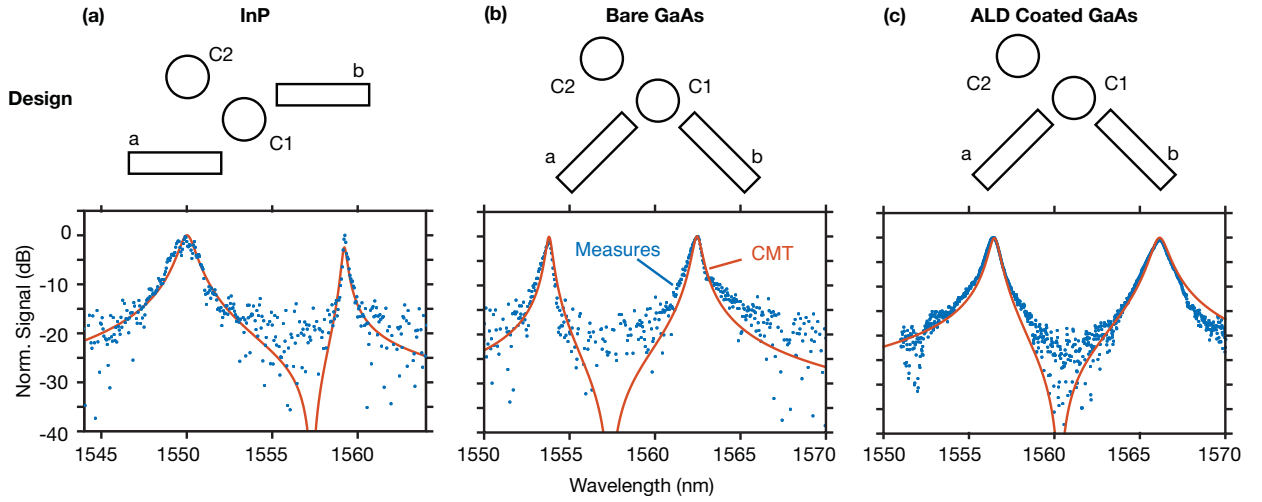


**Fig. 3-9** | Linear transmission calculated by Coupled Mode Theory and characterized on (a) InP, (b) GaAs and (c) ALD coated GaAs

The designs of the samples considered here are all based on two coupled  $H_0$  cavities [44], which are spaced by 3 lattice periods along the  $M$  direction (design further discussed in section 4.1).

In the case of the sample (a), the position of the waveguides is such that the both cavities are coupled to them. The interference between the two paths results into a Fano-like lineshape (Fig. 3-9(a)), which is the sample reported in ref. [66]. Samples (b) and (c) are instead based on a design such as only one of the two cavities are coupled to the waveguides. Consistently, Fano line-shape is absent in the transmission spectra.

The practical interest is that waveguides are on the same side of the sample, thus more convenient for experiments. The transmission minimum is actually a zero of the transmission spectra. The fact that they are not centered can be explained by a slight difference between the two cavity resonances (see table 3.1).

### 3.2.3 | Non-Linear Dynamics

Non-linear effects induce a change in the complex permittivity  $\varepsilon$  which we account for by allowing the complex resonance of each cavity  $\omega_k = \omega_k^0 + i\Gamma_k^0/2$  to be corrected with the contribution  $\Delta\tilde{\omega} = \Delta\omega_k + i\Delta\Gamma_k/2$ . Thus  $M$  becomes:

$$M_{kk}^{NL} = i\Delta\omega_k(A_k) - \Delta\Gamma_k(A_k)/2 \quad (3.26)$$

Param.	Bare GaAs	ALD GaAs	InP	Units
$\omega_1$	192.31	191.89	192.85	$\times 2\pi$ THz
$\omega_2$	192.50	192.13	192.85	$\times 2\pi$ THz
$\mu$	3.3059	3.6581	3.5853	$\times 10^{12}$ s <sup>-1</sup>
$\kappa_1^a$	5.79	7.76	6.36	$\times 10^5$ s <sup>-1/2</sup>
$\kappa_2^a$	0	0	0	$\times 10^5$ s <sup>-1/2</sup>
$\kappa_1^b$	5.79	7.76	6.355	$\times 10^5$ s <sup>-1/2</sup>
$\kappa_2^b$	0	0	3.759	$\times 10^5$ s <sup>-1/2</sup>
$\Gamma_{0,1}$	1.21	1.21	1.21	$\times 10^{-12}$ s <sup>-1</sup>
$\Gamma_{0,2}$	1.21	1.21	1.21	$\times 10^{-12}$ s <sup>-1</sup>

**Table 3.1** | Simulation Parameters value used in the CMT model for bare GaAs, ALD-coated GaAs and InP

This choice implies that the non-linear effect is local at the scale of the cavity. i.e. the non-linearity in cavity  $C_i$  only affects the other cavities  $C_{j \neq i}$  indirectly, through the linear coupling coefficients  $\gamma$  and  $\mu$ .

In the case of semiconductors, three dominant effects take place. The thermo-optic effect, which is slow (microsecond or longer) [60] and it not discussed here <sup>1</sup>. The nonlinear polarizability, i.e. the anharmonicity of the electronic potential, specifically the third order term  $\chi^{(3)}$ , inducing both a change in the real and imaginary part of the refractive index [45], as prescribed by Kramers-Kronig relationship for physical transitions, e.g. absorption/emission. This phenomenon is extremely fast when non-resonant, which is the case of semiconductors.

The term is expressed as:

$$\left(i\Delta\omega_k - \frac{\Delta\Gamma_k}{2}\right)_{Kerr} = |A_k|^2 c_0 \left(i\omega n_2 - \beta_{TPA} \frac{c_0}{2}\right) V_\chi^{-1} \quad (3.27)$$

with  $n_2$  the nonlinear index ( $\Delta n = n_2 I$ ,  $I$  the irradiance),  $\beta_{TPA}$  the two-photon absorption (defined from  $\partial_z I = -\beta_{TPA} I^2$ ) and  $V_\chi$  the nonlinear volume (see appendix A.2.2).

We point out that this time-domain formulation of non-linear responses also accounts for four-wave mixing, as long as the spectral domain of interest is narrow enough to allow the rotating wave approximation underlying the CMT.

<sup>1</sup>Thermal response can be included in the model, by introducing an auxiliary dynamic equation. This is useful when analyzing long-term response or situation with very fast heating.

The third effect is due to the excitation of free carriers, which induces a change of the refractive index. This entails three contributions [58]: band-filling, free-carrier dispersion, and band shrinkage. We note that band shrinkage is negligible for GaAs or InP at Telecom wavelengths, and then will be neglected. In contrast to the nonlinear polarization, the response of the refractive index to the optical excitation is not instantaneous but follows the population of free carriers. It is convenient to define  $N_{eff}^{(k)}$  as the effective carrier density, *i.e.* the carrier density weighted by the distribution of the field inside the cavity (see appendix A.2.3):

$$N_{eff} = \frac{1}{2} \varepsilon_0 \int_V \varepsilon_r N(r, t) |\mathbf{U}(\mathbf{r})|^2 d\mathbf{r} \quad (3.28)$$

The corresponding contribution to the CMT model reads:

$$i\Delta\omega_k - \frac{\Delta\Gamma_k}{2} \Big|_{FC} = i\frac{\omega}{n} \frac{\partial \tilde{n}}{\partial N} \Big|_{FC} N_{eff}^{(k)} \quad (3.29)$$

with the derivative representing the dependence of the complex index of refraction  $\tilde{n}$  on the density of free carriers. Note that the definition of  $N_{eff}$  already takes into account the connection between the refractive index and the frequency of the resonance (see appendix A.2.3)

## 3.2.4 | Free Carriers Dynamics

### 3.2.4.1 | Use of the Ambipolar Model

The modeling of ultrafast carrier dynamics has been broadly addressed in the context of semiconductor optical devices [136]. Here we use a more standard drift-diffusion model [92]. The justification of the underlying approximations is given in appendix A.2.3.

In the absence of doping and external electric field, the evolution of photo-excited carriers can be described in the ambipolar approximation of the drift-diffusion model, where electrons and holes have the same distribution, *i.e.*  $N(\mathbf{r}, t) = P(\mathbf{r}, t)$ , previously described in eq. (3.15). Considering two-photon absorption, the generation term is expressed as:

$$G(\mathbf{r}) = \beta_{TPA} \frac{c_0^2 \varepsilon_0^2}{8\hbar\omega} \varepsilon_r |\mathbf{U}(\mathbf{r})|^4 |A|^4 \quad (3.30)$$

Note that this equation is based on the scalar approximation of the nonlinear tensor (see appendix A.2.2). Integrating  $G(\mathbf{r})$  we obtain the total generation rate, which is equal to the rate of

absorbed photons, hence the equation:

$$c_0^2 \beta_{TPA} \frac{|A|^4}{2\hbar\omega V_\chi} = -\frac{1}{2\hbar\omega} \partial_t |A|^2 \quad (3.31)$$

Which is consistent with eq. (3.27).

Carrier recombination has nonradiative and radiative contributions (see section 3.1.2.2), which are summarized here by a time constant  $\tau$ . In the specific case of photonic nano-structures, where the volume over surface ratio is  $V/S = L_s \simeq 100$  nm corresponding to about the average distance of the carriers from the surfaces, thus surface recombination is extremely important. Considering the Shockley [137] approximation  $\tau_{eff}^{-1} = \tau^{-1} + v_{rec}/L_s$ , the surface recombination may actually dominate the carrier lifetime, as shown in the case of GaAs photonic crystal cavities [65], as in GaAs  $v_{rec}$  might approach the saturation velocity [130] and, in general, is highly dependent on the material and the fabrication process.

This has two implications. First, radiative and non-radiative recombinations in the bulk of the material play a little role, and therefore can be very well approximated with a single time constant  $\tau$ . The second implication is that the validity of the rate equation model needs to be scrutinized in detail.

### 3.2.4.2 | Rate Equations

To clarify this point, let us assume that the carrier population decays following a time constant determined by the dominant process, namely surface recombination. Then, a simple rate equation model could then represent the evolution of the excited carriers in the cavity, which is a very common approximation:

$$\partial_t N_{eff} = -\tau_{eff}^{-1} N_{eff} + \frac{K_{TPA}}{V_c} |A|^4 \quad (3.32)$$

The generation term  $K_{TPA}|A|^4 = \int_V G(\mathbf{r})$  is obtained from eq. (3.31). A carrier volume  $V_c$  is introduced empirically to obtain an effective generation density.

It turns out that this approximation may not be satisfactory in the context of semiconductor nanocavities. Here, diffusion might also lead to an initial, extremely fast change of the carrier distribution *seen* by the cavity, i.e.  $N_{eff}$ . It has been observed experimentally that then the dynamics is slowed down, and more interestingly, in a variety of semiconductors: InP, GaInAsP and Silicon [48, 57, 59, 62]. This behavior has been described with a multi-exponential decay, which is understood as resulting from the successive diffusion of photogenerated carriers to a

larger *reservoir* with volume  $V_x$  and population density  $N_x$ , until recombination takes place. This is readily using one or more auxiliary equations [59]:

$$\partial_t N_{eff} = -\gamma_{diff}(N_{eff} - N_x) + \frac{K_{TPA}}{V_c} |A(t)|^4 \quad (3.33a)$$

$$\partial_t N_x = -\tau_{eff}^{-1} N_{eff} + \gamma_{diff} \frac{V_c}{V_x} (N_{eff} - N_x) \quad (3.33b)$$

Accordingly, an auxiliary carrier diffusion rate  $\gamma_{diff}$  is introduced. If this approach can represent the multi-exponential decay observed experimentally, it is still not satisfactory for several reasons. First, the mode volume and the diffusion rate  $\gamma_{diff}$  are not well-defined, and can only be used as a fitting parameters to coarsely model the diffusion process. Secondly, more than one auxiliary equations may be necessary, as pointed out by Yu et al. for instance [63], therefore mechanically increasing the number of fitting parameters.

Actually, and this is a key point of this paper, the rate equation formalism, entailing exponential decaying dynamics, is not the best choice for modeling a diffusion process. Considering the resolution of the ambipolar formula, with a Gaussian initial spatial distribution  $N(\mathbf{r}, 0)$  centered at some point  $\mathbf{r}_0$ , the exact solution for  $N(\mathbf{r}_0, t)$  is actually a hyperbola, which is ill approximated by exponentials.

In this thesis, we introduce a significant change in the model, consisting in replacing the rate equation with a more suitable representation of the diffusion dynamics. Moreover, since in semiconductor nanostructures this dynamics is essentially non-local, as surface recombination and diffusion dominate, this implies the accurate calculation of the carrier dynamics in the actual geometry. This is achieved in several steps, and will be detailed here below.

### 3.2.5 | Green's Function Formalism

The diffusion equation, previously introduced in eq. (3.15), resulting from the ambipolar approximation, is a linear, partial derivatives equation (see eq. (3.15)). Consequently, the temporal and spatial distribution of the free carriers can be related to the generation term, described in eq. (3.30) through a Green's function  $K(\mathbf{r}, \mathbf{r}'; \Delta\tau)$ :

$$N(\mathbf{r}, t) = \int_{-\infty}^t \int K(\mathbf{r}, \mathbf{r}'; t - \tau) G(\mathbf{r}', \tau) d\mathbf{r}' d\tau \quad (3.34)$$

An interesting similarity appears with photo-reflectance measurements, where the time and

spatial evolution of the temperature, following the excitation with a localized laser spot, are modeled through the Green's function formalism [138, 139]. There, the geometry allows the use of an analytic expression of the Green's function, which considerably eases the calculations. The geometry of PhC cavities, however, is such that the numerical calculation is unavoidable, which is an important point of this work.

As a matter of fact, the calculation of the general Green's function is not necessary here, as the excitation (see eq. (3.30)) is a separable function in the form  $G(\mathbf{r}, \tau) = \psi(\mathbf{r})f(\tau)$ . Therefore, the space integral in eq. (3.34) can be carried out to yield a simpler integral form:

$$N(\mathbf{r}, t) = \int_{-\infty}^t \tilde{K}(\mathbf{r}; t - \tau) |A(\tau)|^4 d\tau \quad (3.35)$$

with the kernel resulting from the above equations:

$$\tilde{K}(\mathbf{r}; \tau) = \beta_{TPA} \frac{c_0^2 \varepsilon_0^2}{8\hbar\omega} \varepsilon_r \int_V K(\mathbf{r}, \mathbf{r}'; \tau) |U(\mathbf{r})|^4 d\mathbf{r}' \quad (3.36)$$

The integral is carried out within the volume occupied by the semiconductor, denoted by  $V$ . Note that  $\tilde{K}(\mathbf{r}; \tau) = 0$  when  $\tau < 0$ , because of causality.

The numerical calculation of the kernel is straightforward. Let us consider the Dirac excitation for eq. (3.35), namely in the form  $|A(t)|^4 = |A_0|^4 \Delta t \delta(t)$  ( $\Delta t$  being an arbitrary small time interval). Using eq. (3.30), this leads to the corresponding initial condition for eq. (3.15):

$$N(\mathbf{r}, 0^+) = G(\mathbf{r}, 0^+) \Delta t \quad (3.37)$$

This represents the distribution of carriers at  $t = 0^+$ , after the Dirac impulse and before any diffusion process takes place. The equation eq. (3.15) is then solved using a time domain finite element technique and the kernel is obtained through:

$$N(\mathbf{r}, t) = \tilde{K}(\mathbf{r}, t) |A_0|^4 \Delta t \quad (3.38)$$

Let us now consider the projection of the carrier distribution in the optical mode, namely the effective carrier concentration introduced in section 3.2.3. A new integral equation, relating  $N_{eff}$  to the excitation  $A(t)$ , is obtained by combining eq. (3.28) with eq. (3.35) and changing the order of the integrals.

$$N_{eff}(t) = \int_{-\infty}^t h_0(t - \tau) |A(\tau)|^4 d\tau \quad (3.39)$$

In the end, the Green's function formalism reduces to an explicit integral equation where the dynamics is contained in a time-dependent function  $h_0(t - \tau)$ , which, consistently with eqs. (3.28), (3.35) and (3.39), is defined as:

$$h_0(\tau) = \frac{1}{2} \varepsilon_0 \int \varepsilon_r \tilde{K}(\mathbf{r}; \tau) |U(\mathbf{r})|^2 d\mathbf{r} \quad (3.40)$$

In the context of signal theory,  $h_0$  is referred to as an impulse response function. Hereafter, it will be referred to it as *effective carrier density response* function. Its initial value, which also corresponds to its maximum, is calculated by inserting eq. (3.36) into eq. (3.40), which does not need solving the diffusion equation:

$$h_0(0^+) = \frac{\beta_{TPAC}^2 \varepsilon_0^3}{16 \hbar \omega} \int_V \varepsilon_r^2 |U(\mathbf{r})|^6 d\mathbf{r}^3 = \frac{\beta_{TPAC}^2}{2 \hbar \omega} V_{3PA}^{-2} \quad (3.41)$$

Thus,  $h_0(0^+)$ , hence the maximum of effective carrier density, only depends on the field of the cavity mode  $U$ . Interestingly, the equation above defines a higher-order nonlinear interaction volume,  $V_{3PA}$ , which is related to the Three-Photon Absorption (3PA).

We note that these formulas are valid for the particular case of two-photon absorption. Linear absorption will be discussed in section 3.2.7.

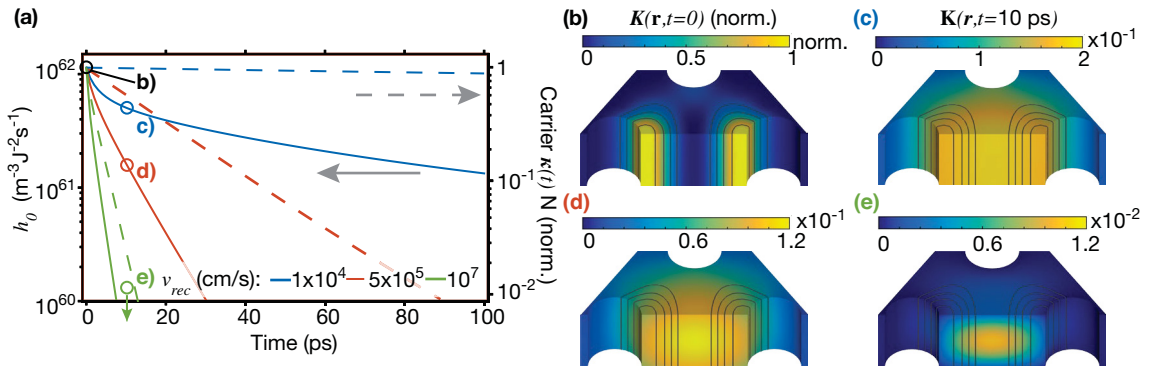


**Fig. 3-10** | (a)  $H_0$  cavity: calculated impulse response  $h_0$  (solid) and the spatially averaged and normalized carrier density  $N/\max(N)$  (dashed), depending on the surface recombination velocity  $S$ . Initial ( $t = t_{0+}$ ) spatial distribution  $N$  of the carriers (b) and at  $t = t_{0+} + 10$  ps with (c)  $S = 10^4$  cm.s $^{-1}$ , (d)  $S = 5 \times 10^5$  cm.s $^{-1}$  and e)  $S = 1 \times 10^7$  cm.s $^{-1}$

As an example,  $h_0$  is calculated for a  $H_0$  photonic crystal resonator (Fig. 3-10), depending on the surface recombination velocity  $v_{rec}$ . First, the comparison between the spatially averaged kernel  $\kappa(t) = \int_V \tilde{K}(\mathbf{r}, t) d\mathbf{r}$  (or, equivalently, the total population of of excited carriers) and  $h_0$  reveals the role of the diffusion. In fact  $h_0$  decays much faster than the total population of the

carriers, as first pointed out in the context of Silicon PhC cavities [61]. This is also apparent in the false-color maps. Here, the distribution of carriers, represented by  $\tilde{K}(\mathbf{r}, t)$  normalized by its maximum at  $t = 0$ , evolves very differently, depending on the surface recombination.

The role of the diffusion becomes less important as the recombination  $v_{rec}$  increases, which is the case of GaAs nanostructures [65, 82, 140], inherently related to its large density of defects at mid-gap [130]. It must be pointed out that the surface recombination is assumed to be identical at any interface, namely at the holes and at the top and bottom side of the slab. This might not be true, as different surfaces are exposed to different fabrication process steps. However, discriminating the values of  $S$  depending on the surface is far from obvious.

In conclusion, given a geometry, the resonator material, and the surface recombination velocity, a unique effective carrier density response function  $h_0$  is enough for modeling accurately the nonlinear dynamics of the resonator, including diffusion effects.

### 3.2.6 | Impact of the Geometry on the Dynamics

The Shockley formula provides a rough estimate of the effective carrier lifetime in sub-wavelength resonators, by assuming an *average* distance from the surface. The model introduced here takes the geometry of the structure into account accurately, as it is based on solving the ambipolar diffusion equation exactly. Thus we apply our model to single out the role of the geometry in determining the nonlinear dynamical response.

Different cavities are considered here, all widely used, namely:  $H_0$  (ref. [44] and Fig. 3-11(a)),  $H_1$  (ref. [141] and Fig. 3-11(b))  $L_3$  (ref. [142] and Fig. 3-11(c)) and  $L_5$  (ref. [142] and Fig. 3-11(d)).

Design	$V_{mod}$ $\times 10^{-18} \text{ m}^{-3}$	$V_\chi$	$V_{3PA}$	$h_0(0)$ (InP) $\times 10^{61} J^{-2} s^{-1} m^{-3}$	(GaAs)
$L_5$	0.08	4	0.88	6.7	4.6
$L_3$	0.057	3	0.67	12	8.1
$H_1$	0.064	2.6	0.60	14	10
$H_0$	0.045	2.2	0.32	51	35

**Table 3.2** | Cavity modal volume  $V_{mod}$ , nonlinear modal volumes  $V_\chi, V_{3PA}$ , and maximum of the effective carrier density response function for several PhC cavity design

To highlight the role of the geometry, the coupled Q factor is set to the same value, namely  $Q=3000$ . What instead is different is the volume of the optical mode, namely  $V_\chi$ , which primarily impacts the level of optical power required for triggering enough nonlinear absorption, and the carrier dynamics, i.e. the  $h_0$  function, which both affects the speed and the amplitude of the nonlinear response. Here it is apparent that geometry is critical, for instance,  $V_\chi$  differs by about an order of magnitude between  $L_3$  and  $H_0$ , and  $h_0$  is more than four times larger in the latter (see table 3.2). Thus order of magnitude difference in energy efficiency can be ascribed to the cavity design.

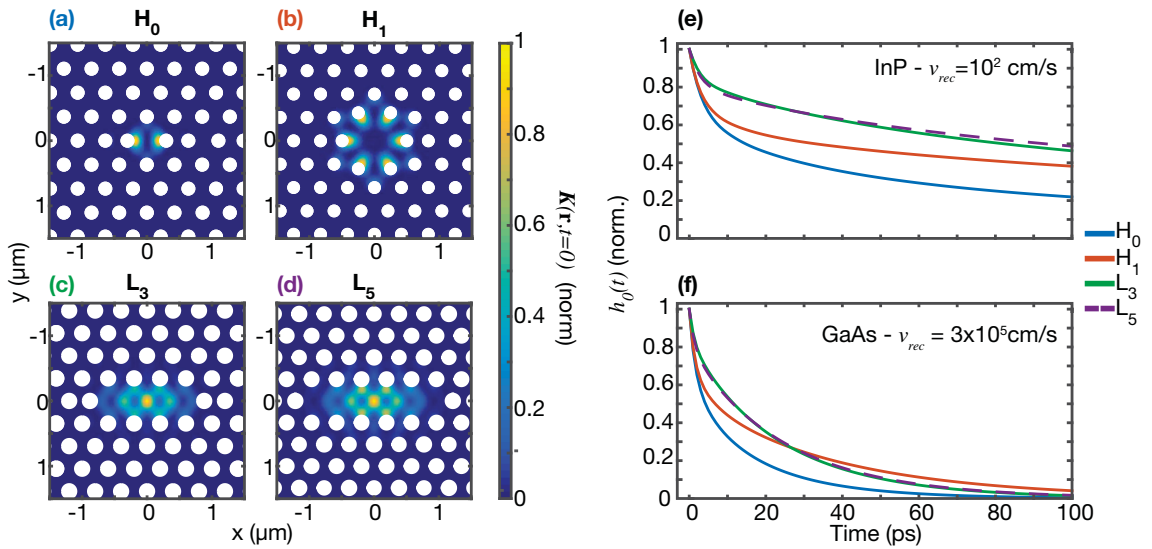


**Fig. 3-11** | Initial distribution of free carriers  $\tilde{K}(r;0)$  calculated for (a)  $H_0$  (b)  $H_1$  (c)  $L_3$  and (d)  $L_5$  design. Decay of the carrier effective response function, normalized:  $h_0(t)/h_0(0)$ , for (e) InP and (f) GaAs.

The impact of geometry on the time response is less straightforward. It is interesting first to consider the initial spatial distribution of the photo-generated carriers, which is directly related to the distribution of the electric field of the optical mode  $|U|^4$ . This is shown in Fig. 3-11, subpanels a-d. It is apparent that in the case of  $H_0$  and  $H_1$  cavities, carriers are generated close to the holes, where they are likely to recombine, whereas in panel c-d it is apparent that they need to diffuse away, before reaching the holes.

This explains in part the different decay of the effective density  $N_{eff}$ , more precisely  $h_0(t)$ , calculated in Figs. 3-11(e) and 3-11(f). Let first consider the short time scale, and the case of low

surface recombination (e.g. InP). It has been first pointed out [61] that an initial phase of fast decay due to diffusion is followed by a slower dynamics. What is interesting here is the role played by the geometry.

The decay of the effective density in the  $H_0$  cavity is way faster, but at least at the very first stage, the  $H_1$  resonator is almost as fast. This is mostly because the initial distribution of photogenerated carriers is much more concentrated in the  $H_{0,1}$  cavities than in the others. After this initial stage, the dynamics of the  $H_1$  slows down and tends to approach the behavior of the  $L_3$  and  $L_5$  structures. Actually, in these two cavities carriers diffuse mostly perpendicular to the cavity main axis, owing to a larger concentration gradient. This explains why the decay of the effective density is almost identical for the two. A few picoseconds after the excitation, the carriers accumulate with a spatial distribution which is roughly Gaussian and extending to the geometric volume of the cavity.

When the surface recombination increases, then the geometry tends to be less important. Considering the case of GaAs with a surface recombination velocity of  $v_{rec} = 3 \times 10^5$  cm/s (this value is further discussed in section 4.3), shown in Fig. 3-11(f), the  $H_0$  is still about twice as fast as the other cavities, but the difference is much less striking. This is consistent with the picture of surface recombination eventually dominating the dynamics.

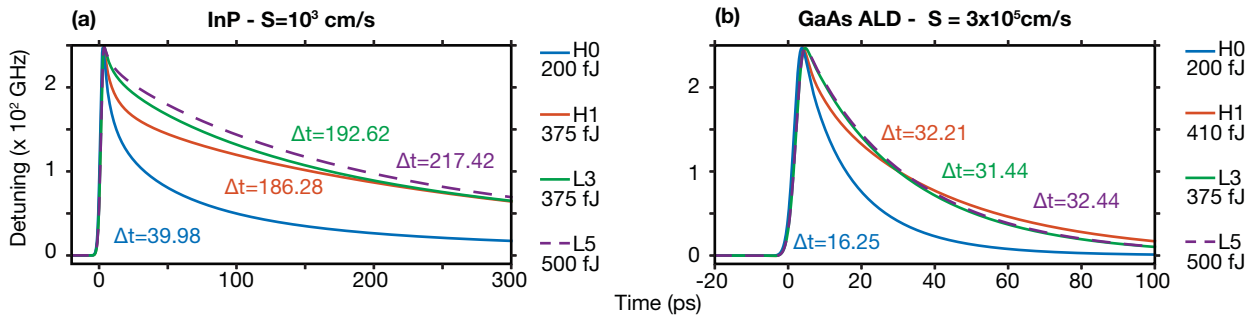


**Fig. 3-12** | Calculated spectral shift for (a) InP and (b) ALD coated GaAs, corresponding to the geometries in Fig. 3-11. The colored text represents the decay time (exponential fit).

The calculated spectral shift  $\Delta\nu$ , which is obtained by solution of the full model, is shown in Fig. 3-12. Here the temporal response is also determined by the optical properties of the resonator (the cavity lifetime) and by the excitation. Still, given the loaded Q factor of the resonators ( $\approx 3000$ , hence cavity lifetime  $Q/\omega \approx 3$ ps) and the duration of the pulses, also in the same range, the decay is clearly dominated by the carrier dynamics. What is clearly visible here is the role of the nonlinear volume  $V_\chi$  on the amount of pulse energy required to achieve a prescribed spectral shift (here 250 GHz), again confirming the net advantage of the  $H_0$  cavity. The difference is substantial but

not as large as table 3.2 might suggest.

### 3.2.7 | Linear Absorption

The modeled discussed here allows the comparison of optical switches activated either by linear or nonlinear absorption. The peculiarity of nonlinear absorption is that the material used for the nonlinear resonator can also be used to create the access waveguides. In fact, at operating power levels, the material is transparent except in the cavity, owing to the enhanced strength of the optical field. Conversely, in optical micro-cavities, nonlinear absorption can be rather an energy-efficient process, in striking contrast with macroscopic cavities, where nonlinear absorption is usually considered as a perturbation.

Also, high linear absorption spoils the Q factor of the cavity, thus, a weak linear absorption is preferable. The most efficient microcavity all-optical switch resulted from by the optimization of the material absorption by choosing the suitable composition of the GaInAsP alloy, such that it entails a weak absorption [48]. Moreover, the nonlinear index change is maximized owing to the band-filling contribution [58].

This situation is considered in our model by introducing a modified version of eqs. (3.30), (3.35), (3.36), (3.38), (3.39) and (3.41), namely:

$$G(\mathbf{r}) = \alpha \frac{c_0 n \varepsilon_0}{2 \hbar \omega} |\mathbf{U}(\mathbf{r})|^2 |A|^2 \quad (3.42a)$$

$$N(\mathbf{r}, t) = \int_{-\infty}^t \tilde{K}(\mathbf{r}; t - \tau) |A(\tau)|^2 d\tau \quad (3.42b)$$

$$\tilde{K}(\mathbf{r}; \tau) = \alpha \frac{c_0 \varepsilon_0}{2 \hbar \omega} \varepsilon_r \int_V K(\mathbf{r}, \mathbf{r}'; \tau) |\mathbf{U}(\mathbf{r})|^2 d\mathbf{r}' \quad (3.42c)$$

$$N(\mathbf{r}, t) = \tilde{K}(\mathbf{r}, t) |A_0|^2 \Delta t \quad (3.42d)$$

$$N_{eff}(t) = \int_{-\infty}^t h_0(t - \tau) |A(\tau)|^2 d\tau \quad (3.42e)$$

$$h_0(t_{0+}) = \frac{\alpha c_0 \varepsilon_0^2}{4 \hbar \omega} \int_V \varepsilon_r |\mathbf{U}(\mathbf{r})|^4 dV = \frac{\alpha c_0}{\hbar \omega V_\chi} \quad (3.42f)$$

We consider two structurally identical devices, aiming at showing that linear and nonlinear absorption induce a different nonlinear dynamics in the cavity. In order to single this contribution out, we have used the same parameters as for the InP H<sub>0</sub> sample discussed in c3.2.6. The sample labeled as “Linear absorption” is made of GaInAsP, as in ref. [48]. The relevant parameters are in table 3.3, however, the surface recombination is arbitrarily taken as that of InP, in order to single out the role

of the geometry and the diffusion process, in addition to the absorption mechanism.

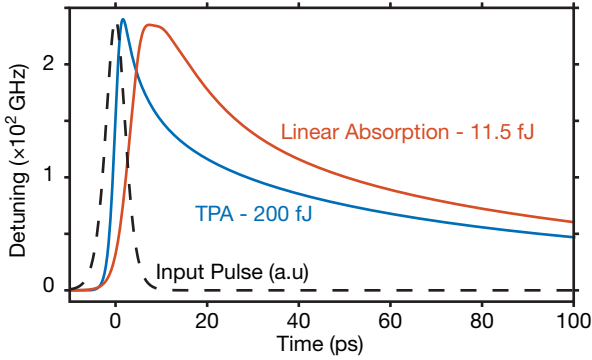


**Fig. 3-13** | Spectral shift in a cavity induced by TPA (blue line) or by linear absorption. The input excitation is also represented (dashed line).

The result is shown in Fig. 3-13. The excitation energy is adjusted to reach the same spectral shift of 250 GHz. As expected, the energy is about a factor 20 lower in the case of the optimized material. It is, however, intriguing to note a striking difference in the dynamics. First, the leading edge of  $\delta\nu$  is much steeper in the case of the nonlinear absorption, which can be understood in the dependence on  $|A|^4$  instead of  $|A|^2$  of the excitation. Second, the faster initial decay, which is related to the diffusion, is largely explained by the stronger gradient of the initial spatial distribution of the photo-excited carriers, i.e.  $|U|^4$  instead of  $|U|^2$ .

**Table 3.3** | Material Parameters value use in the CMT model for GaAs, InP and InGaAsP

Parameters	Symbol	GaAs Value	Ref.	InP Value	Ref	InGaAsP Value	Ref	Units
TPA coeff.	$\beta_{TPA}$	10.2	[143]	15	[144]	65	[48]	cm.GW <sup>-1</sup>
Direct Abso. coeff.	$\alpha$	-	-	-	-	300	[48]	m <sup>-1</sup>
Kerr coeff.	$n_{2I}$	$1.6 \times 10^{-4}$	[143]	$4.4 \times 10^{-5}$	[45]	$3.2 \times 10^{-3}$	[48]	cm <sup>2</sup> .GW <sup>-1</sup>
Free Carrier Disp.	$\left(\frac{\partial n}{\partial N_{eff}}\right)_{FCD}$	$-5.8 \times 10^{-21}$	[58]	$-5.1 \times 10^{-21}$	[58]	$-8.2 \times 10^{-20}$	[48]	cm <sup>3</sup>
Band Filling	$\left(\frac{\partial n}{\partial N_{eff}}\right)_{BF}$	$-2.4 \times 10^{-21}$	[58]	$-3.5 \times 10^{-21}$	[58]	-		cm <sup>3</sup>
FCA	$\frac{\partial \Gamma}{\partial N_{eff}}$	$3.2 \times 10^{-7}$	[58]	$1.1 \times 10^{-6}$	[58]	-		cm <sup>3</sup> .s <sup>-1</sup>
Ambipolar Diff. Coef.	$D_a$	19	[124]	9	[124]	17	[48]	cm <sup>2</sup> .s <sup>-1</sup>

Note that the Q factor here is designed to be smaller than in ref. [48], to be consistent with calculations in the previous sections of our paper. We note that TPA device is faster although the

ambipolar coefficient of InP ( $D_a = 9 \text{ cm}^2/\text{s}$ ) is smaller than InGaAsP ( $D_a = 17 \text{ cm}^2/\text{s}$ ).

This example shows the flexibility of our model and the capability of modeling a variety of devices and materials.

### 3.2.8 | Summary of the Green's Formulation Carrier Dynamics in CMT

We have introduced a model for the dynamical response of nonlinear nanoscale semiconductor resonators. We take into account the carrier diffusion rigorously in the ambipolar approximation by exploiting an impulse response function. This model can be summarized by the main equations listed in table 3.4 below:

Field Dynamics	$\dot{\mathbf{A}} = \mathbf{M} \mathbf{A} - \mathbf{R} \mathbf{S}_{in}$	<b>Table 3.4  </b> Model, summarized
Kerr NL	$i\Delta\omega_k - \frac{\Delta\Gamma_k}{2} =  A_k ^2 c_0 (i\omega n_2 - \beta_{TPA} \frac{c_0}{2}) V_\chi^{-1}$	
Free Carriers NL	$i\Delta\omega_k - \frac{\Delta\Gamma_k}{2} = i\frac{\omega}{n} \frac{\partial \bar{n}}{\partial N} \Big _{FC} N_{eff}^{(k)}$	
Free Carriers Dynamics	$N_{eff}(t) = \int_{-\infty}^t h_0(t - \tau)  A(\tau) ^4 d\tau$	

## 3.3 | Conclusion

In this chapter, it is first discussed the method to solve the drift-diffusion equation coupled to the Poisson one for modeling the carrier dynamics in PhCs using FEM. A fine description of the interfaces is introduced through the Stevenson-Keyes formalism with surface recombination velocity. Verification had been performed comparing FEM results and analytical ones.

Then, a model for the dynamical response of nonlinear nanoscale semiconductor resonators is introduced using the CMT formalism. The carrier diffusion is taken into account in a rigorous way using the ambipolar approximation by exploiting an impulse response function. This impulse response is calculated from the previous FEM discussed. This model avoids unnecessary approximations, which are made using rate equations for carrier dynamics, and also limit the number of fitting parameters, as only the surface recombination is the unknown parameter. Also, this model is used here to highlight the role of the geometry of the resonator and that of the linear

or nonlinear generation of free carriers. This model could also be used for any semiconductor nonlinear resonator and would greatly help the design of sophisticated devices entailing mutually coupled cavities.

## References for Chapter 3 – Theory and Modeling

- [44] Z. Zhang and M. Qiu. *Small-volume waveguide-section high Q microcavities in 2D photonic crystal slabs*. *Opt. Exp.* **12** (2004). – pp. 16, 65, 72, 85, 115.
- [45] R. W. Boyd. *Nonlinear Optics*. Academic Press, 2013. – pp. 16, 66, 76, 164.
- [48] K. Nozaki, T. Tanabe, A. Shinya, S. Matsuo, T. Sato, H. Taniyama, and M. Notomi. *Sub-femtojoule all-optical switching using a photonic-crystal nanocavity*. *Nature Photon.* **4** (2010). – pp. 17, 21, 68, 75–76.
- [57] T. Tanabe, M. Notomi, S. Mitsugi, A. Shinya, and E. Kuramochi. *All-optical switches on a silicon chip realized using photonic crystal nanocavities*. *Appl. Phys. Lett.* **87** (2005). – pp. 19–21, 68, 86.
- [58] B. R. Bennett, R. A. Soref, and J. A. Del Alamo. *Carrier-induced change in refractive index of InP, GaAs and InGaAsP*. *IEEE J. Quantum Electron.* **26** (1990). – pp. 19, 67, 75–76, 117.
- [59] M. Heuck, S. Combrié, G. Lehoucq, S. Malaguti, G. Bellanca, S. Trillo, P. T. Kristensen, J. Mørk, J. P. Reithmaier, and A. de Rossi. *Heterodyne pump probe measurements of nonlinear dynamics in an indium phosphide photonic crystal cavity*. *Appl. Phys. Lett.* **103** (2013). – pp. 19–20, 68–69, 86, 117.
- [60] A. de Rossi, M. Lauritano, S. Combrié, Q. V. Tran, and C. Husko. *Interplay of plasma-induced and fast thermal nonlinearities in a GaAs-based photonic crystal nanocavity*. *Phys. Rev. A* **79** (2009). – pp. 19, 66.
- [61] T. Tanabe, H. Taniyama, and M. Notomi. *Carrier Diffusion and Recombination in Photonic Crystal Nanocavity Optical Switches*. *J. Lightwave Technol.* **26** (2008). – pp. 19, 72, 74, 117.
- [62] T. Tanabe, K. Nishiguchi, A. Shinya, E. Kuramochi, H. Inokawa, M. Notomi, K. Yamada, T. Tsuchizawa, T. Watanabe, H. Fukuda, H. Shinojima, and S. Itabashi. *Fast all-optical switching using ion-implanted silicon photonic crystal nanocavities*. *Appl. Phys. Lett.* **90** (2007). – pp. 20–21, 68, 97.
- [63] Y. Yu, E. Palushani, M. Heuck, N. Kuznetsova, P. T. Kristensen, S. Ek, D. Vukovic, C. Peucheret, L. K. Oxenløwe, S. Combrié, A. de Rossi, K. Yvind, and J. Mørk. *Switching characteristics of an InP photonic crystal nanocavity: Experiment and theory*. *Opt. Exp.* **21** (2013). – pp. 20, 69.
- [65] C. Husko, A. de Rossi, S. Combrié, Q. V. Tran, F. Raineri, and C. W. Wong. *Ultrafast all-optical modulation in GaAs photonic crystal cavities*. *Appl. Phys. Lett.* **94** (2009). – pp. 20–21, 68, 72, 98, 107.
- [66] S. Combrié, G. Lehoucq, A. Junay, S. Malaguti, G. Bellanca, S. Trillo, L. Ménager, J. P. Reithmaier, and A. de Rossi. *All-optical signal processing at 10 GHz using a photonic crystal molecule*. *Appl. Phys. Lett.* **103** (2013). – pp. 20–21, 65, 85–86, 106, 110, 117, 158.

- [82] R. Bose, J. S. Pelc, S. Vo, C. M. Santori, and R. G. Beausoleil. *Carrier dynamics in GaAs photonic crystal cavities near the material band edge*. *Opt. Exp.* **23** (2015). – pp. 21, 72, 105.
- [92] S. M. Sze and K. K. Ng. *Physics of Semiconductor Devices*. John Wiley & Sons, Inc., 2006. – pp. 36, 67, 118–119.
- [111] A. D’Ottavi, E. Iannone, A. Mecozzi, S. Scotti, P. Spano, J. Landreau, A. Ougazzaden, and J. C. Bouley. *Investigation of carrier heating and spectral hole burning in semiconductor amplifiers by highly nondegenerate four-wave mixing*. *Appl. Phys. Lett.* **64** (1994). – p. 51.
- [112] J. Mørk and A. Mecozzi. *Theory of the ultrafast optical response of active semiconductor waveguides*. *J. Opt. Soc. Am. B* **13** (1996). – p. 51.
- [113] A. Mecozzi and J. Mørk. *Theory of heterodyne pump–probe experiments with femtosecond pulses*. *J. Opt. Soc. Am. B* **13** (1996). – p. 51.
- [114] M. Willatzen, A. Uskov, J. Mørk, H. Olesen, B. Tromborg, and A. P. Jauho. *Nonlinear gain suppression in semiconductor lasers due to carrier heating*. *IEEE Photon. Technol. Lett.* **3** (1991). – p. 51.
- [115] K. L. Hall, G. Lenz, E. P. Ippen, U. Koren, and G. Raybon. *Carrier heating and spectral hole burning in strained-layer quantum-well laser amplifiers at 1.5  $\mu\text{m}$* . *Appl. Phys. Lett.* **61** (1992). – p. 51.
- [116] J. Mørk, J. Mark, and C. P. Seltzer. *Carrier heating in InGaAsP laser amplifiers due to two-photon absorption*. *Appl. Phys. Lett.* **64** (1994). – p. 51.
- [117] P. Borri, W. Langbein, J. M. Hvam, F. Heinrichsdorff, and D. Bimberg. *Spectral hole-burning and carrier-heating dynamics in InGaAs quantum-dot amplifiers*. *IEEE J. Sel. Topics Quantum Electron.* **6** (2000). – p. 51.
- [118] E. Garmire and A. Kost. *Nonlinear Optics in Semiconductors II*. Academic Press, 1998. – p. 52.
- [119] A. Fick. *On liquid diffusion*. Reprinted for *J. Membr. Sci.* **100** (1995). – p. 53.
- [120] A. Fick. *On liquid diffusion*. *The London, Edinburgh, and Dublin Philosophical Magazine and Journal of Science* **10** (1855). – p. 53.
- [121] A. Einstein. *Über die von der molekularkinetischen Theorie der Wärme geforderte Bewegung von in ruhenden Flüssigkeiten suspendierten Teilchen*. *Annalen der Physik* **322** (1905). – p. 53.
- [122] D. J. Griffiths. *Introduction to Electrodynamics*. Prentice Hall, 1999. – p. 54.
- [123] C. Kittel. *Introduction to solid state physics*. John Wiley & Sons, 2007. – p. 55.
- [124] M. Levinshtein, S. Rumyantsev, and M. Shur. *Handbook Series On Semiconductor Parameters*. WORLD SCIENTIFIC, 1996. – pp. 55, 76.

- [125] U. Strauss, W. W. Rühle, and K. Köhler. *Auger recombination in intrinsic GaAs*. Appl. Phys. Lett. **62** (1993). – p. 55.
- [126] M. Govoni, I. Marri, and S. Ossicini. *Auger recombination in Si and GaAs semiconductors: Ab initio results*. Phys. Rev. B **84** (2011). – p. 55.
- [127] Y. P. Varshni. *Band-to-Band Radiative Recombination in Groups IV, VI, and III-V Semiconductors (I)*. phys. stat. sol. (b) **19** (1967). – p. 55.
- [128] D. T. Stevenson and R. J. Keyes. *Measurement of Carrier Lifetimes in Germanium and Silicon*. J. Appl. Phys. **26** (1955). – p. 56.
- [129] W. Shockley. *Electrons and holes in semiconductors: with applications to transistor electronics*. Van Nostrand, 1950. – pp. 56, 98.
- [130] D. D. Nolte. *Surface recombination, free-carrier saturation, and dangling bonds in InP and GaAs*. Solid-State Electron. **33** (1990). – pp. 56, 68, 72, 88, 98, 106.
- [131] Comsol. COMSOL Multiphysics. – p. 57.
- [132] C. Manolatou, M. J. Khan, S. Fan, P. R. Villeneuve, H. A. Haus, and J. D. Joannopoulos. *Coupling of modes analysis of resonant channel add-drop filters*. IEEE J. Quantum Electron. **35** (1999). – pp. 62–64.
- [133] G. Lecamp, J. P. Hugonin, and P. Lalanne. *Theoretical and computational concepts for periodic optical waveguides*. Opt. Exp. **15** (2007). – p. 62.
- [134] P. T. Kristensen and S. Hughes. *Modes and Mode Volumes of Leaky Optical Cavities and Plasmonic Nanoresonators*. ACS Photonics **1** (2014). – p. 62.
- [135] J. Lian, S. Sokolov, E. Yüce, S. Combrié, A. de Rossi, and A. P. Mosk. *Dispersion of coupled mode-gap cavities*. Opt. Lett. **40** (2015). – p. 63.
- [136] J. Mark and J. Mork. *Subpicosecond gain dynamics in InGaAsP optical amplifiers: Experiment and theory*. Appl. Phys. Lett. **61** (1992). – p. 67.
- [137] W. Shockley. *Holes and Electrons*. Phys. Today **3** (1950). – p. 68.
- [138] A. Ocariz, A. Sanchez-Lavega, A. Salazar, D. Fournier, and A. C. Boccarda. *Photothermal characterization of vertical and slanted thermal barriers: A quantitative comparison of mirage, thermoreflectance, and infrared radiometry*. J. Appl. Phys. **80** (1996). – p. 70.
- [139] N. Taketoshi, T. Baba, and A. Ono. *Development of a thermal diffusivity measurement system for metal thin films using a picosecond thermoreflectance technique*. Meas. Sci. Technol. **12** (2001). – p. 70.
- [140] A. D. Bristow, J. P. R. Wells, W. H. Fan, A. M. Fox, M. S. Skolnick, D. M. Whittaker, A. Tahraoui, T. F. Krauss, and J. S. Roberts. *Ultrafast nonlinear response of AlGaAs two-dimensional photonic crystal waveguides*. Appl. Phys. Lett. **83** (2003). – pp. 72, 86, 97.

- 
- [141] M. Shirane, S. Kono, J. Ushida, S. Ohkouchi, N. Ikeda, Y. Sugimoto, and A. Tomita. *Mode identification of high-quality-factor single-defect nanocavities in quantum dot-embedded photonic crystals*. J. Appl. Phys **101** (2007). – p. 72.
- [142] Y. Akahane, T. Asano, B.-S. Song, and S. Noda. *High-Q photonic nanocavity in a two-dimensional photonic crystal*. Nature **425** (2003). – p. 72.
- [143] M. Dinu, F. Quochi, and H. Garcia. *Third-order nonlinearities in silicon at telecom wavelengths*. Appl. Phys. Lett. **82** (2003). – p. 76.
- [144] L. P. Gonzalez, J. M. Murray, and S. Krishnamurthy. *Wavelength dependence of two photon and free carrier absorptions in InP*. Opt. Exp. **17** (2009). – p. 76.

# Chapter 4

## All-Optical Signal Processing

---

---

In this chapter it is discussed all-optical signal processing using PhC resonators at high repetition rate. First, InP PhC resonator dynamics is extensively studied through different pump-probe measurements. Then, all-optical operations, namely wavelength conversion and frequency-down conversion of a microwave signal carried optically, are shown at a 10 GHz clock repetition rate. Secondly, in the perspective of speeding up the all-optical gate, PhCs made of GaAs are studied because of its high surface recombination velocity. However, this recombination being too fast, carrier generation is not efficient enough. Therefore poor resonance frequency shift is observed. Therefore, Al<sub>2</sub>O<sub>3</sub> passivation is processed through Atomic Layer Deposition technique which optimizes the carrier lifetime to 10 ps. This allows for the first time to perform high repetition rate all-optical operations in GaAs PhCs. Finally, a new path is described on the speed improvement for all-optical gates, which instead of reducing carrier lifetime, is based on improving the carrier diffusion. This is made possible by P-doping the InP PhC.

### Contents

---

4.1	All-Optical Gate Made in InP . . . . .	85
4.1.1	Sample and Design . . . . .	85
4.1.2	Pump-Probe Measurement and Carrier Dynamics . . . . .	85
4.1.3	Homodyne Pump-Probe Measurement . . . . .	90
4.2	All-Optical Operation Using InP Photonic Crystal . . . . .	92
4.2.1	Wavelength Conversion At 10GHz . . . . .	92
4.2.2	All-Optical Frequency Down Conversion of Microwave Signal At 10GHz . . . . .	94
4.3	Gallium Arsenide Surface Mitigation Using Atomic Layer Deposition . . . . .	97
4.3.1	New Design and Waveguide Positions . . . . .	99
4.3.2	ALD Passivation . . . . .	101
4.3.3	Dynamics of the Free Carriers . . . . .	103
4.3.4	Passivation Effects . . . . .	106
4.3.5	Other Material . . . . .	107

4.4	All-Optical Operation Using GaAs Photonic Crystal . . . . .	109
4.4.1	Operation At GHz Rates . . . . .	109
4.4.2	Ultra-Fast Gating . . . . .	111
4.5	Towards Faster InP Photonic Crystal All-Optical-Gates . . . . .	114
4.5.1	Sample Description . . . . .	114
4.5.2	Time-Resolved Spectral Analysis . . . . .	116
4.5.3	Results and Discussion . . . . .	117
4.5.4	Modeling of P-Doped All-Optical Gates . . . . .	119
4.6	Conclusion . . . . .	120
	References for Chapter 4 . . . . .	122

---

## 4.1 | All-Optical Gate Made in InP

### 4.1.1 | Sample and Design

The design was previously succinctly discussed in section 3.2, and reported in ref. [66]. The photonic crystal is made in a 250 nm thick InP self-suspended membrane, with a period  $a = 450\text{nm}$  and hole radii of  $r = 0.22a$ . The two identical  $H_0$  cavities, made by a displacement of two adjacent hole [44] of  $d_x = 0.16$  along  $x$  axis, and  $d_y = 0.07a$  along the  $y$  one, are placed at a distance of  $3M = -5ax + 3ay\sqrt{3}/2$  from each other's, coupling them together (Fig. 4-1). Therefore, two distinct resonances appear with a Fano line-shape, separated by 10 nm as shown on the previously discussed Fig. 3-9(a) and depicted in Fig. 4-1(b).

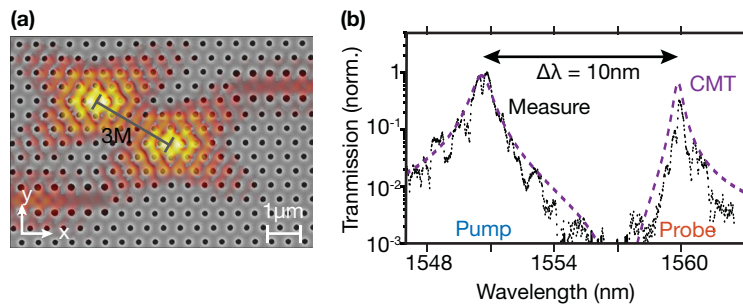


**Fig. 4-1** | (a) SEM image of the Photonic Molecule. Electric Field module at the resonance frequency is superimposed – (b) Transmission spectra of the coupled cavities with in dashed red line the linear CMT modeling

### 4.1.2 | Pump-Probe Measurement and Carrier Dynamics

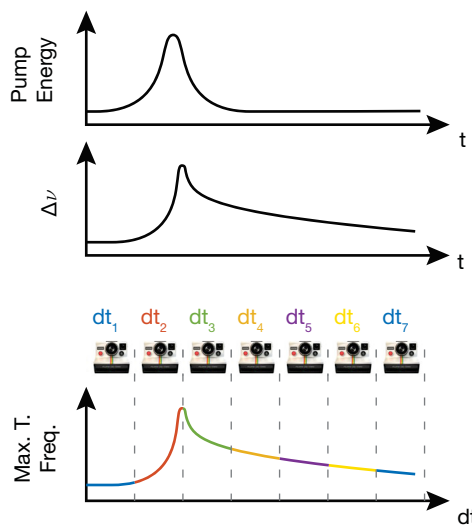


**Fig. 4-2** | Pump-probe principle schematic. The pump pulse is represented on top, which provokes the detuning of the cavity due to free carrier plasma effect, represented below. The probe is represented as a camera taking snapshot at each delay time, reconstructing the whole resonance detuning in time, through the transmission of the probe.

Pump-Probe techniques are extensively used in characterizations of ultra-fast dynamics phe-

nomena [57, 75, 77, 79] as it is not limited by the tools performing the characterization (such as the bandwidth of the photodiode, oscilloscope or OSA) but instead only by the time duration of the probe. Several methods exist, such as heterodyne [59, 68], homodyne [66], or spectrally resolved [140, 145]. For all of those techniques, the main principle remains the same and can be described as follows: the pump ignites the process of the ultra-fast dynamics – which is in our case the two-photon absorption leading to free-carrier plasma effect, shifting the resonances. Then, the delay between the pump and the probe is varied, and the probe signal is measured for each defined delay. It is equivalent of taking a *snapshot* of the state of the resonances for this delay (Fig. 4-2). It is mostly this transmission measurement which changes from a technique to another. In the case of the heterodyne, it is reconstructed from the interference between the probe and a reference, in the homodyne, the probe is modulated and the signal is detected through a locked-in technique, and in the spectrally resolved the probe is not modulated and is simply detected by filtering out the pump. Finally, the whole phenomena dynamics can be reproduced by changing the relative delay over its time-scale (Fig. 4-2).

To fully characterize the effective carrier dynamics in the photonic crystal cavities it is more useful to consider a time and spectrally resolve pump-probe experiment. Because such measurement allows obtaining information not only on the device recovery time but also on the instantaneous frequency shift caused by free-carrier plasma effect, this gives the maximum amount of information available. It is important to note here that such experiment needs a pump and a probe spectrally separated to measure the probe output signal efficiently. It is made possible by the degeneracy raise of the resonance, providing two well-defined ones. The experimental setup is described Fig. 4-3

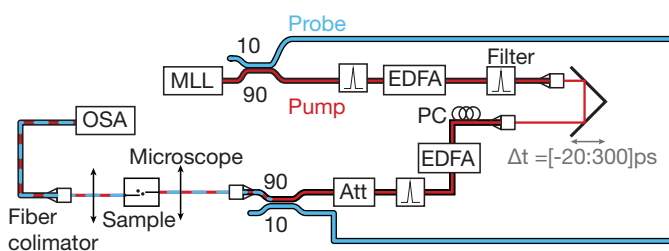


**Fig. 4-3** | Spectrally and temporally resolved pump-probe setup. In red the pump path, in blue the probe path. EDFA: Erbium Doped Fiber Amplifier, PC: Polarizer Controller, Att: Attenuator, OSA: Optical Spectra Analyzer.

The pump and the probe are generated from the same femtosecond MLL, using a 10/90 directional coupler. The pump is going through stages of filtering and amplification to provide the adequate amount of energy to ignite the non-linear effect, and being as broad spectrally as the resonance, which is roughly 0.5 nm large. The pump is spectrally tuned to the highest energy

resonance, with a small blue detuning about the half width of the resonance (0.2nm). In the meantime, the probe is keeping as it. Therefore, the pulse duration is short, providing a good temporal resolution to the measurement – even if the pulse experiences dispersion through fiber stretching the time duration, it still remains in the order of the picosecond or below. The probe spectra remains large, which can be considered as white light over the spectral domain considered. Pump and probe are merged with a 90/10 coupler, to keep as much as possible energy on the pump path, and are sent through a microscope objective focused to the input port. The sample provide a taper on the input and output ports following the design depicted in ref. [146] for low insertion losses. Then, the output signal is directly sent to an Optical Spectrum Analyzer (OSA), with the Region Of Interest (ROI) restrained around the lowest energy resonances. By changing the delay between the pump and the probe, provided by a delay line in the pump path, and acquiring spectra at each delay, it enables to reconstruct the whole dynamics of the system, both spectrally and temporally.

The result is a mapping of the probe intensity transmission regarding time and wavelength (Fig. 4-4(a)).

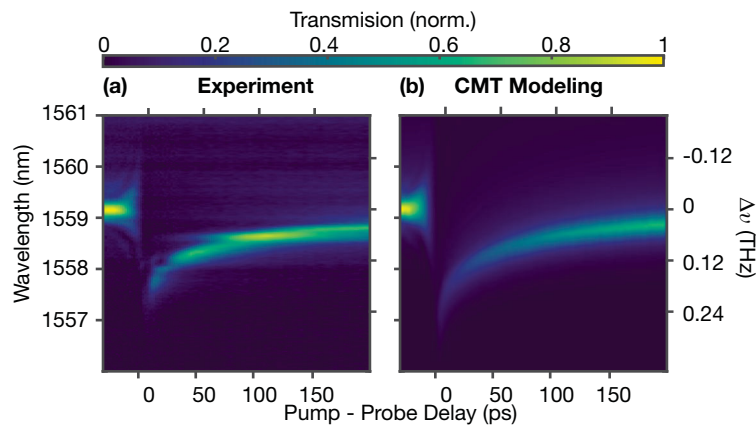


**Fig. 4-4** | Pump Probe resolved temporally and spectrally experiment with on the left experimental results and on the right CMT.

The pump energy coupled to the cavity is about 500 fJ, with a pulse duration of 6 ps, while the pump has an energy of 50 fJ with a pulse duration of 1 ps measured by auto-correlation. It is important to note that the probe seems here to have a fairly high energy compared to the pump, but as the spectra is large, the effective energy of the probe coupled to the resonances is really low (around 1 fJ) and can thus still be considered as a perturbation for carrier generation by two photon absorption.

Simulation was performed (Fig. 4-4(b)), reproducing the exact experiment with the algorithm depicted in section 3.2, and a tremendous agreement is clearly visible between the model and the characterization. The parameters used in this modeling are described in appendix B.1, with a surface recombination velocity  $v_{rec} = 10^3 \text{ cm.s}^{-1}$ . This value is in fair agreement with the literature [130].

In order to obtain quantitative measurement of the frequency shift and the temporal dynamics of the system, the first order moment of the transmission spectra  $\Delta\nu$  (respectively in wavelength  $\Delta\lambda$ ) is taken such that :

$$\Delta\nu(t) = \int_{\nu_1}^{\nu_2} \nu T(\nu, t) d\nu \quad (4.1a)$$

$$\Delta T(t) = \int_{\nu_1}^{\nu_2} T(\nu, t) d\nu \quad (4.1b)$$

where  $[\nu_1, \nu_2]$  defined the spectral region of interest of the pump-probe experiment

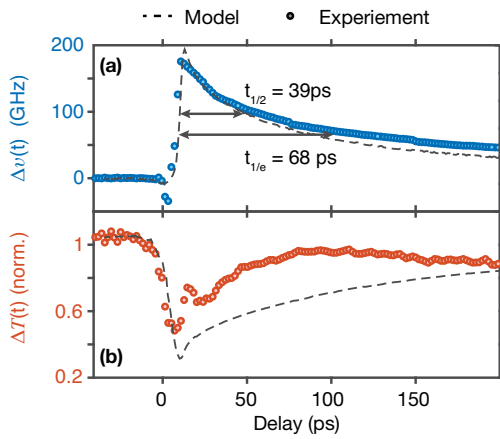
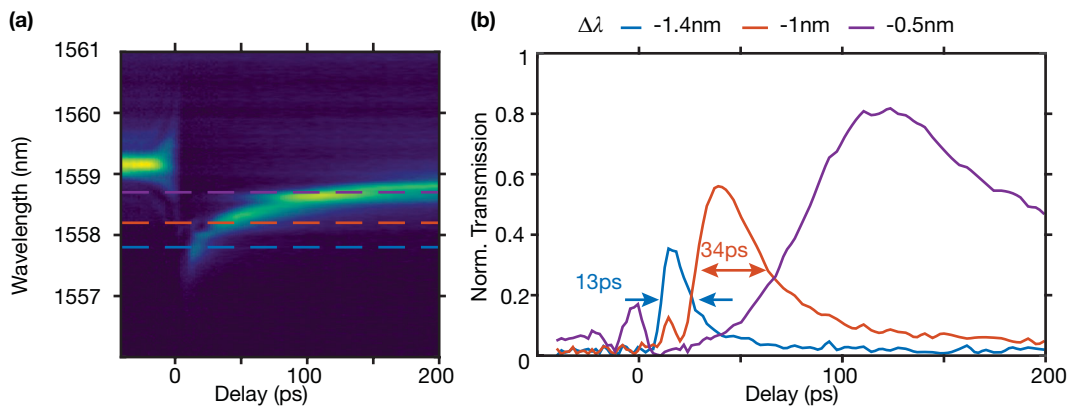


Fig. 4-5 | (a) Frequency first order moment shift and (b) transmission for both experiment (circles) and GMT model (dashed lines).

It is worth noting that the modeling fits well, with the mapping plot, but also reproduces well the first order momentum of the instantaneous frequency shift of the resonances (Fig. 4-5(a)). The transmission (Fig. 4-5(b)) roughly follows the same trend than the experiment. The design of the sample, with a long waveguide going through millimeters of InP, provide defects due to disorder in the transmission spectra. Those defects are not reproduced in the model and could explain the differences. Moreover, Fig. 4-5(a) gives a precious information on the instantaneous bandwidth of

the all-optical switch for a pump energy given [147].

It is important to note here that the time window at  $1/2$  or  $1/e$  of the transmission first order momentum does not provide an estimation of the switching window. In the first approximation, it is easy to consider that the transmission of a Continuous Wave (CW) signal detuned from the resonance by few hundreds of GHz, has a high output transmission only when it cross the center of mass curve. Also, the first rise part of the curve provides a low transmission, due to a high free carrier concentration leading to a high free carrier absorption or to cross absorption. Thus, such time window depicted in Fig. 4-5 provides a useful information of the delay between the pump and a CW converted output signal for wavelength conversion operations.



**Fig. 4-6** | (a) Transmission spectra versus pump-probe delay, with the dashed line the virtually CW input signal with a detuning from the cold cavity of  $\Delta\lambda = -1.4$ ,  $-1$  and  $-0.5$ . – (b) Transmission in time for the considered detuning.

The mapping of the transmission spectra regarding the pump-probe delay and the wavelength provides also information about the switching window of the all-optical gate. Unless using the center of mass, it worth considering a CW input signal detuning from the cold resonances, and plot the transmission spectra at such detuning. This would reproduce accurately the transmission waveform of a wavelength conversion operation.

Three different detunings are taken as an example:  $\Delta\lambda = -1.4$ ,  $-1$  and  $-0.5$  nm from the cold cavity low energy resonance (Fig. 4-6(a)), corresponding roughly to the maximum, half and a third of the maximum spectral shift of the resonator.

Figure 4-6(b), represents the transmission in time for the considered detuning hypothesis for

the CW input signal. The first obvious point is that the more the detuning is getting close to the cold resonance, the more transmitted signal is high. It can be understood as follow: the less the detuning is, the more the resonator have been recovered from the excitation. Therefore, the modification of the effective index is only a perturbation. As absorption is simply linked through a Kramers-Kronig relation to the variation of the optical index, the less modification of the refractive index is, the less absorption the signal will undergo. Thus, a high detuning has a lower transmission than a slight detuning.

However, it is clear that the more detuning from the cold resonance the signal is, the fastest the switching operation is. Therefore, a trade-off between fast operation and high transmitted signal need to be obtained.

### 4.1.3 | Homodyne Pump-Probe Measurement

It has been previously discussed that spectrally resolved pump-probe experiments can provide numerous useful information such as instantaneous frequency shift of the resonances, signal output delay regarding the pump and could also provide an approximation of the output wavelength converted signal. However, for this last property, spectrally resolved experiment does not provide the best signal to noise ratio, as the noise is limited by the OSA which cannot detect signal below -90 dBm. Moreover, this kind of characterization is usually long for well spectrally defined results, as the OSA needs to scan the whole ROI with a fine definition for each pump-probe relative delay.

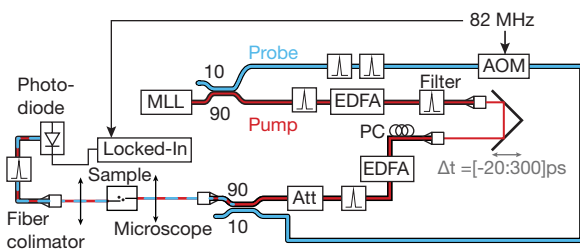
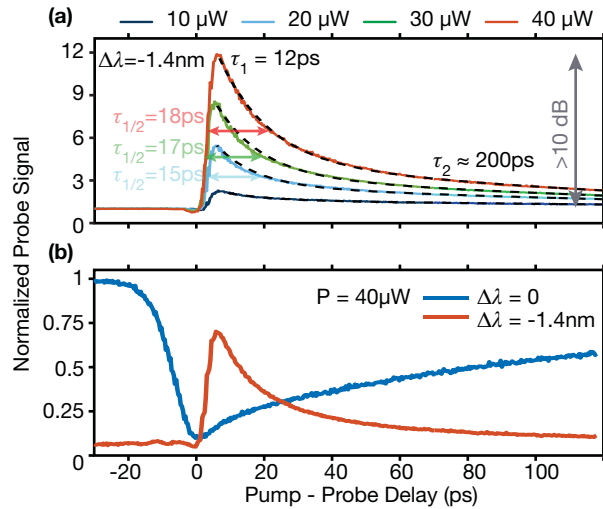


Fig. 4-7 | Homodyne pump-probe experiment setup.

However, other types of pump-probe measurements are more suited for high signal over noise ratio and still provide measurement of the switching operation window. In the homodyne type experiment, the signal is modulated through an Acousto-Optic Modulator (AOM) and the output signal, where the pump is filtered out, is sent to a locked-in detector, thus extra sensible to low transmission variation (Fig. 4-7). To emulate a switching operation, the probe, still generated from the femto-second MLL, is filtered to be align with the low energy resonance with a slight detuning determined, either 0 to perform a switch OFF or negative in wavelength to see for a switch ON

operation. As the probe is spectrally filtered, the time length is stretched to few picoseconds, thus providing less time resolution than the previous spectrally resolved pump-probe experiment.



**Fig. 4-8 | Homodyne Pump-Probe measurements –** (a) Probe power variation from  $10\mu\text{W}$  to  $40\mu\text{W}$  at  $36\text{MHz}$  repetition rate for a detuning from the lowest energy resonance of  $-1.4\text{ nm}$  – (b) Off Measurement with no detuning with the resonance (blue), ON measurement with a detuning of  $-1.4\text{ nm}$  (red).

Figure 4-8(a) represents the experimental results of the homodyne pump-probe measurement for a fixed detuning of  $-1.4\text{ nm}$ , detuning which was previously shown in Fig. 4-6(b), to be fair enough from the cold cavity resonance thus providing a small switching window. In this experiment, the pump power is varied, and for  $40\mu\text{W}$  input power (for a repetition rate of  $36\text{ MHz}$ ), a contrast of  $10\text{dB}$  is achieved, while the switching window is roughly the same than in the spectrally and temporally resolved experiment. The first obvious result to notice is the link between the pump power and the output signal contrast. In addition, it is noticeable that the switching window is reduced when the pump power is decreased. This is easily understandable as follows: when the pump power decreases, the frequency shift of the resonance is lower. Thus, changing the pump power is equivalent of changing the detuning as in Fig. 4-6, the weaker the power is, the more the probe is detuned from the maximum resonance frequency shift.

A double exponential fit is also applied to the pump-probe characterization, resulting in a slow time constant, about  $12\text{ ps}$ , and a long time one, of about  $200\text{ ps}$ . This last one is problematic for switching at high repetition rate, as the all-optical gate would not completely recover between two pump pulses. Therefore, an output signal offset will happen, reducing its contrast.

## 4.2 | All-Optical Operation Using InP Photonic Crystal

The previous section detailed the dynamics of the all-optical switch made of InP and the different important metrics extract from pump-probe characterizations: switching time window, energy for efficient frequency shift, pump-signal delay caused by the all-optical switching operation. However, the practical use of an all-optical switch implies operation at fast ( $>1$  GHz) repetition rate. In this section, it is further discussed experiments at high repetition rate (10 GHz), especially wavelength conversion operations using as an input signal a CW laser and and frequency down conversion of a microwave signal carried optically.

### 4.2.1 | Wavelength Conversion At 10GHz

Wavelength switching operation consists of transferring the modulation from one signal, typically the clock at a wavelength  $\lambda_{clk}$  to a CW laser at a second wavelength  $\lambda_{sig}$ . PhC molecule cavities enable a good spectral separation between the clock, which is set at the highest energy resonances, and the CW aligned with the second resonances, slightly detuned. This provides a spectral separation of about 10nm between those two. Therefore, this system is a perfect candidate for all-optical wavelength conversion operation at high frequency rate.

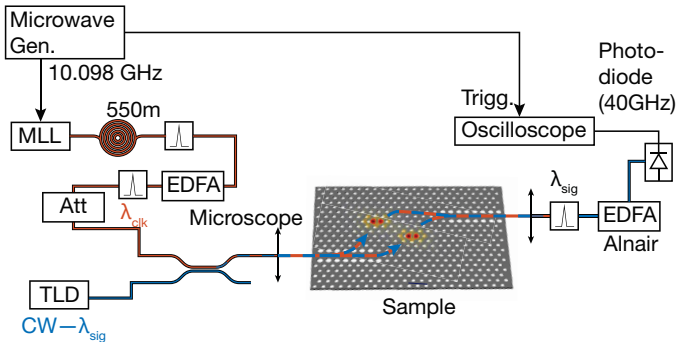


**Fig. 4-9 | 10GHz wavelength conversion.** The MLL is sent to a 550 meters long fiber for pulse shaping. In red the clock path, in blue the CW signal path. The generator locking the MLL is used to trigger the fast oscilloscope

The experiment consists of generating a clock at  $f_{MLL} = 10.098$  GHz by spectrally slicing the output of a MLL diode extending from 1545 to 1555nm (Alcatel-Lucent-Thales III-V Lab), which is sent to a 50/50 directional coupler, and combined with the CW Tunicas laser (Fig. 4-9). The clock is spectrally tuned at 1550 nm, while the probe is blue detuned by roughly 1 nm from the low energy resonance at 1560 nm. Like all the experiments depicted in the previous section, the coupling to the PhC sample is performed using a microscope objective focused on the input of the waveguide.

Then, the output is filtered (0.8 nm band-pass filter centered at the CW laser wavelength in order to reject the pump) and then amplified, using a low noise Erbium Doped Fiber Amplifier (EDFA), and finally detected with a fast photodiode (U2t, 40 GHz) under AC mode. The generated electrical signal is detected by a fast oscilloscope (70 GHz) triggered by the same microwave generator at  $f_{MLL}$  which locks the MLL. Results of such experiment are shown in Fig. 4-10(a), with a clock power per pulse of about 40 fJ (taken into account coupling and propagation losses, we consider that 10% of the input energy arrived to the cavity).

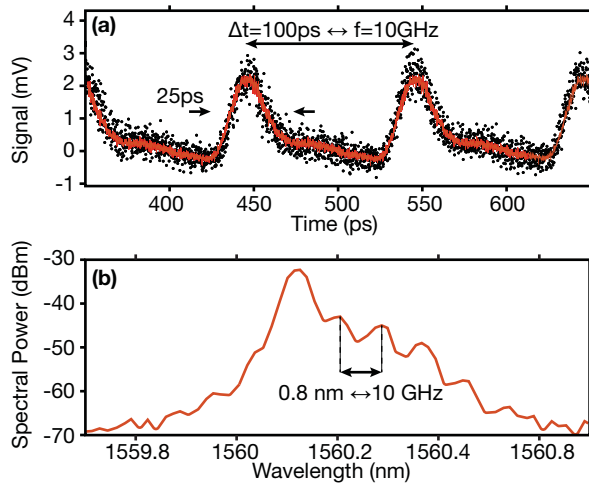


**Fig. 4-10** | Wavelength conversion operation at 10GHz – (a) scope trace of the modulated CW output signal with 25ps switching window – (b) Output signal sent to an OSA with a modulation period of 0.8nm corresponding to 10GHz.

One of the main complications of this experiment is the determination of the effective detuning of the CW signal from the cold cavity. Even if the spectrally resolved and the homodyne pump-probe characterization allows to find the most efficient detuning for high contrast ON switching operation, it does not take into account of the high repetition rate inducing thermal drift. Indeed, the characteristic time constant for thermal diffusion is in the order of few micro-second, thus higher than the temporal period of the clock. Therefore, the sample undergoes heating, inducing a resonance drift toward the red. From modeling, and extraction of the thermal resistivity of the PhC of  $10^5 \text{ K.W}^{-1}$ , the temperature of the sample from a 10 GHz clock with about hundred femtoJoule power excitation rise of few Kelvin. Therefore, the detuning of the CW signal needs to be dynamically optimized, from the value found in the previous section, to a slightly reddish wavelength.

In practice, the detuning is set to maximize the all-optical modulation, e.g., the onset of a spectral comb at the output around the low energy resonance, as shown in Fig. 4-10(b) (Anritsu, resolution 50 pm). In the time domain (Fig. 4-10(a)), this corresponds to a peak (about 25 ps

window) followed by a slower decay. It is consistent with the homodyne characterization as this time window correspond to the convolution between the response of the switch and the photodiode (about 10 ps).

It is interesting to point out that the slow time constant (around 200 ps) does not hinder the fast response, but instead induces a spectral offset of the cavity, provided that the excitation is periodic.

#### 4.2.2 | All-Optical Frequency Down Conversion of Microwave Signal At 10GHz

With the development of the information technologies, broadband communication networks and also new generations of more traditional equipments such as radars, satellites, are all in demand for ultra-wideband ADC. However, the state-of-the art of ADCs has barely followed. For instance, sampling rates of several tens of gigasamples per second (GS/s) for a resolution of at least 10 bits is still a challenging objective. Moreover, the signal to noise ratio of electronic samplers (hence the resolution) is still limited, as the aperture jitter remains high.

A radical new approach, combining photonics and electronics, was proposed in order to overcome the limitations of current electronic A/D converters, in particular in terms of speed. Here, photonics relates to the availability of an ultra-stable clock signal delivered by a MLL [148], which is a key advantage in order to reduce the aperture jitter. This strategy has been considered since the pioneer work of Taylor [10], Tsunoda et Goodman [11]. Moreover, in order to reduce losses over long transport path, the signal microwave signal is carried by an optical signal, thus performing in the optical domain avoid a high cost energy conversion at high speed to perform the A/D signal sampling.

Here, we explore the potential of all-optical sampling of a microwave signal in an integrated nonlinear photonic device and discuss crucial properties such as dynamic range and linearity

The all-optical sampling experiment is represented in Fig. 4-11(a). The microwave signal, at frequency  $f_{MZ}$  and power  $P_{MZ}$ , is transposed to an optical carrier with wavelength  $\lambda_s = 1560\text{nm}$  using a Mach-Zehnder modulator and thus delivered through an optical fiber to the device. The clock (CLK) is obtained by decimating (by gating the pulses through an amplitude modulator) the pulse train generated by a MLL semiconductor diode operating at  $f_{ML} = 10.098\text{ GHz}$ , the same

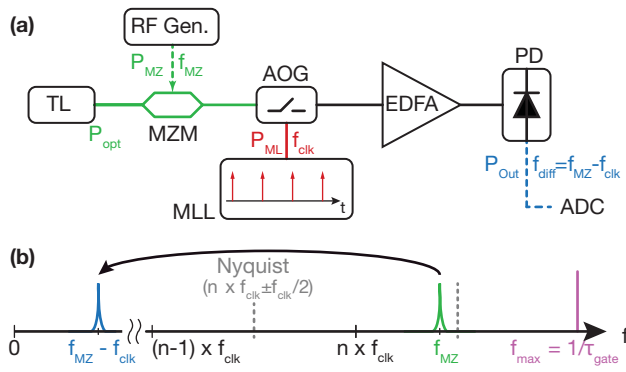


Fig. 4-11 | (a) Optical link schematic of a microwave optical link with temporal discretization prior to transposition in the electrical domain. Plain lines are optical fibers and dashed lines, coaxial cables. – (b) Spectra folding due to down-sampling.

one than in the wavelength conversion experiment, and is sent to the device after a spectral slicing at  $\lambda_{clk} = 1550\text{nm}$  and amplification. The output signal is filtered in order to remove the optical clock and then amplified to be sent to a photodiode. This signal is sent to a fast oscilloscope or an electrical spectrum analyzer without further amplification in order to preserve the bandwidth. As the signal frequency  $f_{MZ}$  is inside the Nyquist band around the  $n^{th}$  harmonic of the clock frequency  $f_{clk}$ , frequency down conversion occurs, creating an output signal with frequency component corresponding to the frequency difference between the input signal and the clock. This is seen temporally as the output signal owns an enveloped corresponding to this difference frequency while the samples taken correspond to the clock repetition rate (Fig. 4-11(b)).

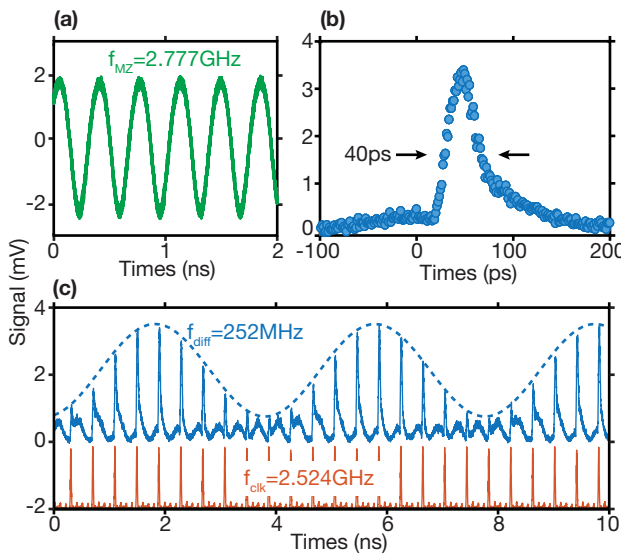
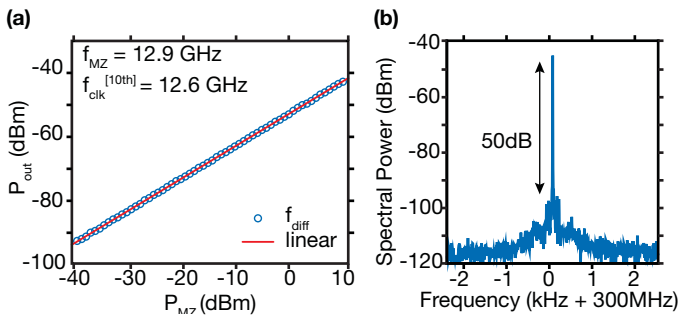


Fig. 4-12 | All-optical sampling in the time domain. (a) Input signal – (b) Output trace when the gate is open – (c) Output trace at the oscilloscope (blue) revealing amplitude modulation at  $f_{diff} = 252\text{MHz}$  and corresponding pulse train of the optical clock (red plot).

The sampling result is shown Fig. 4-12(c), with a clock frequency reduced to  $f_{clk} = f_{ML}/4$  and a signal at  $f_{MZ} = 2.777\text{GHz}$  (Fig. 4-12(a)), which are condition for spectral folding of the high frequency signal due to aliasing. When the clock is on, the response of the gate (Fig. 4-12(b)) is

modulated by the signal and an envelope corresponding at  $f_{diff} = f_{MZ} - f_{clk}$  appears. The average power consumption of the optical clock is about 1.2mW, which corresponds to about 0.4mW in the device due to coupling loss.

The clock is now changed to  $f_{clk} = f_{ML}/8 = 1.26$  GHz and the output signal is observed in the frequency domain using an electrical spectrum analyzer, considering  $f_{MZ} = 12.9$ GHz . The electrical power level of the output signal is plotted along with the difference frequency  $f_{diff}$  as a function of the power level of the modulating signal  $f_{MZ}$  . We observe in Fig. 4-13(a) a linear trend over 50 dB. Harmonic distortion is barely noticeable ( $2 \times f_{diff}$  is 50 dB lower than  $f_{diff}$ ). The electrical spectra at  $f_{diff}$  is shown in Fig. 4-12(b). The effect taking place inside the device is based on non-linear optic, especially TPA. The average power of the clock  $\langle P_{clk} \rangle$  and the signal  $\langle P_s \rangle$  are roughly the same, but the peak power of the clock is about hundred time higher than the peak power of the signal, thus the signal can be considered as a perturbation, which explain the linear trends. The high range can be explain by the system which allows a low noise operation, and the experiment which uses an EDFA (Alnair) inducing low noises.



**Fig. 4-13** | All optical sampling in the frequency domain. (a) Converted signal at  $f_{diff}$  as a function of the level of the modulation and (b) electrical spectra at  $f_{diff}$ .

Further modeling, using the CMT tool described in section 3.2 which takes into account of both the clock and the signal, have been performed reproducing the dynamic of the system.

As shown on Fig. 4-14, for low input power, the signal can still be considered as perturbative, and then the response is linear. For higher power, the linear trend is not followed anymore, and a quadratic response appear. In respect with the modeling, the linear range which is available is about 25 dBm.

In conclusion, we have shown that a photonic crystal *molecule* can be used for all-optical sampling and frequency down-conversion of microwave signals with GHz bandwidth centered around a microwave carrier with about 10 GHz frequency. The very low power required to the

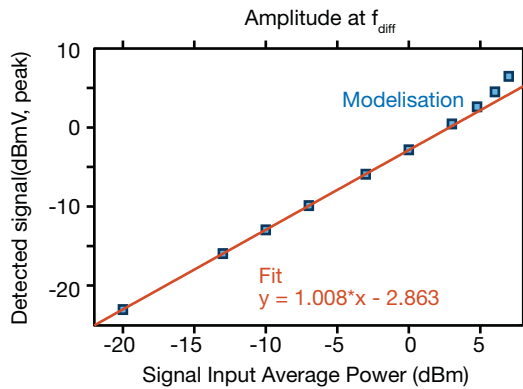


**Fig. 4-14** | Simulation of the output signal power  $P_{out}$  at  $f_{diff}$  regarding the signal RF power  $P_{MZ}$ .

optical clock (about 1 mW average) can be provided by an ultra-compact mode-locked diode laser. Since the size of the optical gate is also very small (the core of it extends over a few squared microns), this allows prospect for massive parallelization of all-optical switching.

### 4.3 | Gallium Arsenide Surface Mitigation Using Atomic Layer Deposition

Using InP-based PhC provides low energy switching operation and enables operations up to 10 GHz, as previously shown. However, due to the recovery long tail of the all-optical gate, rising the repetition rate leads to decreasing the signal output contrast. Moreover, as the all-optical gate has an opening window (considered as the Full Width at Half Maximum (FWHM)) of 18 ps, these InP based all-optical switches are intrinsically limited to process signals at a frequency rate lower than 50 GHz.

To speed up all-optical gates, the standard approach is to reduce the carrier lifetime, by for instance ion-implantation creating defects [62, 74]. However, defects create undesired absorption, therefore reducing the energy efficiency of the all-optical switch.

Another way to achieve fast all-optical switching is to use the intrinsic properties of PhC, namely having a large surface to volume ratio. Indeed, surface recombination plays a crucial role in the relaxation of free carriers in such devices. Earlier investigations at the U. of Sheffield [140] in an AlGaAs PhC bulk structures had shown enhanced surface recombination to be responsible for a sharp decrease in the carrier lifetime, namely  $\tau_{carr}=8$  ps. Earlier investigations in our group in Thales focused on 2D GaAs PhC membranes, where surface to volume ratio is even larger. Such experiments evidenced a recovery time of about 6 ps, suggesting a much shorter carrier lifetime,

once accounting for the duration of the excitation (about 4 ps) and the cavity lifetime (1 ps) [65]. Such fast carrier dynamics is caused by the Fermi-level which is pinned at mid-gap at the surfaces optimizing the recombination of both electrons and holes [130] (see section 3.1.2.3). Therefore, the surface recombination velocity  $v_{rec}$  is in the order of the saturation velocity ( $10^5 \text{ m.s}^{-1}$ ) [130, 149].

Indeed, a sensible estimate of the carrier lifetime  $\tau_{carr} \approx 1 \text{ ps}$  results from the Shockley [129] formula, previously shown in section 3.1.2.3,  $\tau_{carr}^{-1} = \tau_{rec}^{-1} + L^{-1}v_{rec} \approx L^{-1}S$ . A surface recombination velocity previously described was assumed while  $L$  is interpreted as the maximal distance from the surface, which is here about 100 nm. Our accurate 3D diffusion calculations confirm this estimate.

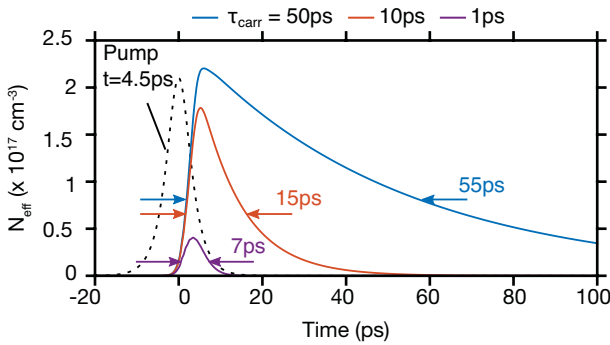


**Fig. 4-15** | CMT modeling of the effective carrier concentration in time for different carrier lifetime:  $\tau_{carr} = 1, 10,$  and  $50\text{ps}$ .

However, the recombination velocity of bare GaAs being too fast, it does not let enough time to build up the carrier density sufficiently to provide an efficient change in the refractive index. As shown in Fig. 4-15, the effective carrier lifetime affects the total effective density of carrier. If the carrier lifetime is too small, as in bare GaAs, low effective carrier concentration is achieved as they recombine almost immediately. The response of such all-optical gate result of reproducing the pump temporal form (Fig. 4-15). Indeed, the dynamics of the carrier density in time not follow an integral form (as it should be considering eq. (3.15)), whereas it has an instantaneous response due to the short recombination lifetime. However, if the carrier lifetime is too low, as in InP, even if the build-up of the carrier density is highly effective, the time recovery is slow, limiting the speed of the all-optical gate. An optimized value results in a carrier lifetime of about the duration of the pump-pulse, in our case about 10 ps, resulting in a good build-up of the carrier density changing efficiently the optical index of the GaAs and still providing a fast switching operation.

Moreover, bare GaAs undergoes photoinduced oxidation under high optical energy density, drifting the resonances inexorably. This problem is crucial for high repetition rate all-optical switching, as this oxidation phenomenon is determined by the average optical power (as the thermal relaxation is long compared to the clock pulse duration). Indeed, under this conditions, the clock will not be tuned to the resonance, and should be continuously adjusted to match the resonance. This further complexity the system. Also, the resonator at some point could exhibit a change in their  $Q$ -factor as an oxide partially replaces the III-V material. Therefore, such bare material cannot be used in an industrialized system.

In this section, we demonstrate the optimization of the effective carrier lifetime in GaAs PhC switch to about 10ps, which is optimal (for the clock pulses duration considered here) for ultra-fast operation. This was accomplished by passivating the surface using a  $\text{Al}_2\text{O}_3$  conformal coating by Atomic Layer Deposition (ALD), which is shown to reduce the surface recombination velocity effectively by more than an order of magnitude. This device can resolve 10 ps separated pulses and still meet the requirements of footprint, power consumption and compatibility with a photonic integrated circuit. Other materials or coating processes were also studied, such as  $\text{HfO}_2$  and chemical oxide removal before ALD coating, showing results not as satisfying as the  $\text{Al}_2\text{O}_3$  conformal coating.

#### 4.3.1 | New Design and Waveguide Positions

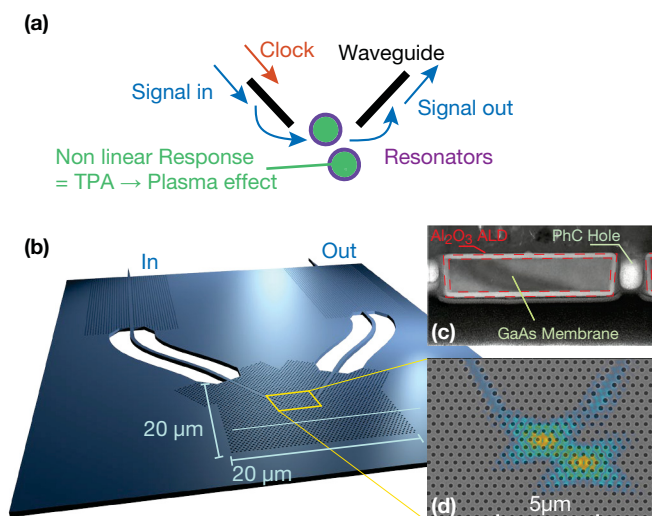


**Fig. 4-16** | (a) Schematic model of the device with coupled cavities connected to access waveguides – (b) 3D schematic view of the device, corresponding to the schematics above – (c) Cross-sectional transmission electron micrograph (TEM) of the PhC slab revealing a conformal  $\text{Al}_2\text{O}_3$  coating and (d) Scanning Electron Microscope (SEM) image of the two coupled cavities and the map of the Electric field intensity superimposed (logarithmic scale)

The nonlinear resonator consists of almost the same design as the one described above in section 4.1.1 for the InP sample, with a change in the PhC period of  $a = 400$  nm due to the small difference of refractive index between InP and GaAs. The main difference introduced here is the position of the suspended input and output PhC waveguides connected to the cavities. They are placed so that they are on the same side of the cleaved sample. It has the advantage that the lengths of the waveguides do not have to be as long as the sample (Fig. 4-16), length determined by the smallest size that can be cleaved (by the operator) of a few millimeters. Therefore, light undergoes fewer losses due to waveguide defects, and a better transmission characterization is possible. Sections of suspended rib waveguides (Fig. 4-16(b)) are designed to efficiently connect the input and output ports to the PhC section where the cavities are.

This changes slightly the experimental setup as both input and output ports are on the same side. The output signal, which is sent to an OSA (as in section 4.1.2), is obtained from the same side than the input signal. Due to the few tenth of micrometers distance between the two channels, and considering the input align with the center of the microscope, a small angle tilts the output beam. Indeed, the output beam is not centered with the microscope objective, and this misalignment leads to a slight angle. Thus can be retrieved by a mirror as shown in Fig. 4-17(a).

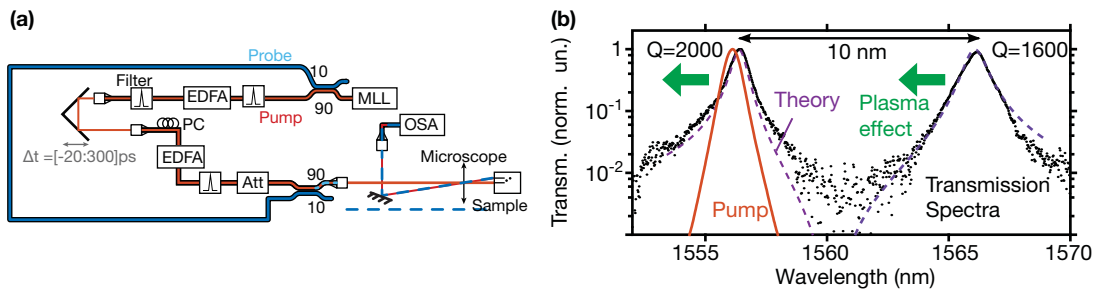


**Fig. 4-17** | (a) Setup of the pump-probe spectrally resolved setup with the input and output port on the same side of the sample – (b) Measured transmission ( $P_{out}/P_{in}$ ) spectrum revealing two resonances located at  $\lambda_b = 1557$  nm (*i.e.* pumped resonance) and  $\lambda_r = 1567$  nm (*i.e.* probed resonance) with Q-factor  $\approx 2000$ . The theoretical lineshape (Coupled Mode Theory) is superimposed (purple dashed line). The spectrum of the pump with offset  $\Delta\lambda_p$  is depicted (red line).

As the previous InP sample, the input and the output channels have mode adapters [146] at their extremities for coupling to the microscope objective. The GaAs PhC is conformally coated by ALD technique with 33 nm of  $\text{Al}_2\text{O}_3$  (Fig. 4-16(c)). The transmission spectra of the sample is represented in Fig. 4-17(b), where the CMT linear simulation is superimposed, showing a very good agreement between the characterization and the model.

### 4.3.2 | ALD Passivation

Surface passivation of semiconductor surfaces has been a field of study since the early 80s [150–154], either to try to move from silicon to better mobility materials such as GaAs [153], lowering surface-related leakage currents and therefore creating good gate transistor interfaces [155] and also because of the reduction of the transistor gate channel increasing the surface to volume ratio [156]. However, common passivation techniques used such as PECVD, MOCVD or other classical deposition techniques [151] have the major drawback not to coat conformally the sample, especially walls or in our case underneath the membrane. Recently, a new type of deposition, namely ALD, has been thoroughly investigated and provides a conform coating for various geometry samples. That is why such a technique was used in this manuscript to encapsulate fully and therefore passivate all the surface of the PhC self-suspended GaAs membrane. All the deposition and process relative to the ALD presented here were performed at the *Institut d'Electronique, de Microelectronique et Nanotechnologies* (IEMN) in Villeneuve d'Ascq (by L. Morgenroth).

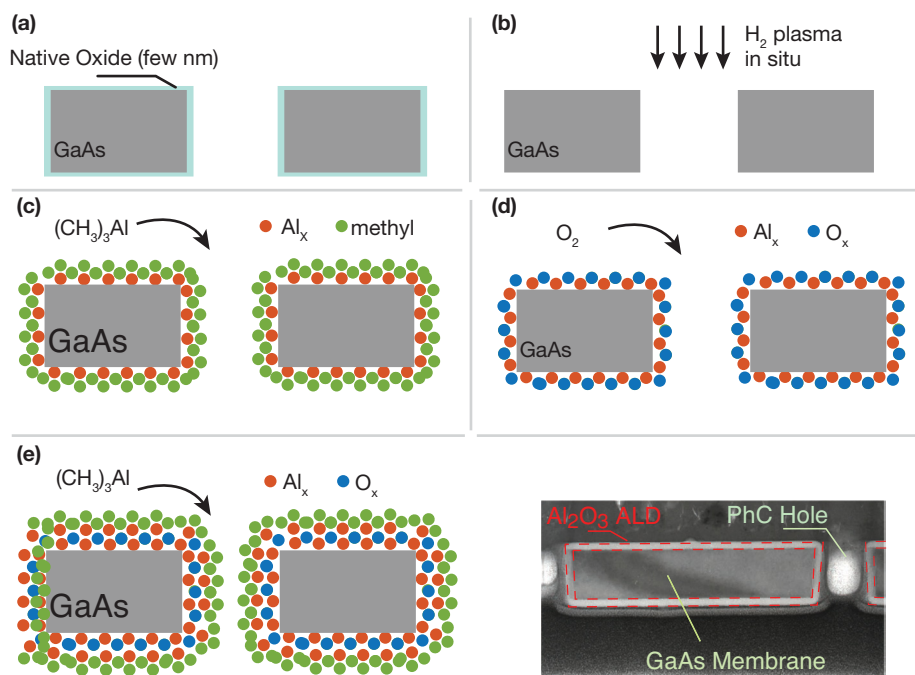


**Fig. 4-18** | ALD process – (a) Side view of the PhC with a native oxide – (b) *in situ* oxide removal by  $H_2$  plasma – (c) Several pulses of TMA to fully saturate the surface of the GaAs – (d)  $O_2$  plasma to create the  $Al_2O_3$  compound. At this stage, only one layer of  $Al_2O_3$  has been created – (e) Steps c and d are repeated until the desired thickness is achieved

III-V materials exposed to air have a native oxide of a few tenths of nanometers (Fig. 4-18(a)) created just by the  $\text{H}_2\text{O}$  and  $\text{O}_2$  present in the air. As the surface passivation is efficient directly when the  $\text{Al}_2\text{O}_3$  is in direct contact with GaAs, an oxide removal step is firstly done. This is easily understandable as with the native oxide the chemical bonds remain the same without or without encapsulation as the native oxide would act as a buffer layer. Thus the passivation does not change the nature of the surface, leading to a less efficient passivation coating. Therefore, a  $\text{H}_2$  plasma (1 min, 50 W,  $300^\circ\text{C}$ ) is performed inside the ALD machine chamber as the oxide removal step (Fig. 4-18(b)). Only after this crucial step, the ALD deposition begin. It first starts with 20 plasma pulses of 100 ms each of precursors, in our case TriMethylAluminium (TMA) to fully saturate the surfaces (Fig. 4-18(c)). As the ALD technique is based on the adsorption of a chemical precursor compound, the coating is conformed over all the surfaces, even below the self-suspended membrane and on the side of the PhC holes. Then, an  $\text{O}_2$  plasma is done, breaking the Al and methyl group bonds, and creating the  $\text{Al}_2\text{O}_3$  compound by simple oxidation of the free Al (Fig. 4-18(d)). At this step, only one monolayer of  $\text{Al}_2\text{O}_3$  was formed. The TMA plasma and the  $\text{O}_2$  plasma are both performed at a temperature of  $300^\circ$ . Finally, each monolayer is created following the previous step until the desired thickness of  $\text{Al}_2\text{O}_3$  is achieved (Fig. 4-18(e)), in our case 30 nm. All those different steps are realized in a Beneq machine from IEMN.

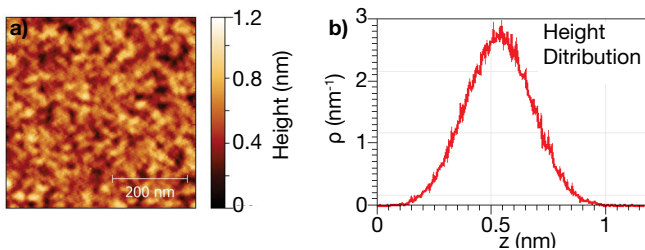


**Fig. 4-19** | (a) AFM measurement of the of the  $\text{Al}_2\text{O}_3$  roughness for the ALD coated sample – (b) Height distribution of the roughness, which correspond to a RMS of 0.15 nm.

A low coating roughness is essential; otherwise, it leads to scattering and therefore increases undesired losses. In order to characterize this aspect, Atomic Force Microscopy (AFM) measurement was performed (at the IEMN) using Dimension 3100 (Bruker-Veeco) machine, with a 10 nm radius cantilever NCHV-A from Bruker ( $f_0 = 320$  kHz,  $k = 42$  N.m $^{-1}$ ), used in a contact mode. The images were acquired over a  $1\ \mu\text{m} \times 1\ \mu\text{m}$  surface at 1 Hz with a 256 pixels resolution (Fig. 4-19(a)). From this mapping, it allows to determine the roughness of the coating statistically, by taking the Root Mean Squared (RMS) of the roughness height distribution which gives an estimation of 0.17 nm (Fig. 4-19(b)). This value is really small compared to the hole radii (about 80 nm)

therefore the ALD roughness can be neglected.

However, even with small roughness, a material is added to the PhC, changing the structure effective index, thus shifting the resonance toward the red. As the  $\text{Al}_2\text{O}_3$  refractive index is relatively small compared of the GaAs, slightly wider holes are accounted in the design for pre-compensating this modification. Also, as the coating modifies the geometry, cavities could undergo a change in their losses induced by the presence of the  $\text{Al}_2\text{O}_3$ , which may change the  $Q$  factor of the coupled resonator. As the design is based on over-coupled cavities to waveguides enabling high transmission, the resonance spectral width modification is negligible. Moreover, it has been shown that ALD coating does not decrease the quality factor of PhC cavities [157, 158]. Therefore, modification of the quality factor of the resonances can be neglected here.

### 4.3.3 | Dynamics of the Free Carriers

To clarify the role of the surface recombination and to assess the impact of surface passivation, we compare here two nominally identically devices, fabricated using a standard PhC process (see section 2.1). One of the samples is coated using the ALD technique previously detailed, while the other remains as it. The recovery dynamics of the all-optical gates is measured with a time-resolved spectral method similar to the one described section 4.1, with the modification detailed above for collecting the output signal from the same side as the input.

A striking difference between the ALD-coated and the reference (uncoated) samples is observed (Figs. 4-20(a) and 4-20(b)). Snapshots of the transmission spectra  $T(\nu, \Delta t)$  resolved at representative pump-probe delays  $\Delta t$  clearly reveal a strong blue shift of the resonance in the ALD-coated sample only (Fig. 4-20(d)). In the other sample (Fig. 4-20(c)) the blue shift is much fainter and dwarfed by a strong decrease of the transmission. A more quantitative figure is the spectral shift which is obtained from the first order moment of the transmission spectra in time (see eq. (4.1)), namely:  $\Delta\nu(t) = \int \nu T(\nu, t) d\nu$ . One can also considered the total spectral transmission in time  $\Delta T(t) = \int T(\nu, t) d\nu$ . Indeed, the spectral shift  $\Delta\nu$  achieved in the un-passivated sample (Fig. 4-21(a)) is weak (35 GHz) when compared to the case of the ALD-coated sample (138 GHz) (Fig. 4-21(b)). Also, the temporal shape of  $\Delta\nu(\Delta t)$  merely follows the instantaneous transmission  $T(\Delta t)$ , suggesting that the device is responding faster than the excitation ( $t_{pulse} = 4.5$  ps).

As illustrated in Fig. 4-15, the extraction of the carrier lifetime from the measurement of the

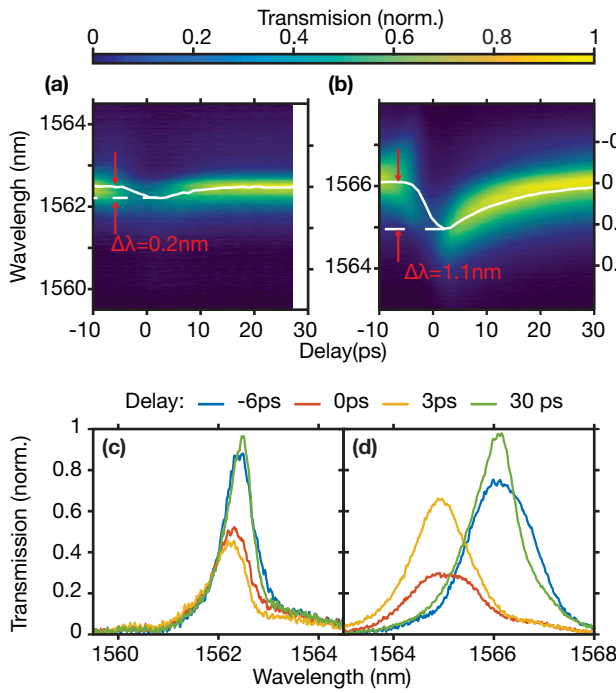


**Fig. 4-20** | Normalized intensity maps corresponding to the time-resolved transmission spectra for (a) uncoated GaAs reference sample and (b) ALD  $\text{Al}_2\text{O}_3$  coated; the first moment order  $\Delta\nu_c(t)$  is superimposed (white solid line). Snapshots of the spectra at different pump-probe delays for the uncoated (c) and ALD coated sample (d).

cavity dynamics deserves some attention and can be performed by modeling the measurement (see section 3.2). Here, all the parameters are either measured or calculated, with the exception of the surface recombination velocity  $v_{rec}$ , which strongly depends on the processing and the passivation technique. We have adjusted this value to achieve the best match with both measured  $\Delta\nu(t)$  and  $T(t)$ , as shown in Figs. 4-21(a) and 4-21(b). The agreement is indeed excellent when  $v_{rec} = 10^5 \text{ m.s}^{-1}$  and  $v_{rec} = 3 \times 10^3 \text{ m.s}^{-1}$  for the uncoated and the coated samples respectively. The parameters used in this modeling are fully given in appendix B.1.

In our model, three-dimensional time domain ambipolar equations are used to calculate the carrier relaxation dynamics, as a function of  $v_{rec}$ . The exact geometry of the experiment, including the initial distribution of the photo-generated carriers  $N(\mathbf{r}, t = 0) \propto |E(\mathbf{r})|^4$  computed by Finite Difference Time Domain (FDTD), is considered. As previously discussed in section 3.2, the result is an *impulse response* function  $h(t, v_{rec})$ , related to the effective carrier density  $N_{eff}$  (Fig. 4-21(c)). Since the model reproduces the experiments with an exceptional accuracy, we extract the carrier lifetimes from the exponential fit of  $h(t)$ , which, in contrast to  $\Delta\nu(t)$  and  $\Delta T(t)$ , is independent from the excitation.

The extracted carrier lifetimes are equal to 1.1 ps and 12 ps for the uncoated and the ALD samples

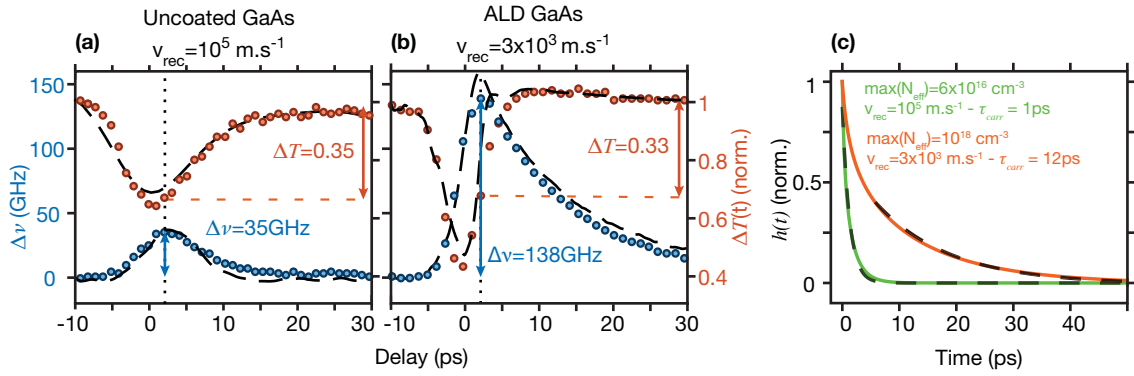


**Fig. 4-21** | Instantaneous detuning  $\Delta\nu(t) = \nu_c(t) - \nu_c(-\infty)$  (left scale) and time-resolved transmission  $T(t)$  (right scale), extracted from the maps in Figs. 4-20(a) and 4-20(b) for respectively the reference (a) and ALD passivated (b) samples. The coupled pump energy is estimated to 300 fJ. Modeling is superimposed (solid dashed line) – (c) Normalized impulse response  $h(t)$  and exponential fit for both reference (green) and ALD (orange) samples in order to extract the carrier lifetimes  $\tau$ .

respectively. Interestingly, the exponential fit is very accurate for the case of the uncoated sample, where the surface recombination velocity  $v_{rec}$  is very fast. In contrast, when  $v_{rec}$  is reduced by the passivation, the initial dynamics of carriers clearly reveals a more rapid time constant (about 1 ps). This is attributed to the effect of rapid diffusion. Because of the nature of nonlinear resonant absorption, carriers are photo-generated within a very tiny area. Ambipolar calculations show that in the case of  $v_{rec} = 3 \times 10^3 \text{ m.s}^{-1}$ , the volume occupied by the carriers rapidly expands from  $2.5 \times 10^{-20} \text{ m}^3$  to  $\approx 8 \times 10^{-20} \text{ m}^3$  after a few picoseconds. This explains the initial fast decrease of the effective carrier density  $N$ .

A very different case is when carriers are injected by an off-plane focused pump, as for instance in ref. [82]: no diffusive contribution to the dynamics has been observed. Also, the dynamic response of the device is strongly modified if the duration of pump pulses is very short (sub-ps).

The analysis of Fig. 4-21(b) near zero delay deserves some further comments. The transmission minimum  $\min(\Delta T(t)) = 0.4$  is an unavoidable consequence of the fact that carriers are injected through nonlinear absorption, causing the signal (the probe) to be absorbed as well. This minimum coincides with the steepest slope of the leading edge of  $\Delta\nu$ , which itself reaches a maximum when the transmission has almost recovered. This behavior is crucial for a practical use of the switch, and it is in striking contrast with the case in Fig. 4-21(a).

Our measurements positively conclude that the conformal growth of a 30 nm thick layer of

$\text{Al}_2\text{O}_3$  on a PhC membrane decreases the surface recombination velocity by more than an order of magnitude. The measurement has been repeated on other devices, with slightly different parameters, e.g. the Q factor ranging from 2000 to 3000. The estimate of the carrier lifetime is  $\tau_{carr} = 11.5 \pm 2$  ps, thereby implying a good control and reproducibility of the properties of the ALD/ $\text{Al}_2\text{O}_3$  passivation.

#### 4.3.4 | Passivation Effects

Hereafter, we interpret our results based on the broad literature covering surface passivation of GaAs using ALD-grown oxides (e.g.  $\text{Al}_2\text{O}_3$  and  $\text{HfO}_2$ ). This research has been carried out in the context of related physical systems, particularly III-V Field Effect Transistors (FET) [159, 160]. There, the functionality is hampered by the slow traps ( $D_{it}$ ) at the semiconductor-oxide interface, leading to the pinning of the Fermi energy level. The growth of  $\text{Al}_2\text{O}_3$  on GaAs by ALD partially removes the native oxide [155]; however, in III-V transistors it is found that a surface treatment is required to ensure the unpinning of the Fermi level by actually reducing  $D_{it}$ .

Thus, before ALD, we treat our structures *in situ* with a Hydrogen plasma, which is known to remove the native oxide and leave a defectless surface [161]. Our finding in the domain of photonic nanostructures is that this step is indeed crucial to reducing the surface recombination, consistently with the literature of III-V field effect transistors (FET) [162, 163]. The large density ( $Q_f \simeq 10^{19} \text{ cm}^{-3}$ ) of fixed charges in the  $\text{Al}_2\text{O}_3$  layer might also play a role, as it has been observed in FETs that this charge can unpin the Fermi level. Interestingly, surface recombination in our ALD passivated GaAs device is still much stronger than in InP PhC structures, such as in ref. [66], since in InP  $v_{rec}$  is below  $10^2 \text{ m.s}^{-1}$  [130]. One explanation could be the fact that the oxide removal step through a plasma is highly anisotropic. Therefore it provides a perfect oxide removal for the top surfaces, a quite good one for the hole sides but none for the below of the membrane, which is then maybe poorly passivated.

Another aspect of GaAs photonic structure relates to stability. It has been shown that non-passivated GaAs photonic crystals undergo a photo-assisted oxidation when exposed to high enough optical power. This is explained as the high-temperature dependence of the oxidation process, favored by local heating. This results into an irreversible drift of the resonance [164], which we also observed

while exciting the GaAs nonlinear cavity investigated in ref. [65] with a GHz repetition rate and was also observed in our uncoated sample (Fig. 4-22). After each pump-probe measurement, the resonances were blue shifted, which is coherent with the transformation of GaAs into its natural oxide. A saturation effect was also observed when several experiments were performed in a row. However, this saturation effect does not last, and only after one night, the oxidation process starts again with light injection. However, such effect was not reproduced with the ALD coated sample and the resonances remain at the same wavelength during the whole experiments. Thus, the conformal growth of  $\text{Al}_2\text{O}_3$  effectively prevents oxidation, as already shown on PhC structures [165]. We confirm that ALD coated samples are remarkably stable even under exposure to intense optical flux.

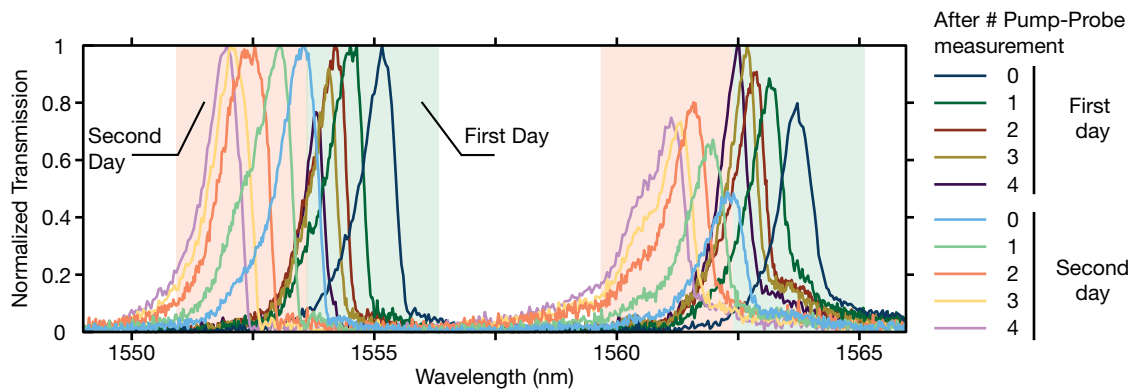


**Fig. 4-22** | Oxidation and resonances shift for the uncoated sample after two sets of pump-probe experiments performed in a row. These two sets of experiment were separated by a day.

#### 4.3.5 | Other Material

$\text{Al}_2\text{O}_3$  is not the only material which is both *high-k* (*i.e.* high dielectric constant  $\epsilon_r$ ), thus has been investigating for micro-electronic purpose especially for transistor surface passivation, and being able to be deposited with ALD technique. Another material highly promising for gate passivation of FET structures is the Hafnium Oxide ( $\text{HfO}_2$ ) which was extensively studied [155, 166–168] and shown promising results [169]. Therefore, a sample coated with  $\text{HfO}_2$  was processed to be compared with the  $\text{Al}_2\text{O}_3$  coating. The same oxide removal through  $\text{H}_2$  *in situ* plasma was done, and the whole ALD process remains the same than for the  $\text{Al}_2\text{O}_3$ . The only modification is the precursor compound, which becomes the TEMAHf (Tetrakis[EthylMethylAmino]Hafnium) which will become Hafnium Oxide by oxidation

Moreover, as it was previously introduced, surface cleaning before passivation is an important key for reducing surface recombination. Even if the deposition of high-k dielectric has the tendency to remove the native oxide [169], it has been proven by our experiment that the  $H_2$  plasma is necessary to remove the oxide. When no plasma is performed, no improvement on the surface recombination velocity is observed. However, other techniques to remove the native oxide exist, such as chemical etching using HCl or HF solutions. Therefore, an other sample was processed and coated with  $Al_2O_3$ , which has been priorly etched by the chloride acid mixture, in an Argon chamber linked to the ALD machine. Thus, the sample is not brought outside the oxygen-free atmosphere, and no native oxide will be recreated.

These two new samples were characterized with the same setup as usual and compared with the  $Al_2O_3$  sample which has shown an improvement in the surface recombination velocity.

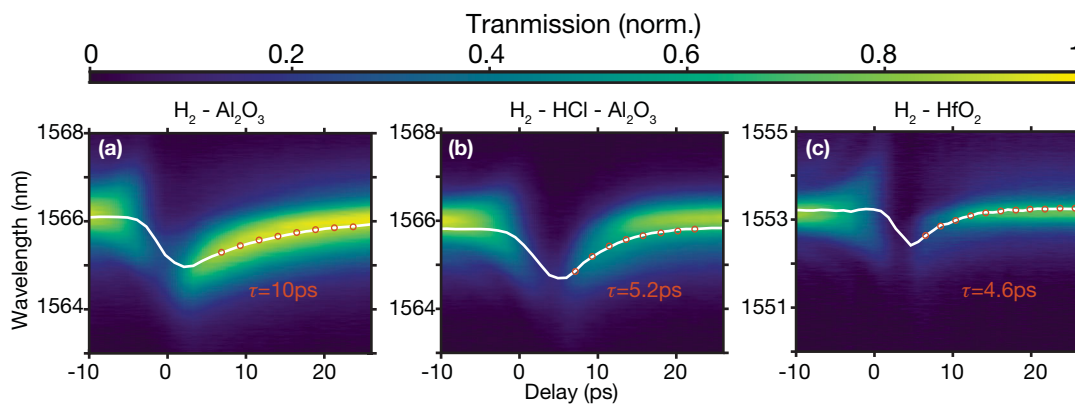


**Fig. 4-23** | Pump Probe experiment for 3 type of ALD coating – (a)  $Al_2O_3$  ( $E_{pmp} = 300$  fJ) – (b)  $Al_2O_3$  with HCl oxide removal prior to deposition ( $E_{pmp} = 800$  fJ) – (c)  $HfO_2$  ( $E_{pmp} = 600$  fJ)

Even if CMT simulation are necessary to fully understand the mechanism of the carrier dynamics in the PhC resonator and obtained a value of the carrier effective lifetime, in first order it is useful to only fit the first order momentum with a simple exponential. Thus, the comparison of the decay rates gives an indication on the carrier lifetime. Figure 4-23 show the experimental results for the three different samples, and it is evident that the  $Al_2O_3$  coating with  $H_2$  plasma is the sample with the higher effective carrier lifetime (Fig. 4-23(a)). The exponential fit leads to a decay rate of 10 ps, which is close to the value found in the previous modeling. This can be explained easily as the carrier lifetime is higher than the pump duration, the exponential fit reproduces only the recovery of the all-optical gate, and the pump effect can be neglected after a few picoseconds.

Compared to the two other samples, the HCl oxide removed sample (Fig. 4-23(b)), and the HfO<sub>2</sub> coated (Fig. 4-23(c)), their exponential fits lead to a faster decay rate, which is in the order of the pump duration. It is also interesting to notice the energy involved for this last two samples to perform an effective spectral shift, which is twice to three times higher than for the Al<sub>2</sub>O<sub>3</sub> sample. It is consistent with the fact that the carrier lifetime is faster (see Fig. 4-15). Such results are not surprising for HCl oxide removal as it was previously reported that using such solution significantly degrades the surface [149, 170].

However, it is important to point out here that the encapsulation effect (different from the passivation effect), disabling the photo-induced oxidation which happens with uncoated samples, has not been observed in any of those three samples. Thus, even if the carrier lifetime is not clearly modified with HfO<sub>2</sub> coating, or with HCl oxide removal, it still creates an effective barrier between the sample and the atmosphere.

We can conclude that the process consisting of an *in situ* oxide removal by H<sub>2</sub> plasma followed by an plasma Al<sub>2</sub>O<sub>3</sub> coating using TMA as a precursor leads to an optimization of the surface recombination to an optimized value, corresponding to a carrier lifetime of about 10 ps, providing both speed and energy efficiency.

## 4.4 | All-Optical Operation Using GaAs Photonic Crystal

Thanks to the mitigation of the surface of the photonic crystal using Al<sub>2</sub>O<sub>3</sub> ALD coating, the carrier life-time has been optimized, thus efficient wavelength shift is achieved enabling all-optical operations such as ultra-fast gating or wavelength conversion. Moreover, non-protected GaAs undergoes photoinduced oxidation leading to a detrimental shifting of the resonance, making the sampled useless for signal processing as the pump will continuously need to be adjusted. In the case of ALD coated sample, this physical phenomenon has been disabled allowing GHz rate operation.

### 4.4.1 | Operation At GHz Rates

Wavelength conversion consists in transferring an intensity pattern, e.g. a sequence of pulses from the pump, at a specified wavelength  $\lambda_p$  to a new wavelength  $\lambda_s$  through all-optical modulation

of a continuous wave probe at  $\lambda_s$ . For practical applications, also including sampling and time-demultiplexing, a meaningful repetition rate is in the GHz range. As the repetition rate increases, the average power dissipated increases too. Moreover, the incomplete recovery of the gate might influence the following pulse. Therefore wavelength conversion is a sensible benchmark for all-optical processing.

The experiment is very similar to ref. [66], and the one presented in the previous section 4.2. It is performed using a fiber mode-locked laser tuned to the high energy resonance and a CW laser tuned to the low energy resonances as the input beams (Fig. 4-24).

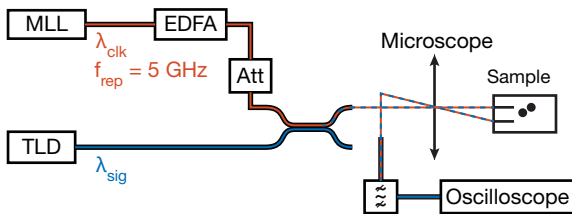


**Fig. 4-24** | Schematic of the wavelength conversion setup with GaAs ALD passivated sample

In this experiment, one has optimized the spectral position of the pulsed pump and the CW probe relatively to the maximum achievable contrast, taking into account and partially compensating for the thermal drift. The CW probe was tuned either on resonance or was blue shifted by about 0.5 nm, which results in a downward or upward modulation of the transmitted probe (Fig. 4-25(a)). This is observed using a 70 GHz sampling oscilloscope (Textronik), a 40 Hz photo-diode (U2t), AC coupled, and a low-noise EDFA which amplifies the transmitted probe, while the pump is filtered out using a doubly tunable filter (Yenista) providing about 50 dB of side-band rejection. We point out that the switching window appears broader (about 30 ps) because of the bandwidth of the detector (Figs. 4-25(a) to 4-25(c)).

The oscilloscope trace is corrected with a DC offset, estimated based on the measured average power to the photodiode and its responsivity (0.9 A/W). This results in a conservative estimate of the modulation contrast, as the ASE noise is not taken into account. The contrast increases monotonically with pump power Figs. 4-25(b) and 4-25(c), until a level of about 120 fJ/pulse (coupled), as apparent in Fig. 4-25(d). The maximum contrast is reached with a coupled average power of about 0.5 mW (190 fJ/pulse). Experiments have been performed at a repetition rate of 5 GHz and were made possible by the  $\text{Al}_2\text{O}_3$  conform coating. Without such encapsulation, ther-

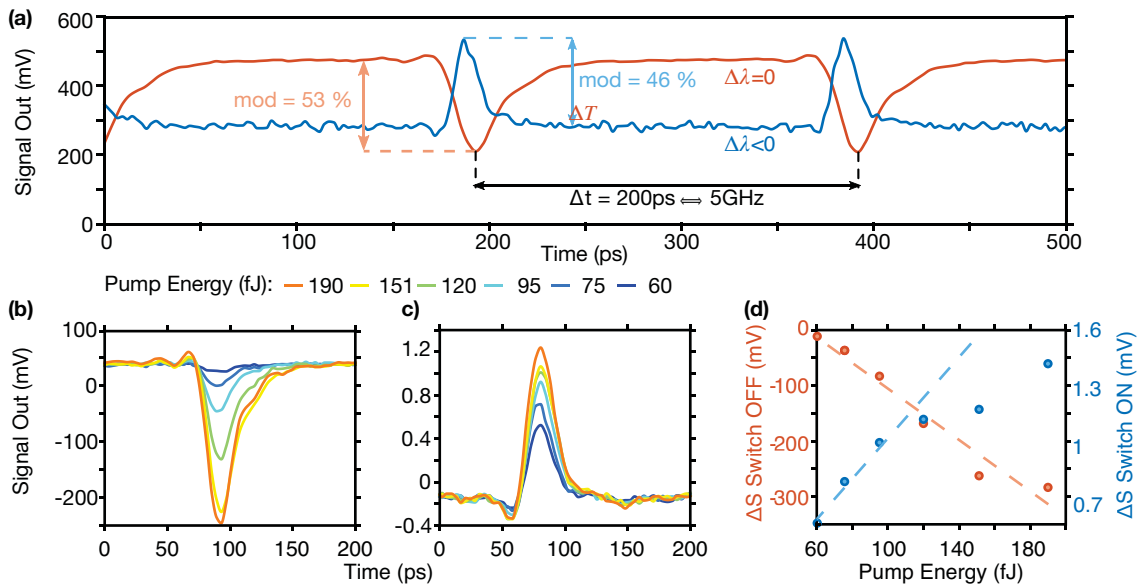


**Fig. 4-25** | Wavelength conversion experiment at 5 GHz with optical resonances at  $\lambda_b = 1543$  nm and  $\lambda_r = 1553$  nm respectively. Oscilloscope traces of the all-optically modulated CW input tuned close to  $\lambda_r$ . (a) operation at zero signal detuning  $\Delta\lambda = \lambda_s - \lambda_r = 0$  (switch off) and negative detuning ( $\Delta\lambda < 0$ ) at maximum pump power. Dependence of the modulation on the pump energy (b) switch off and (c) on – (d) corresponding modulation contrast for switch off (red) and on (blue) and linear fit (dashed).

mally driven oxide would happen, drifting the resonance wavelength and making high repetition rate experiment impossible. This experiment thus proves that no oxides are created because of the thermally induced reaction.

Further increasing the repetition rate to 10 GHz resulted into a substantial decrease of the switching contrast which we believe to be due to a four fold increase of the dissipated power induces a large enough red shift to drive the cavity out of resonance in a microsecond time scale (related to thermal dynamics). This issue could be overcome by a thermal feedback pre-compensating the red shift by locally heating the cavities, either by joule-effect using micro-strip metal [171] or by direct laser heating [172]. Thus, the speed limit of the wavelength operation would be only limited by the temporal response of the gate.

#### 4.4.2 | Ultra-Fast Gating

A more accurate measurement of the operation of the switch is performed through a non-degenerate homodyne technique, where the spectrally broad probe is replaced by a 2 ps long pulse (approximately 0.7 nm wide), still obtained from the same femtosecond laser. We achieved a maximum switching

contrast of 7 dB and a switching window at  $1/e$  of 12 ps (Fig. 4-26) with a pump energy of 200 fJ. Considering that the operation conditions (pump pulse power, duration, and center wavelength) were exactly the same as in the wavelength conversion experiment, this clearly shows that the response measured at the oscilloscope is affected by the instrument itself. Reducing the pump energy to about 100 fJ still allowed a contrast of 3 dB.

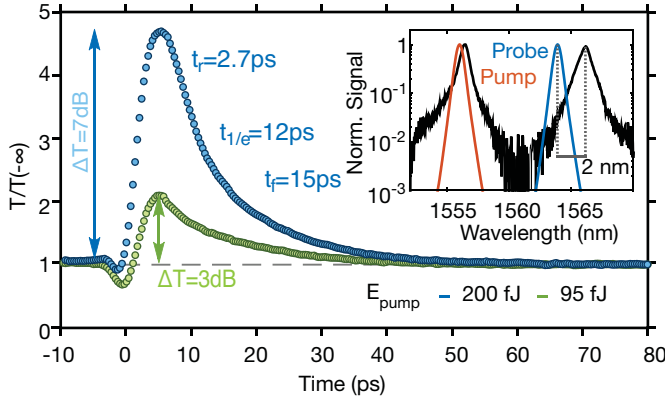


**Fig. 4-26** | Time-resolved homodyne non-degenerate pump-probe measurements at probe detuning  $\Delta\lambda = -2.2\text{nm}$ . Relative probe transmission  $T/T(-\infty)$  vs. pump-probe delay and extracted rise-time  $t_r$ , fall time  $t_f$  and width at  $1/e$ ,

It is interesting to observe the response to a short train of pulses at a very high repetition rate. In Yüce et al. [46], a planar semiconductor cavity was shown to respond to a 4-pulse train at 1 THz rate. Such a fast response results from a Kerr-induced index change, owing to a particular configuration of the semiconductor alloy which suppressed the nonlinear absorption and, consequently, carriers-induced effects. However, the energy density of the focused pump is  $22\text{ pJ}\cdot\mu\text{m}^{-2}$ , implying the pump energy is in the nJ range (more than 4 orders of magnitude larger than in our case) when considering practical values for the diameter of the focused spot ( $> 20\text{ }\mu\text{m}$ ).

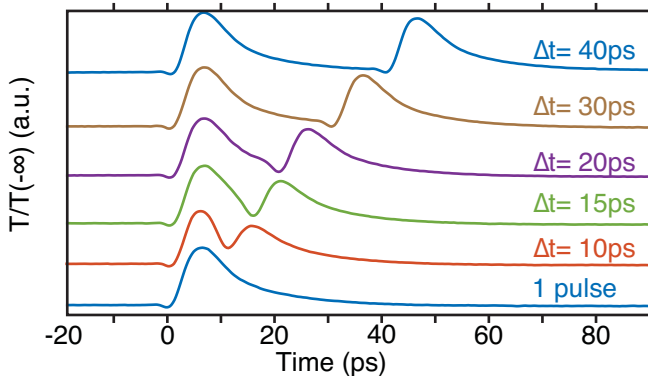


**Fig. 4-27** | Same as Fig. 4-26 but with a sequence of two pump pulses with a separation  $\Delta t$  varying from 0 ps to 40 ps.

In our experiment, two pump pulses with controlled delay  $\Delta t$  are obtained using a delay line (schematic shown further in Fig. 4-28(a) for 4 pulses). This allows to suppress heating issue while

investigating the recovery dynamics, thus the possibility to process high-frequency signal, as the repetition rate of the MLL is only at 36 MHz. When varying  $\Delta t$  from 40 ps to 0 ps, the response of the switch reveals two peaks which remain well defined (Fig. 4-27) even when  $\Delta t$  decreases to 10 ps.

To further explore the capabilities to handle very fast signals, a train of 4 pulses is generated by cascading another delay line, which is adjusted to obtain a pulse spacing of 10 ps. This is shown in Fig. 4-28(a), where it is apparent that the modulation contrast is well above 3 dB, e.g. the 4 pulses are still well-resolved. We also point out that the time resolution of our measurement is related to the duration of the probe, which is limited by the bandwidth of our switch. Shorter probe pulses would give more time resolution but lower contrast. Our choice of 2 ps for the probe results from a trade-off. The bandwidth of the switch depends both on the spectral width of the resonance but also on the instantaneous frequency shift [147], here 140 GHz, as observed with time-resolved spectral analysis (Fig. 4-21(b)).

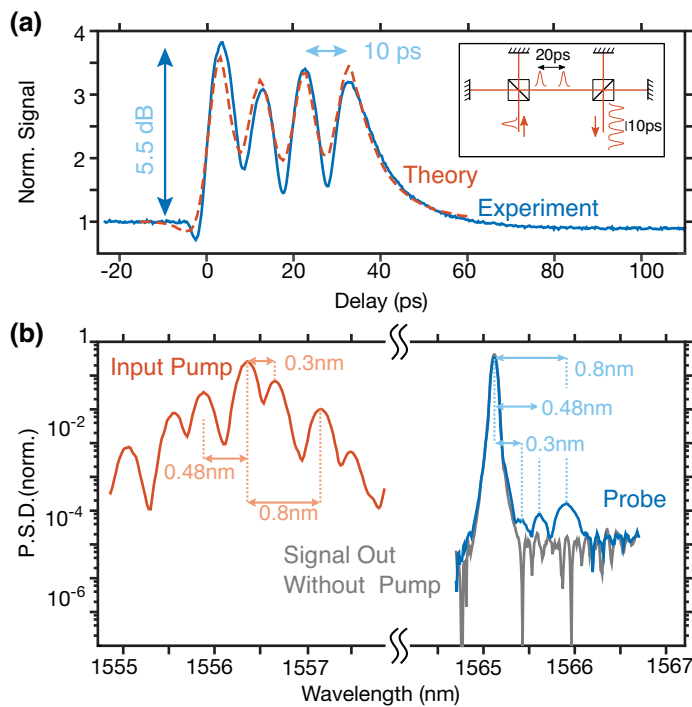


**Fig. 4-28** | (a) Same as Fig. 4-28 but corresponding to an excitation of 4 pump pulses spaced by 10 ps. The pulse energy is 180 fJ and the double Michelson is in the inset. Corresponding CMT modeling of the transmitted signal is represented in dashed red – (b) Transmitted spectra when the probe is replaced by a CW signal with  $\Delta\lambda = -1.2$  nm; Pump spectrum is in red, modulated (not modulated) CW signal in yellow (gray). The OSA resolution is 50 pm.

The observation in the spectral domain of the transmitted spectra of the 4-pulses pump and a CW probe (Fig. 4-28(b)) provides an alternative characterization of the all-optical modulation process.

The shape of the pump spectrum is consistent with 4 pulses spaced by 10 ps (the Fourier transform predicts frequency offset equal to  $1/\Delta t$ ,  $0.63/\Delta t$  and  $0.37.\Delta t$ , hence 0.8 nm, 0.5 nm and 0.3 nm). Three peaks appear on the red side of the probe, with the same spacing as for the pump (0.8 nm, 0.48 nm, and 0.3 nm), thereby indicating a transfer of the pattern to the probe. These peaks disappear when suppressing either the pump or the probe.

In conclusion, these measurements show that the device is responding to a modulation with frequency up to 100 GHz, without thermal drift of the resonance. At this rate and above, patterning effects become important. Conversely, they totally disappear when the pulse spacing is increased ( $> 10$  ps), as apparent in Fig. 4-27. The duration of the modulation is limited to a short period due to the rise in the temperature due to accumulated heat.

## 4.5 | Towards Faster InP Photonic Crystal All-Optical-Gates

The previous section described how to improve the speed of an all-optical gate by using a high surface velocity material. The passivation of those surfaces allows to achieve an ideal value for both speed and energy efficiency. However, Indium Phosphide based nanostructures are however desirable and alternative strategies to accelerate their response have successfully been demonstrated, either based on Fano resonances [173] or by increasing the surface recombination using quantum wells at the surface [68]

Here, we consider the possibility to enhance the relaxation of the free carriers by forcing the minority carrier diffusion regime, which, in InP (and many other III-V semiconductor alloys) is much faster than the ambipolar regime. This is achieved by p-doping the material and is well known in semiconductor device physics, for instance in the context of Quantum Dot amplifiers [174] or untraveling carrier photodiodes [175–177]. We show here that by simply doping an InP nonlinear nanoscale resonator with a moderate level of acceptors (such to avoid heavy free carrier absorption), the response can be made about two fold faster.

### 4.5.1 | Sample Description

The device is made of a 270 nm thick layer of p-doped ( $N_a = 0.5 \times 10^{17} \text{ cm}^{-3}$ ) InP grown on a thicker sacrificial layer of InGaAs using the usual sequence of e-beam patterning, silica hard mask

etching and finally pattern transfer into the III-V layer using Inductively Coupled Plasma (ICP) etching. The sacrificial layer is removed by  $\text{FeCl}_3$  chemical etching. The design consists in the dual-mode resonator obtained by coupling two  $H_0$  photonic crystal cavities [44], as previously shown in sections 4.1 and 4.3. The period of the photonic crystal is  $a = 465$  nm, and the four nearest holes are displaced along orthogonal directions by  $d_x = 0.16a$  (**K** direction) and  $d_y = 0.07a$ .

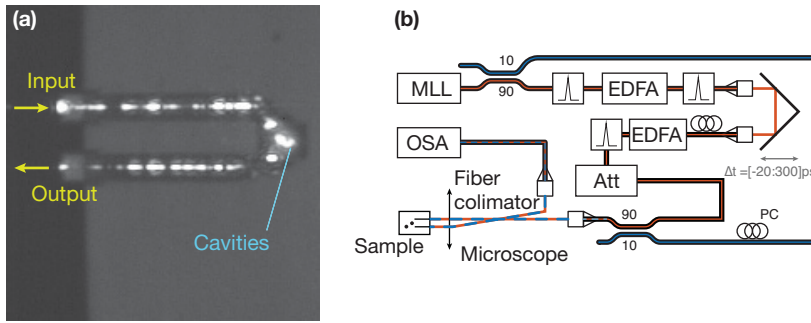


**Fig. 4-29** | (a) Infrared image of the sample from the top. The propagation of the light to and from the resonators is shown when the wavelength is set at the resonance – (b) Experimental set-up. In red the pump path which goes through the delay line, in blue the probe path.

The two cavities are spaced by the vector  $\mathbf{R} = 3a_1 + 3a_2$  (**M** direction). Here, as in the previous section, the input and output coupling paths have been redesigned to minimize the propagation through the PhC waveguide, where both input and output ports are located on the same facet of the chip (Figs. 4-29(a) and 4-29(b)). The much reduced scattering in the PhC waveguide translates into a much smoother transmission spectrum than the InP discussed in section 4.1, which is apparent in Fig. 4-30.

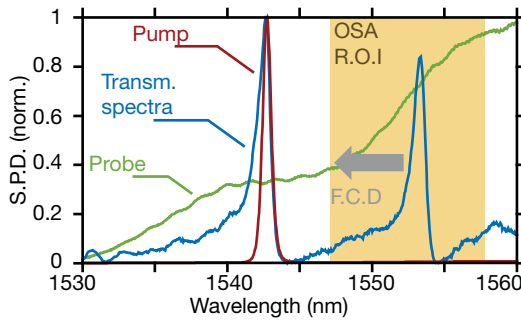


**Fig. 4-30** | Time-resolved experimental transmission spectra centered around the low-energy resonance. Intensity map (a) and (b) extracted time-resolved instantaneous detuning  $\Delta\lambda$ . The characteristic time  $\tau_{1/2}$  corresponds to the delay before the  $\Delta\lambda$  decreases by a factor 2.

The loaded Q factor  $Q_L$  for the two resonances is about 1400, which is much lower than the estimated intrinsic Q factor of the photonic molecule ( $Q_0 > 5 \times 10^4$ ), therefore the resonator is over-coupled and, from the coupled mode theory, the estimated transmission on resonance is  $T = (1 - Q/Q_0)^2 \approx 0.95$ , assuming identical waveguide to cavity coupling strengths on both sides. The loaded Q is very similar to that in section 4.1 and corresponds to a photon lifetime slightly larger than 1 ps and, therefore, almost instantaneous compared to the carrier dynamics.

### 4.5.2 | Time-Resolved Spectral Analysis

The recovery dynamics of the all-optical gate is investigated by observing the evolution of instantaneous detuning of the resonance  $\Delta\lambda$ , which is measured with a time-resolved spectral technique, extensively detailed in the previous sections.

The probe spectrum is obtained by coupling 10% of the laser output power (Fig. 4-29(b)), it is approximately 80 nm broad and almost flat (Fig. 4-30); the autocorrelation trace is approximately 3 ps. The pump is obtained by filtering and amplifying the same laser output, while the pump-probe delay is controlled mechanically with a translation stage (Fig. 4-29(b)). The power spectral density of the probe is at least 2 orders of magnitude below the pump. Moreover, the same measurement was repeated by varying the probe level to confirm the absence of any influence on the dynamics. An Optical Signal Analyzer (OSA), Anritsu with resolution 50 pm and video bandwidth set to 10 Hz is used to obtain the transmission spectra as a function of the delay without any smoothing or averaging.

In the photon-molecule described here, both resonances are shifted by approximately the same detuning  $\Delta\lambda$  and therefore the device is excited with the pump tuned to one resonance while the transmission spectrum of the other is monitored. A representative map of the measurement is shown in Fig. 4-31(a), which clearly reveals the spectral blue shift of the resonance after the excitation by a 3 ps long pump pulse. The instantaneous detuning is extracted from the map by calculating the first order moment of the spectral power density as described in eq. (4.1a), namely  $\Delta\lambda(t) = \int \lambda T(\lambda, t) d\lambda$

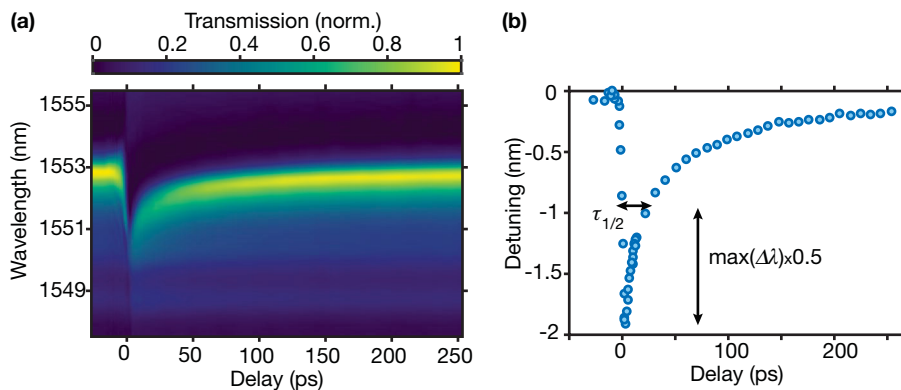


**Fig. 4-31** | (a) Time-resolved experimental transmission spectra centered around the low-energy resonance – (b) Extracted time-resolved instantaneous detuning and related slow and fast time constants  $\tau_1$  and  $\tau_2$

The spectral shift is dominated by the index change due to the injected free carriers, which is at least an order of magnitude larger than the Kerr effect. Therefore, to a good approximation, the density of free carriers in the cavity is related to it through the equation:

$$\Delta\lambda = -\frac{\lambda}{n} \left( \frac{\partial n}{\partial P} P_{eff} + \frac{\partial n}{\partial N} N_{eff} \right) \quad (4.2)$$

Where partial derivatives describe the free carriers index change [58] and  $P_{eff}$  and  $N_{eff}$  are effective *excess* electron and hole densities defined as weighted average (see section 3.2) of the excess carrier spatial distribution  $N - N_d$  and  $P - N_a$  with the normalized optical energy density  $W(\mathbf{r}) = \varepsilon_r \varepsilon_0 |\mathbf{U}(\mathbf{r})|^2 / 2$  of the cavity mode:

$$N_{eff}(t) = \int [N(\mathbf{r}, t) - N_d] W(\mathbf{r}) dV \quad (4.3)$$

and similarly for the holes.

The ambipolar equation does not stand anymore in the situation described in this section. Therefore, the previously described model based on the Green's function (see section 3.2) does not stand anymore too. Indeed, such formulation is valid in the case of a linear partial differential equation, which is not the case for the complete drift-diffusion model (see section 3.1). Also, the decay of the spectral shift is not exponential, neither a bi-exponential fit is satisfactory (see section 3.2). However, in similar nano-scale devices made of InP and Si, it has been pointed out that the initial phase of the decay is related to diffusion, while surface recombination takes over at a later stage of the process [59, 61, 66]. In the following, the relaxation dynamics of the p-doped resonator is investigated as a function of the excitation level, and it is compared to that of a nominally identical but undoped device, which has been discussed in [66]. To this purpose, a characteristic time  $\tau_{1/2}$  has been defined (Fig. 4-31(b)).

### 4.5.3 | Results and Discussion

Let us first consider the case of a relatively large excitation,  $W = 130$  fJ. The theory discussed in ref. [178] can still be used to estimate the initial level of excited carriers  $N_0$  in the cavity using the calculated value of the function  $h_0(0) \approx 6 \times 10^{61} \text{ J}^{-2} \text{ s}^{-1} \text{ m}^{-3}$  for an InP photon molecule. The formula  $P(0) = N(0) \approx h_0(0) W^2 \tau^2 / \Delta t$  (with  $\tau = 1$  ps the cavity lifetime and  $\Delta t$  the pump pulse duration) gives an estimate of  $3.5 \times 10^{-17} \text{ cm}^{-3}$ , exceeding the level of p-doping. Under these conditions,

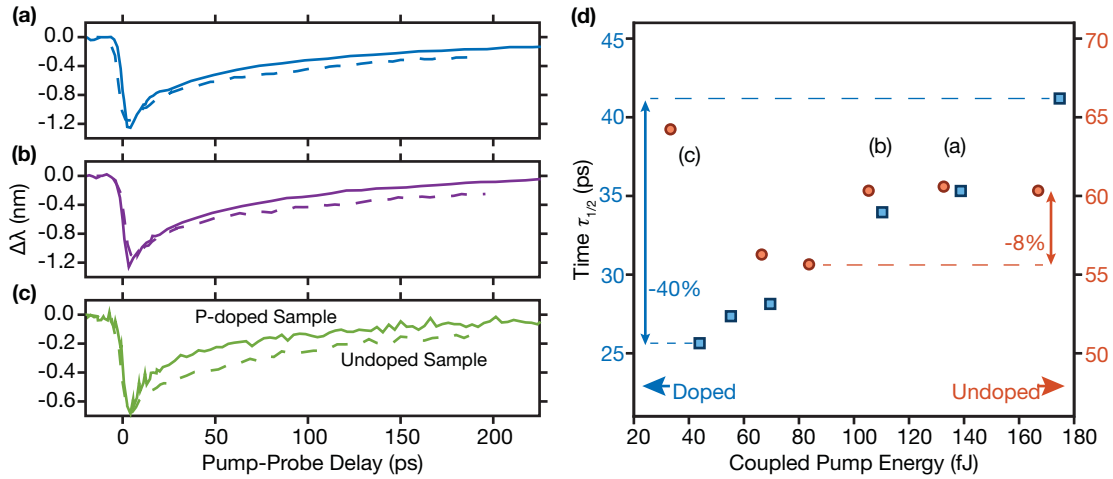


**Fig. 4-32** | Decay of the spectral shift, p-doped device (solid line) and undoped device used as a reference (dashed line). Panels (a), (b) and (c) relate to increasing coupled pump pulse energies: 130 fJ, 110 fJ and 40 fJ respectively. The corresponding excitation energies for the reference sample are 105 fJ, 83 fJ and 33 fJ respectively. Extracted  $\tau_{1/2}$  as a function of the average pump power for the doped (squares) and the undoped (circles) samples (d).

the responses of the two devices are expected to be comparable, which is what is observed in Fig. 4-32(a).

As the injection level is decreased (Figs. 4-32(b) and 4-32(c)), the doped sample shows an increasingly faster recovery. More precisely, the initial decay, associated to diffusion, is faster and stronger, meaning that the carrier density has decreased to a much lower level than the undoped sample. This behavior is also apparent when considering the dependence of the fast time scale  $\tau_{1/2}$  on the excitation power (Fig. 4-32(d)), which decreases from 42 ps to 26 ps (hence a decrease about 40%) as the pump excitation decreases from 170 fJ to 40 fJ. In contrast,  $\tau_{1/2} = 60 \text{ ps} \pm 4 \text{ ps}$  in the case of the undoped sample, showing no apparent trend with the injection level, when considering measurement uncertainty. It must be stressed that the energy of the excitation required to induce the same spectral shift is still in the 100 fJ range, which is only slightly larger than in the case of the undoped sample.

The observed behavior is consistent with the picture of the transition from an ambipolar diffusion regime to a diffusion governed by the minority carriers only, which is well-known in semiconductor devices [92]. As photo-generated carriers are generated in pairs, the condition  $N = P$  holds if the carrier density is much larger than the doping level. Under these conditions, the diffusion process is governed by the ambipolar diffusion constant  $D_a = 2(D_n^{-1} + D_p^{-1})^{-1} = 9.6 \text{ cm}^2 \cdot \text{s}^{-1}$ . In the opposite limit of low injection level,  $N \ll P = N_a$ , only the diffusion of minority carriers

matters, here electrons, which is governed by a much larger diffusion constant  $D_n = 130 \text{ cm}^2\text{s}^{-1}$ . This explains the decrease of the fast time constant with the decrease of the injection level.

The further decay of the carrier density is due to surface recombination, dominated by the surface carrier velocity  $S$ . Following the same analysis as for the bulk Shockley-Read-Hall recombination [92], it is found that the surface recombination velocity is faster in the minority carrier ( $S = \sigma_n v_{th} N'_{st}$ ) than in the ambipolar diffusion regime ( $S = \sigma_a v_{th} N_t$ ), where  $\sigma_n$ ,  $\sigma_p$ ,  $N'_{st}$  and  $v_{th}$  are the capture cross sections for electrons and holes, the surface trap density and the thermal velocity respectively and  $\sigma_a^{-1} = \sigma_n^{-1} + \sigma_p^{-1}$ . This tends to contribute to a faster recovery of the equilibrium. At the highest injection level measured here, the doped sample is still faster than the undoped. While a difference in the surface recombination in the two samples cannot be ruled out, because they have been fabricated with different types of equipment, we point out that a difference is still expected by the modeling, as discussed hereafter.

#### 4.5.4 | Modeling of P-Doped All-Optical Gates

The carrier dynamics in the three-dimensional semiconductor nanostructure has been calculated using the drift-diffusion model described in section 3.1

The geometry considered here is a single  $H_0$  cavity and the initial distribution of the carriers is given by  $N(\mathbf{r})|_{t=0} = P(\mathbf{r})|_{t=0} = C|\mathbf{U}(\mathbf{r})|^4$ , corresponding to two-photon absorption (see section 3.2). The calculation is repeated for different injection levels, namely the initial effective density (eq. (4.3)) is varied from  $\approx 1.5 \times 10^{16}$  to  $\approx 1.5 \times 10^{17} \text{ cm}^{-3}$ . The calculated decay of  $N_{eff}$  is shown in Fig. 4-33(a) for the minimum and maximum injection level and suitably rescaled to evidence the difference between the ambipolar and the minority carrier diffusion regime. At high injection level, the decay is very close to the ambipolar limit until it crosses the doping level and goes through the minority carrier regime. At low injection level, the decay is faster, and the equilibrium is reached much earlier.

From this calculation it is possible to extract  $\tau_{1/2}$ , which is plot in Fig. 4-33(b) as a function of the initial effective density  $N_{eff}(0)$ . As expected, and consistently with the measurements,  $\tau_{1/2}$  increases with the injection level  $N_{eff}(0)$  and then saturates when the doping level has been exceeded by about an order of magnitude. This probably explains why in our measurements the doped device was always faster than the undoped, as such larger injection levels haven't been

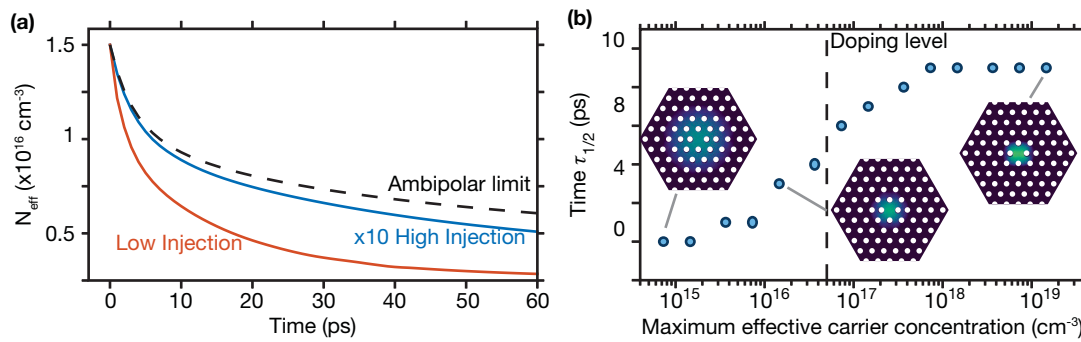


**Fig. 4-33** | (a) Calculated decay of the effective carrier density  $N_{eff}$  for high (blue) and low injection (orange); ambipolar limit corresponding to the undoped device (dashed). – (b) Calculated characteristic time  $\tau_{1/2}$  versus the maximum of the effective carrier density. The dotted line represents the level of p-doping. The distribution of the electrons at  $t = 10 \text{ ps}$  is represented in the insets for different excitation levels.

reached. This behavior is also apparent when considering the spatial distributions of the minority carriers (insets in Fig. 4-33(b)) calculated at a representative time delay 10 ps. It is apparent that electrons have diffused much farther at low injection, which translates into a faster decrease of their effective carrier concentration (i.e. in the center of the cavity). This is in substantial agreement with our measurements and therefore supports the main point of this work, namely that the carrier recovery can be improved by operating the nonlinear optical gate in the minority carrier diffusion regime.

## 4.6 | Conclusion

In this chapter, it is demonstrated efficient and fast all-optical switch made on InP, surface passivated GaAs and P-doped InP.

First, using InP, all optical switch characterization using spectrally and temporally resolved pump-probe is proceeded, enabling to effectively characterized the instantaneous frequency shift of the all-optical gate. Using the previously described new CMT model, a striking match with the experiment is demonstrated leading to a surface recombination characterization of  $10^3 \text{ cm}^{-1}$ . Following, signal processing experiments are done, enabling to demonstrate wavelength conversion with a repetition rate up to 10 GHz, and sampling and frequency down conversion with a repetition rate up to 12 GHz with a remarkable linearity regarding input RF power.

Then, to improve the switching speed, which limits the repetition rate to about 10 GHz with InP, GaAs photonic crystal cavities are studied. To improve the carrier lifetime, which is too short

on this unpassivated material avoiding carrier concentration to build up and efficiently shift the resonance wavelength, ALD passivation using  $\text{Al}_2\text{O}_3$  is performed. This decreases by orders of magnitude the surface recombination and modifies the effective carrier lifetime from about 1 ps to 10 ps. This value is found thanks to the accuracy of the CMT modeling. It gives the all-optical gate a resolution of 10 ps, proven by efficiently processing a burst of four input pulses emulating a repetition rate of 100 GHz. Given this, it is then demonstrated for the first time on GaAs photonic crystal signal processing up to 5 GHz repetition rate.

Finally, in the same perspective of improving the switching speed of all-optical gate, engineering on the carrier dynamics is studied through P-doped InP photonic crystal. By changing the power level of the optical pump, two different carrier diffusion regimes, governing the relaxation dynamics of the device, have been evidenced. An approximately two-fold acceleration of the recovery dynamics has been observed, which has important practical implications, namely the possibility to operate with data signals at 20 Gb/s without any appreciable increase in the energy budget, compared to the slower undoped device. The observed dynamics is well reproduced by a 3D drift-diffusion model taking into account the complex geometry of the device accurately. Importantly, the doping level can be optimized relative to the desired injection level (hence spectral shift)

## References for Chapter 4 – All-Optical Signal Processing

- [10] H. Taylor. *An optical analog-to-digital converter - Design and analysis*. IEEE J. Quantum Electron. **15** (1979). – pp. 10, 94.
- [11] Y. Tsunoda and J. W. Goodman. *Combined optical AD conversion and page composition for holographic memory applications*. Appl. Opt. **16** (1977). – pp. 10, 94.
- [44] Z. Zhang and M. Qiu. *Small-volume waveguide-section high Q microcavities in 2D photonic crystal slabs*. Opt. Exp. **12** (2004). – pp. 16, 65, 72, 85, 115.
- [46] E. Yüce, G. Ctistis, J. Claudon, E. Dupuy, R. D. Buijs, B. de Ronde, A. P. Mosk, J.-M. Gérard, and W. L. Vos. *All-optical switching of a microcavity repeated at terahertz rates*. Opt. Lett. **38** (2013). – pp. 17, 21, 112.
- [57] T. Tanabe, M. Notomi, S. Mitsugi, A. Shinya, and E. Kuramochi. *All-optical switches on a silicon chip realized using photonic crystal nanocavities*. Appl. Phys. Lett. **87** (2005). – pp. 19–21, 68, 86.
- [58] B. R. Bennett, R. A. Soref, and J. A. Del Alamo. *Carrier-induced change in refractive index of InP, GaAs and InGaAsP*. IEEE J. Quantum Electron. **26** (1990). – pp. 19, 67, 75–76, 117.
- [59] M. Heuck, S. Combrié, G. Lehoucq, S. Malaguti, G. Bellanca, S. Trillo, P. T. Kristensen, J. Mork, J. P. Reithmaier, and A. de Rossi. *Heterodyne pump probe measurements of nonlinear dynamics in an indium phosphide photonic crystal cavity*. Appl. Phys. Lett. **103** (2013). – pp. 19–20, 68–69, 86, 117.
- [61] T. Tanabe, H. Taniyama, and M. Notomi. *Carrier Diffusion and Recombination in Photonic Crystal Nanocavity Optical Switches*. J. Lightwave Technol. **26** (2008). – pp. 19, 72, 74, 117.
- [62] T. Tanabe, K. Nishiguchi, A. Shinya, E. Kuramochi, H. Inokawa, M. Notomi, K. Yamada, T. Tsuchizawa, T. Watanabe, H. Fukuda, H. Shinojima, and S. Itabashi. *Fast all-optical switching using ion-implanted silicon photonic crystal nanocavities*. Appl. Phys. Lett. **90** (2007). – pp. 20–21, 68, 97.
- [65] C. Husko, A. de Rossi, S. Combrié, Q. V. Tran, F. Raineri, and C. W. Wong. *Ultrafast all-optical modulation in GaAs photonic crystal cavities*. Appl. Phys. Lett. **94** (2009). – pp. 20–21, 68, 72, 98, 107.
- [66] S. Combrié, G. Lehoucq, A. Junay, S. Malaguti, G. Bellanca, S. Trillo, L. Ménager, J. P. Reithmaier, and A. de Rossi. *All-optical signal processing at 10 GHz using a photonic crystal molecule*. Appl. Phys. Lett. **103** (2013). – pp. 20–21, 65, 85–86, 106, 110, 117, 158.
- [68] A. Bazin, K. Lenglé, M. Gay, P. Monnier, L. Bramerie, R. Braive, G. Beaudoin, I. Sagnes, and F. Raineri. *Ultrafast all-optical switching and error-free 10 Gbit/s wavelength conversion in hybrid InP-silicon on insulator nanocavities using surface quantum wells*. Appl. Phys. Lett. **104** (2014). – pp. 20–21, 86, 114.

- [74] M. Waldow, T. Plötzing, M. Gottheil, M. Först, J. Bolten, T. Wahlbrink, and H. Kurz. *25ps all-optical switching in oxygen implanted silicon-on-insulator microring resonator*. Opt. Exp. **16** (2008). – pp. 21, 97.
- [75] G. W. Cong, R. Akimoto, K. Akita, T. Hasama, and H. Ishikawa. *Low-saturation-energy-driven ultrafast all-optical switching operation in (CdS/ZnSe)/BeTe intersubband transition*. Opt. Exp. **15** (2007). – pp. 21, 86.
- [77] R. Akimoto, S. Gozu, T. Mozume, and H. Ishikawa. *Monolithically integrated all-optical gate switch using intersubband transition in InGaAs/AlAsSb coupled double quantum wells*. Opt. Exp. **19** (2011). – pp. 21–22, 86.
- [79] S. Nakamura, Y. Ueno, and K. Tajima. *Femtosecond switching with semiconductor-optical-amplifier-based Symmetric Mach–Zehnder-type all-optical switch*. Appl. Phys. Lett. **78** (2001). – pp. 21, 86.
- [82] R. Bose, J. S. Pelc, S. Vo, C. M. Santori, and R. G. Beausoleil. *Carrier dynamics in GaAs photonic crystal cavities near the material band edge*. Opt. Exp. **23** (2015). – pp. 21, 72, 105.
- [92] S. M. Sze and K. K. Ng. *Physics of Semiconductor Devices*. John Wiley & Sons, Inc., 2006. – pp. 36, 67, 118–119.
- [129] W. Shockley. *Electrons and holes in semiconductors: with applications to transistor electronics*. Van Nostrand, 1950. – pp. 56, 98.
- [130] D. D. Nolte. *Surface recombination, free-carrier saturation, and dangling bonds in InP and GaAs*. Solid-State Electron. **33** (1990). – pp. 56, 68, 72, 88, 98, 106.
- [140] A. D. Bristow, J. P. R. Wells, W. H. Fan, A. M. Fox, M. S. Skolnick, D. M. Whittaker, A. Tahraoui, T. F. Krauss, and J. S. Roberts. *Ultrafast nonlinear response of AlGaAs two-dimensional photonic crystal waveguides*. Appl. Phys. Lett. **83** (2003). – pp. 72, 86, 97.
- [145] F. Raineri, C. Cojocaru, P. Monnier, A. Levenson, R. Raj, C. Seassal, X. Letartre, and P. Viktorovitch. *Ultrafast dynamics of the third-order nonlinear response in a two-dimensional InP-based photonic crystal*. Appl. Phys. Lett. **85** (2004). – p. 86.
- [146] Q. V. Tran, S. Combrié, P. Colman, and A. de Rossi. *Photonic crystal membrane waveguides with low insertion losses*. Appl. Phys. Lett. **95** (2009). – pp. 87, 100.
- [147] J. B. Khurgin. *Photonic Microresonator Research and Applications*. "Performance of Single and Coupled Microresonators in Photonic Switching Schemes", pp. 227–251. Photonic Microresonator Research and Applications, 2010. – pp. 89, 113.
- [148] A. J. Benedick, J. G. Fujimoto, and F. X. Kärtner. *Optical flywheels with attosecond jitter*. Nature Photon. **6** (2012). – p. 94.

- [149] F. Cadiz, D. Paget, A. C. H. Rowe, V. L. Berkovits, V. P. Ulin, S. Arscott, and E. Peytavit. *Surface recombination in doped semiconductors: Effect of light excitation power and of surface passivation*. J. Appl. Phys **114** (2013). – pp. 98, 109.
- [150] L. Jastrzebski, H. C. Gatos, and J. Lagowski. *Observation of surface recombination variations in GaAs surfaces*. J. Appl. Phys **48** (1977). – p. 101.
- [151] E. Yablonovitch, B. J. Skromme, R. Bhat, J. P. Harbison, and T. J. Gmitter. *Band bending, Fermi level pinning, and surface fixed charge on chemically prepared GaAs surfaces*. Appl. Phys. Lett. **54** (1989). – p. 101.
- [152] E. Yablonovitch, C. J. Sandroff, R. Bhat, and T. Gmitter. *Nearly ideal electronic properties of sulfide coated GaAs surfaces*. Appl. Phys. Lett. **51** (1987). – p. 101.
- [153] R. A. Gottscho, B. L. Preppernau, S. J. Pearton, A. B. Emerson, and K. P. Giapis. *Real-time monitoring of low-temperature hydrogen plasma passivation of GaAs*. J. Appl. Phys **68** (1990). – p. 101.
- [154] L. J. Brillson, M. L. Slade, R. E. Viturro, M. K. Kelly, N. Tache, G. Margaritondo, J. M. Woodall, P. D. Kirchner, G. D. Pettit, and S. L. Wright. *Absence of Fermi level pinning at metal-In<sub>x</sub>Ga<sub>1-x</sub>As(100) interfaces*. Appl. Phys. Lett. **48** (1986). – p. 101.
- [155] M. M. Frank, G. D. Wilk, D. Starodub, T. Gustafsson, E. Garfunkel, Y. J. Chabal, J. Grazul, and D. A. Muller. *HfO<sub>2</sub> and Al<sub>2</sub>O<sub>3</sub> gate dielectrics on GaAs grown by atomic layer deposition*. Appl. Phys. Lett. **86** (2005). – pp. 101, 106–107.
- [156] H. Hasegawa, M. Akazawa, A. Domanowska, and B. Adamowicz. *Surface passivation of III–V semiconductors for future CMOS devices—Past research, present status and key issues for future*. Appl. Surf. Sci. **256** (2010). – p. 101.
- [157] X. Yang, C. J. Chen, C. A. Husko, and C. W. Wong. *Digital resonance tuning of high-Q/V[<sub>sub</sub> m] silicon photonic crystal nanocavities by atomic layer deposition*. Appl. Phys. Lett. **91** (2007). – p. 103.
- [158] M. Gehl, R. Gibson, J. Hendrickson, A. Homyk, A. Säynätjoki, T. Alasaarela, L. Karvonen, A. Tervonen, S. Honkanen, S. Zandbergen, B. C. Richards, J. D. Olitzky, A. Scherer, G. Khitrova, H. M. Gibbs, J.-Y. Kim, and Y.-H. Lee. *Effect of atomic layer deposition on the quality factor of silicon nanobeam cavities*. J. Opt. Soc. Am. B **29** (2012). – p. 103.
- [159] T. Aoki, N. Fukuhara, T. Osada, H. Sazawa, M. Hata, and T. Inoue. *Nitride passivation reduces interfacial traps in atomic-layer-deposited Al<sub>2</sub>O<sub>3</sub>/GaAs (001) metal-oxide-semiconductor capacitors using atmospheric metal-organic chemical vapor deposition*. Appl. Phys. Lett. **105** (2014). – p. 106.
- [160] P. D. Ye. *Main determinants for III–V metal-oxide-semiconductor field-effect transistors (invited)*. J. Vac. Sci. Technol. A **26** (2008). – p. 106.

- [161] N. Razek, K. Otte, T. Chassé, D. Hirsch, A. Schindler, F. Frost, and B. Rauschenbach. *GaAs surface cleaning by low energy hydrogen ion beam treatment*. J. Vac. Sci. Technol. A **20** (2002). – p. 106.
- [162] P. Kordoš, R. Kúdela, R. Stoklas, K. Čičo, M. Mikulics, D. Gregušová, and J. Novák. *Aluminum oxide as passivation and gate insulator in GaAs-based field-effect transistors prepared in situ by metal-organic vapor deposition*. Appl. Phys. Lett. **100** (2012). – p. 106.
- [163] C.-W. Cheng, G. Apostolopoulos, and E. A. Fitzgerald. *The effect of interface processing on the distribution of interfacial defect states and the C-V characteristics of III-V metal-oxide-semiconductor field effect transistors*. J. Appl. Phys **109** (2011). – p. 106.
- [164] H. S. Lee, S. Kiravittaya, S. Kumar, J. D. Plumhof, L. Balet, L. H. Li, M. Francardi, A. Gerardo, A. Fiore, A. Rastelli, and O. G. Schmidt. *Local tuning of photonic crystal nanocavity modes by laser-assisted oxidation*. Appl. Phys. Lett. **95** (2009). – p. 106.
- [165] S. Kiravittaya, H. S. Lee, L. Balet, L. H. Li, M. Francardi, A. Gerardo, A. Fiore, A. Rastelli, and O. G. Schmidt. *Tuning optical modes in slab photonic crystal by atomic layer deposition and laser-assisted oxidation*. J. Appl. Phys **109** (2011). – p. 107.
- [166] P. T. Chen, Y. Sun, E. Kim, P. C. McIntyre, W. Tsai, M. Garner, P. Pianetta, Y. Nishi, and C. O. Chui. *HfO<sub>2</sub> gate dielectric on (NH<sub>4</sub>)<sub>2</sub>S passivated (100) GaAs grown by atomic layer deposition*. J. Appl. Phys **103** (2008). – p. 107.
- [167] L. Ye and T. Gougousi. *In situ infrared spectroscopy study of the interface self-cleaning during the atomic layer deposition of HfO<sub>2</sub> on GaAs(100) surfaces*. Appl. Phys. Lett. **105** (2014). – p. 107.
- [168] J. C. Hackley, J. D. Demaree, and T. Gougousi. *Interface of atomic layer deposited HfO<sub>2</sub> films on GaAs (100) surfaces*. Appl. Phys. Lett. **92** (2008). – p. 107.
- [169] R. Suri, D. J. Lichtenwalner, and V. Misra. *Interfacial self cleaning during atomic layer deposition and annealing of HfO<sub>2</sub> films on native (100)-GaAs substrates*. Appl. Phys. Lett. **96** (2010). – pp. 107–108.
- [170] M.-G. Kang, S.-H. Sa, H.-H. Park, K.-S. Suh, and K.-H. Oh. *The characterization of etched GaAs surface with HCl or H<sub>3</sub>PO<sub>4</sub> solutions*. Thin Solid Films **308-309** (1997). – p. 109.
- [171] Z. Han, G. Moille, X. Checoury, J. Bourderionnet, P. Boucaud, A. de Rossi, and S. Combrié. *High-performance and power-efficient 2×2 optical switch on Silicon-on-Insulator*. Opt. Exp. **23** (2015). – p. 111.
- [172] S. Sokolov, J. Lian, E. Yüce, S. Combrié, G. Lehoucq, A. de Rossi, and A. P. Mosk. *Local thermal resonance control of GaInP photonic crystal membrane cavities using ambient gas cooling*. Appl. Phys. Lett. **106** (2015). – p. 111.
- [173] Y. Yu, W. Xue, H. Hu, L. Oxenloewe, K. Yvind, and J. Moerk. *All-optical switching improvement using photonic-crystal Fano structures*. IEEE Photonics Journal (2016). – p. 114.

- [174] V. Cesari, W. Langbein, P. Borri, M. Rossetti, A. Fiore, S. Mikhlin, I. Krestnikov, and A. Kovsh. *Ultrafast gain dynamics in 1.3  $\mu\text{m}$  InAs/GaAs quantum-dot optical amplifiers: The effect of p doping*. Appl. Phys. Lett. **90** (2007). – p. 114.
- [175] T. Ishibashi, S. Kodama, N. Shimizu, and T. Furuta. *High-Speed Response of Uni-Traveling-Carrier Photodiodes*. Jpn. J. Appl. Phys. **36** (1997). – p. 114.
- [176] K. Kato. *Ultrawide-band/high-frequency photodetectors*. IEEE Trans. Microwave Theory Techn. **47** (1999). – p. 114.
- [177] L. Shen, Y. Jiao, W. Yao, Z. Cao, J. P. van Engelen, G. Roelkens, M. K. Smit, and J. J. G. M. van der Tol. *High-bandwidth uni-traveling carrier waveguide photodetector on an InP-membrane-on-silicon platform*. Opt. Exp. **24** (2016). – p. 114.
- [178] G. Moille, S. Combrié, and A. de Rossi. *Modeling of the carrier dynamics in nonlinear semiconductor nanoscale resonators*. Phys. Rev. A **94** (2016). – pp. 117, 158.

# Chapter 5

## Photo-conductives Switches at Telecom Wavelength

---

---

In this chapter it is discussed the electro-optic sampling system. The optical design, targeting telecom wavelength optical clock, and the integration with MW previously optimized design for photoconductive is explained. First, it is discussed the different types of approaches studied during this thesis to implement such device, including on-top illumination and in-plane optical injection. In a second part, the characterization of the resonant photo-conductive switch is described with first basic optical and electrical measurements to ensure that the fabrication and the design were well performed. Then, signal processing operations with direct signal sampling and frequency-down conversion are further discussed. Finally, improvement regarding the signal processing efficiency of the devices is addressed where the collection area is brought closer to the optical mode using implantation doping.

### Contents

---

5.1	Sample Design . . . . .	129
5.1.1	Optical Design . . . . .	130
5.1.2	Microwave Design . . . . .	138
5.1.3	Integration of Microwave Lines with Optical Resonator . . . . .	139
5.2	Results and Discussions . . . . .	141
5.2.1	Sample Basic Characterizations . . . . .	141
5.2.2	Microwave Characterization . . . . .	142
5.2.3	Signal Processing Operations . . . . .	149
5.3	Perspectives . . . . .	151
5.4	Conclusion . . . . .	153
	References for Chapter 5 . . . . .	155

---



The sample stack structure used to realize the photoswitch consists in a 250 nm GaAs layer bonded to a Si wafer following the process depicted in section 2.2. Without any surface treatment, the carrier lifetime is very short due to strong surface recombination. As demonstrated in section 4.3, ALD- $\text{Al}_2\text{O}_3$  surface coating is an effective way to control and to increase the effective carrier lifetime in a GaAs air-suspended membrane. Thus, ALD- $\text{Al}_2\text{O}_3$  surface coating has been added to the bonding process flow. A first ALD deposition is performed before wafer bonding and a second at the very end of the fabrication for the PhC device. This results in the structure shown in Fig. 5-1(a).

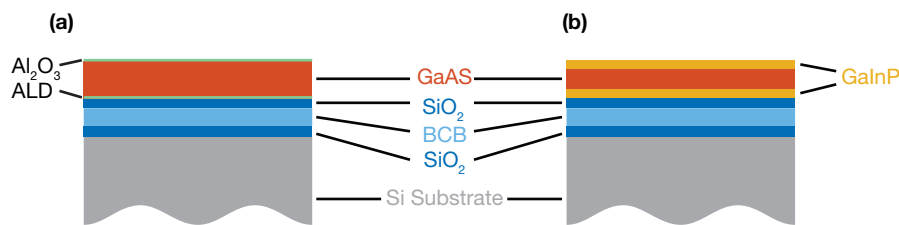


**Fig. 5-1** | Sample stack structures (a) targeted structure with fully ALD-coated surfaces for carrier lifetime control – (b) Test structure with GaInP barriers preventing top and bottom surface recombinations.

## 5.1 | Sample Design

However, these additional deposition steps bring further complexity to the process flow and imply some extra delays (the ALD process not being performed at Thales but at IEMN). Hence a structure leading to fewer process steps was first considered, where the carrier lifetime would still be improved compared to bare GaAs membrane. This device consists of a slab of GaAs surrounded by two layers of GaInP (Fig. 5-1(b)). Thanks to the large band-gap energy mismatch between those two materials (1.43 eV for GaAs and 1.89 eV for GaInP), carriers are pushed away from surfaces. Thus recombinations occur only on the edges of the PhC holes which increases the effective lifetime compared to bare GaAs slab. For the sake of simplicity, the total height of the slab remains the same as GaAs ALD coated sample, allowing to keep the same design. The height of each GaInP barrier is 10 nm, while the GaAs is 230 nm thick. The volume where carriers are photogenerated is slightly lower (TPA being only effective in the GaAs) but it has a minor impact on the total amount of photo-generated carriers (below 10 % variation for the carrier generation).

## 5.1.1 | Optical Design

### 5.1.1.1 | Vertical Optical Injection

The most straightforward approach to excite photoconductive switches that are based on direct absorption has been to light them directly from the top with a beam providing a quasi-uniform illumination over the MW gap.

In the resonant approach and more specifically when TPA is considered, carriers are generated in a tiny volume corresponding to the maxima of the optical electric field. This has two consequences: first, carriers have to diffuse and reach the metal to turn the MW gap conductive, thus leading to complex dynamical response. Secondly, the saturation of the photo-generation, a large modal volume should be preferable as it would maximize the net amount of carriers, therefore improving the ON state of the photoconductive switch.

However, PhC cavities presented previously in chapter 4 are small (indeed, the tiniest in dielectric resonator) and therefore are not well suited for such electro-optic applications. Nonetheless, thanks to the photonic band-gap properties of PhC, delocalized states with high optical density of states appear near the band-edge in certain directions. Indeed, the optical band diagram of PhC with a triangular lattice exhibits in the  $\mathbf{K}$  direction (Figs. 5-2(a) and 5-2(b)) a null gradient (Fig. 5-2(c)), and therefore the light group velocity vanishes. Moreover, the density of states near a band edge diverges [38].

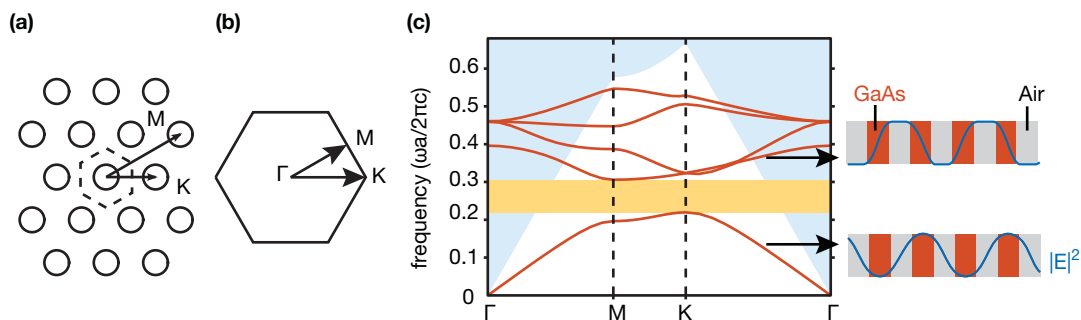


**Fig. 5-2** | (a) Photonic crystal with in dashed the first Brillouin zone – (b) Reciprocal space of the first Brillouin zone with the main directions  $\Gamma$ ,  $M$  and  $K$  – (c) Band diagram of first 5 bands of the photonic crystal, with the light cone in blue and the band gap in yellow. Schematic of the electric field for the first substrate band (bottom) and the first air band (top).

Given this, the delocalized mode in the  $\mathbf{K}$  direction, so-called *edge mode*, exhibits both a confinement of the light in the structure as light does not propagate, and an exaltation of the optical

field thank to the high density of states, making non-linear interaction such as TPA efficient. In addition, the edge mode is in a valence band mode (Fig. 5-2(c)), meaning that most of the electric field is present in the semiconductor and not the air, which is preferable for carrier generation.

In practical cases, the PhC has a finite size and moreover would have to be confined in the MW gap. In order to confine the edge mode, the PhC is surrounded by a PhC with smaller holes (*i.e.* the outer PhC) (Fig. 5-3(a)). Therefore, the delocalized mode is in the band-gap of the outer PhC and is confined in the inner PhC [179]. To increase the confinement of the mode, an apodization of the hole radius of the outer PhC is applied and has been calculated through analytic prolongation of the band diagram in the  $\mathbf{K}$  direction. Therefore, the outer PhC hole radius follows an exponential decay rate following  $r(x) = r_0 \exp\left(\frac{x}{\tau}\right) + r_1$ , where  $r_0$  is the inner PhC hole radius ( $r_0 = 0.22$ ),  $x$  being the axis along the  $\mathbf{K}$  directions normalized to the PhC period,  $r_1$  is the targeted outer PhC hole radius ( $r_1 = 0.17$ ).  $\tau$  is the apodization decay rate and an optimum value of  $\tau = 8$  has been found for both high  $Q$ -factor and good confinement of the optical mode, in order to bring as close as possible the metallic contacts.

Obviously, the bigger the cavity is, the closer the structure approaches the theoretical case described above. For a cavity size of  $19a$  (Fig. 5-3(b)), the calculated  $Q$ -factor given by FDTD modeling is about 50 000. Interestingly, as the localization of the mode in the reciprocal space is far away from the light cone (Fig. 5-3(c)), such design is highly robust, and even if the sample is bonded on silica (leading to a wider light cone) no further losses appear .

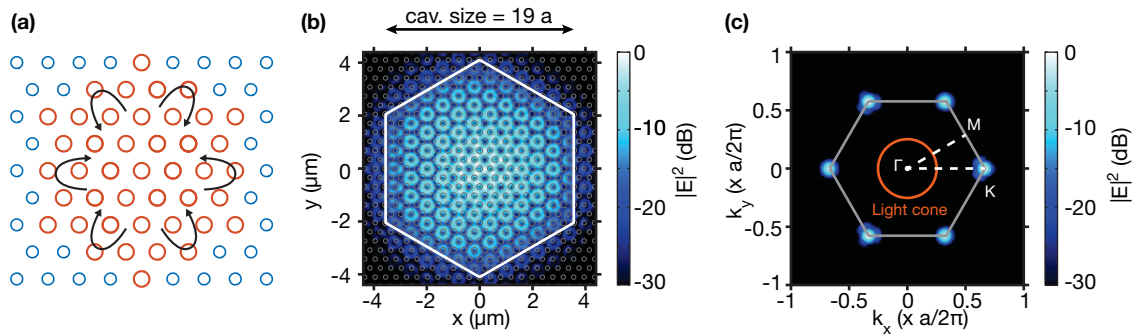


**Fig. 5-3** | (a) Principle of the cavity based on an edge mode (red zone) confined by an outside smaller hole PhC (blue zone) – (b) FDTD modeling of the optical mode for a cavity size of  $19a$  providing a  $Q$ -factor of about 50 000 – (c) Optical mode in the reciprocal space.

As previously pointed out, among all the design for photoconductive switches, most of them consist of the semiconductor, placed in the microwave strip-line gap, illuminated from the top [31, 180–184], following the first ever made experiment [9] of photoconductive switches.

From Fig. 5-3(c), it is obvious that the in-plane confinement of the edge-mode is highly efficient as no electric field component appears around the  $\Gamma$  direction (standing for orthogonal radiation relative to the slab) or even in the light cone. Thus, if no leak occurs in the light cone, coupling from top appears to be highly inefficient. However, this issue can be overcome through *band folding* technique consisting of the modulation of the PhC hole radius with a different periodicity than the PhC [185].

The role of this modulation is apparent in the reciprocal space [186]. As the  $\Gamma$  direction stands for vertical emission, the mode maxima have to be folded to this point. Adding a modulation in a particular direction to the PhC corresponds, in the reciprocal space, of creating an “axis of symmetry” perpendicular to this direction. Thus, folding is induced relative to this axis (Fig. 5-4(a)). Choosing wisely this axis to stand in between  $\Gamma$  and  $\mathbf{K}$  allows an effective vertical extraction of the light. Repeating this step for every  $\mathbf{K}$  points of the first Brillouin zone results in the super-period Brillouin zone of the modulation (Fig. 5-4(a), in red) defined by the vector  $\mathbf{b}'_1$  and  $\mathbf{b}'_2$ . The strength of the extraction is then controlled by the amplitude of the hole radius modulation applied to the PhC

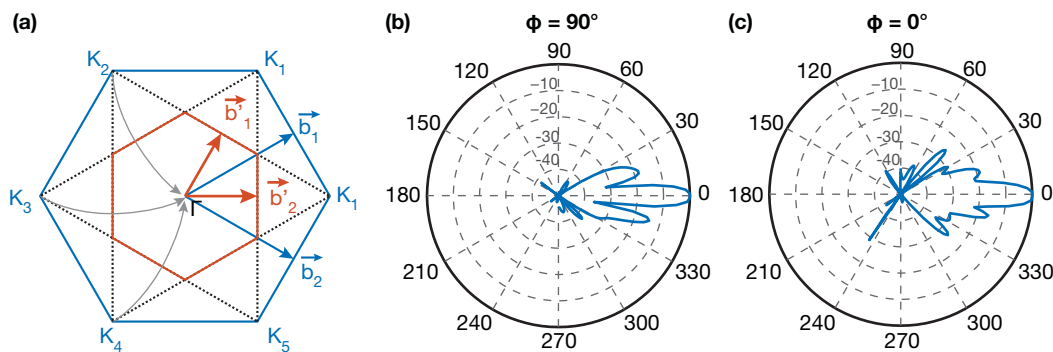


**Fig. 5-4** | (a) Band folding principle where a smaller Brillouin zone (red) provides a symmetry axis between the point  $\mathbf{K}_i$  and  $\Gamma$ . Folding of point  $\mathbf{K}_2$ ,  $\mathbf{K}_3$  and  $\mathbf{K}_4$  are provided while all the  $\mathbf{K}$  point are folded in the  $\Gamma$  direction. – (b) Far field modeling done by FDTD for  $\Phi = 90^\circ$  (i.e.  $xz$  plane). – (c) Far field modeling for  $\Phi = 0^\circ$  (i.e.  $yz$  plane).

Modeling of the far-field emission of the cavity with this extractor gives a well defined normal light emission (Figs. 5-4(a) and 5-4(b)).

Samples following this design have been made on self-suspended GaAs membrane (for the sake of simplicity) and had been characterized (Fig. 5-6) using a cross-polarized setup as in ref. [187] (Fig. 5-5), where light is injected from top with a polarization at  $45^\circ$  from the mode polarization, and a cross-polarized signal is detected, removing efficiently the direct reflection.

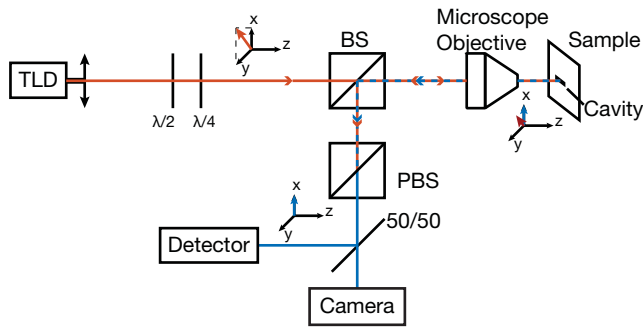


**Fig. 5-5** | Cross polarized setup for resonance characterization of edge-mode cavities. TLD: Tunable Laser Diode, BS; Beam Splitter (50/50), PBS: Polarized Beam Splitter

The resonances found experimentally exhibit a quality factor of about  $Q = 53\,000$  and are extremely close to calculations (Fig. 5-6). Hole radii have been varied in the sample to tune the resonance wavelength. This experimental resonance wavelength variation is in good agreement with the model (Fig. 5-6). Moreover, two modes can be distinguished in modeling, which are clearly seen experimentally (Fig. 5-6).

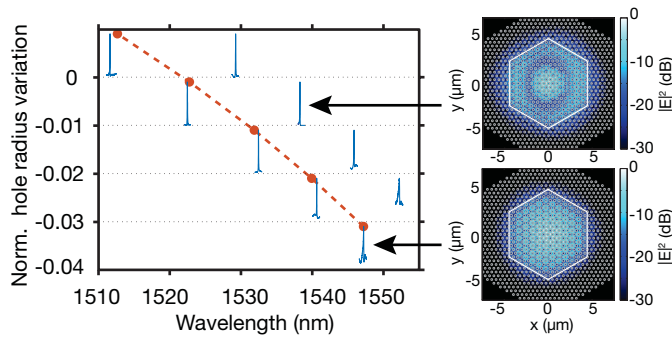


**Fig. 5-6** | Edge mode structure characterization, for different holes size variation. The corresponding modes calculated by FDTD is represented. The red circles corresponds to the mode frequency found in simulation

However, significant drawbacks appear here using this top lighting approach with *edge-mode* cavities. First, this type of cavities has a relatively narrow radiative emission through band-folding technique, making the input coupling difficult as the angle precision is highly demanding. Using  $L_x$  cavity would provide certainly a better tolerance angle [185]. Thus, samples, where a waveguide has been coupled to a  $L_5$  cavity with an extractor (Fig. 5-7) and excited from the top, have been characterized. However, the experimental results only exhibit a total transmission of maximum 1% from the input top laser to the end of the output port. Transmission in the other direction, *i.e.* input coupling to the waveguide and collection vertically to the sample, leads to an efficient transmission of 10% to 20%. This order of magnitude difference is surely due to the mode profile of the input light has to match the light extraction profile to efficiently couple light to the cavity. Thus, if no spatial beam shaping is done, the optical mode mismatch leads to the high losses observed.

Therefore, with just a basic top light lighting with a laser, the optical power would need to be

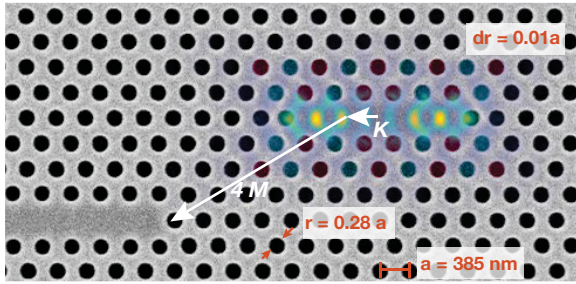


Fig. 5-7 | SEM image of the  $L_5$  cavity with extractor (colored hole) with superimposed the optical mode. A waveguide is coupled to the cavity acting as input or output port depending on the excitation (through waveguide of from top)

greater than by in-plane injection through waveguides to efficiently photo-generate carriers. Also, if beam shaping engineering is involved for exciting the photoconductive switch, this reduce the possibility of integration, compared to direct in plane injection, as top lenses would be needed. Thus, for the photo-conductive switch application, such approach was left behind due to the lack of control of the input coupled power and the direction of in-plane optical injection through waveguide coupled to the cavity was considered.

### 5.1.1.2 | In Plane Optical Injection

Two aspects have to be considered here for the optical design of the cavity. The first one is the fact that the structure being bonded on top of a silica cladding, the light cone is wider, leading to a less efficient vertical confinement. Therefore, high  $Q$ -factor could be more complicated to reach with cavity design for self-suspended membrane. The second point is that this application aims to generate a large net amount of carriers, which means that the effective volume of the carrier generation needs to be high enough to reduce the resistance of the III-V material effectively. This leads to a trade-off between carrier density generation ( $\propto Q/V$ ) and the modal volume. At this point, we can already say that  $H_0$  cavities, as used in chapter 4, might not be the best candidate as they provide the smallest volume for dielectric based cavities.

Cavities based on the width modulation of a cut-off PhC waveguide [41] have been reported to achieve large  $Q$ -factor on silicon-on-insulator [43], and had already been used for electro-optic applications [188].

The design used here consists of PhC with a period  $a = 395$  nm and a hole radius of  $r = 0.26a$ . The waveguide has a width  $W = 0.98W_1$  where  $W_1$  is the width of a waveguide with one row of missing hole (*i.e.*  $W_1 = \sqrt{3}a$ ). This makes the targeted wavelength (*i.e.* resonance wavelength of the cavity) above the transmission band of the waveguide, thus this wavelength is not guided.

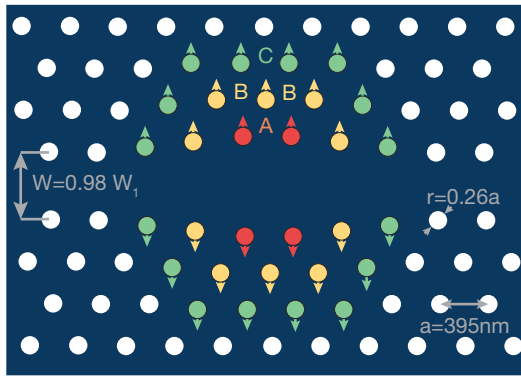


**Fig. 5-8** | Schematic of the cavity. The period used in this design is  $a = 395$  nm, the waveguide made from a one missing row of hole ( $W_1$  waveguide), shrunk such that the width is  $W = 0.98W_1$ . The displacement of the highlighted holes are  $A = 0.0196a$ ,  $B = \frac{2}{3}0.0196a$  and  $C = \frac{1}{3}0.0196a$ .

Several holes are shifted accordingly with Fig. 5-8, where the displacement  $A = a \times ds \times \sqrt{3}/2$ ,  $B = a \times ds \times \sqrt{3}/3$  and  $C = a \times ds \times \sqrt{3}/6$  [41] where  $ds = 0.017$ . It creates a defect in the waveguide, thus the cavity. This values were found by simulation in order to achieve a high intrinsic  $Q$ -factor

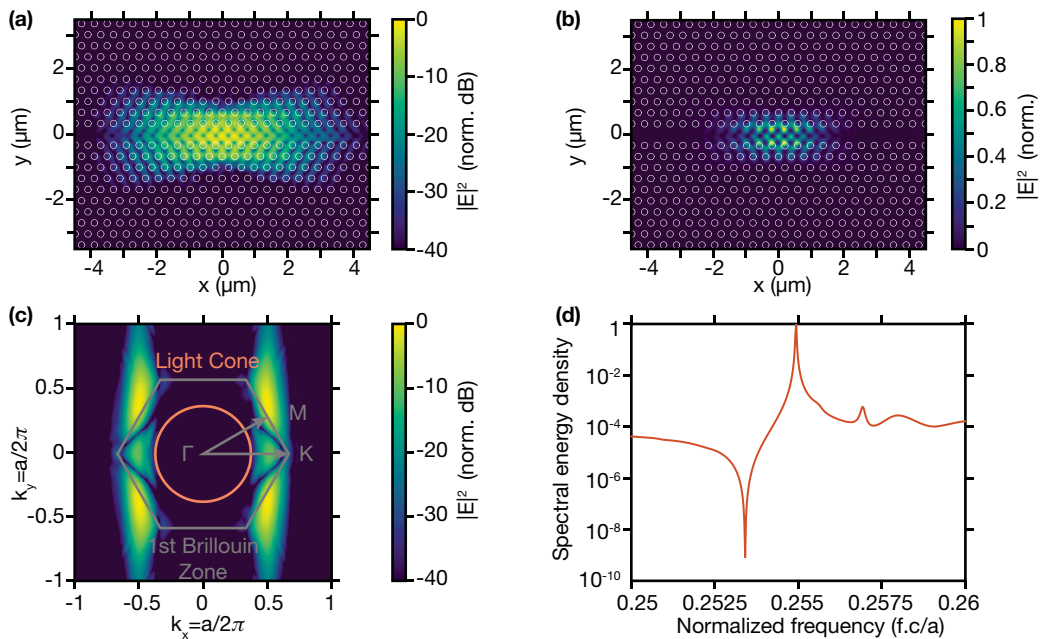


**Fig. 5-9** | FDTD calculation : (a) Square of the electric field spatial mode (logarithm scale) – (b) linear scale – (c) reciprocal space distribution of the electric mode – (d) resonance at  $f_0 = 0.254929 \times c/a \Leftrightarrow \lambda_0 = 1549\text{nm}$  with a quality factor of  $Q = 13\,820$ .

FDTD calculations were performed to compute the spatial mode profile and the  $Q$  factor (Fig. 5-9). From Figs. 5-9(a) and 5-9(b), the spatial mode shows a well confined profile, especially in the transverse direction of the cavity where metal will be placed. The mode profile in the reciprocal space provides a good estimation that out-of-plane losses remain low, as most of the mode is outside

the light cone (Fig. 5-9(c)). Finally, the mode resonance appears at the desired wavelength, about 1550 nm (Fig. 5-9(d)), and the intrinsic  $Q$ -factor is high enough for the targeted application (about  $Q = 1.4 \times 10^5$ ).

### 5.1.1.3 | Waveguide Design

The cavity considered here is based on a PhC waveguide of width  $0.98 \times W_1$ , working below the frequency cut-off (*i.e.* the working wavelength is above the transmission band of the waveguide), that is locally enlarged to localize the photons. Following the same concept, by expanding the waveguide up to  $1.1 \times W_1$ , few rows away from the cavity, an access waveguide can be added close to the cavity (Fig. 5-10).

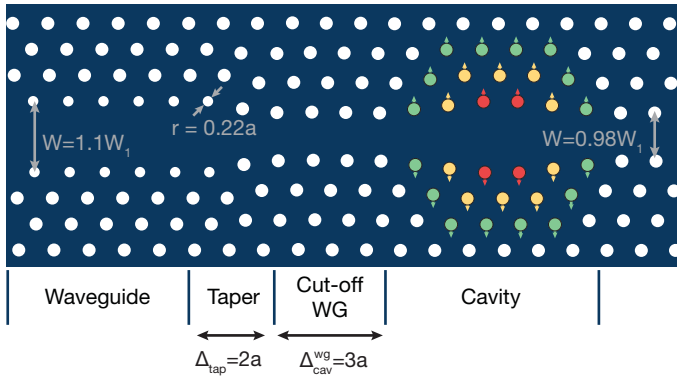


**Fig. 5-10** | Schematic of the cavity with the in-line input waveguide made by stretching the waveguide.  $\Delta_{cav}^{wg}$  is the distance between the end of the coupled waveguide with the cavity.  $\Delta_{tap}$  is the length of the mode adapter of the input waveguide

The distance between the cavity and the input waveguide,  $\Delta_{cav}^{wg}$ , control the mutual coupling strength, thus changing the loaded  $Q$ -factor accordingly. Here, as we want to inject  $ps$  pulses, the loaded quality factor should be around 1000. To enhance the light coupling between the waveguide and the cavity, a taper is made to provide a transition of length  $\Delta_{tap}$  between fast and slow light regime to efficiently inject light into the cavity.

FDTD periodic modelings were performed to determine the parameters for both the input waveguide and the taper. Using a waveguide width of  $W = 1.1 \cdot W_1$  and by increasing the hole size to  $r = 0.28a$  (Fig. 5-11(a)) this allows the waveguide to be under the light cone at the frequency resonance of the cavity, with a relatively low group index of  $n_g = 5.5$  (Fig. 5-11(b)). Using slightly narrower waveguide for the end of the taper results in a real increase in the group index (Fig. 5-11(b)), providing a better light injection to the cavity. However, these parameters lead, at the resonance frequency, to components in the light cone (Fig. 5-11(a)). Nevertheless, considering the length of the taper of few PhC period, the leakage would be negligible.

Non-periodic FDTD simulations using the parameter found previously are performed. This allows us to tune the position of the waveguide to achieve the targeted  $Q$ -factor. The parameters found are a taper length  $\Delta_{tap} = 2a$  and distance between the end of the taper and the beginning of the cavity  $\Delta_{cav}^{wg} = 3a$  (Fig. 5-10, which leads to a loaded  $Q$ -factor of  $Q = 2300$ ).

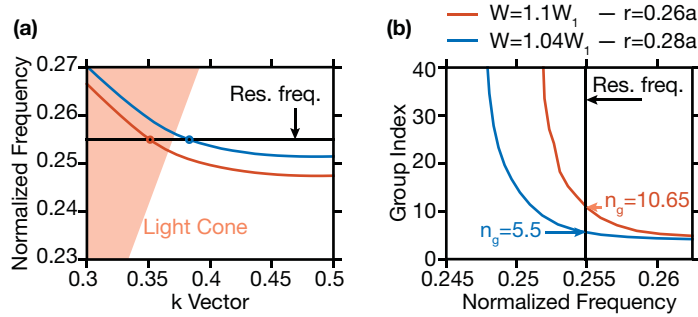


**Fig. 5-11** | (a) Band diagram of the TE mode of the waveguide. The highlighted zone corresponds to the light cone – (b) Group index of the considered TE mode of the waveguide. In all figures, the resonance frequency corresponds to the black line.

#### 5.1.1.4 | Rib Waveguide Design

The input PhC waveguide, coupled to the cavity, being quite short ( $10 \mu\text{m}$ ) an extra waveguide has to be added to bring the light from the sample facet to the PhC structure. It consists of a 250 nm-thick GaAs rib waveguide (Figs. 5-12(a) and 5-12(b)). The width of the waveguide is set to 525 nm to obtain single-mode operation at  $1.5 \mu\text{m}$  for the TE polarization. The mode is well confined as depicted in Fig. 5-12(c) where the module of the y polarization of the magnetic field  $|H_y|$  is represented. Calculations have been performed using a FDFD (Finite Differences in the Frequency Domain) freeware [189]. The realization of such waveguide does not require any extra processing steps as it is defined and etched at the same time as the PhC. Rib waveguide has been preferred because potentially less lossy and much more broadband compare to PhC in particular once bonded on silica. Furthermore, the confinement being less extreme, non-linear absorption and distortion are less severe.

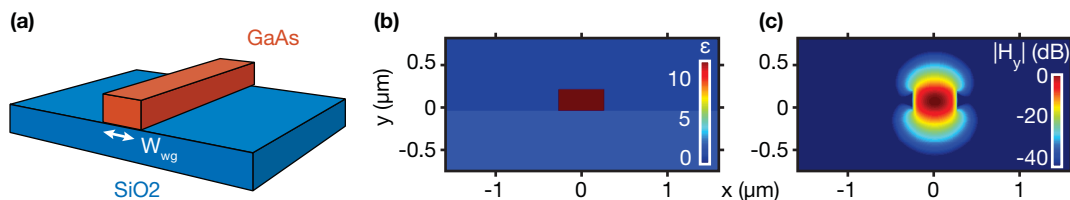


**Fig. 5-12** | (a) Schematic of the rib waveguide structure. Silicon is the bottom cladding material as the sample is bonded on silicon – (b) Mapping of the  $\epsilon$  structure modeled with the FDFD method, with air as top cladding material and silica as bottom cladding material. – (c) Simulation result: mapping of  $|H_y|$  providing a well confined mode in the rib waveguide.

### 5.1.2 | Microwave Design

The first microwave structure of the photoconductive switched considered here is based on coplanar strip-line (Fig. 5-13(a)). This design relies on developments that have been made in the frame of the French ORCHID project. After an initial input section of  $W_{center} = 88 \mu\text{m}$ , which is used to connect the RF-probes, the inner lines are adiabatically narrowed with  $200 \mu\text{m}$ -long tapers. The ground planes, located on both sides, have a constant width of  $W_{gnd} = 500 \mu\text{m}$  over the device and are separated from the inner lines by  $W_{sep} = 60 \mu\text{m}$ . This peculiar configuration allows the inner lines to match in size the RF probe and the cavity. Besides, it performs an impedance matching between the  $50 \Omega$  input (typical impedance of RF cables) and the gap (about  $140 \Omega$ ) impedances. This implies that the carrier generation does not have to reduce the resistance of the gap down to  $50 \Omega$  to provide the best signal transmission. The transmission of such microwave structure is depicted in Fig. 5-13(b) for the OFF state (no lighting) and the ON state ( $10^{24}\text{m}^{-3}$  photo-generated carrier density) leading to a large ON/OFF contrast especially at the low frequency. Electromagnetic modeling of the transmission and reflection parameters using the software HFSS [190] had been performed at Université Pierre et Marie Curie (C. Tripon-Canseliet).

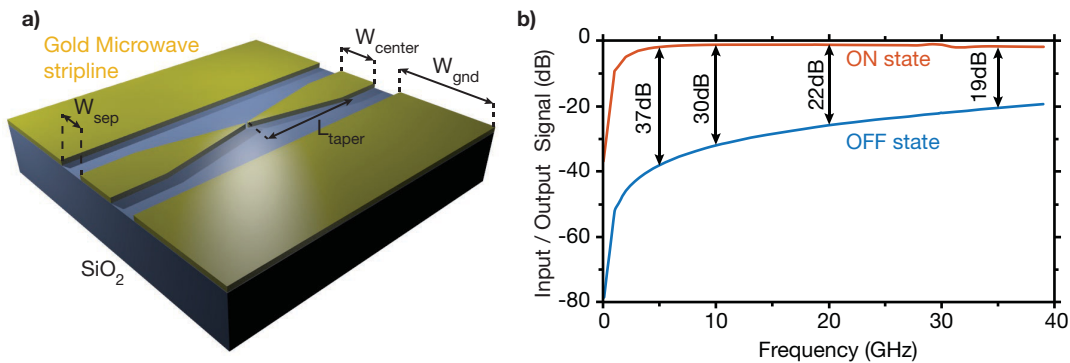


**Fig. 5-13** | (a) Schematic of the design with only one ground pad – (b) Transmission of the microwave tapered strip line with semiconductor discontinuity without lighting (OFF state, blue) and with photo-generation of carrier (ON state, red).

However, such design makes the integration of in-plane optical waveguides more complicated. The first approach would be to create an air bridge allowing the ground plane to pass above the rib waveguide, far enough to prevent optical losses. This requires a much more complex process such as electro-plated deposition, mandatory for a thick metal layer. One can imagine going around the metallic pad using a rib waveguide, but the propagation length becomes large, and

some detrimental effects (pulse distortion through SPM or non-linear absorption) can appear. An alternative solution is to remove one ground pad (Fig. 5-14(a)). To reduce the size of the whole structure and improve the density, if replicated on the sample, the simulated designs undergo a reduction of the ground width to  $200\ \mu\text{m}$ . Such system design still provides a good off state (Fig. 5-14(b)), and even if the ON/OFF ratio is not as good as for the design with two grounds (reduced by about 10 dB), it is sufficient enough in the frame of this thesis to explore the feasibility of such a system.

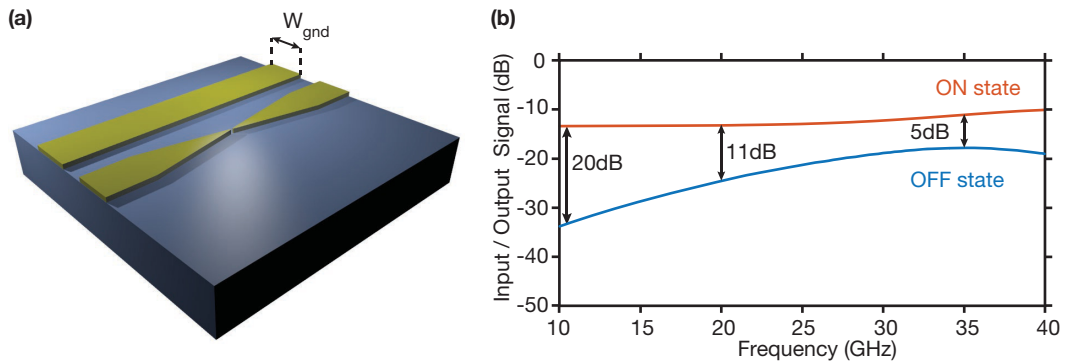


**Fig. 5-14** | (a) Artist's view of the system with two ground pads – (b) ON and OFF electrical transmission spectra modeled with HFSS with a carrier density of  $10^{24}\ \text{m}^{-3}$ .

### 5.1.3 | Integration of Microwave Lines with Optical Resonator

The main issue by combining the MW lines with the optical structure is the overlap between the metallic pad and the optical field of the cavity mode. Indeed, metals at infrared wavelengths introduce losses, which will further decrease the  $Q$ -factor of the cavity. To model this kind of hybrid structure with FDTD method, the mesh has to be highly fine to take into account the skin depth of the metal, of the order of few tenths of nanometers. Over a large structure like this one, it will be highly demanding on computation time. However, adaptive mesh refinement in FDTD would be more suitable for such device. The in-house FDTD software used extensively in this thesis does not provide such feature. Thus, losses introduced by the metallic pad have been modeled using a proprietary software (LUMERICAL), where the metal losses follow a Drude's model and have been performed at the Università di Ferrara (Dr. Gaetano Bellanca).

Four types of simulations have been done, a first one without metallic pad to retrieve the unloaded  $Q$ -factor of the structure (which match the modeled  $Q$ -factor found in section 5.1.1.2), then with three different metal geometries. The width of the and the distance of the metallic pads

from the cavity had been changed (Fig. 5-15) such that  $W = 20a$  and  $D = 2\sqrt{3}a$  from the center of the cavity (structure 1),  $W = 20a$  and  $D = 3\sqrt{3}/2$  (structure 2) and  $W = 15a$  and  $D = 3\sqrt{3}/2$  (structure 3)

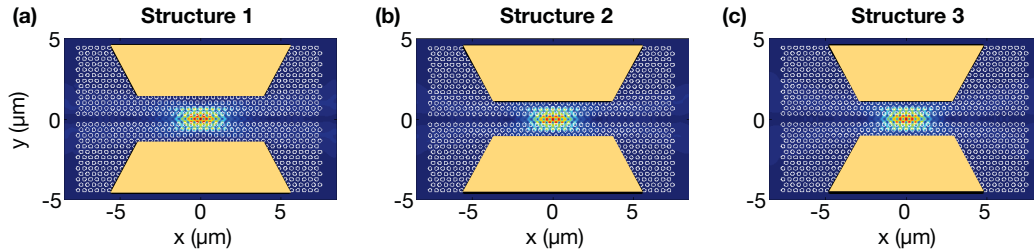


**Fig. 5-15** | FDTD modeling taking into account the losses induced by the metal pads for 3 different configurations. Superimposed to the structure, the optical mode of the cavity.

The computed  $Q$ -factors are reported in table 5.1. It is obvious from such simulations that placing the metal pad at a distance of  $D = 2\sqrt{3}$  does not have a real impact on the optical mode as the cavity  $Q$ -factor remains the same. However, by only bringing the metallic pads closer to one row of PhC divides by two the  $Q$ -factor. Also, the width of the metallic pad does not change the mode interaction with the metal, therefore, we can consider that reducing the metal width at the end of the MW will not bring a further decrease of the  $Q$ -factor.

**Table 5.1** |  $Q$ -factor simulated by LUMERICAL for the structure without metallic pad and for the structure reported in Fig. 5-15

	Without Metal	Struct. 1	Struct. 2	Struct. 3
$Q$ -factor	9318	8080	4880	4770

Taking this last design, we can assume that the loaded  $Q$ -factor of the structure depicted in Fig. 5-11 decreases by a factor 2 the  $Q$ -factor computed in the structure without metallic pads. Therefore, the  $Q$ -factor can be assumed to be  $Q \simeq 1100$  from results found in section 5.1.1.3 and in this section. This value corresponds to the targeted  $Q$ -factor for an input optical pulse of few picoseconds time width.

## 5.2 | Results and Discussions

### 5.2.1 | Sample Basic Characterizations

Basic characterizations are performed to check the process: optical measurement to verify the deviation of the resonance frequency according to the parameter variations and that they are in the range accessible by the MLL (around 1550 nm), and basic electric characterization to ensure that the contacts have a ohmic behavior.

The sample consists of the same structure depicted in section 5.1, where several PhC structures are repeated. Between each structure of the sample, the hole radius variations  $r = 0.26a + dr$  is varied, with  $dr$  changing from  $-16$  nm to  $+4$  nm increasing with a step of 4 nm. The resonances are found using reflective Optical Coherence Tomography (OCT) [191–194] (Fig. 5-16), with wavelength from about 1520 nm to 1560 nm, therefore in the range of the MLL. The OCT setup consists in the first approximation of a Mach-Zehnder interferometer where the sample is placed in one of the arms. The interference signal between the two arms is recorded and provide both a temporal and spectral resolution of the signal.

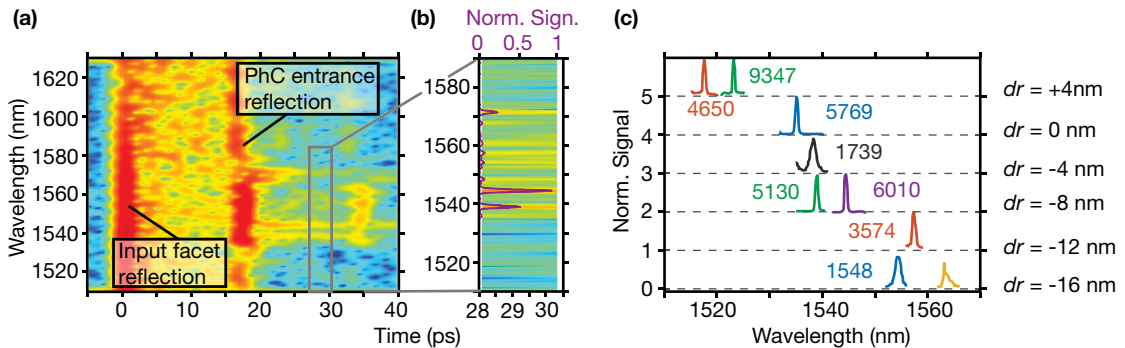


**Fig. 5-16** | (a) OCT intensity mapping of the reflection signal versus time and wavelength – (b) region of interest to find the resonances of the cavity – (c) resonance wavelengths and  $Q$ -factor for the different structures present on chip.

From Fig. 5-16(a), two primary reflections occur: one at the entrance of the sample due to the cut edge (at 0 ps as it is taken as our reference), and another one corresponding to the reflection between the rib waveguide and the entrance of the PhC, at about 15 ps. This corresponds to light traveling twice the length of the rib waveguide of  $450 \mu\text{m}$  (due to the back and forth distance for reflection).

Both those reflections are problematic as they induce losses, and decrease the total energy

coupled to the cavity. However, the photon lifetime in the cavity being  $\tau = Q/\omega_r \simeq 2$  ps, the energy stored in the cavity appears in the OCT mapping after those reflections. Therefore, observing only between 28 and 30.5 ps allows resolving the cavity resonances (Fig. 5-16(b)). Integrating the signal over this time scale provides a well defined signal. This characterization had been performed on all the cavities designed on the chip, and the resonances found exhibit  $Q$ -factors from 1500 to about 10 000 (Fig. 5-16(c))

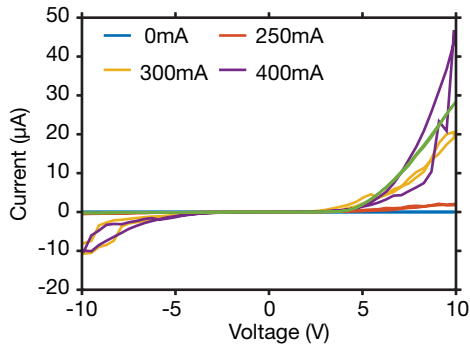


**Fig. 5-17** |  $I(V)$  characterization of the MW gap under illumination from a green laser diode injected vertically. The power of the input light is carried from 0 mA to 400 mA.

Since the structure provides well defined optical resonances with targeted  $Q$ -factor and wavelength, enabling carrier photogeneration through TPA, the second step to ensure that the sample could efficiently act as a photoconductive switch is to characterize the contacts. This is performed using a standard  $I(V)$  measurement protocol, with the semiconductor illuminated by a green laser diode. As depicted in Fig. 5-17, the characterization does not follow any linear trend. Therefore the contacts can not be considered as ohmic. This type of line-shape is more typical of a Schottky junction. However, the weak power level injected with the green laser diode might not be sufficient to generate enough carriers, which could explain why the RF gap remains poorly conductive. Nevertheless, to be certain to obtain a current through the photoconductive switch in further experiments, an external static bias needs to be applied.

### 5.2.2 | Microwave Characterization

Since both optical and electrical properties had been verified, essential MW characterization can be performed. A custom setup had been built during this Ph.D. (Fig. 5-18(a)), consisting of micrometer translation stages for the displacement of the RF probes (CascadeMicrotech - ACP40 - GS and SG) and the optical lens fiber (OZ Optics), feeding the optical clock (Pritel MLL for 2 or 5 GHz, or Optisiv MLL for 36 MHz repetition rate) through the input waveguide (Fig. 5-18(b)). The sample holder is placed in between the RF stages.

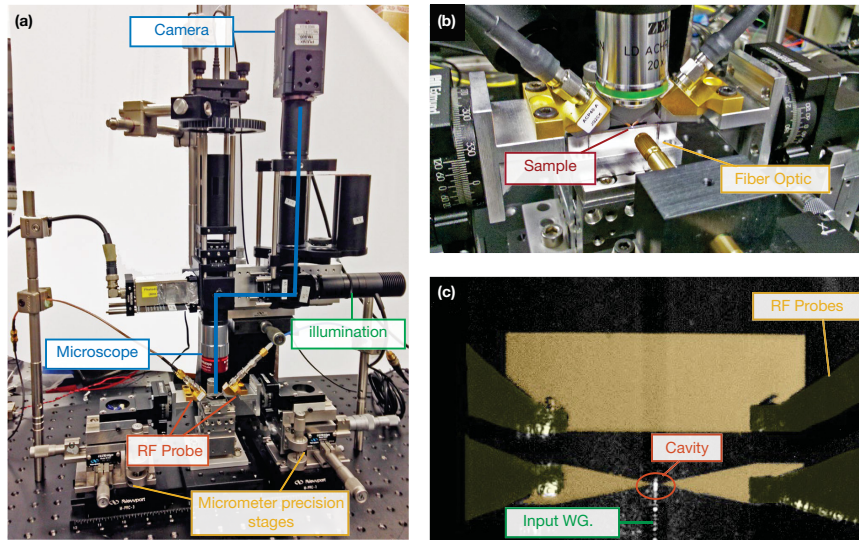


**Fig. 5-18** | Opto-Hyper characterization setup with viewing apparatus and respectively top (a) and side (b) illumination — (c) Colorized infrared image of the photoconductive switch under optical excitation.

Using an Infra-Red (IR) camera (Xenics) allows to observe the resonance of the cavity efficiently, with a well defined spot appearing at the corresponding wavelength in between the MW pads (Fig. 5-18(c)). However, it is also noticeable that the input waveguide undergoes significant losses as the light radiation is clearly visible. It is due to a high side roughness of the waveguide.

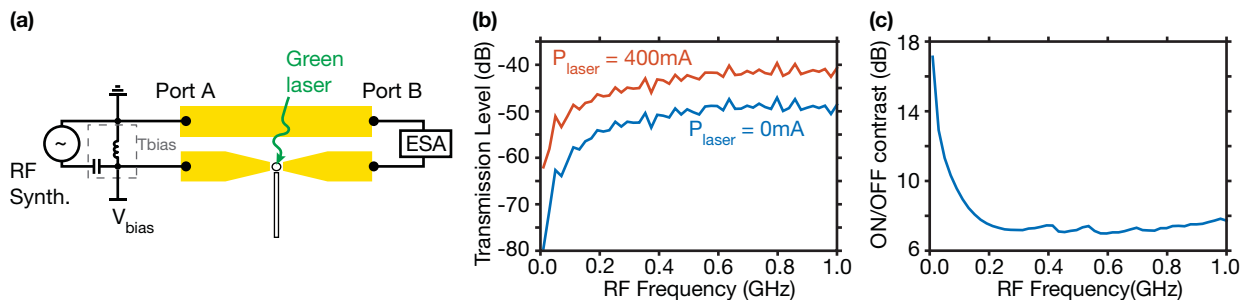


**Fig. 5-19** | (a) Schematic of the setup with RF synthesizer feeding the microstrip line and the bias applied through a bias-T. The output port is plugged to an ESA. The excitation is provided with the green laser diode – (b) ON/OFF transmission signal as a function of the frequency – (c) ON/OFF ratio of the transmitted signal.

The first characterization being made is ON/OFF measurement to ensure that the photoconductive switch follows the same trend than the simulated ON/OFF (*cf* section 5.1.2). A MW synthesizer (Agilent) is plugged, through a RF cable with a bandwidth of 40 GHz, to the input port (*i.e* port A). A static bias of 20 V is also applied with the help of a bias-tee (Fig. 5-19(a)). The output port (port B) is connected to an Electrical Spectrum Analyzer (ESA), with the same type of cable than for the input signal. The synthesizer frequency is swept from 10 MHz to 1 GHz. The ON state is provided by the illumination of the semiconductor with a green laser diode, the same that

we used for the  $I(V)$  characterization. From Fig. 5-19(b), it is apparent that the response of the photoconductive switch follows a long pass filter, due to the capacitance, with a frequency cut-off at about 100 MHz. When carriers are photo-generated, the output signal increases. The ON/OFF contrast follows the predicted trend from the simulation (Fig. 5-19(c)), as at low frequency the ON/OFF ratio is at the highest and decreases when frequency increases. This confirms that the resistance of the MW gap is reduced to provide an ON state.

ON/OFF characterization does not provide all the information to characterize the sample fully. Even if this result stands for the static parameters of the photoconductive switches, the impulse response of the excited MW gap is an essential parameter to know the highest maximum sampling frequency achievable. Indeed, in a usual photoconductive switch, the carrier lifetime determines the switching time, thus the frequency bandwidth of the impulse response. However, here, carriers diffuse and drift away from their generation area before being collected. The impulse response is then non-trivial. This experiment is done by applying a static bias (20 V) from port A, and changing the MW synthesizer from the last experiment with a  $50\ \Omega$  impedance terminator. The optical clock, coming from a Pritel MLL at a repetition rate of 2 GHz is fed to the cavity (Fig. 5-20(a)). Hence, this setup corresponds to the electro-optics analogy of the optical wavelength conversion operation depicted in sections 4.2 and 4.4, where a modulation from a MLL is transferred to a CW signal. Here instead the CW signal is replaced by an electrical bias. Therefore, the response of the MLL (*i.e.* temporal peaks in time and combs in the frequency domain) is transferred in the electrical domain. Hence, sampling a continuous electric signal corresponds to observing the harmonics of the MLL with the ESA, and provides the impulse response of the system.

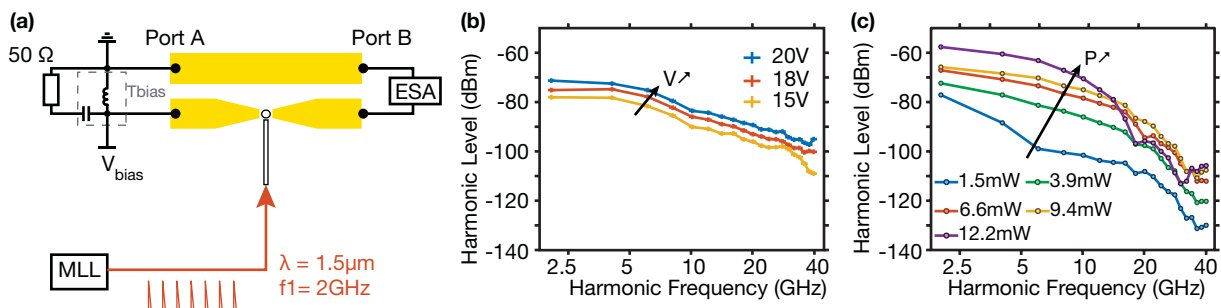


**Fig. 5-20** | (a) Schematic of the impulse response experiment with the MLL at 2 GHz repetition rate – (b) Impulse response with short pulses ( $\approx 3\text{ ps}$ ) with applied static bias variation – (c) Impulse response with long pulses ( $\approx 20\text{ ps}$ ) with optical power variation and 20 V applied static bias.

First, using a short optical pulse width (about 3 ps), the static bias is modified (Fig. 5-20(b)). As expected, the higher the bias, the higher the harmonic peaks. Increasing the bias by 30%, improves the total transmitted signal by 8 dB. However, this does not change the overall behavior of the impulse response. Next, using longer optical pulse width (about 20 ps), the optical power is modified for the same static bias (20 V), and wavelength adjusted accordingly to match resonances which have drift due to heating. Indeed thermal effects cause a dispersion red shifting the resonance, thus the input optical wavelength need to be accordingly tuned when electrical or optical power (both heating the structure).

The more power is fed to the cavity, the higher the harmonics peaks are (Fig. 5-20(c)). However, the overall impulse response in the frequency domain is modified in a nonlinear way by changing the optical power. An interesting aspect of such characterization is the obviously limited bandwidth with a cut-off frequency different by changing the pulse length. For the long pulse length, the bandwidth (at -10 dB) is here limited to about 10 GHz.

To investigate in more detail this limited bandwidth, the temporal response of the system is traced using an ultra-fast oscilloscope (Tektronix sampling scope DSA8300 - 70GHz) (Fig. 5-21(a)) with input pulse length of 2 ps. The temporal impulse response of the photoconductive switch exhibits two time constants: a fast one decreasing by a factor two the signal with a temporal width of about 20 ps (probably limited by the bandwidth of the detector), and a slow decay rate lasting roughly 100 ps. This slow tail explains the limited bandwidth of about 10 GHz of the response.

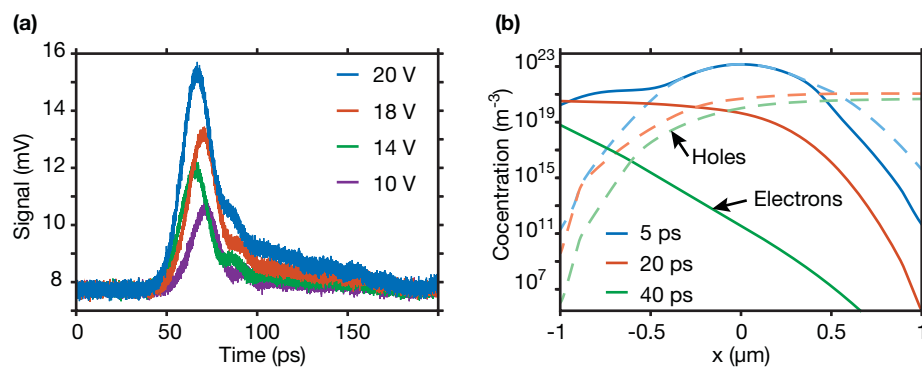


**Fig. 5-21** | (a) Time response of the photoconductive switch measured for different input bias – (b) Hole (dashed lines) and electron (solid lines) concentration space profile obtained by 1D modeling of drift-diffusion equation. The color represent a snapshot of the carrier concentration at 5, 20 and 40 ps (blue, red and green respectively). The input light pulse as a temporal width of 2 ps and center around 5 ps in the modeling.

One dimension modeling is performed taking into account the drift-diffusion equations with carrier velocity saturation. A bias of 3 V is applied (+1.5 V for port 1, -1.5 V for port B), with an input light corresponding to a Gaussian pulse centered around 5 ps with a temporal width of 3 ps. The total integrated generated carriers over time caused by the optical pulse amount to  $5 \times 10^{23} \text{ m}^{-3}$ . In order to fully understand the current process and its different behaviors, the concentration in time for both holes and electrons are represented at various time (Fig. 5-21(b)). From the modeling, it is evident that electrons are captured faster than the holes. At the maximum of the optical pulse (*i.e.* 5 ps), the concentration of holes and electrons remains almost the same. Because of the applied bias, the holes and electrons are separated from each other. After only 20 ps, the electrons and holes are well separated, and both have started to reach the contacts. However, from the snapshot at 40 ps, the electron concentration tends to be negligible while the hole one remains at a high value. Indeed, the mass of holes, inversely proportional to the mobility, is about 10 times greater than the electrons one. Thus, considering the electric field below the limit of saturation velocity (correct for an applied voltage of 20 V over 2  $\mu\text{m}$  gap and the hole saturation velocity field of  $2 \times 10^4 \text{ kV.cm}^{-1}$  [195]), the holes takes 10 times longer to travel the same distance than the electrons. Therefore, it is coherent with the fast, and slow tails observed in the experimental temporal impulse response in Fig. 5-21(a). This result explains the limited bandwidth of the impulse response of the photoconductive switch by the drift of the holes across half the RF gap.

Using long optical pulses, experiments where input optical power is varied has been performed, with wavelength modification to match the drifted resonance, and this for several static biases. The signal transmitted is averaged over all harmonics and is plotted along with the input optical power (Fig. 5-22(a)). Then, the obtained curves are fitted with a linear function in a logarithmic scale, for each static bias applied. The slope of the curve is plotted versus the harmonics frequency and the static bias (Fig. 5-22(b)). In the case of TPA absorption, the carriers generated have a quadratic dependency with the optical power. However, by changing the static bias, the mean total electric signal varies from a linear to a cubic trend.

Such modification of the dependency of the output signal with the optical power by changing the static electrical bias can be understood by the fairly complex dynamic of the carriers in the RF gap.

The time window where electrons and hole concentration profiles are overlapping, then re-

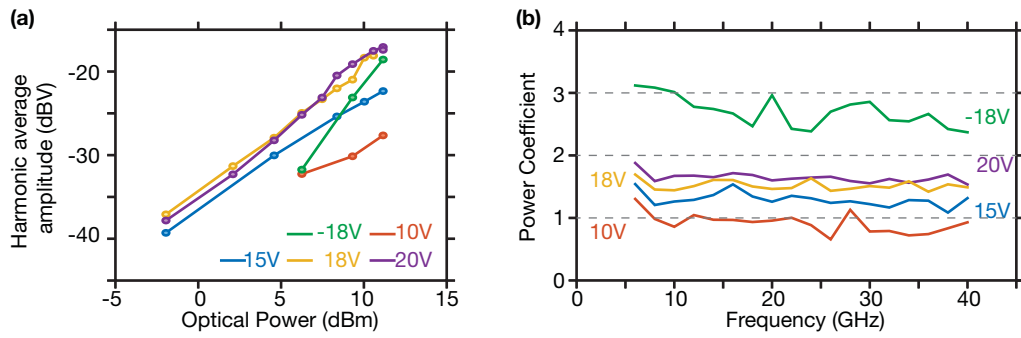


**Fig. 5-22** | (a) Impulse response dependency (average over all the harmonics) regarding the input optical integrated power and applied bias – (b) Slope of the MLL harmonics.

combinations occur, is wider when the static bias is decreased. Therefore, the fitting curve slope remains close to one with the input optical power as most of the carriers recombine. The more the static bias increases, the more we reach the quadratic regime, corresponding to TPA absorption, where most of the generated carrier are captured. When a negative bias is applied, the slope gets close to three. As the contacts are not ohmic, but follow more an asymmetric Schottky junction profile (see Fig. 5-17), an internal electric field could exist due to contact asymmetry. Turning the bias to a negative value might add up to the internal electric field. This total field, internal plus external, could lead the photo-generated carriers to collide with each other, and start an avalanche phenomena, which could explain this cubic trend.

For each power of the optical pump depicted in the experiment Fig. 5-20, the wavelength of the laser has been slightly adjusted to match the optimal wavelength of the loaded cavity. This maximizes the power coupled to the resonator, resulting in a reduction of the RF gap resistance as more carriers are generated and a higher current circulation through the junction (Fig. 5-23(a)). Indeed, the more power the cavity receives, the more the temperature increases, either due to carrier recombinations, or free carrier absorption which, therefore red-shift the resonance frequency (Fig. 5-23(b)). It is important to understand which process causes the temperature rise. Three main contributions occur: carrier relaxation to the band-edge as the excitation energy is higher than the band-gap energy, resulting in the emission of a phonon, carrier recombinations, and Joule

heating.

$$P_{diss} = P_{joule} + P_{rec} + P_{phon} \quad (5.1a)$$

$$P_{joule} = VI \quad (5.1b)$$

$$P_{phon} = P_{abs} \left( 1 - \frac{E_g}{2\hbar\omega} \right) \quad (5.1c)$$

$$P_{rec} = \frac{P_{abs}}{2\hbar\omega} (1 - \eta) E_g \quad (5.1d)$$

where  $P_{abs}$  is the effective optical power absorbed in the cavity,  $E_g$  the band-gap energy of GaAs and  $\eta$  a coefficient taking into account the carrier collection.

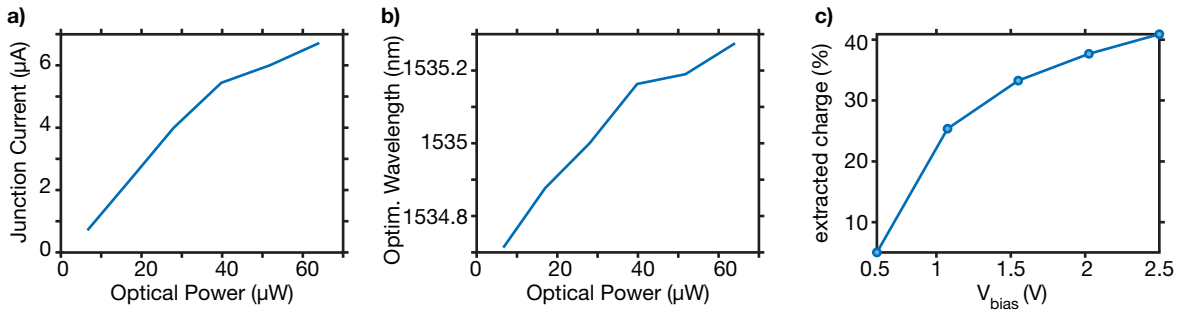


**Fig. 5-23** | Characterization of (a) the current circulating through the junction versus optical power of the input MLL – (b) Resonance wavelength with respect to the optical power. (c) Modeling of the carrier captured rate in function of the applied static bias.

Knowing that the current circulating through the junction can be rewritten in term of carrier generation such that  $I = q\eta P_{abs}/2\hbar\omega$ , the total dissipated power can be rewritten:

$$P_{diss} = \frac{P_{abs}}{2\hbar\omega} ((qV - E_g)\eta + 2\hbar\omega) \quad (5.2)$$

Here, two parameters are unknown from eq. (5.2): the absorbed optical power  $P_{abs}$  which is rather complicated to estimated to due waveguide losses and also as no transmission measurement can be performed; and the carrier collection efficiency  $\eta$ . However, for a qualitative comparison to determined which physical effect causes the heating, the determination of  $P_{abs}$  can be neglected as it is involved in all the term in the equation above. The determination of the carrier collection can be roughly estimated by drift-diffusion modeling as depicted in Fig. 5-23(c).

Using the parameters of the experiment, namely  $V = 20$  V, a band gap of GaAs of  $g = 1.424$  eV, and a photon energy of  $\hbar\omega = 0.815$  eV, and if the collection efficiency  $\eta$  is higher than 10%, the total power dissipation is mostly driven by Joule heating. This value is in agreement with modeling

of the carrier collection. Drift-diffusion modelings, in a 1D structure where only the static bias is a parameter, show an increase of the extracted carrier rate (*i.e.* the total amount of carriers captured by the contact over the total amount of carriers photo-generated). This value is in most of the cases over 10% (Fig. 5-23), the hypothesis value taken above to explain the behavior of the system. Even if the contacts in the system are not perfect ohmic contacts like in the modeling, as the applied bias is largely above the one implemented in the simulations, we could consider that this value of 10% extracted carrier rate is reasonable, which comfort the idea of Joule heating in the system.

### 5.2.3 | Signal Processing Operations

Electro-optic signal processing operations are now studied and discussed. The main motivation here is first to create new frequency by mixing the input signal at a frequency  $f_0$  with the clock frequency  $f_1$  creating a new output signal at the frequency  $f_1 \pm f_0$ . Such operation is the basic block of signal processing as depicted in section 1.1. In a second time, the experiments will focus on frequency-down conversion, folding the input frequency to the baseband, resulting in an output mixed signal at low frequency. This is in great interest to directly address ADCs (see section 1.1.1)

First, the optical sampling, *i.e.* direct mixing, of a MW signal is performed. Considering the laser pulses as a Dirac frequency comb  $\delta(n \times f_1)$  with  $n$  being an integer and  $f_1$  the repetition rate of the laser and the RF signal following a temporal sinusoid form (therefore on a Dirac peak in frequency space  $\delta(f_0)$ ), the resulting frequency mixed signal corresponds to  $f_{out} = \delta(n f_1) * \delta(f_0) = \delta(n f_1 \pm f_0)$  (Fig. 5-24(a)). Here, only the first harmonic of the laser is considered for the mixing operation.

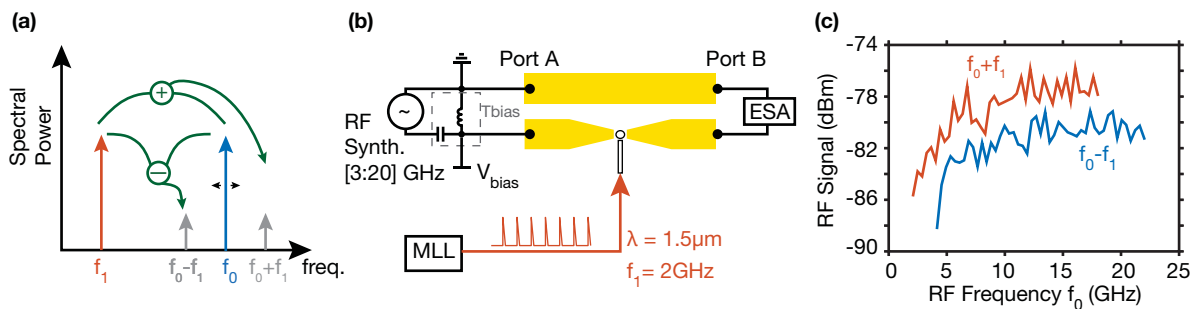


**Fig. 5-24** | (a) Spectral content consecutive to frequency mixing product generation – (b) Schematic of the setup with a RF synthesizer providing the MW signal ( $P_{rf}^{in} = 12$  dBm) sampled by the MLL optical clock at 2 GHz and Telecom wavelength – (c) Sum and difference frequency output signal for input frequency from 1 to 20 GHz.

The experiment consists of injecting a MW signal created by a RF synthesizer (Agilent) plugged

to the port A, with its frequency varying from 1 GHz to 20 GHz. A bias of 20 V is applied through a bias-tee (Fig. 5-24(b)). The optical clock is injected as in section 5.2.2 with a Pritel Telecom wavelength MLL tuned to the cavity resonance at a repetition rate of 2 GHz, with an average input power coming out of the laser of 32 mW. The pulse duration is about 2 ps. The spectrum of the output signal is measured using an ESA, with focusing on the mixing result frequencies.

Output mixed signal is observable over a span of almost 20 GHz (Fig. 5-24c), following the same low-pass filter trend, described earlier (see Fig. 5-20). Even if the sum and difference signals follow the same trend, the power ratio between them is of about 3 dB. Such behavior can be explain by the electrical transmission spectra of the photoconductive switch (*c.f.* section 5.2.2). Indeed, to obtain the same frequency for the sum and difference mixed frequency, one need to change the value of the input signal frequency. For instance, given a frequency of 3 GHz, the input signal is set to 4 GHz to obtain the corresponding sum mixed signal, while it is set to 7 GHz to obtain the same frequency for the difference output mixed signal. Therefore, the frequency difference of the input signal is  $2f_1$  between the two operations. Thus following the transmission spectra of the photoconductive switch previously characterized, a level difference of about 4 dB is observed at a 4 GHz span. This value corresponds to the level difference between the sum and difference output mixed signal observed in Fig. 5-24(a).

We show here that GaAs photonic crystal based photoconductive switch can efficiently process and sample electric MW signals over 20 GHz. This is the first demonstration, from our knowledge, of signal processing at telecom wavelengths with an optically resonant photo-conductive switch using TPA.

However, even if direct mixing enables to sample an input signal efficiently, it is of great interest to perform frequency-down conversion at the same time that the sampling operation for further simplifying the whole processing chain (*c.f.* section 1.1.1).

Frequency down-sampling consists of mixing the input RF signal with its closest  $n^{\text{th}}$  harmonic of the clock. The RF signal being in the Nyquist band of frequency width  $f_1$ , this results in a mixing signal in the band base, thus at low frequency (Fig. 5-25(a)). This enables to both efficiently sample and frequency down-convert the input signal. Experimentally, the setup is the same than in Fig. 5-24, where the frequency of the input MW signal is adjusted to match the 4<sup>th</sup>, 7<sup>th</sup> and 10<sup>th</sup> harmonic of the MLL (*i.e.* 8, 14 and 20 GHz respectively), and this for the same input power of 12 dBm. The static bias of 20 V is still present, and the input optical clock power remains the same

as previously (32 mW). Then, the frequency is swept in the whole Nyquist band, from  $nf_1 - f_1/2$  to  $nf_1 + f_1/2$ . The resulting down-sampled signal is observed with an ESA.

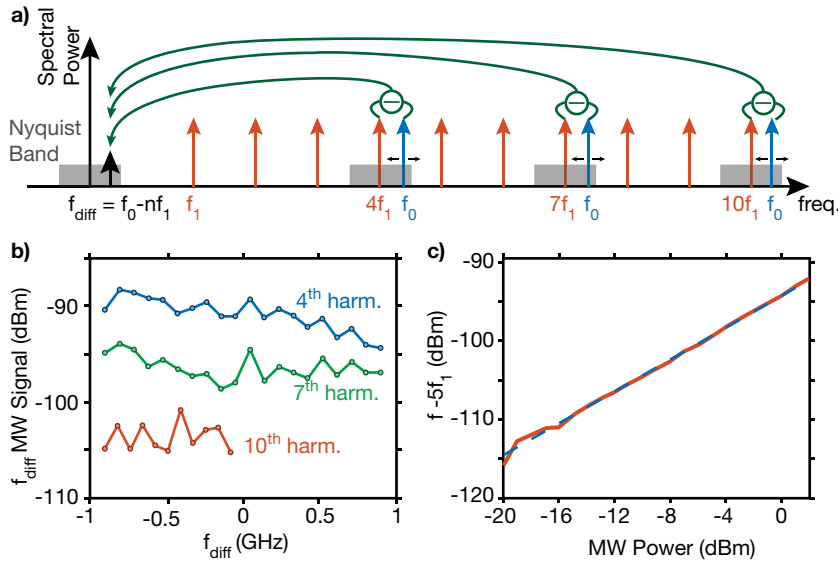


**Fig. 5-25** | (a) Sampling and frequency down-conversion principle sketch – (b) Sub-sampling output signal for the corresponding matched laser harmonics – (c) Output signal power regarding the input RF power for the sub-sampling operation using the 5<sup>th</sup> harmonic of the MLL.

Figure 5-25b shows the down-sampled signal, with respect of the laser harmonic selected. First, for the same harmonic, the output signal remains roughly constant. Secondly, when a higher laser harmonic is selected, the output RF signal level decreases. This is coherent with the impulse response measured in Fig. 5-20(c). The impulse response shows a difference of 6 dB between the 4<sup>th</sup> and the 7<sup>th</sup> harmonics, value which is observable in the down-sampling results (Fig. 5-25(b)). However, the difference between the 7<sup>th</sup> and the 10<sup>th</sup> is of 3 dB in the impulse response. This difference observed in Fig. 5-25(b) is however higher. The irregular signal level for the 10<sup>th</sup> harmonic frequency down-conversion could explain the difference observed.

An other critical aspect in signal processing application for further digitalization is the linearity of the mixer with the input RF power. Thus, selecting the 5<sup>th</sup> laser harmonic (*i.e.* matching the RF synthesizer to 10 GHz) and varying the power from -20 to 2 dBm (*i.e.* more than two decade variation), the output sub-sampled signal remains extremely linear (Fig. 5-25).

### 5.3 | Perspectives

Even if the photoconductive switch enables to sample and sub-sample electrical RF signals with an optical clock provided by a 1.5  $\mu\text{m}$  MLL, the output signal remains low. Further electrical amplifiers would improve this signal, but could bring further noise, and therefore reduce the ENOB. Thus, it

is essential to reduce electrical losses in the photoconductive switch.

As explain earlier, the main difference between *classical* photoconductive switches based on direct absorption with the structure studied here is the localization of the photo-generated carriers. Indeed, in the direct absorption process, the whole MW gap is illuminated. Thus carriers are immediately captured by the ohmic contacts. In our case, even if the photo-generated carrier density remains the same than in the classical system, carriers have to travel to the contacts. This decreases the concentration, thus the effective conductivity of the ON state. Also, the transport speed being limited by the hole drift speed in the case of an external bias ,or by the ambipolar diffusion constant in the case where no bias would be applied (which is roughly the same than the hole diffusion constant), the shorter the travel distance the larger the bandwidth of the photoconductive switch will be. Therefore, bringing closer the contacts would lead to significant benefit on the figure of merit of the system.

One-dimensional modeling had been performed where the contact positions have been varied, for the same optical power injection, thus same photo-generated carrier concentration (Fig. 5-26). By moving the contacts as close as one PhC period, the resistivity of the ON state would be reduced by a factor of about 300 compared to our current ohmic contacts position (about  $3 \mu\text{m}$ ). This would also lead to a travel distance divided by 7.5, therefore improving the bandwidth to at least 75 GHz.

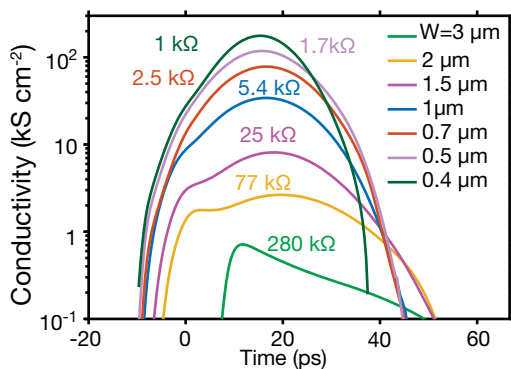


**Fig. 5-26** | Modeling of photoconductive switch conductance for a MW gap width from  $3 \mu\text{m}$  to  $0.4 \mu\text{m}$ . The corresponding resistance for a section of  $2 \mu\text{m} \times 250 \text{nm}$  is reported.

However, as pointed out before (see section 5.1.3), bringing closer the ohmic contacts to the cavity is not straightforward as it creates optical losses, and in our situation, the lowest distance limit is already reached. Nevertheless, other possibilities than metallic contacts exist to collect carriers. By highly doping the GaAs PhC below the Ohmic contact until the edge of the cavity (Fig. 5-27), the semiconductor in this region could be considered as degenerated with a low

resistance. The carriers generated in the cavity will be collected as soon as they enter the doped area. This reduces the MW gap and is almost equivalent to bringing closer the ohmic contacts. Even if doped semiconductor induces optical losses, mostly due to free carrier absorption, it is orders of magnitude lower than losses caused by metal.

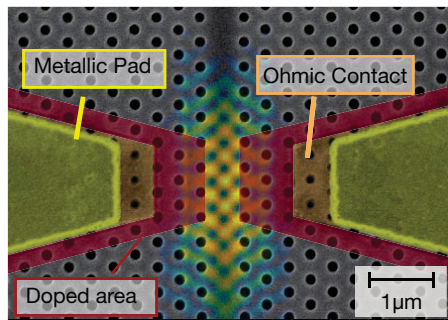


**Fig. 5-27** | SEM image of the photoconductive switch with superimposed optical mode of the cavity, and artist's view of the doping implantation area from the ohmic contact to the edge of the cavity (red)

The fabrication of such sample has unfortunately started at the end of this Ph.D., and the sample is still under processing at the time this thesis is written. However, the first crucial steps have already been performed and are highly encouraging. Indeed, implantation was carried out at IEMN in regards of alignment marks, and then bonding was done bonding. Alignments of the now embedded alignment marks in the BCB were successful which implies that the whole process flow can be continued (Fig. 5-28).

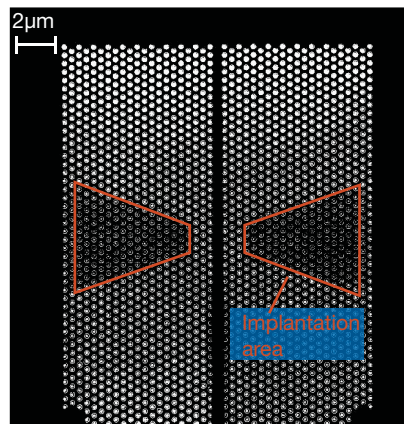


**Fig. 5-28** | SEM image of the processed PhC aligned with the previous step of Si implantation. The doped area are darker than the rest of the sample and are highlighted through the red lines.

## 5.4 | Conclusion

In this chapter, several design approaches for resonant photoconductive switches using telecom wavelength optical clock were discussed. First, a try of reproducing classical photoconductive switch

through on-top illumination was attempted using delocalized mode in photonic crystal (edge-modes) and the possibility to design the PhC to provide light extraction at the vertical from the slab through band-folding technique. However, this approach was dropped as the optical coupling provided by such structure was not sufficient enough for the targeted applications. Moving to in plane light injection with both PhC and rib waveguides while using a modulated cut-off waveguide cavity enabled to effectively provide optical resonances in a GaAs bonded on Si structure. To integrate the MW design previously optimized with the optical resonator, optimizations of the RF pads position were performed (Università di Ferrara) in order to bring as close as possible the contacts to collect efficiently the generated carriers while keeping a large enough  $Q$ -factor. For the first time to our knowledge, signal processing at telecom wavelength using resonant and nano-structured photo-conductive switches was performed and proved to process signal both by sampling it with an efficient bandwidth up to 20 GHz, and to frequency-down convert RF signal with a remarkable linearity regarding the input RF power over two decades. However, great improvements are still possible, especially by bringing closer the collection areas from the optical mode (*i.e.* the carrier generation area). In order to not increase optical losses by the presence of the metallic pads a sampled where doping implantation is currently in process. Such design, from drift-diffusion modeling and the extraction of the ON conductance of the system, could improve by order of magnitude the signal processing efficiency than the one from the structure studied in this chapter.

## References for Chapter 5 – Photo-conductives Switches at Telecom Wavelength

- [9] D. H. Auston. *Picosecond optoelectronic switching and gating in silicon*. Appl. Phys. Lett. **26** (1975). – pp. 10, 12–13, 131.
- [31] S. El Amari, A. De Angelis, D. Arnaud-Cormos, V. Couderc, and P. Leveque. *Characterization of a Linear Photoconductive Switch Used in Nanosecond Pulsed Electric Field Generator*. IEEE Photon. Technol. Lett. **23** (2011). – pp. 15, 131.
- [38] J. D. Joannopoulos and S. G. Johnson. *Photonic Crystals*. Springer Science & Business Media, 2001. – pp. 15, 130, 164.
- [41] E. Kuramochi, M. Notomi, S. Mitsugi, A. Shinya, T. Tanabe, and T. Watanabe. *Ultra-high-Q photonic crystal nanocavities realized by the local width modulation of a line defect*. Appl. Phys. Lett. **88** (2006). – pp. 16, 134–135.
- [43] Z. Han, X. Checoury, L.-D. Haret, and P. Boucaud. *High quality factor in a two-dimensional photonic crystal cavity on silicon-on-insulator*. Opt. Lett. **36** (2011). – pp. 16, 134.
- [179] S.-H. Kwon, S.-H. Kim, S.-K. Kim, Y.-H. Lee, and S.-B. Kim. *Small, low-loss heterogeneous photonic bandedge laser*. Opt. Exp. **12** (2004). – p. 131.
- [180] F. W. Smith, H. Q. Le, V. Diadiuk, M. A. Hollis, A. R. Calawa, S. Gupta, M. Frankel, D. R. Dykaar, G. A. Mourou, and T. Y. Hsiang. *Picosecond GaAs-based photoconductive optoelectronic detectors*. Appl. Phys. Lett. **54** (1989). – p. 131.
- [181] Z. D. Taylor, E. R. Brown, J. E. Bjarnason, M. P. Hanson, and A. C. Gossard. *Resonant-optical-cavity photoconductive switch with 0.5% conversion efficiency and 10W peak power*. Opt. Lett. **31** (2006). – p. 131.
- [182] X. Zheng, Y. Xu, R. Sobolewski, R. Adam, M. Mikulics, M. Siegel, and P. Kordoš. *Femtosecond response of a free-standing LT-GaAs photoconductive switch*. Appl. Opt. **42** (2003). – p. 131.
- [183] D. Krökel, D. Grischkowsky, and M. B. Ketchen. *Subpicosecond electrical pulse generation using photoconductive switches with long carrier lifetimes*. Appl. Phys. Lett. **54** (1989). – p. 131.
- [184] K. H. Tan, S. F. Yoon, S. Wicaksono, W. K. Loke, D. S. Li, N. Saadsaoud, C. Tripon-Canseliet, J. F. Lampin, D. Decoster, and J. Chazelas. *Low temperature grown GaNAsSb: A promising material for photoconductive switch application*. Appl. Phys. Lett. **103** (2013). – p. 131.
- [185] N.-V.-Q. Tran, S. Combrié, and A. de Rossi. *Directive emission from high-Q photonic crystal cavities through band folding*. Phys. Rev. B **79** (2009). – pp. 132–133.

- [186] C. M. Lim and G. H. Song. *Theoretical demonstration of DBR-assisted super-periodic photonic-crystal light-emitting diodes with narrow divergence angles*. *Optics Communications* **283** (2010). – p. 132.
- [187] H. Altug and J. Vučković. *Experimental demonstration of the slow group velocity of light in two-dimensional coupled photonic crystal microcavity arrays*. *Appl. Phys. Lett.* **86** (2005). – p. 132.
- [188] L.-D. Haret, X. Checoury, F. Bayle, N. Cazier, P. Boucaud, S. Combrié, and A. de Rossi. *Schottky MSM junctions for carrier depletion in silicon photonic crystal microcavities*. *Opt. Exp.* **21** (2013). – p. 134.
- [189] A. B. Fallahkhair, K. S. Li, and T. E. Murphy. *Vector Finite Difference Modesolver for Anisotropic Dielectric Waveguides*. *J. Lightwave Technol.* **26** (2008). – p. 137.
- [190] Ansoft. *ANSYS HFSS - High Frequency Electromagnetic Field Simulation*. – p. 138.
- [191] C. Caër, S. Combrié, X. Le Roux, E. Cassan, and A. de Rossi. *Extreme optical confinement in a slotted photonic crystal waveguide*. *Appl. Phys. Lett.* **105** (2014). – p. 141.
- [192] M. Choma, M. Sarunic, C. Yang, and J. Izatt. *Sensitivity advantage of swept source and Fourier domain optical coherence tomography*. *Opt. Exp.* **11** (2003). – p. 141.
- [193] A. Parini, P. Hamel, A. de Rossi, S. Combrié, N.-V.-Q. Tran, Y. Gottesman, R. Gabet, A. Talneau, Y. Jaouen, and G. Vadala. *Time-Wavelength Reflectance Maps of Photonic Crystal Waveguides: A New View on Disorder-Induced Scattering*. *J. Lightwave Technol.* **26** (). – p. 141.
- [194] S. R. Chinn, E. A. Swanson, and J. G. Fujimoto. *Optical coherence tomography using a frequency-tunable optical source*. *Opt. Lett.* **22** (1997). – p. 141.
- [195] V. L. Dalal. *Temperature Dependence of Hole Velocity in p-GaAs*. *J. Appl. Phys* **42** (1971). – p. 146.

# Conclusion and Perspectives

---

---

In this Ph.D. thesis, signal processing, both in an electro-optic or an all-optical way, is addressed using photonic crystal cavities made of III-V materials, especially InP and GaAs.

Fabrication is first discussed where self-suspended membrane, the most used process here in Thales for the fabrication of PhC, is described but led to issues when metallic contacts needed to be introduced for the electro-optic system process-flow. Attempts of using other under-etching processes have been tried, but in vain, leading to change the approach of self-suspended membrane. Indeed, only a lower refractive index is needed for the layer above and below the PhC slab. Given this, if SiO<sub>2</sub> is present below, the vertical light confinement still occurs. Thus, adhesive bonding, using BCB which possesses a refractive index close to the SiO<sub>2</sub> one, of III-V material on top of a Si wafer, was performed in this thesis. No further under-etching is needed to provide vertical light confinement. Then metallic pad can be deposited without any issue.

Modeling was addressed during this Ph.D. thesis, both for carrier dynamics in nanostructured devices and optically through the Coupled Mode Theory formalism. First, implementation using proprietary software is discussed and verifications are performed using comparison with the analytical solution of basic problems to ensure that the model is working correctly. Then, using the solution of the ambipolar approximation of the carrier diffusion in PhC cavities, CMT formalism is modified to introduce this solution as impulse response for complete modeling of the all-optical gate. This has a major impact on the accuracy of such model, as approximations for the carrier dynamics are no longer needed, and limit the number of fitting parameter to only one: the surface recombination velocity.

All-optical signal processing is then performed at telecom wavelengths, using InP, passivated GaAs and P-doped InP. First, using InP, wavelength conversion at a repetition rate up to 10 GHz was performed, and frequency down conversion with a clock at 12 GHz was done, with a striking

linearity regarding the input RF power. However, the system undergoes a long time constant concerning its recovery, making it difficult to increase the repetition rate over 10 GHz and still keeping a good output signal contrast. In this perspective, GaAs photonic crystal cavities are studied. However, GaAs entails a high surface recombination velocity, which prevents the carrier concentration to build up. To solve this issue, ALD passivation using  $\text{Al}_2\text{O}_3$  is performed decreasing by two orders of magnitude the surface recombination velocity, and modifying the effective carrier lifetime from about 1 ps to 10 ps, values found thanks to the accuracy of the newly introduced formalism in the CMT modeling. This all-optical gate exhibits a time switching resolution of 10 ps, demonstrated by efficiently processing a burst of four input pulses emulating a repetition rate of 100 GHz. Also, wavelength conversion at 5 GHz is demonstrated. This limitation of 5 GHz for the clock repetition rate is, from our guess, limited by the thermal drift of the resonance. Finally, with the same aim to speed up the all-optical switching time, engineering on the carrier dynamics is studied through P-doped InP photonic crystal. Thanks to the doping, the carrier dynamics reaches the minority carrier diffusion regime, which is in this case electrons, with an order of magnitude higher diffusion coefficient. Using this sample, the switching time is improved by a factor greater than 2.

Electro-optic signal processing with an active material made of GaAs PhC is finally demonstrated. Thanks to the enhancement of the optical field due to the PhC cavity, two-photon absorption process occurs to create a carrier density high enough to lower the resistance of the semiconductor, enabling the electric signal to be detected at the output port. However, an applied DC voltage is still necessary as the ohmic contacts are relatively far away from the generation area, due to optical design necessity, to effectively separate holes and electrons and avoiding them to recombine before they reach the RF microstrip line. Direct signal mixing is demonstrated with a frequency clock rate at 2 GHz and with an input frequency signal up to 20 GHz. Moreover, frequency down conversion operations are measured with an input signal frequency rate also up to 20 GHz, owing to a linearity with the input RF power over 20 dB.

The results demonstrated in this Ph.D. thesis are really promising, for both types of optically assisted signal processing, and resulted in conference proceedings [67, 196–200], leading to obtain a travel grant to assist at CLEO 2015 (Milton/Chang travel Grant – OSA) and the best poster award at CLEO 2016. It also led to published article [66, 178, 201]. First, it is the first time that PhC based photoconductive switches are demonstrating, which use Telecom wavelength for the optical clock.

The system can still greatly be enhanced, especially by bringing closer the collection area. The most suited way would be to create a doped area surrounding the PhC cavity, allowing close carrier collection without bringing metal closer to the optical field, which would lead to high optical losses. We believe that this photoconductive switch approach can in the future leads to great results.

Moreover, all-optical signal processing using one optical switch is now mature enough, through the fabrication process, the modeling, and the experimental tools developed before this thesis and during it. We believe that the next step would be to cascade several all-optical gates to perform either demultiplexing with different resonance wavelength for each gate or cascading switches to decrease the signal processing frequency by a factor of the number of gates. Thanks to the model developed here, a complete design of such system would be both accurate and relatively easy.

## References for Conclusion and Perspectives

- [66] S. Combrié, G. Lehoucq, A. Junay, S. Malaguti, G. Bellanca, S. Trillo, L. Ménager, J. P. Reithmaier, and A. de Rossi. *All-optical signal processing at 10 GHz using a photonic crystal molecule*. Appl. Phys. Lett. **103** (2013). – pp. 20–21, 65, 85–86, 106, 110, 117, 158.
- [67] G. Moille, A. de Rossi, G. Lehoucq, A. Martin, L. Bramerie, M. Gay, and S. Combrié. *A Highly Linear All Optical Gate Based on Coupled Photonic Crystal Cavities*. Nonlinear Photonics. (2014). – pp. 20, 158.
- [178] G. Moille, S. Combrié, and A. de Rossi. *Modeling of the carrier dynamics in nonlinear semiconductor nanoscale resonators*. Phys. Rev. A **94** (2016). – pp. 117, 158.
- [196] G. Moille, A. de Rossi, G. Lehoucq, C. Tripon-Canseliet, L. Morgenroth, F. Neuilly, D. Decoster, G. Bellanca, and S. Combrié. *GaAs Photonic Crystal Switch for Electro-Optic Sampling*. Conference on Lasers and Electro-Optics. (2016). – p. 158.
- [197] G. Moille, A. de Rossi, and S. Combrié. *All-optical gates based on photonic crystal resonators*. SPIE Photonics Europe. (2016). – p. 158.
- [198] G. Moille, S. Combrié, K. Fuchs, M. Yacob, J. P. Reithmaier, and A. de Rossi. *Towards faster InP photonic crystal all-optical-gates*. International Conference on Photonics in Switching. (2015). – p. 158.
- [199] S. Combrié, A. Martin, G. Moille, G. Lehoucq, A. de Rossi, J. P. Reithmaier, L. Bramerie, and M. Gay. *An efficient all-optical gate based on photonic crystals cavities and applications*. 16th International Conference on Transparent Optical Networks (ICTON). (2014). – p. 158.
- [200] G. Moille, S. Combrié, G. Lehoucq, L. Morgenroth, F. Neuilly, D. Decoster, and A. de Rossi. *Recovery Time Control in a Nanophotonic Nonlinear Gate Using Atomic Layer Deposition*. Conference on Lasers and Electro-Optics. (2015). – p. 158.
- [201] G. Moille, S. Combrié, L. Morgenroth, G. Lehoucq, F. Neuilly, B. Hu, D. Decoster, and A. de Rossi. *Integrated all-optical switch with 10 ps time resolution enabled by ALD*. Laser Photon. Rev **10** (2016). – p. 158.

# Appendix A

## Modeling

### A.1 | Analytic Formulation for PN Junction

#### A.1.1 | PN Junction

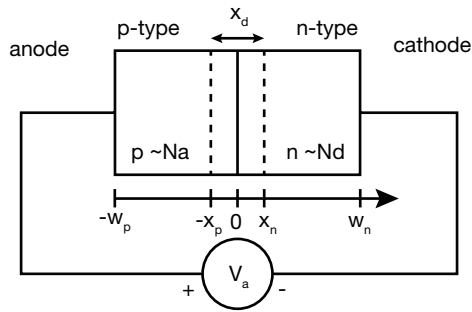


Fig. A-1 | PN junction geometry

Poisson equation :

$$-\epsilon_0 \epsilon_r \nabla \cdot \nabla V = \rho = q(p - n + N_d - N_a) \quad (\text{A.1})$$

In the full depletion approximation  $\rho = q(N_d - N_a) \forall -x_p \leq x \leq x_n$ . Therefore, the Poisson equation is straightforward and results in

$$V = 0 \quad \forall \quad x < -x_p \quad (\text{A.3})$$

$$V = q \frac{N_a}{2\epsilon_r \epsilon_r} (x + x_p)^2 \quad \forall \quad -x_p \leq x \leq 0 \quad (\text{A.4})$$

$$V = -q \frac{N_d}{2\epsilon_r \epsilon_r} (x + x_n)^2 \quad \forall \quad 0 < x \leq x_n \quad (\text{A.5})$$

$$V = \phi_{bi} \quad \forall \quad x_n < x \quad (\text{A.6})$$

with  $\phi_{bi}$  the built-in potential calculated as  $\phi_{bi} = \frac{k_B T}{q} \ln \left( \frac{N_a N_d}{n_i^2} \right)$  with  $n_i$  being the intrinsic concentration such that  $n_i = \sqrt{N_c N_v} \exp \left( -\frac{E_g}{2k_B T} \right)$

Therefore, the depletion width is defined as

$$x_n = \sqrt{\frac{2\epsilon_r \epsilon_r N_a (\phi_{bi} - V_a)}{q N_d (N_a + N_d)}} \quad (\text{A.7a})$$

$$x_p = \sqrt{\frac{2\epsilon_r \epsilon_r N_d (\phi_{bi} - V_a)}{q N_a (N_a + N_d)}} \quad (\text{A.7b})$$

### A.1.2 | Carrier Density

At the metal contact, it is assumed to be at thermal equilibrium due to extrem high recombination, therefore:

$$p(x = w_n) = p_{n0} = \frac{n_i^2}{N_d} \quad (\text{A.8a})$$

$$n(x = -w_p) = n_{p0} = \frac{n_i^2}{N_a} \quad (\text{A.8b})$$

The full depletion approximation yield to:

$$p(x = x_n) = p_{n0} \exp \left( \frac{V_a}{V_t} \right) \quad (\text{A.9a})$$

$$n(x = -x_p) = n_{p0} \exp \left( \frac{V_a}{V_t} \right) \quad (\text{A.9b})$$

with  $V_t = \frac{k_B T}{q}$

By applying boundary condition to the general solution of the diffusion equation for each of the quasi-neutral regions, leads to:

$$ap(x \geq x_n) = p_{n0} + p_{n0} \left( e^{V_a/V_t} - 1 \right) \left( \cosh \left( \frac{x - x_n}{L_p} \right) - \coth \left( \frac{w'_n}{L_p} \right) \sinh \left( \frac{x - x_n}{L_p} \right) \right) \quad (\text{A.10a})$$

$$an(x \leq -x_p) = n_{p0} + n_{p0} \left( e^{V_a/V_t} - 1 \right) \left( \cosh \left( \frac{x + x_p}{L_n} \right) + \coth \left( \frac{w'_p}{L_n} \right) \sinh \left( \frac{x + x_p}{L_n} \right) \right) \quad (\text{A.10b})$$

with  $L_{n,p}$  being the diffusion length of respectively the electrons and holes defined as  $L_{n,p} = \sqrt{D_{n,p} \tau_{SRH}}$ , and with the quasi neutral regions  $w'_{n,p} = w_{n,p} - x_{n,p}$

The concentration in the depletion region are calculated such that the Fermi level doesn't change:

### A.1.3 | Band Diagram

The semiconductor is defined by its band gap, thus we define the conduction and valence band such that:

$$E_c = -q * V + \frac{E_g}{2} \quad (\text{A.11a})$$

$$E_v = -q * V - \frac{E_g}{2} \quad (\text{A.11b})$$

The intrinsic energy level is defined such that :

$$E_i = \frac{E_c + E_v}{2} + \frac{1}{2} k_B T \ln \left( \frac{N_v}{N_c} \right) \quad (\text{A.12})$$

From the carrier concentration, it is easy to calculate the Quasi Fermi level such that:

$$F_n = E_i + k_B T \ln \left( \frac{N}{n_i} \right) \quad (\text{A.13a})$$

$$F_p = E_i - k_B T \ln \left( \frac{P}{n_i} \right) \quad (\text{A.13b})$$

### A.1.4 | Current

The current, both drift and diffusion contribution, can be easily calculated from the quasi Fermi-level such that:

$$\mathbf{J}_n = -n\mu_n \nabla F_n \quad (\text{A.14a})$$

$$\mathbf{J}_p = p\mu_p \nabla F_p \quad (\text{A.14b})$$

therefore, the total current density is  $J_{tot} = J_n + J_p$

## A.2 | Coupled Mode Theory -- Supplementaries

### A.2.1 | Approximations in the CMT

Let us consider the simple case of one cavity coupled to a waveguide, and  $|\gamma| \gg |\Gamma_0|$ . At steady state and at resonance  $\omega = \omega_k$ , eq. (3.21) reduces to  $0 = -\frac{\gamma}{2} A + \kappa S_{in}$ , hence  $|A|^2 = 2\gamma^{-1} |S_{in}|^2$ . Moreover, the energy density in the waveguide is related to the power by the group velocity  $v_g$  and the waveguide cross section  $\sigma_{wg}$ , hence the energy density in the waveguide is  $W_{wg} = \frac{|S_{in}|^2}{v_g \sigma_{wg}} = 2\frac{\gamma W_{cav} V_{cav}}{v_g \sigma_{wg}}$ , thus the ratio  $\frac{W_{cav}}{W_{wg}} = \frac{v_g \sigma_{wg}}{2\gamma V_{cav}}$ . Assuming the normal mode of the cavity is the stationary

counterpart of the travelling waveguide modes (e.g.  $L_3$ ,  $L_5$  cavities and line defect waveguides built out of the same lattice), then  $V_{cav}/\sigma_{wg} \approx L_{cav}$  the waveguide length and therefore  $2\frac{V_{cav}}{\sigma_{wg}v_g}$  is the cavity round-trip time  $\tau_r$ . This allows interpreting  $\frac{v_g\sigma_{wg}}{2\gamma V_{cav}}$  as  $\gamma^{-1}\tau_r^{-1} = 1/F$  the inverse of the finesse of the cavity, which is a well know result. In a single-mode cavity such as  $H_0$ , this number is very close to the Q factor.

## A.2.2 | Calculation of the Kerr and TPA Nonlinear Terms

The nonlinear interaction terms have been derived in the context of the coupled mode theory in countless publications and monographies, see e.g. [38]. For the sake of consistency with our own notation, we provide here the derivation of the nonlinear coefficients.

With the usual approximations (rotating wave, set of orthogonal normal modes  $\mathbf{U}$ ), the nonlinear perturbation of the complex envelope reads:

$$\partial_t A = -i \frac{\exp(i\omega t)}{4\omega} \int_V \mathbf{U}^* \partial_t^2 \mathbf{P}_{NL} dV \quad (\text{A.15})$$

The specific case of the third order susceptibility (Kerr nonlinearity) is considered here. Following Boyd [45]:

$$\mathbf{P}_{NL} \cdot \mathbf{E}^* = n_2 \epsilon_r \epsilon_0^2 c_0 \frac{2|\mathbf{E}|^4 + |\mathbf{E} \cdot \mathbf{E}|^2}{3} \quad (\text{A.16})$$

which in the case of a single cavity mode becomes:

$$\partial_t A = -i \frac{\omega n_2 c_0}{4} \int_V \epsilon_0^2 \epsilon_r \chi_r \frac{2|\mathbf{U}|^4 + |\mathbf{U} \cdot \mathbf{U}|^2}{3} dV |A|^2 A \quad (\text{A.17})$$

where we account for the inhomogeneity of the nonlinear tensor by introducing a factor  $\chi_r = \frac{\chi^{(3)}(\mathbf{r})}{\chi_{max}^{(3)}}$ , where  $\chi_{max}^{(3)}$  is related to  $n_2$ . This equation is rewritten as:

$$\partial_t A = i \Delta\omega(A) A = -|A|^2 V_\chi^{-1} c_0 n_2 \omega \quad (\text{A.18})$$

This defines the instantaneous frequency shift and the *Kerr* volume:

$$V_\chi^{-1} = \frac{\epsilon_0^2}{4} \int_V \epsilon_r \chi_r \frac{2|\mathbf{U}|^4 + |\mathbf{U} \cdot \mathbf{U}|^2}{3} dV \quad (\text{A.19})$$

The two photon absorption is related to the Kerr effect, and is treated accordingly. By generalizing eq. (A.18) with a complex frequency shift  $\Delta\omega + i\frac{\Gamma}{2}$  and the related nonlinear index with  $n_2 + i\beta_{TPA}\frac{c_0}{2\omega}$ .

Consistently, the generation term eq. (3.30) should be corrected:

$$G(\mathbf{r}) = \beta_{TPA} \frac{c_0^2 \varepsilon_0^2}{8\hbar\omega} \varepsilon_r \frac{2|\mathbf{U}|^4 + |\mathbf{U} \cdot \mathbf{U}|^2}{3} \mathbf{A}^4 \quad (\text{A.20})$$

In the geometries considered here, the scalar approximation of  $V_\chi$  is reasonably accurate, the discrepancy being about a few percent or less, and, therefore, can be safely used.

### A.2.3 | Approximations in Modeling the Carriers

Depending on the time scale considered, the dynamics of carriers is described by models of increasing complexity. The main assumption here is that the excitation is never shorted than 1 ps. Consequently, it is expected that excited carriers have already relaxed to their quasi-equilibrium distribution, which is described by quasi-Fermi levels. Thus, effects of carrier heating are ignored, and the energy released by thermalized carriers, namely  $2\hbar\omega - E_g$  is considered as heat. We also consider that the injected power is not large enough to induce the saturation of the absorption, which is reasonable since large enough spectral shift is achieved without reaching carrier density above  $10^{18} \text{ cm}^{-3}$ .

The effective carrier density  $N_{eff}$  is introduced to relate the calculation of the diffusion equation to the spectral shift of the resonance. The perturbation analysis is used to connect the change of the dielectric permittivity  $\Delta\varepsilon$  to the spectral shift  $\Delta\omega$ :

$$\Delta(\omega^2) = -\omega^2 \frac{\int \varepsilon_0 \Delta\varepsilon_r |\mathbf{U}|^2 dV}{\int \varepsilon_0 \varepsilon_r |\mathbf{U}|^2 dV} \quad (\text{A.21})$$

Hence:  $\Delta\omega = -\frac{\omega}{4} \int \varepsilon_0 \Delta\varepsilon_r |\mathbf{U}|^2 dV$ . Moreover  $\Delta\varepsilon_r = 2n\Delta n = 2n(\partial_N n + \partial_P n)$ , which, in the ambipolar approximation  $N = P$  becomes  $\partial_{N_a} n = \partial_N n + \partial_P n$ . Finally:

$$\Delta\omega = -\frac{\omega}{2} n \varepsilon_0 \frac{\partial n}{\partial N_a} \int N |\mathbf{U}|^2 dV \quad (\text{A.22})$$

Consider a volume with uniform carrier density  $N(\mathbf{r}) = N_{eff}$  and  $\varepsilon_r$ . Then eq. (A.22) becomes:

$$\Delta\omega = -\frac{\omega}{n} \frac{\partial n}{\partial N} N_{eff} \quad (\text{A.23})$$

Comparing eq. (A.22) and eq. (A.23) leads to the definition of the effective carrier density:

$$N_{eff} = \int N \frac{\varepsilon_0 \varepsilon_r |\mathbf{U}|^2}{2} dV \quad (\text{A.24})$$



# Appendix B

## All-Optical Signal Processing

### B.1 | Parameters Used for Modelling Pump-Probe Experiment

Param.	Bare GaAs	ALD GaAs	InP	Units
$\omega_1$	192.31	191.89	192.85	$\times 2\pi$ THz
$\omega_2$	192.50	192.13	192.85	$\times 2\pi$ THz
$\mu$	3.3059	3.6581	3.5853	$\times 10^{12}$ s <sup>-1</sup>
$\kappa_1^a$	5.79	7.76	6.36	$\times 10^5$ s <sup>-1/2</sup>
$\kappa_2^a$	0	0	0	$\times 10^5$ s <sup>-1/2</sup>
$\kappa_1^b$	5.79	7.76	6.355	$\times 10^5$ s <sup>-1/2</sup>
$\kappa_2^b$	0	0	3.759	$\times 10^5$ s <sup>-1/2</sup>
$\Gamma_{0,1}$	1.21	1.21	1.21	$\times 10^{-12}$ s <sup>-1</sup>
$\Gamma_{0,2}$	1.21	1.21	1.21	$\times 10^{-12}$ s <sup>-1</sup>
$v_{rec}$	$1 \times 10^7$	$3.3 \times 10^5$	$1 \times 10^3$	cm.s <sup>-1</sup>
$D_a$	19	19	19	cm <sup>2</sup> .s <sup>-1</sup>
$E_{pmp}$	100	150	500	fJ
$E_{prb}$	1	1	1	fJ
$\omega_{pmp}$	192.99	192.66	193.38	$\times 2\pi$ THz
$\omega_{prb}$	191.93	191.39	192.30	$\times 2\pi$ THz
$t_{pmp}$	5	5	6	ps
$t_{prb}$	< 0.5	< 0.5	1	ps

**Table B.1** | Simulation Parameters value used in the CMT model (described in section 3.2) which are matching with the experimental pump-probe results for the bare GaAs, ALD-coated GaAs and InP shown in chapter 4







# Acronyms

---

---

<b>A</b> _____	<b>FEM</b> .....Finite Element Method
<b>ADC</b> .....Analogue to Digital Converter	<b>FIB</b> .....Focused Ion Beam
<b>AFM</b> .....Atomic Force Microscopy	<b>FWHM</b> .....Full Width at Half Maximum
<b>ALD</b> .....Atomic Layer Deposition	<b>H</b> _____
<b>AOG</b> .....All-Optical Gate	<b>H<sub>0</sub></b> .....Zeros missing hole cavity
<b>AOM</b> .....Acousto-Optic Modulator	<b>I</b> _____
<b>C</b> _____	<b>ICP</b> .....Inductively Coupled Plasma
<b>CMT</b> .....Coupled Modes Theory	<b>IF</b> .....Intermediate Frequency
<b>CW</b> .....Continuous Wave	<b>IR</b> .....Infra-Red
<b>D</b> _____	<b>M</b> _____
<b>DSP</b> .....Digital Signal Processing	<b>MBE</b> .....Molecular Beam Epitaxy
<b>E</b> _____	<b>MLL</b> .....Mode-Locked Laser
<b>ebeam</b> .....electron-beam lithography	<b>MOCVD</b> .....Metalorganic Chemical Vapor Deposition
<b>EDFA</b> .....Erbium Doped Fiber Amplifier	<b>MW</b> .....MicroWave
<b>ENOB</b> .....Effective Number Of Bits	<b>O</b> _____
<b>ESA</b> .....Electrical Spectrum Analyzer	<b>OCT</b> .....Optical Coherence Tomography
<b>F</b> _____	<b>ODE</b> .....Ordinary Differential Equation
<b>FDFD</b> .....Finite Time Frequency Domain	<b>OSA</b> .....Optical Spectrum Analyzer
<b>FDTD</b> .....Finite Time Difference Domain	

---

<b>P</b> _____	<b>RMS</b> .....Root Mean Squared
<b>PDE</b> .....Partial Differential Equations	<b>ROI</b> .....Region Of Interest
<b>PECVD</b> .....Plasma-Enhanced Chemical Vapor Deposition	<b>S</b> _____
<b>PhC</b> .....Photonic Crystal	<b>SEM</b> .....Scanning Electron Microscopy
	<b>SRH</b> .....Shockley-Read-Hall
<b>R</b> _____	<b>T</b> _____
<b>RF</b> .....Radio Frequency	<b>TLD</b> .....Tunable Diode Laser
<b>RIE</b> .....Reactive-Ion Etching	<b>TPA</b> .....Two Photon Absorption

# List of Symbols

---



---

<b>Symbols</b> _____	$E_t$ .....Trap energy [eV]
$\lambda$ .....Optical wavelength [m]	<b>F</b> _____
$\nu$ .....Optical frequency [Hz]	$f_0$ .....Local oscillator frequency [Hz]
<b>A</b> _____	$f_0$ .....Optical clock repetition frequency [Hz]
$a$ .....Photonic crystal period [m]	<b>G</b> _____
<b>C</b> _____	$\Gamma_0$ .....Intrinsic decay rate [ $2\pi \times$ Hz]
$c_0$ .....Light velocity in vacuum [ $\text{m}\cdot\text{s}^{-1}$ ]	<b>H</b> _____
<b>D</b> _____	$h_0$ .....Impulse response of the optical resonator [ $\text{J}^{-2}\cdot\text{m}^{-3}\cdot\text{s}^{-1}$ ]
$dr$ .....Hole radius variation [normalized]	<b>N</b> _____
$D_a$ .....Ambipolar diffusion constant [ $\text{cm}^{-2}\cdot\text{s}^{-1}$ ]	$N_{eff}$ .....Effective carrier concentration [ $\text{cm}^{-3}$ ]
$D_n$ .....Electron diffusion constant [ $\text{cm}^{-2}\cdot\text{s}^{-1}$ ]	$n_g$ .....Optical group index
$D_p$ .....Hole diffusion constant [ $\text{cm}^{-2}\cdot\text{s}^{-1}$ ]	$n_i$ .....Intrinsic carrier concentration [ $\text{cm}^{-3}$ ]
<b>E</b> _____	$N$ .....Electron concentration [ $\text{cm}^{-3}$ ]
$E_c$ .....Conduction band energy [eV]	<b>P</b> _____
$E_g$ .....Band gap energy [eV]	$P$ .....Hole concentration [ $\text{cm}^{-3}$ ]
$E_v$ .....Valence band energy [eV]	<b>Q</b> _____
$\varepsilon$ .....Material permittivity	
$\varepsilon_0$ .....Vacuum permittivity [ $\text{F}\cdot\text{m}^{-1}$ ]	
$E_s$ .....Surface trap energy [eV]	

---

<b>Q-factor</b> .....Quality Factor	$\mu_p$ .....Hole mobility [ $\text{cm}^{-2} \cdot \text{V} \cdot \text{s}^{-1}$ ]
<b>R</b> _____	<b>V</b> _____
$r$ .....Photonic Crystal Hole Radius [normalized]	$V_\chi$ .....Non-linear optical volume [ $\text{m}^3$ ]
<b>U</b> _____	<b>W</b> _____
$\mu_n$ .....Electron mobility [ $\text{cm}^{-2} \cdot \text{V} \cdot \text{s}^{-1}$ ]	$\omega_0$ .....Resonance pulsation [ $2\pi \times \text{Hz}$ ]

# Chemical Elements

---

---

<b>A</b> _____	<b>L</b> _____
<b>Au</b> .....Gold	<b>LTG-GaAs</b> .....Low-Temperature Grown GaAs
<b>B</b> _____	<b>PMMA</b> .....PolyMethyl MethAcrylate
<b>BCB</b> .....BenzoCycloButene	<b>N</b> _____
<b>G</b> _____	<b>Ni</b> .....Nickel
<b>GaAs</b> .....Gallium Arsenide	<b>S</b> _____
<b>GaInP</b> .....Gallium Indium Phosphide	<b>Si</b> .....Silicon
<b>Ge</b> .....Germanium	<b>SiO<sub>2</sub></b> .....Silica
<b>I</b> _____	<b>T</b> _____
<b>InGaAs</b> .....Indium Gallium Arsenide	<b>TMA</b> .....TriMethylAluminium
<b>InP</b> .....Indium Phosphide	



# List of Figures

---

---

1-1	ENOB Vs input frequency according to Walden . . . . .	8
1-2	Different sampling case . . . . .	9
1-3	ADC power consumption . . . . .	9
1-4	Processing chain for sampling and under-sampling case . . . . .	10
1-5	Laser jitter – integrated MLL . . . . .	11
1-6	ENOB Vs input frequency according to Khilo . . . . .	12
1-7	Auston’s principle for the photoconductive switch . . . . .	13
1-8	Schematic of all-optical switching . . . . .	18
1-9	Normalized effective carrier concentration in time . . . . .	20
1-10	State of art of the all-optical switch . . . . .	21
2-1	III-V alloyed lattice matched diagram . . . . .	34
2-2	Layout schematic example . . . . .	35
2-3	SEM image of the under etching issue . . . . .	36
2-4	SEM image of the under-etching result with a FIB cut . . . . .	37
2-5	SEM image of different attempt to under-etch the structure . . . . .	38
2-6	SEM image of a FIB cut after under-etching with Ti/Pr contacts . . . . .	39
2-7	Cracked membrane after resist deposition prior to metal deposition. . . . .	40
2-8	Bonding process . . . . .	41
2-9	Press for bonding . . . . .	42
2-10	BCB phase diagram . . . . .	42
2-11	Bonded structure . . . . .	43
2-12	Badly thinned samples . . . . .	43
2-13	Well process bonded samples . . . . .	44
2-14	Final sample for photoconductive switch . . . . .	46
3-1	Current continuity schematic . . . . .	53
3-2	Recombination process . . . . .	55
3-3	Ambipolar approximation schematic . . . . .	57

3-4	Analytic Vs modeled PN junction . . . . .	59
3-5	Modeled temporal diffusion . . . . .	60
3-6	Current conservation verification . . . . .	61
3-7	Schematic of one cavity coupled to an input and output port . . . . .	62
3-8	Two coupled cavities and access waveguides and related parameters in the CMT model. . . . .	63
3-9	Linear Transmission calculated and form experiment . . . . .	65
3-10	Calculated impulse response $h_0$ and the spatially averaged and normalized carrier density, with spatial distribution at several time for $H_0$ cavity . . . . .	71
3-11	Decay of the effective carrier density for several design . . . . .	73
3-12	Calculated spectral shift for InP and GaAs for different design . . . . .	74
3-13	Direct and TPA absorption instantaneous frequency shift comparison . . . . .	76
4-1	Photonic Molecule SEM picture . . . . .	85
4-2	Pump-probe principle schematic . . . . .	85
4-3	Spectrally and temporally pump-probe setup . . . . .	86
4-4	Results from Pmp Probe resolved temporally and spectrally experiment . . . . .	87
4-5	Frequency first order moment shift . . . . .	88
4-6	Transmission spectra versus pump-probe delay, . . . . .	89
4-7	Homodyne pump-probe experiment setup. . . . .	90
4-8	Homodyne Pump-Probe measurements . . . . .	91
4-9	10GHz wavelength conversion on InP PhC . . . . .	92
4-10	Wavelength conversion operation at 10GHz . . . . .	93
4-11	Optical link schematic . . . . .	95
4-12	All-optical sampling in the time domain . . . . .	95
4-13	All optical sampling in the frequency domain . . . . .	96
4-14	Simulation of the output signal power $P_{out}$ at $f_{diff}$ regarding the signal RF power $P_{MZ}$ . . . . .	97
4-15	CMT modeling with modification carrier lifetime . . . . .	98
4-16	ALD coated sample . . . . .	99
4-17	Pump Probe experimental setup and device transmission spectra . . . . .	100
4-18	ALD process steps . . . . .	101
4-19	ALD roughness measurement . . . . .	102
4-20	Pump-Probe result for ALD coated and uncoated samples . . . . .	104
4-21	Transmission and Spectral shift for coated and uncoated sample . . . . .	105
4-22	Oxidation and resonances shift for the uncoated sample . . . . .	107
4-23	Pump Probe results for different passivation material . . . . .	108
4-24	Schematic of the wavelength conversion setup with GaAs ALD passivated sample . . . . .	110
4-25	Wavelength conversion experiment at 5GHz on GaAs PhC . . . . .	111

4-26	Time-resolved homodyne non-degenerate pump-probe measurements . . . . .	112
4-27	Time-resolved homodyne non-degenerate pump-probe measurements with two pulses	112
4-28	Time-resolved homodyne non-degenerate pump-probe measurements with 4 pulses and output signal spectra . . . . .	113
4-29	Sample image and transmission spectra . . . . .	115
4-30	Transmission spectra of the InP doped sample . . . . .	115
4-31	Time-resolved experimental transmission spectra . . . . .	116
4-32	Comparison of the dynamics of P-doped and undoped InP all-optical gate . . . . .	118
4-33	Calculated decay of the effective carrier density . . . . .	120
5-1	Sample stack structures . . . . .	129
5-2	Band Diagram of triangular lattice PhC . . . . .	130
5-3	PhC edgemode principle . . . . .	131
5-4	Band folding principle for light extraction . . . . .	132
5-5	Cross polarized setup for resonance characterization of edge-mode cavities. TLD: Tunable Laser Diode , BS; Beam Splitter (50/50), PBS: Polarized Beam Splitter . .	133
5-6	Edge-mode structure characterization . . . . .	133
5-7	SEM image of the L <sub>5</sub> cavity with extractor (colored hole) with superimposed the optical mode. A waveguide is coupled to the cavity acting as input or output port depending on the excitation (through waveguide of from top) . . . . .	134
5-8	Cavity Design for Electro-Optical sampling application . . . . .	135
5-9	FDTD simulations of the cavity . . . . .	135
5-10	Waveguide defect cavity for electro-optics sampling with in-line coupled waveguide	136
5-11	FDTD simulation of the input PhC waveguide . . . . .	137
5-12	Rib waveguide design . . . . .	137
5-13	Transmission of the microwave strip lined for ON and OFF state . . . . .	138
5-14	One ground system . . . . .	139
5-15	FDTD simulation with metal pads . . . . .	140
5-16	Cavity optical characterization . . . . .	141
5-17	ON/OFF RF characterization . . . . .	142
5-18	Microwave Setup . . . . .	143
5-19	Basic MW characterization . . . . .	143
5-20	Impulse response of the photoconductive switch . . . . .	144
5-21	Time response of the photoconductive switch . . . . .	145
5-22	Impulse response dependence Vs static bias and optical power . . . . .	147
5-23	Current Vs optical power . . . . .	148
5-24	Electro-optic sampling operation . . . . .	149
5-25	Sub-sampling operation and output signal dependency of input power . . . . .	151
5-27	Doping area for better ON conductivity . . . . .	153

5-28 SEM image of the PhC aligned with the implantation . . . . .	153
A-1 PN junction geometry . . . . .	161

# List of Tables

---

---

2.1	Self-suspended photonic crystal membrane fabrication summary (case of GaAs). . .	36
2.2	Adhesive bonding process summary (case of GaAs). . . . .	45
3.1	Simulation Parameters value used in the CMT model for bare GaAs, ALD-coated GaAs and InP . . . . .	66
3.2	$V_{\chi}$ and $h_0(0)$ for several PhC design . . . . .	72
3.3	Material Parameters value use in the CMT model for GaAs, InP and InGaAsP . . . .	76
3.4	Model, summarized . . . . .	77
5.1	$Q$ -factor simulated by LUMERICAL for the structure without metallic pad and for the structure reported in Fig. 5-15 . . . . .	140
B.1	Simulation Parameters value used in the CMT model (described in section 3.2) which are matching with the experimental pump-probe results fir the bare GaAs, ALD-coated GaAs and InP shown in chapter 4 . . . . .	167





# Titre: Dynamique Non-Linéaire dans les Nano-Structures Semiconductrices pour le Traitement du Signal

**Mots-Clés:** Traitement du Signal, Optique Intégrée, Optique Non-Linéaire, Semiconducteur, Cristaux Photoniques

**Résumé:** Cette thèse porte sur la numérisation de signaux hyperfréquences en utilisant une horloge optique, possédant une gigue temporelle très faible en comparaison des horloges électroniques. Une faible gigue est un facteur clé de l'échantillonnage à haute performance, car l'horloge commande l'ouverture d'une "porte" qui extrait les échantillons du signal à intervalles réguliers. Cette thèse décrit deux approches originales : l'échantillonnage purement optique et l'échantillonnage électro-optique. Une porte électro-optique se constitue d'une ligne coplanaire transportant le signal électrique. Cette ligne présente une discontinuité qui devient conductrice sur commande optique grâce à un matériau photoconducteur. Les alliages semi-conducteurs du groupe III-V sont souvent utilisés car la mobilité de ces porteurs photo-générés est suffisamment élevée, ce qui est favorable à une bonne conductivité à l'état "on". Le GaAs, en particulier, présente l'avantage d'une conductivité faible à l'état "off" du fait de la largeur de la bande interdite électronique. Cela explique l'intérêt de ce matériau, cependant, cela impose aussi une contrainte sur la longueur d'onde de la source laser, expliquant l'utilisation de sources autour 800 nm.

Dans cette thèse l'utilisation de sources laser à verrouillage de modes à fibre, développées dans le domaine des Télécoms, donc plus facilement accessibles, tout en gardant le GaAs comme matériaux actif est explorée. Cela est possible en exaltant

l'efficacité de l'absorption à deux photons, effet faible dans la plupart des structures. L'approche suivie porte sur l'utilisation d'une cavité à cristaux photoniques. Le très fort confinement et le très faible volume occupé par le mode optique se traduit en une très forte absorption non linéaire. De plus, la nano-structuration du semi-conducteur réduit de manière considérable le temps de vie des porteurs, ce qui permet un retour suffisamment rapide à l'état "off". L'étude se conclut par la démonstration de la fonction d'échantillonnage.

La même fonction a été étudiée dans le cas où le signal hyperfréquence se trouve sur une porteuse optique. La fonction porte "tout optique" est réalisée par un résonateur à cristaux photoniques. La génération de porteurs par absorption à deux photons induit un déplacement spectral de la résonance, ce qui est exploité pour moduler la transmission du dispositif. Une porte optique rapide, capable en principe de traiter des signaux dépassant les 50 GHz a été montrée. Cette porte requiert une puissance de commande de l'ordre de 200 fJ/impulsion, ce qui est suffisamment faible pour utiliser des sources lasers compactes (diode laser) et, de ce fait, outre sa très faible taille, peut être intégrée facilement.

# Title: Non-Linear Dynamics in Semiconductor Nano-Structures for Signal Processing

**Keywords:** Signal Processing, Integrated Optics, Non-linear Optics, Semiconductor, Photonic crystals

**Summary:** This thesis is focused on the digitalization of radio-frequency signal using optical clock, allowing a low time jitter compared to electronic clocks. A low jitter is a key factor for high performance sampling, as the clock commands the "gate" opening which extracts the signal samples at regular intervals. This thesis describes two original approaches: all-optical sampling and electro-optics one.

An electro-optic gate is based on radio-frequency transmission strip-line carrying the electric signal. A discontinuity in this strip-line occurs which become conductive, thanks to the optical command provided by the clock, due to a photo-conductive material. Semiconductor alloys from the III-V groups are widely used thanks to the high mobility of the photo-generated carriers allowing a high "on" state. In particular, GaAs present a good "off" state due to its band-gap energy. However, this restrains the optical clock wavelength explaining the use of optical sources around 800 nm.

In this thesis, the focus was made on using mode-locked lasers in the Telecom range, thus using the improvement made on these sources during the past decades, while keeping GaAs as the active material in the electro-optic sampler. This is made possi-

ble by exalting the efficiency of two-photon absorption, which is usually weak in common structures. The approach followed here is to use a photonic crystal cavity. Thanks to its high optical mode confinement, non-linear absorption becomes efficient enough to generated carriers to modify the resistivity of the material. In addition, the nano-structuration of the material reduce tremendously the carrier lifetime, owing to switch from an "on" to "off" state fast enough to sample high frequency signals.

The same function has been studied in the case where the signal is not carried electrically but optically. The all-optical gate function is realized using two photonic crystal resonators coupled together. The carrier generation by two-photon absorption induces a spectral shift of the resonance, used to modulate the transmission of the device. A fast all-optical gate, enabling signal processing up to 50 GHz is demonstrated here. The gate only requires a control power of about 200 fJ per pulses, which is low enough to use integrated optical sources (laser diodes) and, thanks to the small footprint, be easily integrated.

Cette thèse porte sur la numérisation de signaux hyperfréquences en utilisant une horloge optique, possédant une gigue temporelle très faible en comparaison des horloges électroniques. Une faible gigue est un facteur clé de l'échantillonnage à haute performance, car l'horloge commande l'ouverture d'une "porte" qui extrait les échantillons du signal à intervalles réguliers. Cette thèse décrit deux approches originales : l'échantillonnage purement optique et l'échantillonnage électro-optique.

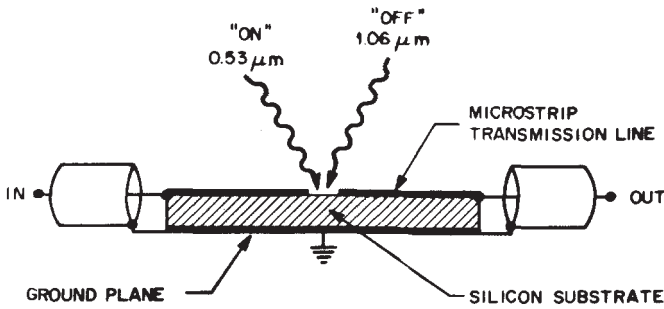


Figure 1 – Schéma du photo-commutateur proposé par Auston

Une porte électro-optique se constitue d'une ligne coplanaire transportant le signal électrique (fig. 1). Cette ligne présente une discontinuité qui devient conductrice sur commande optique grâce à un matériau photoconducteur. La génération de porteur étant uniforme sur la totalité de la discontinuité RF, le temps de vie des porteurs détermine entièrement le temps de commutation de la porte. Le principe du photo-commutateur a été développé pendant les années 70 par Auston [1]. Cependant, ce dernier travaillait avec du Silicium, relativement massive, entraînant un temps de vie des porteurs long et donc un temps de commutation tout aussi long.

Les alliages semi-conducteurs du groupe III-V sont souvent utilisés car la mobilité de ces porteurs photo-générés est suffisamment élevée, ce qui est favorable à une bonne conductivité à l'état "on". Le GaAs, en particulier, présente l'avantage d'une conductivité faible à l'état "off" du fait de la largeur de la bande interdite électronique. Cela explique l'intérêt de ce matériau, et les différentes études menées sur la modification du temps de vie des porteurs, notamment par croissance à base température du GaAs le réduisant à quelques picosecondes [2]. Cependant, cela impose aussi une contrainte sur la longueur d'onde de la source laser, expliquant l'utilisation de sources autour 800 nm [3].

Dans cette thèse l'utilisation de sources laser à verrouillage de modes à fibre, développées dans le domaine des Télécoms, donc plus facilement accessibles, tout en gardant le GaAs comme matériaux actif est explorée. Cela est possible en exaltant l'efficacité de l'absorption à deux photons, effet faible dans la plupart des structures. L'approche suivie porte sur l'utilisation d'une cavité à cristaux photoniques. Le très fort confinement et le très faible volume occupé par le mode optique se traduit en une très forte absorption non linéaire. De plus, la nano-structuration du semi-conducteur réduit de manière considérable le temps de vie des porteurs, ce qui permet un retour suffisamment rapide à l'état "off". L'étude se conclut par la démonstration de la fonction d'échantillonnage avec

l'utilisation d'une horloge optique à  $1.5 \mu\text{m}$  et une cadence de 2 GHz. La fonction de conversion de fréquence en bande de base est aussi démontrée (fig. 2).

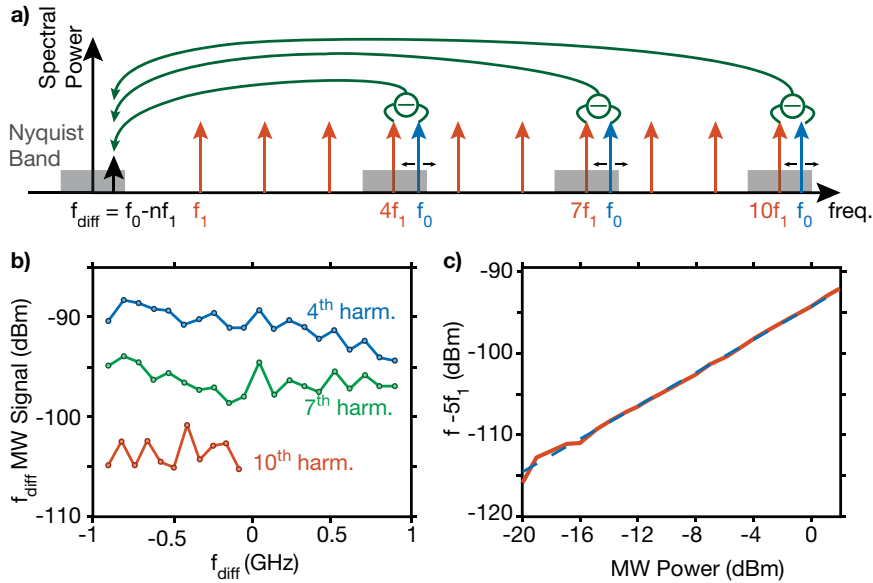


**Figure 2** – a) Principe de la décente en fréquence d'un signal micro-onde — b) Mesure du signal ramené en bande de base en utilisant la 4ème, 7ème et 10ème harmonique du laser à 2 GHz — c) Linéarité de l'opération en fonction de la puissance RF d'entrée

La même fonction a été étudiée dans le cas où le signal hyperfréquence se trouve sur une porteuse optique. La fonction porte “tout optique” est réalisée par un résonateur à cristaux photoniques. La génération de porteurs par absorption à deux photons induit un déplacement spectral de la résonance, ce qui est exploité pour moduler la transmission du dispositif. Une porte optique rapide, capable en principe de traiter des signaux dépassant les 50 GHz à été montrée. Cette porte requiert une puissance de commande de l'ordre de 200 fJ/impulsion, ce qui est suffisamment faible pour utiliser des sources lasers compactes (diode laser) et, de ce fait, outre sa très faible taille, peut être intégrée facilement.

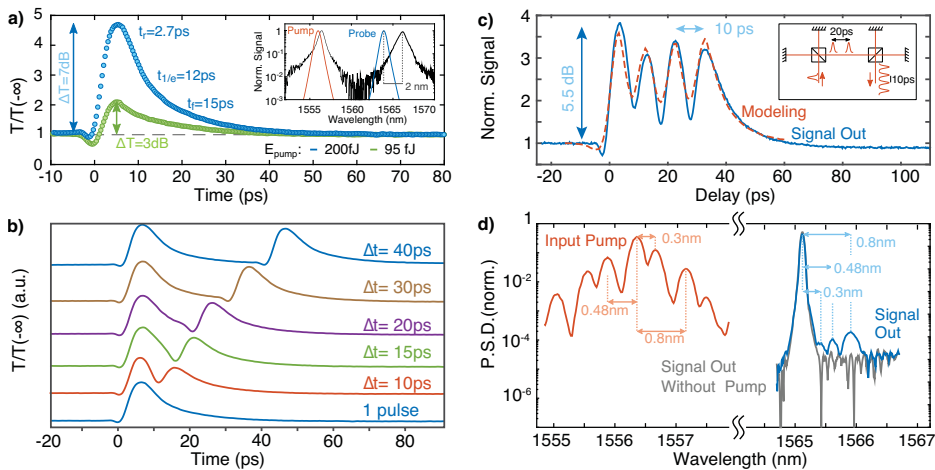


**Figure 3** – a) Mesure homodyne de la dynamique du système — b) Mesure homodyne avec 2 impulsions séparées temporellement — c) Mesures avec 4 impulsions séparées de 10 ps — d) Spectre en entrée et sortie avec 4 impulsions séparées de 10 ps

## Bibliographie

- [1] D. H. Auston. *Picosecond optoelectronic switching and gating in silicon*. *Appl. Phys. Lett.* **26** (1975). – p. 2.
- [2] K. H. Tan, S. F. Yoon, S. Wicaksono, W. K. Loke, D. S. Li, N. Saadsaoud, C. Tripon-Canseliet, J. F. Lampin, D. Decoster, and J. Chazelas. *Low temperature grown GaNAsSb: A promising material for photoconductive switch application*. *Appl. Phys. Lett.* **103** (2013). – p. 2.
- [3] C. Tripon-Canseliet, S. Faci, A. Pagies, V. Magnin, S. Formont, D. Decoster, and J. Chazelas. *Microwave On/Off Ratio Enhancement of GaAs Photoconductive Switches at Nanometer Scale*. *J. Lightwave Technol.* **30** (2011). – p. 2.